Development of Human iPSC-Derived 3D Cortical Constructs for Repair of Traumatic Brain Injury

Dr Mona Abdelfatah Mokhtar Mohamed Barkat

St John's College, University of Oxford
Department of Physiology, Anatomy and Genetics

Thesis submitted in fulfilment of the requirements for the degree of Doctor of Philosophy

University of Oxford
Michaelmas Term 2025

Development of Human iPSC-Derived 3D Cortical Constructs for Repair of Traumatic Brain Injury

Thesis submitted in fulfilment of the requirements for the degree of Doctor of Philosophy

University of Oxford
Michaelmas Term 2025

Dr Mona Abdelfatah Mokhtar Mohamed Barkat

St John's College, University of Oxford
Department of Physiology, Anatomy and Genetics

Supervised by

Professor Zoltán Molnár

Professor Francis Szele

Professor Pawel Swietach

ABSTRACT

Traumatic brain injury (TBI) causes neuronal loss and disruption of cortical circuitry, and current therapeutic strategies remain limited. Cell-based approaches hold promise, yet repairing the cerebral cortex is particularly challenging due to its complex structural and functional organisation. I hypothesised that, following TBI, implantation of 3D neuronal constructs derived from temporally specified early and late neuronal progenitor cells (ENPCs and LNPCs) can enhance implant survival and enable identity-dependent integration with the host cortex. Furthermore, the implantation of two-layered neuronal tissue that mimics key aspects of cortical lamination would facilitate the reconstruction of cortical columnar circuits by promoting both local and long-range connectivity.

Human-induced pluripotent stem cells (hiPSCs) were differentiated into cortical neurons with distinct laminar fates: ENPCs, enriched in CTIP2+ subcerebral neurons, and LNPCs, enriched in SATB2+ callosal projecting neurons. Both populations are composed of excitatory glutamatergic and inhibitory GABAergic phenotypes that established functional synaptic networks, as confirmed by calcium imaging. hiPSCs-derived ENPCs and LNPCs were used to generate 3D ENPC and LNPC constructs, respectively, using a droplet-based microfluidic system. 3D constructs retained fundamental laminar-specific molecular profiles and exhibited distinct network activity reflecting their temporal developmental identity. When 3D ENPC and LNPC constructs were assembled into two-layered neuronal tissues, mimicking basic aspects of cortical lamination, they exhibited inter-laminar structural and functional connections. Functional calcium imaging of the two-layered neuronal tissue and cross-correlation analysis revealed temporal coordination between the two layers, consistent with reciprocal interactions.

In vivo, implantation of hiPSC-derived RFP+ NPC constructs into postnatal NOD-SCID mice with aspiration-induced cortical injury resulted in robust survival, vascularisation, and progressive neuronal differentiation of the implants. RFP+ NPC implants contributed to circuit reconstruction in vivo, evidenced by implant-derived projections that extend across major white matter tracts, reaching cortical, subcortical, and subcerebral targets. Subsequently, 3D ENPC or 3D LNPC constructs were implanted separately into the same TBI model and evaluated after two months. They displayed distinct axonal projection patterns that matched their neuronal identities. The 3D ENPC implants preferentially targeted subcortical regions and white matter pathways, while 3D LNPC implants exhibited localised cortical projections.

Finally, the implantation of two-layered neuronal tissues further advanced architectural reconstruction, with ENPC compartment extending long-range connections, and LNPC compartment supporting local integration, thereby recapitulating the complementary projection patterns of deep- and upper-layer cortical neurons. Together, these findings demonstrated that temporal identity could influence the projection patterns and integration of the implants into the host brain, and that spatially patterned cortical tissues can restore both local and long-range connectivity. Further research is required to determine whether the implantation of 3D neuronal constructs, along with their structural integration, can restore the functional aspects of cortical circuitry. My thesis highlights the importance of constructing 3D neuronal tissues comprising predefined neuronal subtypes as a foundation for anatomically guided and personalised neural repair strategies following cortical injury.

ACKNOWLEDGEMENTS

I want to express my sincere gratitude to my supervisors. I am especially grateful to Professor Zoltán Molnár, who provided me with the opportunity to join his laboratory and pursue my DPhil at the University of Oxford. I am equally thankful to Professor Francis Szele for his continuous support throughout my work. My sincere thanks also go to Professor Pawel Swietach; I feel fortunate to have you as a supervisor. I sincerely appreciate your time, your encouragement, and all the scientific and non-scientific conversations we shared.

I am thankful to my colleagues and laboratory members for their support and collaboration. I am particularly grateful to Dr Luana Campos Soares, with whom I worked closely on this project. My thanks also go to Miss Gretchen Greene, whose positivity and high spirit consistently uplifted the group, along with her strong commitment; to Dr Elisa Marozzi Cruz, for her valuable contributions to the project; and to Miss Rabeah Abdul Razak, for her kindness and warm smile. I am equally thankful to Mr Stanley Sau, a master's student, for his dedication and thought-provoking questions. I would also like to acknowledge my collaborators in Professor Hagan Bayley's group. I want to express my gratitude to Dr Linna Zhou for her thoughtful guidance and to Dr Yufan Xu and Dr Mingyu Li for their significant contributions.

Special thanks also to my colleagues across the wider group: Marlene, Jemima, Jun, Zubaida, Talia, and Diana, as well as members of Zoltán's group, including Dr Eri Kawashita, Dr Anna Hoerder-Suabedissen, Dr Sara Bandiera, Dr Florina Szabó, Dr Shiva Nischal, Dr Auguste Vadisiute, and Miss Marissa Mueller. I am also grateful to Dr Fernando Messore for his thoughtful conversations; to Mr Mohammed Abuelem for his assistance; and to Miss Flore Chedotal, not only for her help but also for the delightful cakes she brought to our laboratory meetings. I would also like to thank Dr Balzbeta Hulikova, in Pawel's group, for her invaluable guidance in setting up calcium imaging.

I would also like to extend my sincere thanks to the examiners of my Confirmation of Status, Professor Colin Akerman and Professor Esther Becker, for their valuable feedback and constructive suggestions, which helped to strengthen and refine the direction of this thesis.

I would also like to acknowledge the generous financial support of the Egyptian Ministry of Higher Education and Scientific Research and the Egyptian Cultural and Educational Bureau

in London, with special thanks to Professor Rasha Hussein and all the members of the bureau for their assistance and encouragement.

I am deeply grateful to my friends, who have been a source of strength, joy, and encouragement throughout this journey. My heartfelt thanks go to Dr Alaa Baazaoui, Dr Munazza Ebtikar, Miss Archana Ramesh, and Dr Filippos Sytilidis. A special mention goes to Professor Afaf El-Sagheer, Dr Zainab Hamid, Dr Heba Hashem, and my closest friend, Dr Jihad Kilany. I am particularly grateful to my friend Dr Heba Abdallah, with whom I started this journey and who will soon finish hers.

Finally, I extend my deepest gratitude to my parents, whose unconditional love and steadfast support made this journey possible. To my brothers, Mr Mohamed, Mr Abdullah, Mr Abdo, Mr Mokhtar, and Mr Atfi, for their love, encouragement, and belief in me, as well as to their wives and children, who have consistently provided me with warmth and affection.

STATEMENT

I confirm that the work presented in this thesis is my own unless specifically indicated. My research is part of a larger collaborative project led by Professors Zoltán Molnár, Francis Szele and Hagan Bayley. Professor Sally Cowley supplied the human iPSC line, while the culturing of iPSCs and differentiation into cortical neurons were performed in Professor Francis Szele's laboratory. The development of the microfluidic system used in this work and fabrication of the 3D neuronal constructs were conducted by postdoctoral fellows Dr Yufan Xu, Dr Mingyu Li, and Dr Linna Zhou in Professor Hagan Bayley's laboratory, Department of Chemistry at the University of Oxford. Calcium imaging was performed in Professor Pawel Swietach's laboratory.

Within this collaborative framework, the specific contributions per chapter are as follows:

Chapter 2:

I led the optimisation of the differentiation protocol, including tissue culture work and characterisation of iPSC-derived cortical neurons using immunohistochemistry and PCR, followed by assessment of functional activity and network functionality using calcium imaging. The data acquisition, analysis, and figure preparation were conducted by me.

Implantation of cell suspension injections and collection of brains were carried out by Dr Soares. Reconstruction of axonal projections after transplantation of ENPCs and LNPCs using Neurolucida was carried out by Dr Soares. The related data are presented in Figure 2.19A, C.

Chapter 3:

I led the preparation of iPSC-derived cortical neurons for printing and the collection and retrieval of the constructs after printing. I led the characterisation of 3D neuronal constructs using immunohistochemistry, followed by assessment of functional activity and network functionality using calcium imaging. Data acquisition, analysis, and figure preparation were performed by me.

The fabrication of microfluidic chips, setup preparation, and execution of the printing process were conducted by Dr Yufan Xu, Dr Mingyu Li, and Dr Linna Zhou in Professor Hagan Bayley's laboratory.

Professor Pawel Swietach developed the original script for calcium imaging data analysis and spike detection algorithms. Dr Soares helped in training the algorithms to detect calcium spikes by manually identifying the spikes and inputting this information into the system.

Chapter 4:

Implantation of 3D constructs was performed by Dr Soares. Brain collection was carried out jointly by Dr Soares and me. Sectioning of the brains was conducted collaboratively by Dr Soares, Miss Gretchen Greene, and me.

I led the collection and processing of brains implanted with RFP+ NPCs, including sectioning and performing immunohistochemistry for cortical and proliferation/apoptosis markers, as well as glial reaction and human-specific markers for Neurolucida tracing. Data acquisition, analysis, and figure preparation were performed by me for this immunohistochemistry cohort. I have utilised Neurolucida software to trace projections of RFP+ NPC implants. Immunostaining to assess vascularisation of RFP+ NPC implants, volume reconstruction of the RFP+ NPC implants using Neurolucida, and associated quantification were conducted by Dr Soares. The related data are presented in Figure 4.6B, D and Figure 4.10B, C.

I led the processing of brains implanted with 3D ENPC and 3D LNPC constructs, including immunohistochemistry to assess host glial responses and synapse formation. For brains implanted with two-layered neuronal tissues, I performed immunohistochemistry using human-specific markers to identify and trace the graft compartments and the projections. I acquired, analysed, and plotted the resulting imaging datasets. Mr Stanley and Miss Gretchen Greene used Neurolucida software to reconstruct axonal projections after implantation of 3D ENPC and LNPC constructs and of two-layered neuronal tissue. The related data are presented in Figure 4.8B, C and Figure 4.14B, C. MEA data acquisition was conducted collaboratively by Dr Fernando Messore, Miss Flore Chedotal, Mr Mohammed Abuelem, and me. Dr Fernando Messore developed the original script for the MEA data analysis. By the time I was able to conduct the experiment independently, I had carried out the data analysis and prepared the figures. I also acknowledge the specific technical guidance and support provided by colleagues and collaborators in the Acknowledgements section of this thesis.

Table of Contents

List of Figures

List of Tables

Abbreviations

Abbreviation	Definition
ACSF	Artificial cerebrospinal fluid
AM-MSCs	Amniotic fluid-derived mesenchymal stem cells
AMPA	α-amino-3-hydroxy-5-methyl-4-isoxazolepropionic acid
ATN	Immunodeficient athymic nude
BBB	Blood–brain barrier
BDNF	Brain-derived neurotrophic factor
BM-MNCs	Bone marrow-derived mononuclear cells
BM-MSCs	Bone marrow-derived mesenchymal stem cells
BMP	Bone-Morphogenetic Protein
BSA	Bovine serum slbumin
CA	Cornu ammonis
CCI	Controlled cortical impact injury
CGE	Caudal ganglionic eminence
CNMF	Constrained non-negative matrix factorization
CNS	Central nervous system
CNTF	Ciliary neurotrophic factor
CP	Cortical plate
CSF	Cerebrospinal fluid
CSPGs	Chondroitin sulphate proteoglycans
DG	Dentate gyrus
Dil	1,1′-Dioctadecyl-3,3,3′,3′-tetramethylindocarbocyanine perchlorate
DMSO	Dimethyl sulfoxide
DPF	Day post-Fusion
DPP	Day post-printing
ECM	Extracellular matrix
EE	Environmental enrichment
EEG	Electroencephalography
EGF	epidermal growth factor
EGTA	Ethylene glycol-bis(2-aminoethylether)-N,N,N',N'-tetraacetic acid
ENPCs	Early neuronal progenitor cells
ES	Electrical stimulation
ESCs	Embryonic stem cells
FNPSCs	Fetal neuronal/progenitor stem cells
FPI	Fluid percussion injury
GABAergic	Gamma-aminobutyric acid (GABA)-ergic
GCS	Glasgow Coma Scale
GDNF	Glial cell line-derived neurotrophic factor
GelMA	Gelatin methacrylate
HA	Hyaluronic acid
hSYP	Human specific Synaptophysin
IFN-γ	Interferon-γ
IHI	Inter hemispheric inhibition
IL-10	Interleukin-10
IL-1β	Interleukin-1β
INs	Interneurons

IO	Superparamagnetic iron oxide nanoparticle
IP3R	Inositol trisphosphate receptor
IPCs	Intermediate progenitor cells
iPSCs	Induced pluripotent stem cells
LDHV	Lactate dehydrogenase-elevating virus
LNPCs	Late neuronal progenitor cells
M1	Primary motor cortex
MEA	Multielectrode array
MEG	Magnetoencephalograms
MEP	Motor-evoked potential
MGE	Medial ganglionic eminence
MPA	Mycophenolate Mofetil
MPI	Month post-implantation
MPT	Month post-transplantation
MSCs	Mesenchymal stem cell
mtDNA	Mitochondrial DNA
MZ	Marginal zone
NGF	Nerve growth factor
NGN2	Neurogenin-2
NIM	Neural induction medium
NMDA	N-methyl-D-aspartate
NMDG	N-methyl-D-glucamine
NMM	Neural maintenance medium
NOD-SCID	Non-obese diabetic severe combined immunodeficient
NS	Number of slices
NSCs	Neuronal stem cells
NT-4	Neurotrophin-4
OExo	Organoid-derived exosomes
P7	Postnatal day 7
PB	Phosphate buffer
PBBI	Penetrating ballistic-like brain injury
PDGF	Platelet-derived growth factor
PDMS	Polydimethylsiloxane
PEG	Polyethylene glycol
PET	Positron emission tomography
PFA	Paraformaldehyde
PG ESCs	Parthenogenetic stem cells
pHEMA	Poly (2-hydroxyethyl methacrylate)
pHPMA	Poly (N-(2-hydroxypropyl) methacrylamide)
PN	Projection glutamatergic neurons
POA	Preoptic area
PP-TMS	Paired-pulse Transcranial Magnetic Stimulation
PSD-95	Postsynaptic density protein 95
PTFE	Polytetrafluoroethylene
QSI	Stoelting Quintessential Stereotaxic Injector
RFP	Red fluorescent protein
RGCs	Radial glial cells
ROCK	Rho-associated protein kinase
ROIs	Regions of interest
ROS	Reactive oxygen species
RyR	Ryanodine receptor
SIRPα	Signal Regulatory Protein alpha

SP	Subplate
TBI	Traumatic brain injury
tDCS	Transcranial direct current stimulation
TNF-α	Tumour Necrosis Factor-α
TRPC	Transient receptor potential canonical channel
UC-MSCs	Umbilical cord-derived mesenchymal stem cells
VEGF	Vascular endothelial growth factor
vRGCs	Ventricular radial glial cells
VZ	Ventricular zone
WPI	Week post-implantation
WPT	Week post-transplantation

Chapter :1 Introduction

1.1 Cerebral cortex organisation and development

1.1.1 Organisation of the cerebral cortex

The mammalian cerebral cortex is the foundation for higher cognitive functions, sensory perception, and the initiation of voluntary movements. Structurally, it exhibits a six-layered laminar organisation, with various cell types arranged into intricate circuits. Functionally, it is subdivided into specialised areas that are responsible for specific sensory, motor, or cognitive processes (Jones and Rakic, 2010, Kaas, 2012). There are two main types of neurons in the cerebral cortex: projection neurons (PNs) and interneurons (INs). PNs are primarily glutamatergic excitatory neurons, comprising approximately 80% of the cortical neurons (Gorski et al., 2002). Intracortical PNs include commissural neurons, which project to the contralateral hemisphere, and associative neurons, which connect regions within the same hemisphere. Subcortical PNs send their axons to the thalamus, cortico-thalamic PNs, and subcerebral PNs, send their axons to the brain stem and spinal cord (Molyneaux et al., 2007). INs are GABAergic inhibitory neurons that account for the remaining 20% of cortical neurons (Anderson et al., 2001) and provide the primary inhibitory input within cortical circuits (Kepecs and Fishell, 2014).

The cortical column is considered the fundamental structural and functional unit of the cerebral cortex, spanning the cortical layers vertically. The upper layers, layers I/II-III, are generally referred to as the supragranular layer, layer IV as the granular layer, and lower layers, layers V and VI, as the infragranular layers. The relative thickness and cellular composition of cortical layers vary across cortical areas (Molnár et al., 2020). Each layer is distinguished by characteristic neuronal subtypes and marker expression, including CUX1and CUX2 in layers II/III (Nieto et al., 2004, Yang et al., 2020), RORβ in layer IV (Schaeren-Wierners et al., 1997), CTIP2 in subcerebral PNs of layer V and to a lesser extent in corticothalamic neurons of layer VI (Arlotta et al., 2005), and FOXP2 in layer VI (Hisaoka et al., 2010).

This laminar architecture supports the canonical cortical microcircuit, with each layer contributing to the overall function of the cortical columnar unit (Fig. 1.1) (Bosman and Aboitiz, 2015). Layer VI PNs send excitatory axons to the thalamus and receive excitatory and inhibitory inputs from superficial cortical and subcortical regions (Gilbert, 1983). Layer V PNs

integrate diverse excitatory and inhibitory inputs and innervate subcerebral structures, including the spinal cord and brainstem. Layer IV is the primary target for thalamic afferents and mediates processing of sensory input (Kostovic and Goldman-Rakic, 1983). Layer III PNs project to ipsilateral and contralateral cortical regions, facilitating horizontal intracortical communication (Mrzljak et al., 1988), while also receiving convergent inhibitory inputs from INs located within the same layer and in deeper layers. Layer II PNs connect to nearby cortical areas and receive diverse synaptic inputs, contributing to local information processing. Finally, Layer I contains a dense plexus of axonal terminals from other cortical layers that form synapses onto the apical dendrites of pyramidal neurons located in deeper laminae (Bosman and Aboitiz, 2015). Together, this highly structured circuitry facilitates the dynamic integration and propagation of information essential for cortical function. Reconstructing both the structural cytoarchitecture and the functional circuitry remains a key challenge for regenerative therapies aimed at restoring cortical function after injury.

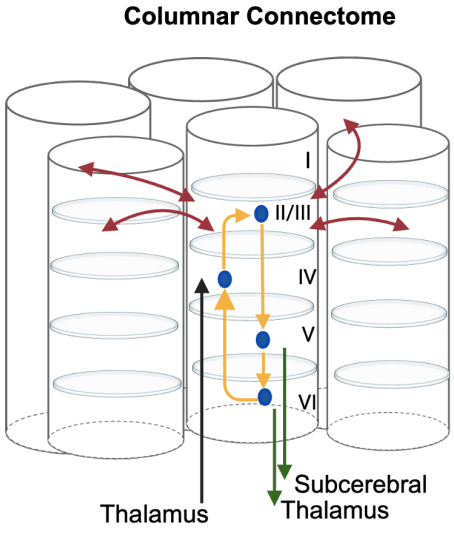

Figure 1.1 The canonical cortical column and its connections
The cortical column spans across the cortical layers. Layer VI PNs send excitatory axons to the thalamus (green arrow) and Layers V/VI project to subcerebral targets (green arrows). Layer IV receives inputs from the thalamus (black arrow). Layers II/III send outputs to other cortical columns within the same cortical area (red arrows). All six layers share information through inter-laminar connections (yellow arrows). Redrawn from (Roe, 2019).

1.1.2 Corticogenesis

Corticogenesis is the developmental process by which the cerebral cortex acquires its characteristic laminar architecture and connectivity. It begins with the generation of cortical neurons from progenitor cells, followed by post-mitotic migration, differentiation, and the establishment of synaptic connections that shape cortical circuitry (Noctor et al., 2004).

PNs and INs arise from distinct progenitors and follow different migratory routes. Excitatory PNs are generated locally from radial glial cells (RGCs) within the dorsal telencephalon (pallium) (Gorski et al., 2002, Rakic, 1971). In contrast, most GABAergic INs arise from the ventral telencephalon (subpallium), particularly the medial and caudal ganglionic eminence (MGE, CGE) and preoptic area (POA) (Gelman et al., 2009, Fishell, 2007).

The primary progenitors in the ventricular zone (VZ) are the ventricular radial glial cells (vRGCs), which undergo asymmetric division to generate vRGC and a nascent PN. In addition to their proliferative role, the radial glia also provide a scaffold along which new neurons can migrate radially toward the cortical plate (CP) (Kriegstein and Noctor, 2004). Additionally, vRGCs produce intermediate progenitor cells (IPCs) that undergo symmetric divisions to generate either neurons or further IPCs. The earliest-born neurons form the preplate, which later splits into the marginal zone (MZ) and subplate (SP) as additional neurons arrive in the CP (Luskin and Shatz, 1985). Cortical layering follows an inside–out sequence, with the deep layers populated first, followed by the upper layers (Tan and Shi, 2013).

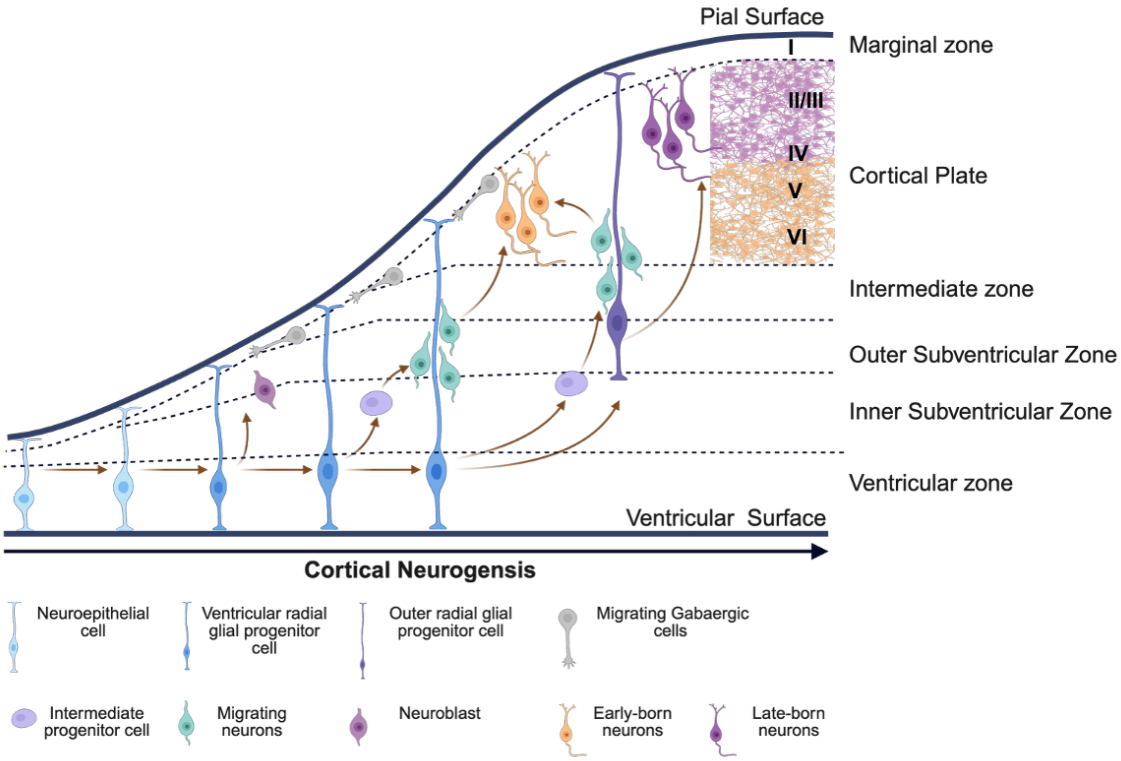

Figure 1.2 Schematic illustration of cortical neurogenesis and neuronal migration in the developing mammalian cortex
The cortical wall is organised into the ventricular zone, inner and outer subventricular zones, intermediate zone, cortical plate, and marginal zone. Neuroepithelial cells in the ventricular zone give

rise to vRGCs, which undergo asymmetric divisions to generate vRGCs and a nascent PN. IPCs undergo symmetric divisions to generate either neurons or further IPCs. Newly born excitatory PNs migrate radially along radial glial fibres and populate the cortical layers in an inside-out pattern. GABAergic INs originate from the ganglionic eminences and migrate tangentially into the developing cortex. Arrows indicate proliferative divisions and migratory routes. Redrawn from (Molnár et al., 2019).

INs migrate tangentially from subpallial regions to the cerebral cortex, traversing the MZ before integrating into local circuits (Miyoshi and Fishell, 2011). Their laminar positioning is largely determined by birthdate and subtype identity (Molyneaux et al., 2007, Kriegstein and Noctor, 2004), although some late-born INs can be redirected to superficial layers independently of their birthdate (Kohwi and Doe, 2013, Miyoshi and Fishell, 2011). Following neurogenesis, gliogenesis begins as RGCs switch to a gliogenic fate, giving rise to astrocytes, marking the transition from neuronal to glial production (Kriegstein and Noctor, 2004).

During corticogenesis, cortical network maturation is shaped by calcium signalling (Arjun McKinney et al., 2022). Calcium spikes display characteristic spatiotemporal patterns that regulate key neuronal differentiation processes, including neurotransmitter signalling, dendritic growth, and axonal development (Rosenberg and Spitzer, 2011). Distinct activity patterns are observed at successive developmental stages of corticogenesis, creating a comprehensive framework for the maturation of the neuronal network. This process begins with a phase of uncorrelated neural activity, followed by synchronised oscillations that give way to more complex network activity postnatally (Wu et al., 2024). Calcium spikes arise from both extracellular influx and intracellular release (Grienberger and Konnerth, 2012). Intracellularly, inositol trisphosphate receptors (IP3R) and ryanodine receptors (RyR) mediate the release of calcium from internal stores (Bootman and Bultynck, 2020). Calcium influx is mediated through various receptors and channels, including ionotropic glutamate receptors (AMPA, NMDA), voltage-gated calcium channels, nicotinic acetylcholine receptors, transient receptor potential type C channels and ORAI channels (Grienberger and Konnerth, 2012).

1.1.3 Arealisation of the cerebral cortex

The arealisation of the cerebral cortex, including the specification of the primary motor cortex (M1), is driven by a coordinated interaction between intrinsic transcriptional gradients and extrinsic signalling (Grove and Fukuchi-Shimogori, 2003). M1 is initially patterned and positioned within the rostral neocortex through a high anterior-to-posterior expression gradient of PAX6, accompanied by low levels of EMX2 (O'Leary et al., 2007). As thalamocortical

afferents from thalamic nuclei, including motor-related nuclei, innervate the cortical plate, they reinforce the identity of cortical areas, including M1, by driving region-specific gene expression and facilitating laminar differentiation (Vue et al., 2013, López-Bendito and Molnár, 2003).

M1 is characterised by the presence of layer V pyramidal PNs, which establish long-range corticobulbar and corticospinal tracts (Economo et al., 2018). In primates, M1 further displays subregional specialisation with the emergence of functional motor maps shaped by both genetic programmes and experience-dependent plasticity (Sanes and Donoghue, 2000).

1.1.4 Extracellular matrix (ECM) of the brain

The brain ECM accounts for approximately 20% of the adult brain's volume (Tonnesen et al., 2023). The brain ECM is a network scaffold occupied by cellular components of the brain and produced mainly by astrocytes and neurons (Nicholson and Sykova, 1998). It regulates fundamental neural processes, including neurite outgrowth, synaptogenesis, and synaptic plasticity (Dityatev et al., 2010). The ECM consists mainly of hyaluronic acid (HA) (Bignami et al., 1993), chondroitin sulphate proteoglycans (CSPGs), such as lecticans (Lander et al., 1996), and glycoproteins like tenascins. It contains relatively low amounts of collagen, fibronectin, and laminin (Ruoslahti, 1996, Bellail et al., 2004).

HA is considered the structural backbone of the ECM. It is a negatively charged glycosaminoglycan that attracts sodium ions, promoting water retention and hydration of brain tissue that contributes to brain stiffness (Bignami et al., 1993). Lecticans represent a key structural family of CSPGs in the brain, comprising aggrecan, versican, neurocan, and brevican. Neurocan and brevican are brain-specific and interact with HA and tenascins through distinct binding domains to stabilise the extracellular network (Yamaguchi, 2000). The tenascin family provides additional cell-binding sites within the ECM, with tenascin-C and tenascin-R having significant roles in the central nervous system (CNS). Tenascin-C modulates cell adhesion and detachment during migration (Anlar and Gunel-Ozcan, 2012, Jakovcevski et al., 2013), while tenascin-R stabilises the ECM by cross-linking lecticans (Yamaguchi, 2000, Suttkus et al., 2014).

Collagen in the nervous system includes fibrillar collagens, types I and III, and non-fibrillar type IV. While types I and III are implicated in signalling and repair, type IV is a core constituent of basement membranes, including those at the blood-brain barrier (BBB) (Chen et

al., 2015, Banerjee et al., 2016). Fibronectin, though sparse in the CNS, supports neuronal outgrowth, modulates synaptic activity, and exerts anti-inflammatory effects following injury (Liesi et al., 1986, Wang et al., 2013b). Laminins are heterotrimeric glycoproteins composed of α, β, and γ chains that form the basal lamina of blood vessels and neural tissues (Durbeej, 2010). In the CNS, laminin is essential for axon guidance, neuronal adhesion, and circuit formation during development (McKerracher et al., 1996, Luckenbill-Edds, 1997). Its strong interactions with integrins make it a key determinant of neuronal survival and guidance during CNS development (Durbeej, 2010).

Neural ECM is organised into perineuronal nets, dense reticular matrices surrounding neuronal bodies. Structurally, it consists of HA linked to the neuronal surface, bound by lecticans, with tenascin-R crosslinking the matrix. They buffer ions, protect against oxidative stress, and restrict excessive synapse formation (Suttkus et al., 2014, Yamaguchi, 2000, Wang and Fawcett, 2012). Peri-synaptic ECM, another specialised ECM structures, regulate growth factor sequestration and synaptic stabilisation (Frischknecht and Gundelfinger, 2012).

In addition to cellular and chemical properties, mechanical characteristics are essential for neuronal survival and neurite extension (Lu et al., 2006, Elkin et al., 2007). Stiffness varies not only between white and grey matter, but also across different developmental stages, during homeostasis, and in pathological conditions. These variations play a crucial role in regulating essential cellular functions, including density, migration, attachment, and communication (Lu et al., 2006). Experimental evidence highlights the importance of designing biomaterials that closely replicate the mechanical properties of native CNS tissue (Discher et al., 2005, Engler et al., 2006).

1.2 Traumatic brain injury (TBI)

Traumatic brain injury (TBI) is a catastrophic clinical problem because of its profound neurological and systemic consequences. It is defined as structural damage to brain tissue caused by an external mechanical force applied to the skull or brain, leading to temporary or permanent impairments in motor and cognitive function (Maas et al., 2010). The severity of TBI is clinically graded using the Glasgow Coma Scale (GCS) into mild, moderate, and severe categories, as follows: mild (13–15), moderate (9–12), and severe (<9) (Ghaffarpasand et al., 2013).

TBI comprises both focal and diffuse injuries (McGinn and Povlishock, 2016). Focal injuries result from direct impact and manifest as contusions or hematomas, and are associated with tissue necrosis, oedema, and BBB disruption. Diffuse injuries result from acceleration-deceleration or rotational forces, causing extensive axonal shearing across white matter tracts (McGinn and Povlishock, 2016).

Beyond the initial mechanical insult, TBI initiates a complex secondary injury cascade. Excessive glutamate release and excitotoxic activation of ionotropic receptors, leading to influx of calcium and sodium ions and efflux of potassium (Matsushita et al., 2000). These ionic alterations result in mitochondrial dysfunction (Lozano et al., 2015a), the accumulation of reactive oxygen species (ROS), and the activation of proteolytic enzymes, ultimately leading to cell death (Saatman et al., 2010). These events promote glial reaction and infiltration of peripheral immune cells, augmenting neuroinflammation (McGinn and Povlishock, 2016).

Astrocytes and microglia orchestrate a complex glial response after TBI that can be both protective and detrimental; this dual role of microglia and astrocytes has made them key targets for developing neuroprotective and regenerative strategies (Karve et al., 2016).

Astrocytes are the primary cells responsible for maintaining homeostasis in the CNS. They respond rapidly to injury by forming a glial scar, which isolates the damaged core from surrounding healthy tissue (Cieri and Ramos, 2025). This reactive astrocytosis exerts both protective and detrimental effects. On the one hand, they support brain repair through uptake of excitotoxic glutamate, stabilisation of extracellular ion balance, and BBB repair (Sofroniew and Vinters, 2010). On the other hand, they secrete pro-inflammatory molecules that enhance interactions with microglial cells and increase BBB permeability (Cieri and Ramos, 2025).

Microglia, the resident immune cells of the CNS, are activated by glutamate receptor signalling that triggers further glutamate release (Kaushal and Schlichter, 2008), and concurrent downregulation of astrocytic glutamate transporters, which reduces clearance and further elevates extracellular glutamate concentrations (Takaki et al., 2012). They undergo morphological transformation into pro-inflammatory M1 or anti-inflammatory M2, depending on environmental cues. M1 microglia secrete various cytokines that aid in clearing cellular debris (Zhao et al., 2025), while M2 microglia release trophic factors such as Nerve Growth Factor (NGF), Glial Cell Line–Derived Neurotrophic Factor (GDNF), and Brain-Derived

Neurotrophic Factor (BDNF) that promote neuronal survival, angiogenesis, and remyelination (Hu et al., 2015).

Classification of microglia into M1 proinflammatory and M2 anti-inflammatory is based on in vitro modelling of their responses to different immune stimuli, as assessed by transcriptional profile and phagocytic activity (Michelucci et al., 2009). This classification is an oversimplified framework for microglia and necessitates moving away from binary descriptors (Paolicelli et al., 2022). Consistent with this, Jha et al. generated a multi-model murine TBI single-cell atlas to resolve microglial heterogeneity with respect to covariates such as sex, region, and time. They identified multiple transcriptionally distinct microglial subtypes that were not well captured by binary inflammatory classification but instead followed state-like programmes that varied with injury context (Jha et al., 2024).

1.3 Different models of TBI and factors influencing the outcomes

A wide range of animal models has been developed to study TBI; despite anatomical and physiological differences from the human brain, they still replicate the primary and secondary cascades that define TBI. Commonly used models of TBI include fluid percussion injury (FPI), cortical impact injury (CCI), weight drop injury, penetrating ballistic-like brain injury (PBBI), and aspiration lesion model (Fesharaki-Zadeh and Datta, 2024).

In FPI models, the injury occurs when a pendulum strikes the piston of a fluid reservoir, creating a pressure pulse transmitted to the intact dura through a craniotomy. The craniotomy is either positioned midline or laterally over the parietal bone. The percussion produces brief displacement and deformation, with injury severity scales with pulse strength (McIntosh et al., 1989, McIntosh et al., 1987). The CCI model utilises a pneumatic or electromagnetic impact device to deliver a rigid impactor onto the exposed, intact dura through a unilateral craniotomy, typically located between bregma and lambda. This results in cortical tissue loss, acute subdural hematoma, axonal injury, concussion, and BBB disruption. Different mechanical factors, such as time, velocity and depth of impact, can be modulated to control the severity of the injury (Dixon et al., 1991). Weight-drop models apply a guided free-falling mass onto the exposed skull, with or without craniotomy. The severity of an injury can be modulated by adjusting the mass of the weight and the height of the fall (Feeney et al., 1981, Flierl et al., 2009). PBBI simulates penetrating injury using high-velocity projectiles that create a temporary cavity in the brain significantly larger than the projectile itself. The severity of the injury depends on the

projectile trajectory and the amount of energy transferred to the brain tissue (Williams et al., 2005).

Among these models, the aspiration lesion provides a controlled method for generating a focal cortical lesion by surgically removing a defined region. It creates a precise and reproducible lesion, making it advantageous for studying cell transplantation and tissue regeneration in a controlled environment. Unlike impact models, aspiration injuries do not involve mechanical compression or deformation of surrounding tissue. Moreover, it allows for the creation of a cavity into which the graft can be placed immediately after the injury. Therefore, this model was chosen in this thesis as the platform for testing the implantation of cortical constructs during the acute phase of brain injury.

Each model enables adjustment of injury parameters to control the severity, but it also presents limitations due to species-specific structural and behavioural differences. These differences complicate cross-species comparisons and the translation of preclinical findings to clinical human outcomes (Xiong et al., 2013). While in clinical settings, TBI severity is typically graded by GCS, preclinical studies rely on mechanical parameters, histopathological markers, and behavioural assessments to categorise injuries into mild, moderate, or severe (Xiong et al., 2013).

Several interrelated variables shape the outcome of TBI in both experimental and clinical contexts. The type of injury, whether focal or diffuse, blunt or penetrating, along with its anatomical location, critically influences tissue damage (Xiong et al., 2013). Age is another factor, as an aged brain has diminished antioxidant enzyme capacities (Delage et al., 2021b) and modulates injury through exaggerated glial reactivity (Norden and Godbout, 2013). The immune and inflammatory responses also play a crucial role in secondary injury, as persistent microglial activation and dysregulated cytokine production further exacerbate neuronal loss (Loane and Kumar, 2016).

Systemic comorbidities such as hypertension, diabetes, and obesity are known to impair cerebrovascular function and worsen TBI outcomes. Similarly, pre-existing psychiatric disorders and substance use complicate recovery trajectories (Hanafy et al., 2021). Endocrine dysregulation, including stress-induced glucocorticoid elevation and disrupted hormonal homeostasis, has also been shown to exacerbate neuroinflammation and metabolic dysfunction (Giordano et al., 2020).

Biological sex also significantly influences TBI outcomes (Krukowski, 2021). Preclinical studies indicate that female sex hormones have a neuroprotective effect (Bramlett and Dietrich, 2001). Similarly, clinical outcomes reported fewer comorbidities in menopausal and perimenopausal females compared to males following TBI (Berry et al., 2009), and another study reporting the role of the progesterone hormone in enhancing neurological recovery in patients with TBI (Junpeng et al., 2011). However, other reports contradict these findings, with females exhibiting the worst outcomes following TBI (Farace and Alves, 2000). This controversy highlights a gap in understanding sex-specific mechanisms in TBI, which likely involve complex interactions among hormonal, metabolic, and immune factors.

In addition to biological differences, environmental and rehabilitative conditions shape the outcome following TBI. In preclinical studies, enriched housing promotes sensorimotor and social stimulation, facilitating functional gains (Tapias et al., 2022). Similarly, in clinical settings, early multidisciplinary rehabilitation and strong social support are positively associated with improved outcomes (Nie et al., 2024). Together, these variables highlight the multifactorial nature of TBI outcomes and underscore the importance of incorporating biological, systemic, and environmental factors into both experimental design and clinical trials.

1.4 Cell therapy for TBI

TBI results in irreversible neuronal loss and circuitry disruption, while the adult brain has a limited intrinsic capacity for repair and remodelling (Vanacore et al., 2024). Conventional clinical approaches can stabilise patients and limit secondary injury, but do not restore lost neural networks (Tsai et al., 2024). Cell-based therapies have emerged as a promising approach for structural and functional restoration following TBI (Adugna et al., 2022). Stem cell-based therapies for TBI have demonstrated multiple beneficial effects in preclinical studies, including graft survival, multilineage differentiation, modulation of glial reactivity, promotion of angiogenesis, and support of functional recovery. These outcomes are mediated by several mechanisms, including direct cell replacement, immunomodulation, neuroprotection, and structural remodelling through biobridge mechanism (Adugna et al., 2022).

Various cell sources have been explored in preclinical models, including fetal neuronal/progenitor stem cells (FNPSCs) (Ma et al., 2012), adult brain-derived progenitors (Sun et al., 2011), embryonic stem cells (ESCs) (Haus et al., 2014), and induced pluripotent

stem cells (iPSCs) (Schantz et al., 2024). As well as mesenchymal stem cells (MSCs) from bone marrow (BM-MSCs), umbilical cord (UC-MSCs), amniotic fluid (AM-MSCs) and adipose tissue (Zhang et al., 2022).

Cell therapy strategies include both cell suspension injections and the implantation of 3D neuronal tissues. I will discuss these approaches, with emphasis on the different pluripotent stem cells employed, their potential structural and functional outcomes, and the mechanisms that mediate these effects.

1.4.1 Cell suspension injection

Among the earliest and most widely used strategies for delivering stem cells to the injured brain is the transplantation of dissociated neuronal stem or progenitor cells in suspension. This approach has been extensively investigated in rodent models of TBI and forms the foundation of the current understanding of neural replacement therapies. Early studies demonstrated the potential of exogenous cells to survive, differentiate and migrate across hemispheres following cortical injury (Wennersten et al., 2004). Moreover, neuronal integration with allografts has been reported in organotypic human cortical cultures, underscoring the translational relevance of this approach (Grønning Hansen et al., 2020). In the following sections, I will compare findings from studies that used cell suspension for TBI and highlight key factors affecting therapeutic efficacy and the underlying mechanisms.

1.4.1.1 Cell sources for cell suspension transplantation

1.4.1.1.1 Fetal neuronal/progenitor stem cells (FNPSCs)

FNPSCs were among the first cell sources investigated for their neuroregenerative potential. For instance, transplantation of human FNPSCs derived from a 10-week gestational forebrain into the peri-lesional cortex of immunosuppressed rats resulted in graft survival and multilineage differentiation (Wennersten et al., 2004). Similarly, human FNPSCs transplanted into the ipsilateral hippocampus survived and differentiated into neurons at 2 weeks post-transplantation (WPT), accompanied by significant cognitive improvement (Gao et al., 2006). By contrast, mouse FNSPCs transplanted into the striatum one week after CCI preferentially differentiated into oligodendrocyte precursor cells. This was aligned with sustained motor function and marked recovery in spatial learning over 14 months post-transplantation (MPT) (Shear et al., 2004).

The neuronal subtypes derived from FNPSCs also mediate the recovery following TBI. Transplantation of GABAergic neurons derived from rat FNPSCs into the peri-lesional cortex of adult rats seven days after CCI resulted in significant sensorimotor recovery, compared to transplantation of astrocytic precursors (Becerra et al., 2007). Although transplantation of FNPSCs can promote sustained motor improvement, these effects do not necessarily translate into recovery of cognitive functions, which remains an unresolved challenge. Transplantation of murine C17.2 FNPSCs into either the ipsilateral or contralateral cortex–hippocampus interface three days after injury in immunocompetent adult C57BL/6 mice demonstrated long-term graft survival, with different differentiation profiles. Although motor recovery was observed in both groups, no cognitive improvement was reported (Riess et al., 2002).

Genetic modification of transplanted FNPSCs, whether by overexpressing neurotrophins such as NGF or BDNF, or transcriptional regulators like CEND1, enhances survival, neuronal fate commitment, synaptic integration, and functional recovery. Transplantation of rat HiB5 FNPSCs-overexpressing NGF into the cortex of adult male Wistar rats 24 h after FPI improved neuromotor and cognitive function compared with controls transplanted with unmodified FNPSCs (Philips et al., 2001). Similarly, transplantation of BDNF-overexpressing FNPSCs three days after TBI resulted in superior survival, enhanced neuronal differentiation, and increased synaptic protein expression compared with unmodified FNPSCs (Ma et al., 2012). At the transcriptional level, overexpression of the fate determinant CEND1 in transplanted FNPSCs promoted neuronal differentiation, reduced glial scarring, and improved functional recovery in models of cortical injury compared to grafts of control FNPSCs (Wang et al., 2022b, Makri et al., 2010).

Although promising results have been obtained, other studies have highlighted the challenges of poor graft survival. For instance, transplantation of commercial NPSCs into the peri-lesional area one week after CCI resulted in only 1.4–1.9% of the grafted cells being retained at 2 WPT (Harting et al., 2009). Similarly, transplantation of mouse FNPSCs into the injured brain parenchyma resulted in detectable grafts in only a few brains (Wallenquist et al., 2009).

1.4.1.1.2 Adult brain tissue

Several studies have investigated the potential of neural progenitor cells (NPCs) derived from adult brain tissue in promoting repair following TBI. Compared with embryonic sources, adult tissue-driven NPCs exhibit more restricted neurogenic potential. For instance, NPCs derived

from the SVZ of the brains of adult rats were transplanted into the peri-lesional cortex two days after FPI. By 2-4 WPT, grafted cells migrated from the graft core into the surrounding tissue and differentiated into astrocyte and oligodendrocyte lineages (Sun et al., 2011). Similarly, Koutsoudaki et al., used postnatal hippocampal-derived NPCs in penetrating hippocampal injury. Both NPCs and IGF-I-transduced NPCs survived, migrated to myelin-rich regions near the lesion, and differentiated into oligodendroglia, but not into neurons or astrocytes. This was associated with a reduced glial reaction and restoration of spatial learning abilities (Koutsoudaki et al., 2016). These findings highlight a dual mechanism of functional recovery through both remyelination and modulation of inflammation, underscoring the therapeutic promise of these NPCs.

Together, these studies suggest that adult brain-derived NPCs contribute to TBI repair not through direct neuronal replacement, but primarily via glial-mediated mechanisms such as remyelination, astrocytic support, and the attenuation of inflammation.

1.4.1.1.3 Embryonic stem cells (ESCs)

ESCs are pluripotent cells capable of indefinite self-renewal and differentiation into derivatives of all three germ layers (Huang et al., 2015). These properties make them attractive for regenerative application in TBI. However, their clinical translation is limited by ethical concerns and the risk of teratoma formation when transplanted without controlled differentiation (Mountford, 2008).

Early studies illustrated both the therapeutic potential and the inherent risks associated with the transplantation of undifferentiated ESCs (Riess et al., 2007). Transplantation of undifferentiated mouse ESCs into the injured cortex of immunocompetent rats three days after lateral FPI led to improved motor performance. Although early graft survival was observed in all animals, only one animal retained viable grafts at 7 WPT. Additionally, 20% of the total transplanted animals developed tumours. This study highlights the tumourigenic risk associated with uncontrolled proliferation (Riess et al., 2007). Subsequent approaches focused on lineage-committed ESC derivatives to mitigate tumourigenic risk. Haus et al., implanted CD133-enriched, xeno-free, hESCs-derived neuronal stem cells (NSCs) into immunodeficient rats with CCI. The grafts survived for up to 5 MPT, and differentiated into mature neurons, astrocytes, and oligodendrocytes with no evidence of tumorigenesis (Haus et al., 2014). Similarly, Hoane and colleagues grafted ESC-derived neuronal and glial precursors into the

lesion cavity of adult rats, seven days after CCI. The transplanted cells migrated to subcortical regions and differentiated into mature neuronal and glial lineages (Hoane et al., 2004).

Moreover, Liu and colleagues showed the feasibility of ESC-based strategies in non-human primates by transplanting GFP-labelled, rhesus ESC-derived NSCs into the cortices of monkeys post-TBI (Liu et al., 2024a). The cells localised at the injury site for over a year and differentiated into synaptically integrated neurons. Though behavioural improvements were not significant, the long-term survival and integration support translational potential (Liu et al., 2024a).

Cryobanked hESC-derived NSCs have also been applied in chronic injury with long-term promising outcomes. Transplantation of cryopreserved hNSCs into six cortical sites of rats four weeks after CCI resulted in survival of over 50% of the cells and increased the neuronal survival in the ipsilateral hippocampus at 3 MPT. The transplanted animals demonstrated significant recovery in spatial learning and memory, as well as a reduced risk-taking behaviour (Badner et al., 2021).

Parthenogenetic stem cells (PG ESCs) are pluripotent cells derived from the chemical activation of oocytes. Although they lack a paternal genome, these cells retain the ability to self-renew (Brevini and Gandolfi, 2008) and differentiate into functional neuron-like cells (Ahmad et al., 2012). Lee et al., demonstrated a dose-dependent therapeutic effect of PG ESCs-derived NSCs after intracerebral injection in a rat model of moderate TBI. Moderate and high doses significantly improved motor and cognitive performance, relative to low doses. These findings emphasise the role of cell dosage in driving regenerative outcomes, suggesting that an adequate cell number is necessary to elicit neuroprotective and functional benefits (Lee et al., 2019).

1.4.1.1.4 induced pluripotent stem cells (iPSCs)

iPSCs were first introduced by Takahashi and Yamanaka in 2006, when mouse fibroblasts were reprogrammed into iPSCs using viral vectors to express OCT4, SOX2, c-MYC and KLF4 (Takahashi and Yamanaka, 2006). This groundbreaking technique was adapted for use in human cells the following year (Takahashi and Yamanaka, 2006, Takahashi et al., 2007). Unlike ESCs, iPSCs bypass ethical concerns and offer the possibility of autologous transplantation. However, some challenges remain regarding genomic stability, reprogramming efficiency, and the risk of tumorigenesis (Yamanaka, 2020).

Multiple rodent studies have demonstrated that iPSC-derived NPCs can survive, differentiate, and integrate after transplantation into the injured cortex. Tang et al., transplanted human iPSC-derived NPCs, labelled with superparamagnetic iron oxide nanoparticles (SPIOs), into the peri-lesional cortex of adult rats one week after CCI. The grafts differentiated into neurons and astrocytes and were non-invasively tracked with MRI for up to four weeks (Tang et al., 2013). These results align with a study conducted with Jiang et al., using a similar CCI model implanted with rat iPSC-derived NPCs labelled with SPIOs. Manganese-enhanced MRI was conducted at four weeks, revealing functional activity of the grafts, which was abolished by the calcium-channel blocker, confirming synaptic integration (Jiang et al., 2019). Together, these studies validate the feasibility of long-term tracking of functional integration of iPSC-derived NSCs *in vivo*.

Modulating cellular states through preconditioning or genetic engineering has further enhanced therapeutic efficacy. Transplantation of hypoxia-preconditioned iPSC-derived NPCs into paediatric rats three days after CCI improved social and behavioural deficits, correlating with elevated expression of oxytocin and its receptor (Wei et al., 2016). To reduce the tumourigenic risk, iPSC-derived NSCs were engineered to express a suicide gene, yeast cytosine deaminase-uracil phosphoribosyl transferase (yCD-UPRT) upon administration of 5-fluorocytosine. This approach enabled the selective ablation of undifferentiated and tumourigenic cells and was associated with reduced cerebral atrophy and improved sensorimotor recovery (Imai et al., 2023).

Beyond cell-intrinsic modifications, the host environment has a significant influence on regenerative potential. Dunkerson et al., showed that iPSC transplantation combined with environmental enrichment (EE) fully restored cognitive performance in adult rats post-CCI to levels comparable to those of uninjured controls (Dunkerson et al., 2014).

Recent studies have evaluated the therapeutic potential of human iPSC-derived NPCs in a CCI model in piglets, as a transition step from rodent models to clinically relevant large-animal systems. iPSC-derived NPCs were injected into peri-lesional brain tissue five days after craniectomy. At 12 WPT, they acquired multilineage differentiation potential and reduced neuroinflammation (Schantz et al., 2024). A follow-up study investigated the synergistic effects of iPSC-derived NPCs transplantation and postoperative physical rehabilitation. One-month-old piglets received iPSC-derived NPCs injections a week post-injury, then they began

a 12-week progressive treadmill regimen a week later. MRI analysis revealed a significant reduction in lesion volume, midline shift, and white matter degradation following both interventions. However, only the combined treatment produced superior outcomes, including enhanced neuroblast proliferation, attenuated astrocytosis, and significant improvements in motor and exploratory behaviours (Schantz et al., 2025a).

Despite promises, iPSCs still raise safety concerns regarding the potential for de novo mutations. iPSCs can accumulate de novo mitochondrial DNA (mtDNA) mutations during reprogramming and long-term culture, leading to the formation of immunogenic neoepitopes and immune responses, even in autologous settings. This finding has profound implications in the field of cell therapy for TBI, where immune activation can exacerbate injury and limit graft survival. Furthermore, it explains the discrepancy between *in vitro* potential and *in vivo* efficacy observed in some iPSC-based graft studies, emphasising the importance of genetic screening of iPSC lines in future clinical protocols (Deuse et al., 2019).

Collectively, these studies demonstrate the potential of iPSC-based therapies for repairing TBI. They confirm the feasibility of long-term graft survival and tracking, show the impact of cellular preconditioning and genetic engineering, and highlight translational relevance through large-animal validation. Nevertheless, they also reveal critical safety concerns, particularly related to immunogenicity, which must be addressed in future clinical applications.

1.4.1.2 Therapeutic mechanisms of cell suspension transplantation

Beyond the choice of cell source, the mechanisms of action underlying suspension injections are diverse.

1.4.1.2.1 Cell replacement

Cell replacement is a fundamental mechanism by which transplanted cells contribute to tissue repair after TBI. Several studies have documented the capacity of transplanted exogenous cells to survive, migrate, and differentiate in the host brain. However, genuine neuronal replacement is often limited, particularly when delivery routes other than local intraparenchymal transplantation are used (Skardelly et al., 2014).

The differentiation potential of transplanted cells into different lineages varies across studies; some studies show multilineage differentiation of hESCs-derived NSCs into neuronal and glial fates, including astrocytes, oligodendrocytes, and microglia. For instance, hESC-derived NSCs

had long-term survival for up to 5 MPT, with differentiation into mature neurons, astrocytes, and oligodendrocytes. However, a significant percentage of cells remained Nestin-positive and undifferentiated even after 20 WPT (Haus et al., 2016).

Other reported more restricted fates, with differentiation confined largely to neurons and astrocytes only. Interestingly, a common feature among these studies was the peri-lesional site of graft transplantation. For example, peri-lesional transplantation of FNPSCs was accompanied by differentiation into neurons and astrocytes, but not oligodendrocytes (Wennersten et al., 2004). Similarly, the majority of peri-lesionally transplanted FNPSCs differentiated into DCX+ neuroblasts, with a small fraction differentiating into astrocytes (Gao et al., 2016). Likewise, hypoxia-preconditioned mouse iPSC-derived NPCs transplanted into peri-contusion regions differentiated into neurons and astrocytes 2 WPT (Wei et al., 2016). Another piece of evidence supporting the role of the brain region in driving the differentiation of transplanted cells is shown by the transplantation of murine C17.2 NSCs into the ipsilateral and contralateral hemispheres of the same brain. The NSCs transplanted into the ipsilateral hemisphere expressed both neuronal and astrocytic markers, whereas the grafts in the contralateral hemisphere primarily differentiated into neurons, showing no glial expression (Riess et al., 2002). By contrast, transplanted mouse FNPSCs may adopt an oligodendroglial fate, rather than differentiating into other cell types, after being transplanted into the striatum (Shear et al., 2004). Similarly, postnatal hippocampal NPCs differentiated into oligodendroglia after being transplanted into the injured hippocampus (Koutsoudaki et al. 2016).

1.4.1.2.2 Immunomodulation mechanism

Beyond direct cell replacement, transplanted NSCs modulate the post-injury microenvironment through passive and active immunomodulation. Transplanted hNSCs mediated a microglial transition from M1 to M2, resulting in decreased levels of proinflammatory cytokines and increased levels of anti-inflammatory cytokines as early as seven days post-transplantation (Gao et al., 2016). The NSCs actively regulate immune responses by monitoring and counteracting inflammatory metabolism via the succinate–SUCNR1 pathway axis. The activated macrophages release extracellular succinate, which binds to SUCNR1/GPR91 on NSCs, triggering the secretion of the immunomodulatory prostaglandin E_2. This cascade reduces succinate levels in the cerebrospinal fluid (CSF) and shifts microglia from a pro-inflammatory to an anti-inflammatory phenotype (Peruzzotti-Jametti et al., 2018). The immunomodulatory effect is also dose-dependent, with high-dose hNSC transplantation (1.6

million cells) resulting in significantly reduced microglial activation and a more ramified microglial morphology compared to low-dose transplants (0.16 million cells) (Andreu et al., 2023). Importantly, immunomodulation can be achieved via non-invasive routes of stem cell therapy. Intranasal administration of hNSCs resulted in a decrease in gene expression signatures associated with microglial activation and macrophage function (Amirbekyan et al., 2023).

1.4.1.2.3 Neuroprotection mechanism

Cell therapy has been shown to promote endogenous neuron survival, neurogenesis, and synaptic neuroplasticity in both cortical and hippocampal regions (Badner et al., 2021). These effects appear to arise primarily through neurotrophin-mediated mechanisms rather than direct cell replacement. Mechanistic illustration shown by Yan et al., who demonstrated that NSCs promoted recovery by elevating cortical levels of neurotrophic factors, including BDNF, GDNF, NGF, Neurotrophin-3 (NT-3), and ciliary neurotrophic factor (CNTF) (Yan et al., 2013). Similarly, transplantation of BDNF-overexpressing NSCs increased BDNF mRNA expression at 1 and 2 WPT (Ma et al., 2012). In addition, the transplantation of mouse-derived NSCs elevated BDNF and Synaptophysin levels in the injured brain, while BDNF knockdown downregulated key pathways, including Wnt and GSK3-β (Xiong et al., 2018). These findings further support BDNF's central role in mediating structural and synaptic repair following NSC transplantation.

These trophic effects are passage- and dose-dependent. High-passage hNSCs significantly increased the number of surviving endogenous neurons within both the dentate gyrus (DG) and cornu ammonis (CA) regions of the hippocampus, with no significant differences between vehicle and low-passage hNSCs at 20 WPT (Haus et al., 2016). Additionally, transplantation of high-dose, PG ESCs-derived NSCs enhanced neuronal survival in the peri-lesion cortex and increased the expression of neural lineage and myelination markers (Lee et al., 2019).

1.4.1.2.4 Biobridge mechanism

Tajiri and colleagues introduced a novel therapeutic concept, the biobridge mechanism, to explain how transplanted cells facilitate brain repair (Tajiri et al., 2013). Their experiments involved MSCs transplanted into injured rat brains, where the cells formed a temporary scaffold linking the SVZ with the damaged cortical tissue. This cellular bridge was enriched in matrix metalloproteinases that remodelled the surrounding ECM and enabled the migration of the endogenous NPCs toward the injury site. Over time, this cellular bridge was gradually

replaced by host-derived cells, suggesting a role in supporting and guiding rather than permanently integrating (Tajiri et al., 2014, Tajiri et al., 2013).

1.4.1.3 Factors influencing the outcomes of cell suspension injection in TBI

1.4.1.3.1 Cell passage

Cell passage number is a critical determinant of the therapeutic efficacy of NSC transplantation, with high-passage NSCs (Passage 27) exhibiting a significantly higher neurotrophic effect relative to low-passage NSCs (Passage 7) (Haus et al., 2016). This study emphasises the crucial role of quality control and passage optimisation in preparing stem cell lines for clinical use.

1.4.1.3.2 Cell dose

The neuroprotective and immunomodulatory effects of NSC transplantation are dose-dependent, necessitating adequate dosing to elicit measurable regenerative effects. Moderate and high doses of NSCs reduced gliosis, enhanced myelination, and increased peri-lesional neuron survival (Lee et al., 2019). Similarly, transplantation of high-dose NSCs had a significant immunomodulatory effect compared to low-dose NSCs (Andreu et al., 2023). Together, these studies confirm that subtherapeutic doses are insufficient to elicit measurable benefits and emphasise the need for dose optimisation.

1.4.1.3.3 Transplantation window

The timing of transplantation relative to injury progression significantly influences therapeutic outcomes. Studies have examined transplantation during the acute (24–72 h), subacute (3–14 days), and chronic (> 14 days) phases post-injury, showing varied outcomes due to the changing pathological environment of the injured brain.

Transplantation during the acute phase targets early neuroinflammatory cascades and limits secondary damage, facilitating functional recovery (Shang et al., 2022). Studies demonstrated that NSC transplantation within 24–72 h after injury enhanced motor recovery, increased synaptic plasticity, and upregulated neurotrophic factors (Xiong et al., 2018, Ma et al., 2012). Similarly, NGF-expressing NPCs transplanted 24 h after FPI promoted hippocampal neuron survival (Philips et al., 2001), while fetal NSCs transplanted within 24 h exhibited BDNF-mediated cognitive recovery (Gao et al., 2006). However, the highly inflammatory environment may compromise graft survival and increase the risk of adverse effects, such as tumour formation (Riess et al., 2007).

The subacute phase coincides with the partial resolution of acute inflammation, is considered the most favourable window for transplantation, as it reduces inflammatory hostility while facilitating graft survival and integration (Shang et al., 2022). Transplantation of E14.5-derived NPCs seven days after CCI improved both motor and cognitive recovery, with benefits lasting up to one year (Shear et al., 2004). Similarly, hNPCs transplanted during this window promoted hippocampal neurogenesis and restored cognition (Blaya et al., 2015, Haus et al., 2016). However, other studies have reported motor improvement but no cognitive gains with NSCs transplanted seven days after injury (Harting et al., 2009, Hoane et al., 2004).

Cell therapy in the chronic phase of TBI offers opportunities for neuronal differentiation and modulation of glial responses (Shang et al., 2022). Transplantation of hNSCs four weeks post-CCI improved spatial learning, reduced risk-taking behaviour, and enhanced hippocampal neuronal survival and DG morphology (Badner et al., 2021). In contrast, Zhang et al., reported that human post-mitotic neurons transplanted into rodent brains four weeks after lateral FPI integrated into the host brain but did not result in significant motor or cognitive improvements (Zhang et al., 2005).

Collectively, while the subacute phase appears to provide the favourable window for engraftment and functional benefit, both acute and chronic transplantation windows offer distinct therapeutic opportunities. Acute delivery may modulate early inflammatory cascades, whereas chronic transplantation can promote long-term regeneration and plasticity. Ultimately, the optimal timing of transplantation should be aligned with the pathophysiological stage of injury and the intended therapeutic mechanism.

1.4.1.3.4 Administration route

Various delivery routes have been explored for cell therapy in TBI, each offering distinct advantages and limitations regarding targeting precision, invasiveness, and translational feasibility. Intracerebral injection is considered the most direct and invasive method in preclinical studies, enabling precise delivery of cells into the injured cortex and overcoming obstacles such as cell migration across the glial scar barrier. Intracerebral injection facilitated engraftment, differentiation, and structural integration (Blaya et al., 2015). However, the lesion may present an unfavourable microenvironment for direct injection, which potentially lowers the survival rate of transplanted cells (Wallenquist et al., 2009).

Intrathecal delivery into the CSF allows broader distribution of the cells in the CNS, bypassing the BBB, with a promising outcome. Intrathecal administration of peripheral nerve–derived stem cell spheroids significantly improved sensory and motor function, with considerable tissue recovery in damaged areas (Shin et al., 2024). Likewise, intranasal delivery offers a non-invasive way to bypass systemic circulation, promoting cell migration to injured hippocampal areas and reducing neuroinflammation (Amirbekyan et al., 2023).

Systemic intravenous delivery is the most common route of delivery; it is easily accessed and minimally invasive, but it raises concerns about poor CNS homing, dilutional effects, and the risk of entrapment in different organs (Pischiutta et al., 2021, Leibacher and Henschler, 2016). In a comparative study, the therapeutic efficacy of local and systemic delivery of NPCs was evaluated, with both delivery routes yielding sustained motor improvements, reduced lesion volumes, and increased neuronal survival over a 12-week period. However, follow-up studies showed only transient benefits from systemic delivery (Skardelly et al., 2011, Skardelly et al., 2014). The different outcomes between the two studies suggest that systemic delivery may enhance early recovery through a paracrine effect. Still, local delivery is more effective for targeted tissue preservation and long-term recovery.

In summary, direct routes such as intracerebral and intraventricular administration offer superior CNS targeting and cell retention but are more invasive. In contrast, indirect routes such as intrathecal and intravenous delivery are more clinically feasible but may require optimisation to improve targeting efficiency and durability of effects.

1.4.1.4 Limitations of cell suspension injection

Despite the promising results of cell suspension transplantation, several limitations restrict its therapeutic potential. First, poor graft survival is common in the hostile post-injury environment, in addition to limited cell retention within the lesion cavity (Wallenquist et al., 2009, Amer et al., 2017). Secondly, the lack of anatomical structure in cell suspensions hinders reconstruction of the laminar cytoarchitecture of the cortex, which is crucial for functional recovery. Moreover, uncertain lineage differentiation and limited synaptic circuit integration further limit their efficacy (Grade and Gotz, 2017). These shortcomings have led the field to adopt tissue-based strategies, utilising cerebral organoids and 3D bioengineered cortical tissue.

1.4.2 Organoid implantation for TBI

Brain organoids are stem cell-derived 3D neuronal tissues with a self-organising cellular architecture that resembles the structural and functional properties of the developing brain. They have been utilised as a platform for studying brain development, investigating neurodevelopmental disorders, and drug discovery (Lancaster and Knoblich, 2014). Advances in neuronal differentiation enable the generation of organoids with different regional identities, including cortex (Eiraku et al., 2008), forebrain (Birey et al., 2017), hippocampus (Sakaguchi et al., 2015), choroid plexus (Pellegrini et al., 2020), striatum (Miura et al., 2020), thalamus (Xiang et al., 2019), hypothalamus (Wataya et al., 2008), midbrain (Jo et al., 2016), and cerebellum (Muguruma et al., 2015).

Organoid transplantation provides several benefits over cell suspension injection. Organoids act as a multicellular built-in niche to restore lost cells after TBI. Their microenvironment effectively supports the implanted cells, making them less susceptible to inflammation, which ultimately enhances their survival and recovery. Moreover, protocols consistently produce brain–region–specific organoids, allowing for better anatomical and functional alignment with the injured area. Restoration of structural repair and tissue continuity is achievable through the implantation of 3D organoids.

In the following sections, I will review studies on organoid implantation into both intact and injured cortex and explore the underlying mechanisms behind the observed outcomes.

1.4.2.1 Organoid implantation into intact cortex

The implantation of human brain organoids into an intact rodent cortex provides critical insight into the baseline integration capacity under physiological conditions. The rationale of these studies was to allow implanted organoids to mature within a structurally intact host brain. Across multiple studies, this approach has yielded robust evidence for graft survival, vascularisation, neuronal differentiation, and functional integration. Pioneered work demonstrated long-term survival of hESC-derived cerebral organoids upon transplantation into the retro-splenial cortex of adult non-obese diabetic severe combined immunodeficient (NOD-SCID) mice. Within one week, two-photon microscopy revealed host-derived vascularisation, with functional blood flow. By six months, optogenetic stimulation confirmed the integration of graft-derived neurons into the host's synaptic circuits (Mansour et al., 2018). Similarly, transplantation of hiPSC-derived cortical organoids into the retro-splenial cortex of adult

female NOD-SCID mice resulted in their vascularisation as early as 9 weeks post-implantation (WPI), as captured using two-photon imaging. Organoid cells migrated to the adjacent cortex, with evidence of human-mouse synaptogenesis. Visual stimuli elicited electrophysiological responses in the organoid, mirroring those of the surrounding cortex, indicating sensory-driven integration (Wilson et al., 2022).

Given that the absence of vasculature is a significant limitation in organoid maturation *in vitro*, strategies to enhance vascular support have been investigated, yielding promising outcomes (Mei et al., 2025). Prevascularisation of the organoids through co-culturing with human umbilical vein-derived endothelial cells resulted in the formation of internal tube-like vessels. When transplanted into the sensory cortex of adult NOD-SCID mice, these vessels anastomosed with the host vasculature, establishing a functional network that supported graft survival and maturation at 2 months post-implantation (MPI). This work highlights the importance of vascular support for long-term engraftment (Shi et al., 2020).

The cellular composition and secretome profile of organoids vary across different maturation stages (Yentur et al., 2025), which in turn shape the outcomes of implantation. Implantation of either 6-week or 10-week hiPSC-derived cerebral organoids into the frontal cortex of severe combined immunodeficiency (SCID) mice resulted in high survival rates. However, younger grafts extended more corticospinal projections by 12 WPI, though at the expense of higher proliferative activity that raises the risk of overgrowth (Kitahara et al., 2020).

Progressive circuit integration has been observed across multiple studies with organoid implantation. When hiPSC-derived cerebral organoids were implanted into the medial prefrontal cortex of adult NOD-SCID mice, they survived and developed corticospinal-like projections. Bidirectional connectivity was evidenced by both spontaneous graft activity and host neuron responses to light stimulation of the organoid at 3 and 5 MPI (Dong et al., 2021). Extending this work, Revah et al., transplanted hiPSC-derived cortical organoids into the somatosensory cortex of newborn immunodeficient athymic nude (ATN) rats. Organoids developed advanced structural integration with thalamic and cortical inputs, as well as widespread axonal projection outputs. Human neurons within the graft responded to light and whisker stimulation, and optogenetic activation of graft neurons induced reward-seeking behaviour, indicating functional recruitment into host sensory and motivational circuits (Revah et al., 2022).

Electrical stimulation (ES) has emerged as a strategy to enhance organoid maturation prior to implantation. Bioelectricity was input into cortical organoids by ES with a multi-electrode array (MEA). When ES-pretreated hiPSC-derived organoids were implanted into the primary sensory cortex of NOD-SCID mice, they exhibited enhanced vascularisation, greater synaptic integration, and more extensive projections compared to controls. Functional assessments revealed improved locomotor activity and recognition memory, while electrophysiological recordings confirmed synchronous firing between graft and host cortices, indicative of functional integration (Li et al., 2024).

Collectively, these preclinical studies of organoid implantation into intact cortex reveal the intrinsic potential of organoids to structurally and functionally integrate with the host brain. Yet the interpretation of results and applicability in the TBI context still differ because the inflammatory condition can alter the integration potential. Therefore, while these studies establish feasibility and reveal cellular and circuit-level outcomes, they must be complemented by injury models to assess the true translational potential of organoid therapy for brain repair.

1.4.2.2 Organoid implantation into TBI

The implantation of human pluripotent stem cell–derived organoids into rodent models of TBI has provided critical insight into their therapeutic potential under pathological conditions. I will present the findings according to outcome domains, covering axonal outgrowth and neuronal integration, functional recovery, vascular integration, and immune modulation and compatibility.

1.4.2.2.1 Axonal outgrowth and neuronal integration

Implanted brain organoids consistently demonstrate the capacity to extend axons into host tissue and to establish synaptic connections; however, the organisation and functional consequences of this outgrowth vary across models. Early evidence of axonal growth was shown after implantation of a cerebral organoid into the frontoparietal cortex of neonatal CD1 mice with cortical lesions. However, this outgrowth lacked organised projection patterns, even 4 WPI (Daviaud et al., 2018). Later, more structured connectivity was reported with the implantation of ESC-derived cerebral organoids into the motor cortex of adult rats with biopsy-induced lesions. Graft-derived cells migrated along white-matter tracts and colonised distant brain regions in both the ipsilateral and contralateral cortices. This was also accompanied by increased synaptic marker expression relative to the injured controls, indicating enhanced implant-host connectivity (Wang et al., 2020b).

Additional evidence was obtained with the implantation of hESCs-derived cortical organoids into SCID mice 7 days after CCI of the sensorimotor cortex. Neuronal progenitors within the graft differentiated into multiple subtypes and extended long projections bilaterally, with evidence of synapse formation. MEA recordings of acute brain slices revealed spontaneous activity and stimulus-evoked responses in graft regions 70 days post-implantation, confirming functional activity of human neurons in the graft (Bao et al., 2021).

Bidirectional and circuit-specific integration of organoids into the damaged visual network was shown by implantation of hiPSC-derived organoids of occipital identity into adult rats with cortical aspiration lesions in the visual cortex. Efferent projections extended into adjacent and subcortical regions, especially visual system-related thalamic nuclei. In parallel, the organoids received afferent inputs from both host visual areas and the retina. Extracellular recording of the graft showed spontaneous activity as early as 1 MPI with spike characteristics comparable to those of native neurons. Two months later, the graft responded robustly to visual stimuli, with some neurons displaying orientation selectivity comparable to that of native visual cortical neurons (Jgamadze et al., 2023).

From a translational perspective, axonal outgrowth is a protracted process that requires months of sustained graft survival and patient stability. Furthermore, because primate brains span an approximately 350-fold size range and larger brains have longer pathway lengths and conduction delays, reconstruction of long-range circuits demands longer observation windows than in rodents (Ardesch et al., 2022, Caminiti et al., 2009). In a fundamental study, 10-week cerebral organoids were implanted into the precentral gyrus of monkeys. Graft survival and vascularisation were detected in two out of four monkeys at 12 WPI. Fibres targeted the surrounding cortical area as well as the subcortical tissue, though not into distal tracts such as the internal capsule (Kitahara et al., 2020). These findings necessitate the need for extended observation periods to confirm axonal extensions over greater distances.

Collectively, organoids implanted into injured brains can send long-range efferent projections, receive afferent inputs, and integrate into functional neural circuits. However, their cellular heterogeneity raises concerns regarding off-target projections that may disrupt intact host networks. Future strategies to refine connectivity would include the use of regionally specified neuronal subtypes, chemotactic guidance cues, or biomaterial scaffolds to direct axonal growth along physiologically appropriate pathways.

1.4.2.2.2 Functional recovery

Functional recovery is a key translational standard, and several studies demonstrate behavioural improvements following organoid implantation. When cortical organoids were implanted into a lesioned motor cortex, motor abilities were restored as early as the 5th day post-implantation, reaching normal levels three weeks later (Wang et al., 2020b). Improvements in cognitive function after organoid implantation have been reported in mouse models, including enhanced spatial learning and memory, as measured by the Morris water maze and passive avoidance tests (Bao et al., 2021), as well as improved performance in the novel object recognition memory test (Kim et al., 2022).

These results demonstrate that organoids can survive in injured brain environments and contribute to the repair of functional circuitry, leading to measurable behavioural gains. However, further studies with long-term assessments using standardised behavioural tests would enhance understanding of the mechanisms underlying recovery and ensure reproducibility across models, thereby strengthening the translational relevance of organoid-based therapies.

1.4.2.2.3 Vascular integration

Vascularisation is a prerequisite for the survival and maturation of grafted neural tissue, ensuring delivery of oxygen and nutrients (Nwokoye and Abilez, 2024). Across multiple studies, transplanted cerebral organoids consistently exhibited robust infiltration by host-derived vasculature. Early evidence of angiogenesis was reported within 2 WPI, with extensive CD31+ networks observed throughout the graft and maintained up to four weeks (Daviaud et al., 2018, Wang et al., 2020b). Subsequent work confirmed angiogenesis at a later stage, 4 WPI, by identifying CD31+ endothelial structure (Bao et al., 2021). The presence of host-derived vasculature correlated with reduced apoptosis and preserved graft volume, underscoring the central role of vascular integration in sustaining viable and functional implants (Jgamadze et al., 2023).

Although vascularisation is consistent, it does not occur immediately, leaving organoids susceptible to ischemia and shrinkage during the early post-implantation period. Addressing this vulnerability will be crucial for successful clinical translation. Future strategies may include pre-vascularisation of the organoids or genetic modification to overexpress pro-

angiogenic factors. Moreover, long-term monitoring is necessary to ensure the establishment of a functional neurovascular unit that can sustain grafts over extended periods.

1.4.2.2.4 Immune modulation and compatibility

Xenograft transplantation of human cells into rodent brains faces the challenge of immune rejection (Jiang et al., 2021), necessitating the use of immunodeficient animals (Bao et al., 2021) or immunosuppressants (Wang et al., 2020b, Kim et al., 2022, Jgamadze et al., 2023). Beyond compatibility, studies demonstrated an anti-inflammatory effect of organoids, evidenced by a decrease in astrocytosis and microglial activation in peri-lesional tissue after implantation (Kim et al., 2022, Bao et al., 2021). Even in the absence of measurable anti-inflammatory effects, organoid implantation did not exacerbate immune responses at the injury site, with levels of pro-inflammatory cytokines and activated glial markers no higher than those of injured controls (Wang et al., 2020b). Nevertheless, the reliance on immunosuppression or immunodeficient animals limits translational relevance, and future work should incorporate immunocompetent hosts in long-term studies. A deeper understanding of host–graft immune crosstalk dynamics could reveal opportunities to apply organoids not only as structural replacements but as modulators of post-injury inflammation, enhancing both survival and integration.

1.4.2.3 Therapeutic mechanisms of organoid implantation for TBI

1.4.2.3.1 Cell replacement

In experimental TBI, grafted human cerebral organoids can contribute to repair through direct cell replacement. Transplanted organoids differentiated into neurons and enhanced motor recovery (Wang et al., 2020b). In a mouse CCI model, organoid grafts survived in lesion cavities, differentiated into cortical neurons, sent long-range projections, and improved spatial learning, consistent with the structural replacement of lost neurons (Bao et al., 2021). Forebrain organoids placed into the visual cortex integrated structurally and functionally, exhibiting reciprocal synaptic connectivity with host pathways (Jgamadze et al., 2023). Collectively, these data support cell replacement, maturation, and axon pathfinding of graft-derived human neurons as a key mechanism by which organoid transplantation can restore circuits after TBI.

1.4.2.3.2 Promotion of host neurogenesis and neuronal plasticity

While most studies focus on the fate and integration of grafted cells, emerging evidence suggests that organoid implantation may also stimulate endogenous neurogenesis and promote neuronal plasticity after TBI. For example, increased endogenous neurogenesis has been

reported within the DG 2 WPI (Kim et al., 2022). Similarly, upregulation of DCX (Bao et al., 2021) and Nestin (Daviaud et al., 2018) has been reported at the peri-implant site. Although the interpretation of these results is limited by the absence of lineage-tracing approaches, they still suggest that organoid transplantation may stimulate a regenerative response from endogenous progenitors.

Clarifying the interplay between graft and host neurogenesis could open new avenues for dual therapies that not only replace damaged tissue but also potentiate intrinsic neurogenesis. Future studies should employ specific markers, birth-dating strategies, and reporter mouse lines to distinguish host-derived neuroblasts and neurons from grafted cells.

1.4.2.3.3 Secretome profile and paracrine signalling

Beyond structural integration, organoids exert therapeutic effects through their secretome profile, which includes a wide range of immunomodulatory, angiogenic, and neurotrophic factors. Transplantation of cerebral organoids into a TBI model was associated with the upregulation of BDNF, NGF, and Epidermal Growth Factor (EGF) in the ipsilateral hippocampus, interpreted as a contribution to the paracrine functions of the transplanted organoids (Wang et al., 2020b).

Mechanistic insights have been elucidated through *in vitro* models. Microglia-containing cerebral organoids release anti-inflammatory cytokines such as IL-10 and Transforming Growth Factor-β (TGF-β), consistent with the immunomodulatory effects reported *in vivo* (Hong et al., 2023). Similarly, organoid-derived exosomes (OExo) exhibited antioxidant activity, including reduced ROS production, preservation of antioxidant capacity, and downregulation of pro-apoptotic genes (Ji et al., 2023). Cerebral organoids also secrete Vascular Endothelial Growth Factor (VEGF) and activate VEGF pathways (Fumado Navarro et al., 2025), contributing to angiogenic repair and consistent with the vascularisation observed *in vivo*. Furthermore, OExo are enriched for neurotrophins such as Neurotrophin-4 (NT-4) and GDNF, that promote neuronal differentiation (Ji et al., 2023).

Proteomic profiling further underscores the developmental stage–specific nature of the organoid secretome. At day 35 of differentiation, the profile is enriched in synaptic and adhesion-related proteins, including synaptic adhesion molecules, cell adhesion molecules, and ECM remodelling proteases, which are implicated in corticogenesis and circuit assembly. By day 50, the secretome shifts toward an ECM-rich composition, with collagens, laminins, and

fibronectin that consolidate neuronal survival and stabilise network connectivity. Total protein secretion increases with time, with distinct molecular signatures aligning with datasets from fetal brain organoids and CSF (Yentur et al., 2025).

Collectively, these findings establish the secretome as a key mediator of organoid-based repair, extending therapeutic potential beyond structural cell replacement. However, there is a lack of systematic profiling of secretome dynamics. Future research using high-throughput proteomic and transcriptomic platforms will be essential to identify key effector molecules and optimise organoid-derived or exosome-based strategies as clinically relevant, cell-free therapies.

1.4.2.4 Factors determining the outcomes of organoid implantation in TBI

The therapeutic efficacy of organoid implantation in TBI is influenced by multiple interrelated variables, including host characteristics, lesion parameters, graft properties, and methodological factors (Fig. 1.3).

Host-related factors such as age, sex, immune status, and general health influence graft survival and integration. Age is a critical, non-adjustable determinant of regenerative capacity (Vanacore et al., 2024). To date, no study has directly compared organoid implantation across different age groups. Only one study mentioned the implantation of organoids into 7-day-old and 6-week-old mice. While both age groups were used in the experiments, the study did not explicitly compare the age-related outcomes (Kitahara et al., 2020). Sex has significant implications in TBI studies, as male and female brains respond differently to injury (Krukowski, 2021). Most studies discussed here relied on male rodents, limiting the generalisation of findings and overlooking the potential influence of sex hormones and chromosomal differences on host-graft dynamics. Including both sexes and monitoring of hormonal status post-implantation would improve translational value.

Lesion-specific parameters, including site, size, number, and accessibility, impact the outcomes. Most studies targeted the sensorimotor and retro-splenial cortices due to their accessibility and well-defined functional outputs; however, other cortical regions remain underexplored. Regional differences in cortical vascularisation may further affect graft viability. Notably, the primary motor, sensory, and visual cortices, along with the ventral retro-splenial cortex, possess a dense cerebrovascular network (Wu et al., 2022), suggesting that implantation in these areas may enhance graft survival.

Species-specific characteristics are another factor that influences outcomes of organoid implantation. Most preclinical studies were conducted on rodents, with only one study including large animals, underscoring the need for additional large-animal studies to bridge rodent–human gaps. To date, one non-human primate study has transplanted human cerebral organoids into 3-year-old monkeys, reporting graft survival with host vascularisation and short-range axonal outgrowth by 12 WPI (Kitahara et al., 2020).

Organoid-related factors, such as the developmental stage and cellular composition of the organoid, profoundly influence integration. Early-stage organoids (<24 days) retain high proliferative capacity and plasticity but lack the structural organisation necessary for mature synaptic connectivity (Yentur et al., 2025). By contrast, late-stage organoids (>90 days) display enhanced architectural complexity and synaptic development but are more prone to necrosis due to prolonged *in vitro* culture. Intermediate-stage organoids (30–60 days) achieve a balance between cellular diversity and early neuronal commitment, which promotes graft survival and integration (Bao et al., 2021, Kim et al., 2022). It has been reported that implantation of 6-week-old cerebral organoids into a TBI mouse model resulted in more axon extensions compared to 10-week-old organoids (Kitahara et al., 2020). Similarly, 55-day-old organoids yielded higher neurogenesis and increased cell survival compared to their 85-day-old counterparts, suggesting that a greater abundance of neuronal progenitors at the time of implantation may enhance tissue restoration (Wang et al., 2020b). Brain organoids lack mesodermal-derived lineage, and recent protocols have incorporated endothelial cells (Cakir et al., 2019, Sun et al., 2022, Shi et al., 2020, Pham et al., 2018) and microglia-like cells into brain organoids (Ormel et al., 2018), thereby enhancing the physiological relevance of the organoid.

Methodological variables, such as the implantation window, surgical protocols, and follow-up duration, can further influence graft integration. To date, there have been limited studies addressing the optimal timing for organoid implantation. One report found that delayed implantation of 10-week-old organoids following injury led to greater axonal extension compared to immediate implantation of organoids of the same age (Kitahara et al., 2020), consistent with insights previously discussed in cell suspension transplantation. Surgical protocols also lack standardisation. While most studies use stereotactic delivery into lesion cavities, others place intact organoids onto the cortical surface, which complicates the comparisons across studies.

Follow-up duration is another limitation, with most studies terminating before 6 WPI, which interferes with the assessment of long-term graft survival, integration, and even tumourigenic potential. Furthermore, the first week after implantation remains an underexplored window, despite being a critical window for acute rejection and inflammatory responses.

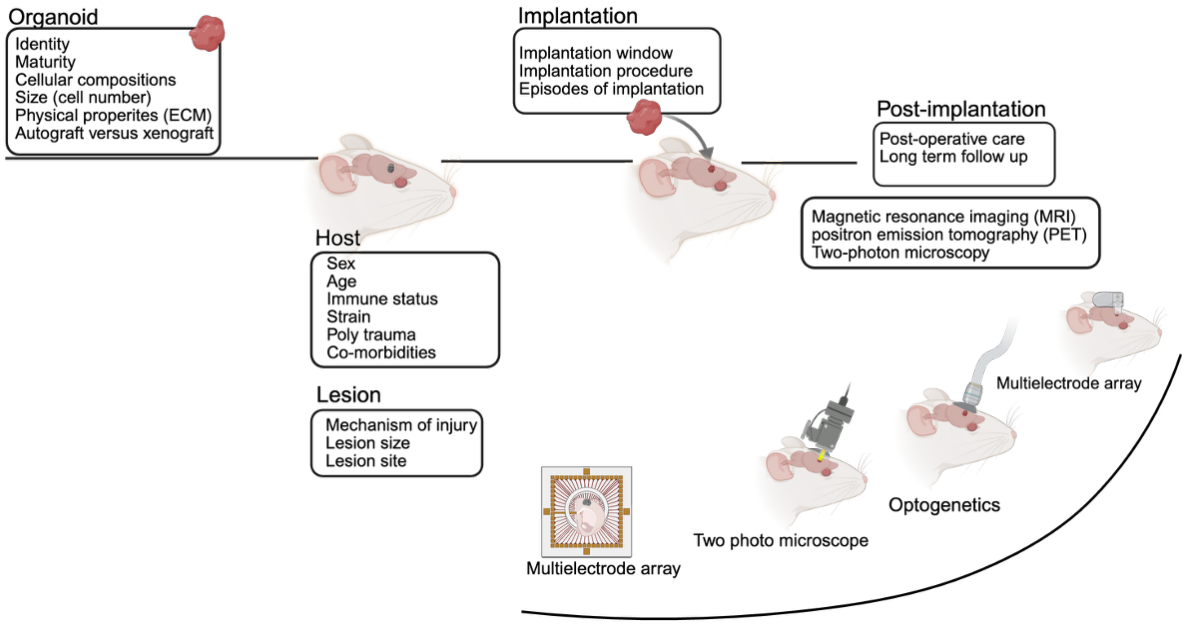

Figure 1.3 Factors influencing the outcome of organoid implantation
The success of organoid implantation relies on several factors. These include the developmental stage, subtype composition, regional identity, and ECM properties of the organoids. Host-related aspects, such as sex, age, immune status, and strain, also play significant roles. Additionally, the size, site, and number of lesions are important determinants. Proper operative technique and post-operative follow-up further contribute to the overall outcome.

1.4.2.5 Limitations of organoid implantation for TBI

While organoids offer promising avenues for brain repair, several intrinsic and methodological limitations constrain the translational potential of organoids for TBI. A major issue is the absence of essential cell types, particularly microglia and oligodendrocytes, which are critical for immune regulation and remyelination, respectively. The absence of a functional microvasculature component restricts the delivery of nutrients and oxygen, leading to the development of cellular necrotic cores and impairing the survival and maturation of the graft (Kofman et al., 2022). In addition, variability in organoid differentiation can lead to inconsistencies across batches, which complicates the standardisation and comparisons between studies (Andrews and Kriegstein, 2022). Organoid platforms offer minimal control

over spatial organisation because the lamination in organoids is arranged in largely random orientations around neural rosettes (Lancaster et al., 2013). This randomness prevents alignment with host cortical architecture and restricts the ability to reconstruct columnar organisation.

1.4.3 3D bioengineered neuronal tissue

1.4.3.1 Biomaterials employed in bioengineering neuronal tissue *in vitro*

Unlike organoid technology, which relies on the inherent self-organisation of stem cells, bioengineered 3D neural models employ pre-designed biomaterial scaffolds that are seeded with iPSC-derived cells, immortalised cell lines, or primary neural cells (Hopkins et al., 2015). Cortical areas differ in their biomechanical and physical properties; therefore, scaffold properties should be adjusted accordingly to support graft survival and lineage specification (Blaeser et al., 2016, Ortinau et al., 2010). Biomaterials used in neural tissue engineering can be broadly classified into naturally derived and synthetic scaffolds.

The frequently used natural polymers for scaffold design in neural tissue engineering are collagen, gelatin, HA, chitosan, elastin, and alginate. Collagen type I enhances neuronal survival, attachment, and neurite outgrowth (Tang-Schomer et al., 2014). Furthermore, it supports the differentiation of NSCs into neurons, astrocytes, and oligodendrocytes in dense 3D cultures, while also enabling the generation of excitable neurons with appropriate polarity and receptor expression (Watanabe et al., 2007a, Ma et al., 2004). Despite these advantages, its rapid degradation and non-physiological abundance in the brain limit long-term guidance (Antoine et al., 2014). Gelatin is derived from collagen degradation and exhibits lower immunogenicity, whereas gelatin methacrylate (GelMA) is a synthetic gelatin with mechanical properties that resist immediate degradation, thereby improving stability (Wang et al., 2017a).

HA is abundant in brain ECM and modulates neural progenitors toward neuronal or glial fates (Seidlits et al., 2010). It tends to support stem cell quiescence and inhibit neurite outgrowth; therefore, it is increasingly incorporated into composite scaffolds to guide the differentiation of neural stem cells into more complex CNS constructs (Preston and Sherman, 2011). HA alone cannot retain its structure, so it is combined with other biomaterials to enhance its printability, mechanical stability, and biological properties (Petta et al., 2020).

Alginate, a polysaccharide derived from brown algae, forms hydrogels when combined with calcium ions. Alginate hydrogels provide a hydrated environment that supports the diffusion of nutrients and molecules, while also allowing the entrapment of cells within bioink formulations (Lee and Mooney, 2012). To enhance its mechanical and biochemical properties, alginate is often combined with other biomaterials, such as agarose, collagen, or chitosan. Agarose, another plant-derived polysaccharide, is non-degradable and sensitive to temperature and pH changes. It can form stable networks and cross-link with different polymers to enhance structural integrity (Mahendiran et al., 2021). Importantly, combining alginate and agarose has been shown to influence the physical properties of bioinks, supporting the differentiation of hNSCs into functional neurons (Gu et al., 2016).

Matrigel is a reconstituted basement membrane extract, derived from the murine Engelbreth–Holm–Swarm sarcoma, that closely resembles the ECM in both composition and function. It is rich in laminin, collagen type IV, proteoglycan perlecan, and the glycoprotein entactin. Matrigel provides a supportive scaffold that promotes cell differentiation, proliferation, and migration (Novikova et al., 2006). It also contains numerous growth factors, including TGF, EGF, Fibroblast Growth Factor (FGF), and Platelet-Derived Growth Factor (PDGF), as well as proteases that regulate cell signalling, angiogenesis and tissue repair (Kleinman and Martin, 2005). These properties make it widely used in neuronal cultures, and Matrigel-based bioinks have been successfully utilised for bioprinting hiPSC-derived spinal neurons (Joung et al., 2018) and cortical neurons (Zhou et al., 2020, Jin et al., 2022, Joung et al., 2018); resulting in promising neuronal survival and functional maturation.

1.4.3.2 Bioengineered neuronal tissue for TBI

The introduction of biomaterial scaffolds into stem cell-based therapy of TBI enhances stem cell survival and reduces the detrimental effect of the injury microenvironment compared to cell suspension transplantation. For instance, hiPSC-derived neurons grown in polymeric scaffolds and transplanted into injured mouse brains exhibited greater survival compared to those injected as a cell suspension (Carlson et al., 2016). Similarly, Francis and colleagues reported that peptide-based scaffolds supported the maturation and survival of hiPSC-derived dopaminergic neurons compared with neurons transplanted in suspension (Francis et al., 2020).

Both natural and synthetic biomaterials have been studied for TBI therapy (Aqel et al., 2023). The hydrogel is a favourable scaffold because its mechanical properties can be modified to

mimic those of the brain, thereby facilitating the transmission of signals between cells (Li et al., 2022). Natural and synthetic hydrogels utilised for brain repair, including agarose, collagen type I, HA, chitosan, alginate, methylcellulose, polyethylene glycol (PEG), Poly (N-(2-hydroxypropyl)methacrylamide) (pHPMA), and Poly(2-hydroxyethyl methacrylate) (pHEMA) (Hopkins et al., 2015, Woerly et al., 2008, Lesny et al., 2002).

Collagen-based scaffolds have received particular attention for their biocompatibility and ability to support cellular adhesion and differentiation (Tang-Schomer et al., 2014). Implantation of collagen-based scaffolds loaded with hBM-MSCs reduced lesion volume and improved sensorimotor performance and spatial learning after CCI (Lu et al., 2007). Similarly, collagen-embedded hBM-MSCs supported greater corticospinal axonal outgrowth and improved motor and cognitive function when compared to controls (Mahmood et al., 2013). Furthermore, a collagen–chitosan scaffold encapsulating BM-MSCs improved motor and cognitive outcomes, and increased VEGF expression, thereby enhancing angiogenesis at the injury site after transplantation in the TBI model (Yan et al., 2019). Additional studies using different cell sources and species further support the utility of collagen-based biomaterials. Implantation of human amniotic-derived progenitor cells, combined with a collagen type I scaffold, improved motor performance and reduced axonal degeneration in the thalamus and corpus callosum (Chen et al., 2011).

Beyond collagen, other naturally derived scaffolds have also shown promise for neural repair. Implantation of a gelatin hydrogel loaded with BM-MSCs into a TBI model reduced lesion size and inflammation, enhanced the survival and proliferation of endogenous neural cells, and promoted recovery of motor coordination and cognitive function (Li et al., 2021). Zheng et al., developed GelMA hydrogel functionalized with polydopamine nanoparticles carrying stromal cell-derived factor-1 and seeded with hAM-MSCs. When implanted into a TBI model, it reduced the lesion size, facilitated the regeneration of endogenous nerve cells, and promoted neuronal differentiation of hAM-MSCs (Zheng et al., 2021).

Recently, attention has shifted toward biomaterials derived from brain ECM, which offer superior biological relevance. Brain-derived decellularised ECM (BdECM) bioink preserved ECM proteins and brain-like stiffness; NSCs encapsulated in BdECM exhibited high viability with restrained proliferation and enhanced neuronal differentiation. In a rat TBI model, iPSC-

NSCs delivered in BdECM evoked a reduced glial response and differentiated into mature neurons (Bae et al., 2021).

Together, these studies underscore the crucial role of the ECM in facilitating the survival, integration, and regenerative efficacy of transplanted neuronal cells. Biomaterial scaffolds consistently enhanced cellular retention, reduced lesion volume, promoted axonal outgrowth, and improved motor and cognitive outcomes. Building on this foundation, the current thesis explores the design and transplantation of 3D cortical constructs that incorporate defined extracellular architecture, Matrigel, and region-specific neuronal subtypes for TBI repair.

1.4.3.3 Modelling the multilayer architecture of the cerebral cortex *in vitro*

Few studies have explored the feasibility of bioprinting to reproduce aspects of cortical architecture. A six-layer cortical-like construct was successfully fabricated using an extrusion bioprinter with RGD-modified gellan gum, it is a gellan gum hydrogel that has been covalently linked with a short peptide containing the Arginine-Glycine-Aspartic acid (RGD) sequence. A simplified three-layer structure containing primary cortical neurons in the outer layers supported cell survival, differentiation, and network formation (Lozano et al., 2015b). Building on this early study, a droplet-based bioprinting approach was developed to generate simplified, two-layer cortical tissues from hiPSC-derived NPCs. When implanted into *ex vivo* mouse brain slices, these printed cortical tissues extended axons into the host parenchyma, supported reciprocal neurite ingrowth, and exhibited synchronised calcium spikes with host neurons, confirming functional coupling between graft and host (Jin et al., 2022).

In a more recent study, 3D bioprinting of multi-layered brain tissues was achieved by placing striatal and cortical neuronal layers side by side within a designated hydrogel scaffold. Their constructs supported the survival and differentiation of NPCs. Importantly, cortical neurons projected their axons toward striatal neurons and established a functional synaptic network, resembling the long-range neuronal connections in the brain (Yan et al., 2024). Another study reported the development of a six-layered, 3D cortical brain model that integrates multicellular layers and microscale continuous fibres to simulate neuronal orientation and interaction (Wang et al., 2024). A novel bioprinting platform combining direct ink writing and electrohydrodynamic fibre printing was developed to fabricate the model, utilising GelMA-fibrinogen bioink. The aligned fibres directed neuronal orientation, resulting in neurite extensions reaching 200–300 μm (Wang et al., 2024). Another brain-like tissue with a layered

gradient pore construct was fabricated using multi-nozzle printing and a gelatin-alginate-collagen bioink. By varying collagen concentrations, cortical-like laminar structures were produced with gradient pore sizes (20–150 μm) and mechanical properties adjusted to match the softness of brain tissue. The constructs achieved high printing accuracy and cell survival rates, with rapid cell proliferation within the scaffolds, confirming their suitability for biological applications (Pei et al., 2021). Together, these studies demonstrate that bioprinting can overcome the spatial randomness of organoids and enable controlled recapitulation of cortical lamination and projection patterns between different brain regions.

1.4.3.4 Limitations of biomaterials use in brain repair

Biomaterials for CNS repair hold promise; however, developing biodegradable and biocompatible scaffolds remains a significant challenge. An ideal scaffold for neural tissue repair should match both the biochemical and biophysical properties of brain ECM (He et al., 2012). They should provide sufficient mechanical strength to provide physical support and prevent tissue collapse. They should maintain appropriate permeability to enable the exchange of nutrients, oxygen, and secreted factors (Cadena et al., 2021). Additionally, they should be biocompatible, supporting cellular infiltration and regeneration (Maclean et al., 2018). Mismatching these properties can complicate the condition; for instance, implantation of a material with a higher stiffness than that of the native brain elicits foreign body reactions, including neuroinflammation and gliosis (Moshayedi et al., 2014). Furthermore, natural biomaterials such as Matrigel exhibit batch variability, which hinders the consistency of the scaffold (Anderson et al., 2008).

The synthetic biomaterials offer greater reproducibility but often lack inherent biological properties. Moreover, the degradation of synthetic polymers and their degradation products can alter the surface properties of biomaterials over time, potentially impacting macrophage behaviour and the inflammatory response (Anderson and Jones, 2007).

1.4.4 Cell therapy in clinical trials for TBI and Parkinson's disease

Based on the promising results from the preclinical work, early-phase clinical trials have investigated the applicability of stem cell therapies for patients with TBI. Bone marrow-derived mononuclear cells (BM-MNCs) are the most commonly used cell type, and intrathecal administration is the preferred delivery route (Saboori et al., 2024).

Cell therapy studies in TBI are either for cell replacement or as cell delivery for tissue support. In a cell replacement strategy, the therapeutic intervention depends on long-term survival, differentiation, and functional integration of the transplanted cells into host circuits to restore lost neurons and connectivity. By contrast, clinical studies use BM-MNCs or MSCs, primarily aim to modulate the hostile post-injury environment rather than restoring neurons (Cox, 2018). In this approach, transplanted cells act via paracrine and immunomodulatory mechanisms that support endogenous repair, through attenuating secondary neuroinflammation, promoting phagocytic clearance of cellular debris, preserving BBB integrity, and reducing oedema and oxidative stress (Liao et al., 2015).

BM-MNCs are commonly used due to several practical and translational advantages. From a practical perspective, isolation of BM-MNCs is relatively simple, requires minimal processing, and yields a good number of cells (Nguyen et al., 2023). From a translational perspective, BM-MNCs have robust preclinical proof of concept and demonstrated safety in Phase 1 clinical trials for TBI, with no serious adverse events or toxicity reported (Cox et al., 2011). Their 5-8 micron size allows for biologically appropriate intravenous delivery with reduced pulmonary sequestration (Fischer et al., 2009). Additionally, autologous grafts do not require in vitro culture expansion; they are easily accessible, avoid the risks of uncontrolled growth associated with embryonic or fetal stem cells, and do not raise ethical concerns related to cell origin (Cox et al., 2017). Mechanistically, BM-MNC administration after TBI has been linked to neuroprotective effects in preclinical models, including preservation of early BBB integrity and modulation of innate immune responses, including increased apoptosis of activated microglia (Bedi et al., 2013).

In pioneering work, Cox et al., demonstrated the safety of intravenous autologous BM-MNCs in children with severe TBI (Cox et al., 2011). Another trial evaluated the combination of intracerebral and intravenous administration of human umbilical cord blood stem cells, which improved neurological function at 6 months without causing toxicity (Zhang et al., 2008).

Later in 2013, two additional clinical trials reported motor improvements in TBI patients following cell therapy. Intrathecal administration of allogeneic UC-MSCs was found to be safe and effective in alleviating chronic motor deficits (Wang et al., 2013c). Likewise, autologous BM-MSCs transplanted into TBI patients with cerebral lesions via lumbar puncture improved motor function in approximately 40% of patients (Tian et al., 2013).

Later studies in 2017 demonstrated modulation of inflammation, in addition to improvements in neurological outcomes. Patients with chronic severe TBI received either intravenous or intrathecal injections of autologous MSC-derived NSCs, experienced varying degrees of improved neurological function with no reported adverse events (Wang et al., 2017b). Similarly, paediatric patients received an intravenous injection of BM-MNCs, reported improved recovery, and showed reduced systemic inflammatory markers, including Tumour Necrosis Factor-α (TNF-α), interleukin-1β (IL-1β), IL-10, and Interferon-γ (IFN-γ), within 6 months of treatment (Cox Jr et al., 2017). Moreover, a recent study that administered autologous BM-MNCs intravenously to patients with acute severe TBI revealed neurological improvement (Cox Jr et al., 2024).

Collectively, these studies support the safety and efficacy of stem cell-based therapy through various delivery routes and cell types. However, further trials are necessary to define optimal cell sources, dosages, delivery methods, and treatment windows to achieve consistent, long-term neurological benefits for patients with TBI.

Beyond TBI, the strongest clinical precedent for neuronal transplantation comes from Parkinson's disease, where fetal and, more recently, pluripotent stem cell–derived dopaminergic grafts have been evaluated in human clinical trials. Parkinson's disease, a neurodegenerative disease that affects the dopaminergic cells in the substantia nigra pars compacta (Lotharius and Brundin, 2002). The earliest clinical trials implanted fetal nigral tissue into one striatum of two Parkinson's patients under immunosuppression. The surgery was safe but produced no major clinical improvement, with only small, measurable gains in movement speed and a slightly stronger levodopa response. Brain imaging showed no clear evidence of graft function (Lindvall et al., 1989). Another early clinical study included six Parkinson's patients who received a one-sided transplant of embryonic midbrain tissue into the striatum and were tracked for up to six years. Brain scans later showed strong dopamine activity in the grafts, and most patients had meaningful symptom improvement and slightly lower L-dopa requirements, as well as longer benefit from each dose (Wenning et al., 1997).

A subsequent landmark study was a double-blind, randomised controlled trial of forty patients with severe Parkinson's disease, comparing bilateral embryonic mesencephalic cell transplants into the putamen with sham surgery and following them for one year. On the main patient-reported global change outcome, there was no meaningful difference between the transplant

and sham groups at one year. However, patients aged 60 or younger who received transplants showed improvement on standard Parkinson's measures when tested off medication, whereas older patients did not benefit. Most transplant recipients showed evidence of graft survival or growth, but about 15% developed recurrent dystonia or dyskinesias after initial improvement, despite reductions or discontinuation of levodopa (Freed et al., 2001).

A further 24-month double-blind, placebo-controlled trial in 34 advanced Parkinson's patients tested bilateral fetal nigral transplants versus a placebo procedure. Overall, transplantation did not significantly improve off-medication motor scores compared with placebo, though the four-donor group showed a small average improvement while placebo worsened, and milder patients did show a significant treatment effect. Imaging and postmortem findings confirmed dopamine neuron survival and increased striatal fluorodopa uptake, but 56% of transplanted patients developed persistent off-medication dyskinesias (Olanow et al., 2003). The open-label TransEuro trial evaluated fetal ventral mesencephalic tissue transplants in 11 patients with Parkinson's disease. At three years, there was no overall clinical improvement on the primary outcome, and major graft-induced dyskinesias were not seen. PET imaging showed increased dopamine uptake in seven patients at 18 months, with near-normal restoration occurring in only one (Barker et al., 2025). Collectively, these fetal programs demonstrated proof of principle but also exposed several barriers that limit their broader use, including constrained tissue availability, batch-to-batch and surgical variability. Together, these factors made fetal tissue difficult to standardise and scale for broad deployment as a therapy (Barker et al., 2013).

The modern clinical wave aims to replace fetal tissue with pluripotent stem cell–derived dopaminergic progenitors prepared under controlled conditions, with defined identity and criteria. A phase I/II trial at Kyoto University Hospital transplanted iPS-cell–derived dopaminergic progenitors into both sides of the putamen in seven Parkinson's patients and followed them for 24 months. There were no serious adverse events, and MRI showed no graft overgrowth or tumour formation. The motor scores improved in most participants. PET imaging showed biological activity, with increased 18F-DOPA uptake in the putamen, greater in the higher-dose group. Overall, the results suggest that the grafts survived, made dopamine, and appeared safe, with possible clinical benefit (Sawamoto et al., 2025). In parallel, an open-label phase I trial tested hESC-derived dopamine-neuron progenitors, transplanted into both putamina of twelve patients with Parkinson's disease, with one year of immunosuppression. At 1 year, the primary safety and tolerability goals were met without adverse effects. By 18

months, 18F-DOPA PET uptake in the putamen increased, consistent with graft survival. Clinical measures were stable or improved, with no graft-induced dyskinesias reported (Tabar et al., 2025).

Recently, an ongoing phase 1/2a dose-escalation trial of an autologous graft strategy is testing whether ANPD001 cells, an autologous dopaminergic neuronal precursor therapy, can be safely implanted into the brain to mature into dopamine-producing neurons in patients with sporadic Parkinson's disease. Participants who undergo neurosurgery are tracked for safety, symptom progression, and cell survival through clinical assessments and MRI and PET scans for 5 years. After that, safety follow-up continues annually by phone for 10 more years, for a total of 15 years of monitoring (NCT06344026, 2024).

1.5 Hypothesis and the project's aims

Cell therapy for TBI has shown promising results in preclinical studies. However, current approaches remain limited in their translational potential. Cell suspension transplantation has demonstrated cell survival and differentiation; however, it is limited by low long-term survival, lack of structural organisation, and insufficient synaptic integration. These limitations have prompted the field to explore 3D neuronal tissue. Organoid implantation into the injured brains showed encouraging outcomes, including neuronal integration with reciprocal connections, vascularisation, immune modulation, and improvement in motor and cognitive functions. However, cerebral organoids also have shortcomings, such as core necrosis due to insufficient oxygen and nutrient diffusion, which constrains cellular maturation. Their cellular heterogeneity may lead to off-target projections, thereby reducing specificity in circuit reconstruction. Additionally, there is limited control over the spatial organisation of cells due to the inherent self-organisation nature of organoids.

Laminar organisation is the key to cortical function, yet this remains an unmet challenge in regenerative medicine. Effective therapy requires more than simply injecting cells; it requires reconstructing tissue continuity and ensuring that the layering identity of the host cortex is matched to guide integration and prevent off-target projections.

To address these gaps, this thesis develops and explores the properties and utility of 3D neuronal constructs engineered to reproduce the basic laminar organisation and spatial cellular distribution of the native cerebral cortex. Human iPSCs are differentiated into early neuronal

progenitor cells (ENPCs) and late neuronal progenitor cells (LNPCs), which correspond to deep- and upper-layer cortical neurons, respectively. Using a droplet-based microfluidic technique, I generate 3D ENPC and LNPC constructs that are assembled into two-layered neuronal tissues, replicating key features of cortical lamination. I hypothesised that, following TBI, implantation of 3D neuronal constructs derived from temporally specified ENPCs and LNPCs would enhance implant survival and enable identity-dependent integration with the host cortex. Furthermore, the implantation of two-layered neuronal tissue that mimics cortical lamination could facilitate the reconstruction of cortical columnar circuits by promoting both local and long-range connectivity.

To test this hypothesis, the thesis is structured into experimental aims corresponding to Chapters 2-4, as outlined below. Each chapter has a specific introduction, methods, results and discussion. Chapter 5 is the general discussion.

1.5.1 Aim of Chapter 2: Differentiation of hiPSCs into Deep-and Upper-Layer Cortical Neurons

The overall aim of Chapter 2 is to establish and validate a reproducible differentiation protocol to generate hiPSC-derived cortical neuronal progenitors that reflect distinct temporal stages of corticogenesis, including ENPCs and LNPCs. This protocol provides the cellular basis for subsequent fabrication of 3D constructs (Chapter 3) and *in vivo* implantation studies (Chapter 4).

Aim 2-1: Optimise hiPSC differentiation into deep- and upper- cortical neurons

To validate the dorsal telencephalic fate of the human progenitors and assess the laminar identities of ENPCs and LNPCs, I will perform immunocytochemistry to examine the expression of pluripotency markers (OCT4, NANOG, SOX2) and the neuroectoderm marker PAX6. I will then conduct immunocytochemistry to identify characteristic layer-specific transcriptional factors, including deep-layer markers (CTIP2, TBR1), the layer IV marker (RORβ), and upper-layer markers (SATB2, BRN2). To complement this, I will use qPCR to quantify the expression of cortical layer-specific genes (CTIP2, SATB2) as well as neuronal maturation markers (MAP2, RBFOX3). Furthermore, I will characterise neuronal phenotypes and examine potential synapse formation. To achieve this, I will use immunocytochemistry to identify neuronal subtypes, labelling excitatory neurons with VGLUT1 and inhibitory INs with

GABA. Finally, I will assess synaptic maturation by co-staining for presynaptic Synapsin-1 and postsynaptic density protein-95 (PSD-95) and analyse their co-localisation and synaptic density.

Aim 2-2: Determine the functional activity and network connectivity of ENPCs and LNPCs

To investigate how temporal identity shapes the neuronal activity and network organisation, I will record spontaneous calcium activity of ENPCs and LNPCs using calcium imaging. I will then analyse calcium spike dynamics, including firing frequency, global synchrony index, rise time, decay time, and half maximal spike width. To further characterise network organisation, I will apply graph theory analysis to the calcium imaging data to assess network topology and connectivity patterns in ENPC- versus LNPC-derived networks. I will examine receptor functionality through pharmacological perturbation of glutamatergic and GABAergic signalling. To achieve this, I will apply exogenous neurotransmitters (GABA and glutamate) during calcium imaging, after recording baseline activity, to monitor acute network responses. Finally, I will apply receptor antagonists such as gabazine (a GABA-A receptor blocker) and picrotoxin (a GABA-A chloride channel blocker) to evaluate their effects on calcium activity.

Aim 2-3: Establish ENPC and LNPC populations as cell sources for 3D constructs and *in vivo* implantation

To validate cortical identity *in vivo*, I will transplant ENPCs and LNPCs into the motor cortex of postnatal day 7-8 (P7-P8) NOD-SCID mice and subsequently investigate both their cortical identity and integration within the host brain. I will perform immunohistochemistry on brain sections using cortical layer markers, CTIP2 and SATB2, to determine whether the transplanted ENPCs and LNPCs maintain their intended layer-specific differentiation *in vivo*. To identify grafted human cells, I will utilise human-specific markers, including human neural cell adhesion molecule (hNCAM) and human nuclear antigen (HuNu). Finally, detailed Neurolucida tracings of axons will be conducted to map the extent and pattern of integration of transplanted cells into the host brain regions.

1.5.2 Aim of Chapter 3: Droplet-Based Microfluidic Technique to Fabricate 3D Constructs

This chapter investigates the development of droplet-based microfluidic technique to fabricate 3D constructs of ENPCs and LNPCs. It examines whether these constructs retain laminar-

specific molecular identities and achieve functional maturation. Furthermore, the chapter explores the assembly of ENPC and LNPC constructs into two-layered neuronal tissues, mimicking cortical lamination, and examines how spatial organisation influences network connectivity and inter-laminar communication.

Aim 3-1: Establish a reproducible droplet-based microfluidic method for the fabrication of 3D neuronal constructs

To develop a platform for generating 3D constructs, polydimethylsiloxane (PDMS)-based microfluidic chips with defined channel geometries and inlet–outlet dimensions will be designed and fabricated. To evaluate the suitability of these constructs for downstream applications, I will assess cell viability at 1, 8, and 14 days after fabrication using a live–dead assay on freshly printed constructs.

Aim 3-2: Evaluate viability, proliferation, and neuronal differentiation of 3D ENPC and LNPC constructs

To assess whether the 3D constructs maintain their capacity to proliferate and differentiate into defined laminar identities after fabrication, I will evaluate cell survival and proliferation using immunostaining for Ki-67 to identify proliferating cells and Cleaved Caspase-3 to detect apoptotic cells. I will then investigate laminar identity markers by performing immunocytochemistry for CTIP2 and SATB2 expression in 3D ENPC and LNPC constructs. To further determine neuronal and glial fate, I will conduct immunostaining for GABA and S100β, respectively. Finally, I will demonstrate synaptic network formation by co-immunolabelling for presynaptic Synapsin-1 and postsynaptic PSD-95.

Aim 3-3: Define functional activity and network connectivity in 3D ENPC and LNPC constructs

To examine how temporal identity shapes neuronal activity and network organisation in 3D environments, I will record spontaneous calcium signals of 3D ENPC and LNPC constructs after dual loading with Fluo-4 and Fura-Red. I will then quantify spike dynamics, including firing frequency, global synchrony index, rise time, decay time, and half maximal spike width. To further characterise network connectivity and reveal the differences between ENPC and LNPC network organisations in a 3D environment, I will apply graph theory analysis by

computing matrices for average edge weight, average path length, clustering coefficient, and modularity.

Aim 3-4: Assemble 3D ENPC and LNPC constructs into two-layered neuronal tissues and assess structural and functional inter-laminar integration *in vitro*

I will manually fuse 3D ENPC and LNPC constructs to generate two-layered neuronal tissues to analyse their structural and functional properties, and to explore whether these two-layered neuronal tissues can replicate key aspects of cortical column organisation and inter-laminar interactions. Confocal microscopy will be used to assess maintenance of lamination, track neurite projections at the interface. I will perform immunostaining for layer-specific markers to verify the retention of cortical identity. To evaluate inter-laminar functional connectivity, I will record the calcium activity and apply temporal cross-correlation analysis to reveal the temporal correlation of signalling and identify leader–follower dynamics between the compartments.

1.5.3 Aim of Chapter 4: Implantation of 3D Neuronal Constructs into TBI Model

This chapter examines the structural integration of 3D constructs implanted into the TBI model. All implantation studies will utilise P7-P8 NOD-SCID mice with an aspiration lesion in the motor cortex as a model of TBI.

Aim 4-1: Assess the survival, differentiation, and structural integration of 3D RFP+ NPC implants following TBI

To evaluate the supportive microenvironment of transplanted constructs that promotes implant survival, neuronal differentiation, and integration following TBI, I will implant 3D RFP+ NPC constructs into P7–P8 mice with cortical lesions and assess the feasibility of long-term survival, vascularisation, and host integration at 2 WPI and 2 MPI. I will evaluate implant proliferation and survival using immunostaining for Ki-67 and Cleaved Caspase-3 at both time points. Cortical neuronal differentiation will be evaluated by immunostaining for CTIP2 and SATB2, while implant-host interaction will be assessed by analysing blood vessel ingrowth (CD31) and glial responses (Iba1, GFAP) over time. Finally, I will map axonal outgrowth and anatomical connectivity using Neurolucida software to reconstruct axonal projections and identify target regions at 2 WPI versus 2 MPI.

Aim 4-2: Compare the structural integration of 3D ENPC and LNPC implants with host brains *in vivo*

To investigate how the temporal identity influences the integration patterns after implantation, I will selectively implant 3D ENPC and LNPC constructs and compare their structural integration and connectivity with the host brain at 2 MPI. Axonal outgrowth and anatomical connectivity will be traced using Neurolucida software to reconstruct axonal projections and identify target regions at 2 MPI. Synaptic formation will be assessed using immunohistochemistry for human-specific Synaptophysin and PSD-95. Glial reactivity will be evaluated by immunohistochemistry for Iba1 and GFAP to examine potential differences in immune responses to 3D ENPC and LNPC implants. To assess the functional activity of the host brain after implantation of constructs, spontaneous extracellular activity will be recorded using an MEA system from acute brain slices implanted with 3D ENPC and LNPC constructs at 2 MPI.

Aim 4-3: Evaluate the integration potential of two-layered neuronal tissues that mimic key aspects of cortical lamination

To investigate whether pre-assembled two-layer neuronal tissues, that mimic key aspects of cortical lamination, can integrate differently from single-layer grafts and potentially reestablish both local and long-range projections, I will implant two-layer cortical tissues into the TBI model and assess their structural integration at 2 MPI. The compartment-specific axonal projections will be mapped and reconstructed to determine the projection patterns of ENPC compartment versus LNPC compartment using Neurolucida software.

By achieving these aims, this thesis will demonstrate whether engineered 3D cortical neuronal constructs can overcome the current limitations of cell therapy for TBI.

Chapter :2 Differentiation of hiPSCs into Deep- and Upper-Layer Cortical Neurons

2.1 Introduction

The mammalian cerebral cortex is organised into six layers, each characterised by distinct neuronal subtypes and projection patterns (Molyneaux et al., 2007). In rodents, transcription factors CTIP2 and SATB2 specify subcerebral neurons in layer V and callosal PNs in layer II/III, respectively (Srinivasan et al., 2012). Neurons expressing CTIP2 give rise to corticospinal projections (Arlotta et al., 2005), while SATB2 is a transcription factor necessary for callosal projection neuron identity (Alcamo et al., 2008). The cytoarchitecture and lamination of the cerebral cortex are fundamental for the establishment of functional microcircuits, with each layer contributing to the overall function of the cortical column (Bosman and Aboitiz, 2015).

The breakthrough of hiPSCs has provided a powerful tool for studying human corticogenesis *in vitro* and for regenerative medicine (Kim et al., 2014, Lee et al., 2024). Multiple differentiation protocols have been developed using either monolayer or 3D embryoid body cultures of hiPSCs (Muratore et al., 2014). Monolayer-based dual-SMAD inhibition protocols use Noggin and SB431542 to antagonise Bone-Morphogenetic Protein (BMP) and TGF-β/Activin signalling pathways, thereby promoting neuroectodermal fate (Chambers et al., 2009, Shi et al., 2012a). More recent refinements incorporate additional pathway modulators, including the Wnt inhibitor DKK-1, the BMP receptor inhibitor DMH-1, and the Sonic Hedgehog antagonist cyclopamine, to further reinforce dorsal cortical identity (Autar et al., 2022). An alternative strategy involving the forced expression of neurogenic transcription factors, Neurogenin-2 (NGN2), has emerged to generate iPSC-derived cortical neurons within two weeks (Zhang et al., 2013). Furthermore, co-expression of NGN1 and NGN2 increases the efficiency of excitatory fate acquisition compared with NGN2 alone (Goparaju et al., 2017).

Recapitulating laminar identity is essential in cell therapy for TBI with cortical lesion. Generating ENPCs enriched in deep-layer fate and LNPCs enriched in upper-layer fate supports the generation of cortical lamination and restores the distinct projection patterns that support cortical function. While many differentiation protocols achieve broad cortical identity (Shi et al., 2012b, Boissart et al., 2013, Espuny-Camacho et al., 2013, Bahmad et al., 2017,

Gunhanlar et al., 2018), fewer have demonstrated the ability to generate laminar-specific PNs sequentially, recapitulating some aspects of *in vivo* corticogenesis (Shi et al., 2012a, Espuny-Camacho et al., 2013).

This chapter aimed to develop and validate a reproducible protocol for differentiating hiPSCs into ENPCs and LNPCs, serving as a cellular basis for building 3D constructs (Chapter 3) and for *in vivo* implantation in TBI models (Chapter 4). I established a differentiation protocol that generates temporally distinct populations of cortical neurons, characterised their molecular and functional properties *in vitro*, and demonstrated their potential for application in 3D tissue engineering and implantation studies. The first objective focused on optimising and validating the differentiation of hiPSCs into deep- and upper-layer cortical neurons. Following neural induction, the dorsal telencephalic identity of the progenitors was confirmed through the downregulation of pluripotency markers and upregulation of dorsal telencephalic markers. The temporal specification of progenitors was assessed via immunostaining for CTIP2, TBR1, SATB2, and BRN2, with support from quantitative PCR (qPCR). Neuronal subtypes were assessed by immunocytochemistry for both excitatory and inhibitory neurons, and synaptic maturity was evaluated by co-localisation of Synapsin-1 and PSD-95. The second objective involved defining the functional properties of ENPCs and LNPCs and how their temporal identities affect network activity. Spontaneous neuronal activity was captured through calcium imaging and analysed for firing frequency, global synchrony index, and other spike dynamics metrics. Graph theory analysis was used to evaluate the network connectivity pattern. Receptor function was assessed via pharmacological modulation of glutamatergic and GABAergic pathways. Finally, ENPCs and LNPCs were implanted into the motor cortex of P7-P8 NOD-SCID mice to evaluate their potential for integration with different brain regions. Integration was examined through immunohistochemistry for human-specific markers, followed by mapping of projection and connectivity using Neurolucida software.

2.2 Methods

2.2.1 Culture of hiPSCs

2.2.1.1 Cell line of hiPSCs

A single hiPSC line (AH016-3), reprogrammed from dermal fibroblasts using integration-free Sendai vectors expressing OCT4, SOX2, KLF4 and c-MYC, was used in parental (unlabelled) and RFP-expressing derivative forms (AH016-3 Lenti_RFP_IP), both provided by Prof. Sally Cowley (Haenseler et al., 2017, Sandor et al., 2017). hiPSCs were cultured on Geltrex™ (Gibco® Life Technology) coated six-well plates in mTeSR™ Plus medium (STEMCELL Technologies). Aliquots of Geltrex, 400 µl each in 50-mL centrifuge tubes, were prepared on ice and stored at -80°C until use. To prepare a working stock of Geltrex, an aliquot was transferred from -80°C to -20°C overnight and then to 4°C for a few hours before mixing it with cold advanced DMEM/F-12 (Life Technologies) using pre-chilled pipettes to prevent premature gelation. The diluted solution was stored at 4°C for up to two weeks. For coating the plates, 2 mL of diluted Geltrex was added to each well of the 6-well plates and incubated overnight.

2.2.1.2 Thawing of cryopreserved hiPSCs

Cryopreserved hiPSCs were stored in a liquid nitrogen tank. For thawing, a vial was retrieved on dry ice and briefly immersed in a 37°C water bath until only a small crystal of ice remained. Under sterile conditions, the cells were transferred to 9 mL of pre-warmed mTeSR Plus medium in a 15 mL conical tube and centrifuged at 200 × g for 5 min. The pellet was gently resuspended in 2 mL of fresh mTeSR Plus medium supplemented with 10 µM Y-27632 ROCK inhibitor (STEMCELL Technologies), to enhance post-thaw survival. Cells, from one vial, were plated into one well of a Geltrex-coated 6-well plate. The medium was changed daily with 2 mL of mTeSR Plus per well, pre-equilibrated to room temperature for at least 1 h before use. Y-27632 ROCK inhibitor was omitted from the medium after the first 24 h. When cultures reached approximately 90% confluency, passaging was done at a 1:3 ratio. After aspiration of medium, cells were washed with Dulbecco's phosphate-buffered saline (DPBS, Sigma-Aldrich Corporation) and incubated with 1 mL of 0.5 mM EDTA (Gibco® Life Technology) at 37°C for 8–10 min. Cells were gently dissociated in mTeSR Plus supplemented with 10 µM Y-27632 ROCK inhibitor to preserve colony integrity (Schwartz et al., 2011, Watanabe et al., 2007b), and then evenly distributed into new Geltrex-coated wells. On the following day, the old medium was replaced by a fresh medium, but without the ROCK inhibitor.

2.2.1.3 Cryopreservation of hiPSCs

When the cells reached approximately 90% confluency, hiPSCs were cryopreserved in freezing medium composed of 90% mTeSR Plus medium and 10% dimethyl sulfoxide (DMSO, Sigma-Aldrich Corporation). Cells were detached with 0.5 mM EDTA at 37°C for 8-10 min, as previously described. Cells were then resuspended in mTeSR Plus medium and centrifuged at 200 × g for 5 min. The pellet was resuspended in freezing medium and transferred to cryovials. Vials were placed in a Mr. Frosty™ freezing container (Thermo Fisher Scientific) and transferred to -80°C overnight, then moved to liquid nitrogen for long-term storage. The composition of the freezing medium is detailed in Table 2.1.

Table 2.1 Composition of freezing medium for hiPSCs (10 mL)

Item	Volume	Final conc.	Stock conc.	Supplier	Catalogue no.
mTeSR™ Plus medium	9 mL	90%	–	STEMCELL Technologies	1027-076
DMSO	1 mL	10%	–	Sigma-Aldrich Corporation	D2650-100ML

2.2.2 Differentiation protocol to generate deep- and upper-layer cortical neurons

The differentiation protocol had two phases: the neuronal induction phase, from day 0 to day 7, followed by the neuronal differentiation phase, from day 8 to day 70.

2.2.2.1 Neuronal induction phase

Successful induction required a confluent monolayer of hiPSCs with no signs of spontaneous differentiation. To ensure this, cells were passaged at a 3:2 ratio 24 h prior to induction. On day 0, mTeSR Plus medium was aspirated, and the cells were washed with DPBS before the addition of neural induction medium (NIM). The medium was supplemented with dual SMAD inhibitors, SB431542 and LDN193189. SB431542 inhibits the Lefty/Activin/TGF-β pathways by blocking the phosphorylation of ALK4, ALK5, and ALK7 receptors, which induce the mesenchymal-to-epithelial transition (Inman et al., 2002). LDN193189 is a derivative of dorsomorphin and a selective inhibitor of BMP type I receptor ALK2 and ALK3 (Sanvitale et al., 2013). The medium was replaced daily until the 7th day of induction. The composition of the NIM is detailed in Table 2.2A.

2.2.2.2 Neuronal differentiation phase

On Day 7, the cells were passaged using 0.5 mM EDTA at a 2:3 ratio and plated onto poly-L-ornithine/laminin-coated 6-well plates. For the rest of the day, cells were supplemented with

NIM containing 10 µM Y-27632 ROCK inhibitor. From Day 8, medium was replaced with Neural Maintenance Medium (NMM), refreshed daily until Day 34 and every other day thereafter. The composition of the NMM is detailed in Table 2.2B. The cells were passaged on day 9 of *in vitro* differentiation (DIV 9) and DIV 12 at a 1:2 ratio using EDTA as previously described. For subsequent passages on DIV 19, DIV 24, DIV 29, and DIV 34, Accutase (Life Technologies) was used. Initially, the cells were washed twice with DPBS, and 1 mL of Accutase was added per well and incubated for 5-7 min, then resuspended in 3 mL of NMM and centrifuged at 200 × g for 5 min. The pellet was resuspended in NMM containing 10 µM Y-27632 ROCK inhibitor and replated onto poly-L-ornithine/laminin-coated wells. From Day 40 onwards, 2 µg/mL laminin was added to the medium every five days to reduce detachment and clumping of neurons (Baron-Van Evercooren et al., 1982).

Table 2.2 Composition of NIM and NMM

(A) Neural Induction Medium (100 mL)

Item	Volume	Final conc.	Stock conc.	Supplier	Catalogue no.
DMEM/F12 Medium	~49 mL	–	1X	Life Technologies	21331020
Neurobasal Medium	~49 mL	–	1X	Life Technologies	21103-049
B27 supplement	1 mL	1X	50X	Life Technologies	17504044
N2 supplement	0.5 mL	1X	100X	Life Technologies	17502-048
GlutaMax	1 mL	1X	100X	Life Technologies	35050-038
LDN193189	10 µL	100 nM	1 mM	Sigma-Aldrich Corporation	SML0559
SB431542	100 µL	10 µM	10 mM	Cambridge Bioscience	ZRD-SB-50

(B) Neural Maintenance Medium (100 mL)

Item	Volume	Final conc.	Stock conc.	Supplier	Catalogue no.
DMEM/F12 Medium	~49 mL	–	1X	Life Technologies	21331020
Neurobasal Medium	~49 mL	–	1X	Life Technologies	21103-049
B27 supplement	1 mL	1X	50X	Life Technologies	17504044
N2 supplement	0.5 mL	1X	100X	Life Technologies	17502-048
GlutaMax	1 mL	1X	100X	Life Technologies	35050-038

2.2.2.3 Stock preservation of the hiPSC-derived cortical progenitors

On DIV 24, neuronal progenitors were either *in vitro* cultured for downstream applications or cryopreserved for future use. For cryopreservation, cells were dissociated using Accutase and pelleted by centrifugation. The pellet was resuspended in freezing medium, and the suspension was transferred into cryovials, which were stored overnight at -80°C in a Mr. Frosty freezing

container and then transferred to liquid nitrogen for long-term storage. The composition of the freezing medium is detailed in Table 2.3.

Table 2.3 Composition of freezing medium for hiPSC-derived cortical progenitors (10 mL)

Item	Volume	Final conc.	Stock conc.	Supplier	Catalogue no.
NMM	9 mL	–	–	–	–
DMSO	1 mL	–	–	Sigma-Aldrich Corporation	D2650-100ML
Y-27632 ROCK inhibitor	5 µL	5 µM	10 mM	STEMCELL Technologies	72304-5mg

2.2.2.4 Recovery of the hiPSC-derived cortical progenitors

Vials of hiPSC-derived cortical progenitors were retrieved from the liquid nitrogen tank and rapidly thawed in a 37°C water bath until only a small ice crystal remained. The contents were slowly transferred dropwise into 9 mL of pre-warmed NMM in a 15 mL Falcon tube to minimise osmotic shock. Cells were centrifuged at 200 × g for 5 min, and the pellet was resuspended in NMM supplemented with 10 µM Y-27632 ROCK inhibitor. Each vial was plated onto a 6-well plate pre-coated with poly-L-ornithine and laminin. The following day, the medium was replaced with fresh NMM without Y-27632 ROCK inhibitor.

Unless otherwise stated, reagents were obtained from commercial sources and used according to the manufacturer's instructions. A comprehensive list of all reagents, suppliers, and catalogue numbers is provided in the Appendix (Table 6.1-6.7)

2.2.3 Characterisation of the hiPSC-derived cortical neurons

2.2.3.1 Immunocytochemistry of the monolayer-cultured neurons

For immunocytochemistry, cells were seeded on poly-L-ornithine/laminin-coated 18-well slides (Ibidi, Thistle Scientific). At designated time points, the cells were washed with DPBS and fixed using 4% paraformaldehyde (PFA, Thermo Fisher Scientific) for 15 min at room temperature. After fixation, the cells were rinsed three times with DPBS, each for 10 min, and then stored in the dark at 4°C until use. On the day of immunocytochemistry, the fixed cells were rinsed with phosphate-buffered saline (PBS) and permeabilised with 0.5% Triton X-100 (Thermo Fisher Scientific) for 10 min. They were then blocked in PBS containing 5% Bovine Serum Albumin (BSA, Sigma-Aldrich Corporation) and 0.2% Triton X-100 for 1.5 h. Primary antibodies were diluted in 1% BSA and 0.2% Triton X-100 in PBS and applied overnight at 4°C. The following day, the cells were washed three times with PBS, and then incubated with

secondary antibodies (1:500) and DAPI (1:1000) for 1.5 h. Finally, the cells were washed three times with PBS and then mounted with FluorSave mounting medium (Sigma-Aldrich Corporation). The primary and secondary antibodies used in this study are detailed in Tables 6.5 and 6.6.

2.2.3.2 Confocal microscopy imaging and quantification analysis

Samples were imaged using a confocal microscopy (Zeiss LSM780) equipped with 20X, 40X oil-immersion, and 63X oil-immersion objectives. Negative controls were included in the staining runs; however, in the interest of figure clarity, they are not shown in the presented figures. Three independent differentiation experiments (biological replicates, n) were conducted. In each replicate, at least three different fields were imaged per marker. Marker-positive cells were manually counted and expressed as a percentage of total DAPI-positive cells. For each biological replicate, the average from the three fields was calculated. The averages from the three independent experiments were then used for statistical analysis.

For the analysis of the progressive expression of cytoskeletal markers throughout differentiation (at DIV 24, DIV 45, and DIV 70). Images of MAP2 and Nestin immunostaining were captured with 20X magnification. The images were processed using ImageJ software (NIH, version 2.14.0/1.54f). Images were manually thresholded, and the percentage of positive area relative to the total field area was quantified. All analyses were conducted using three independent differentiation experiments, except for Nestin at DIV 24 and DIV 70, where only two replicates were analysed.

Synaptic density of ENPCs and LNPCs was assessed using images captured with a 63X oil-immersion objective at 2x digital zoom. A Z-stack of 10 planes separated by a 1 µm interval was acquired and processed with ImageJ software. The images were flattened using the Z-Project Max Intensity function, and then the background was subtracted using the Subtract Background function (rolling ball radius = 50). Synapsin-1 and post-synaptic PSD-95 puncta were quantified using the SynBot plugin (Savage et al., 2024). Manual thresholding was utilised to detect puncta in each channel for each image, with area thresholds set between 40 and 200 pixels for the minimum and maximum sizes, respectively. To detect co-localisation, the radius and coordinates of each punctum in the first channel were calculated and compared with those in the second channel. Puncta were considered colocalised if the distance between them was less than the sum of their radii (Savage et al., 2024). All synaptic density values were

normalised to the field area. A negative control is provided in the Supplementary Material (Fig. 6.1A), showing no signal in the SYN1 and PSD-95 channels above background.

2.2.3.3 Molecular analysis (RT-qPCR)

2.2.3.3.1 RNA isolation

Total RNA was extracted from neuronal cultures at DIV 24, DIV 45, and DIV 70 using the Monarch® Total RNA Miniprep Kit (New England BioLabs) according to the manufacturer's instructions. Cells were enzymatically dissociated using Accutase, pelleted, and then washed with DPBS. They were either processed immediately or stored at -80°C. For RNA extraction, pellets were thawed at room temperature and resuspended in 600 µL of RNA Lysis Buffer with gentle pipetting. All centrifugation steps were conducted at 16,000 × g for 30 s, unless stated otherwise. Lysates were transferred to a gDNA Removal Column and centrifuged to remove gDNA. The flow-through was mixed with an equal volume of ethanol and applied to an RNA Purification Column. The sample was then centrifuged, followed by washing with 500 µL of RNA Wash Buffer and another centrifugation step.

A mixture of 5 µL of DNase I and 75 µL of DNase I Reaction Buffer was added directly to the top of the matrix and incubated for 15 min at room temperature. The column was then washed with 500 µL RNA Priming Buffer, followed by two sequential washes with 500 µL RNA Wash Buffer. RNA was eluted with 30–100 µL nuclease-free water into an RNase-free tube. The eluted RNA was treated with an additional in-tube DNase I digestion to avoid genomic DNA amplification. For each 40 µL RNA sample, 5 µL DNase I and 5 µL DNase I Reaction Buffer were added, and samples were incubated for 20 min at room temperature. For each 50 µL treated sample, 100 µL of RNA Lysis Buffer was added, followed by an equal volume of ethanol. The binding and elution steps described above were then repeated. The eluted RNA was either stored at -80°C or placed on ice for the subsequent step of cDNA synthesis. The quality and yield of the RNA were assessed using a NanoDrop One Spectrophotometer (Thermo Fisher Scientific).

2.2.3.3.2 cDNA synthesis

Reverse transcription was performed using the LunaScript® RT SuperMix Kit (New England BioLab). Preparation of cDNA, No-RT control, and No template controls were prepared as indicated in the tables 2.4-2.6.

Table 2.4 cDNA synthesis protocol

Components	20µl Reactions	Final concentration
LunaScript RT SuperMix (X5)	4 µL	1X

RNA Sample	Variable	(up to 1 µg)
Nuclease-free water	To 20 µL	

Table 2.5 No-RT control protocol

Components	20µl Reactions	Final concentration
No-RT Control Mix (X5)	4 µL	1X
RNA Sample	Variable	(up to 1 µg)
Nuclease-free water	To 20 µL	

Table 2.6 No template controls protocol

Components	20µl Reactions	Final concentration
LunaScript RT SuperMix (X5)	4 µL	1X
Nuclease-free water	16 µL	

The microcentrifuge tubes were placed in a ProFlex PCR System thermocycler (ThermoFisher Scientific) with the following programme (Table 2.7):

Table 2.7 cDNA synthesis thermal programme

Step	Temperature	Time
Primer Annealing	25°C	2 min
cDNA Synthesis	55°C	10 min
Heat Inactivation	95°C	1 min

The synthesised cDNA templates were stored in a -20°C freezer.

2.2.3.3.3 RT-qPCR performance

Amplification was performed using the Luna® Universal qPCR Master Mix (New England BioLab), and PCR reactions were quantified with the QuantStudio™ 5 Real-Time PCR System (Thermo Fisher Scientific). In the qPCR plate (Thermo Fisher Scientific), each 20 µL reaction was prepared as shown in Table 2.8.

Table 2.8 Master Mix for qPCR

Components	20µl reaction	Final concentration
Luna Universal PCR Mix	10 µL	1X
Forward primer (10 µM)	0.5 µL	0.25 µM
Reverse primer (10 µM)	0.5 µL	0.25 µM
Template cDNA	Variable	< 100 ng
Nuclease-free water	To 20 µL	

For preparation, the Luna Universal qPCR Master Mix and other reaction components were thawed and kept on ice. Master mixes were prepared with an additional 10% excess and aliquoted into wells before the addition of cDNA templates. Plates were sealed with optically transparent film (Thermo Fisher Scientific) and then centrifuged at 200 × g for 1 min to remove air bubbles. The plate was placed in the Real-Time PCR System, following the thermocycling protocol (Table 2.9):

Table 2.9 qPCR thermal programme

Cycle step	Temperature	Time	Cycles
Initial denaturation	95°C	60 s	1
Denaturation	95°C	15 s	40-45
Extension	60°C	30 s (+ plate read)	
Melt Curve	60-95°C	Various	1

Because housekeeping gene expression can vary during neural differentiation, reference genes must be empirically validated for stability at different differentiation stages and conditions (Augustyniak et al., 2019). Relative gene expression was calculated from three technical replicates per sample. To improve robustness, three independent housekeeping genes were used as internal references, including ATP5O (Cordella et al., 2022), PRDM4, and UBE4A (Vaughan-Jackson et al., 2022). A panel of candidate reference gene, ATP5O, PRDM4, UBE4A, and S18 were screened for expression stability across differentiation stages using the BestKeeper algorithm (Pfaffl et al., 2004). It is an Excel-based reference-gene stability tool that works on raw CT values. It first calculates descriptive statistics for each candidate housekeeping gene, including the SD and coefficient of variation, where higher variability indicates poorer stability. It then constructs a BestKeeper Index and evaluates each candidate by Pearson correlation against this index to identify the reference genes that are most internally consistent across samples (Pfaffl et al., 2004). The final set of ATP5O, PRDM4, and UBE4A was chosen based on minimal expression variability across conditions, and the geometric mean of their CT values was used to normalise target gene expression across samples. Fold changes were calculated using the ΔΔCT method, with DIV 24 as the reference time point. Primer sequences for neurogenesis-related genes are provided in Table 2.10, and consumables are listed in Appendix Table A2.

Table 2.10 List of primers for RT-qPCR

Target	Direction	Sequence (5′–3′)	Manufacturer
ATP5O	Forward	ACTCGGGTTTGACCTACAGC	Life Technologies
	Reverse	GGTACTGAAGCATCGCACCT	Life Technologies
PRDM4	Forward	CCAAAGCAGCTTGTTCTCCGTC	Life Technologies
	Reverse	TAGAGGTCCAAAGCAAGTCCGC	Life Technologies
UBE4A	Forward	CCTTTGCCAGATGGCTACAGCT	Life Technologies
	Reverse	CTCCAGGGAATCTGCTGATGTC	Life Technologies
MAP2	Forward	CAGGAGACAGAGATGAGAATTCC	Life Technologies
	Reverse	CAGGAGTGATGGCAGTAGAC	Life Technologies
RBFOX3 (NeuN)	Forward	GTAGAGGGACGGAAAATTGAGG	Life Technologies
	Reverse	CATAGAATTCAGGCCCGTAGAC	Life Technologies
SATB2	Forward	CCTTACGCAAATCTCAGACAA	Life Technologies
	Reverse	CCAGATATCTACCAGCAAGTCAG	Life Technologies
CTIP2	Forward	GAGTACTGCGGCAAGGTGTT	Life Technologies
	Reverse	TAGTTGCACAGCTCGCACTT	Life Technologies
SOX2	Forward	CACACTGCCCCTCTCAC	Life Technologies

	Reverse	GCTGTAGTG GTTAGACGCTG	Life Technologies

2.2.3.4 Measuring and analysing functional connectivity from calcium signalling data

Calcium imaging enables the simultaneous monitoring of calcium spikes across large numbers of neurons (Grienberger and Konnerth, 2012). When coupled with graph theory analysis, it facilitates a quantitative assessment of functional connectivity. Graph theory generates a graphical representation of the neuronal network, where nodes represent neurons and edges reflect pairwise correlation coefficients. It enables the computation of mathematical metrics such as edge weight, path length, modularity, and clustering coefficient that provide insights into the functional connectivity and topography of neural networks (Nelson and Bonner, 2021).

ENPCs and LNPCs were separately plated onto poly-L-ornithine/laminin-coated 4-well Ph+ slides at a seeding density of 1.5×10^5 cells/cm^2. ENPCs were plated two weeks prior to imaging, while LNPCs were plated three weeks before imaging. Cells were cultured in NMM until 48 h before experiments, at which point the medium was replaced with BrainPhys medium (STEMCELL Technologies).

2.2.3.4.1 Calcium imaging of ENPCs and LNPCs in monolayers

Two calcium indicators were used for calcium imaging: Fluo-4 AM and Fura-Red AM (Thermo Fisher Scientific). To prepare stock, 50 µg Fluo-4 AM was reconstituted in 44 µL DMSO and 500 µg Fura-Red AM was reconstituted in 500 µL of 10% Pluronic® F-127 (Thermo Fisher Scientific). Vials were protected from light and stored at -20°C. Monolayers were loaded with a mixture of 5 µM Fluo-4 AM and 12 µM Fura-Red AM in 0.125% Pluronic F-127 and then incubated at 37°C and 5% CO_2 for 30 min. Cells were then washed with BrainPhys imaging medium (STEMCELL Technologies) and incubated for an additional 30 min to allow for intracellular dye de-esterification. This combination of calcium indicators is spectrally resolvable and peak responses to calcium change in opposite directions, enabling pseudo-ratiometric imaging and analysis (Takahashi et al., 1999, Assinger et al., 2015).

Pseudo-ratiometric time-lapse imaging was performed using a confocal microscope (Zeiss, LSM710) equipped with a stage-top incubator (Thistle Scientific) to produce a physiological condition of 37°C and a humidified atmosphere of 5% CO_2. 488 nm laser light was used to simultaneously excite Fluo-4 and Fura-Red. Fluorescence emissions were separated by a dichroic mirror at 580 nm and measured as a Fluo4 channel (bandpass 500-580 nm) and a Fura-

Red channel (longpass >580 nm). Imaging was conducted using an EC Plan-Neofluar 40X/1.30 oil immersion objective, capturing 800 frames at a frame rate of 1.27 Hz with a resolution of 256 × 526.

2.2.3.4.2 Pharmacological interrogation of neuronal phenotypes

To investigate the pharmacological profile of neuronal networks containing glutamatergic and GABAergic neurons, relevant neurotransmitters were applied and withdrawn under continuous superfusion at a rate of 3 mL/min using a switcher to alternate between two perfusion lines. Solutions were heated with a feedback heating block in series with the superfusion lines. Cultures were equilibrated with imaging medium superfusate for 3 min prior to baseline imaging. The protocol consisted of recording the baseline of spontaneous activity, followed by the activity after application of one of the pharmacological agents listed in Table 2.11.

Pharmacological agents were dissolved in a phenol red-free imaging medium; its composition is illustrated in Table 6.9.

Table 2.11 Pharmacological agents used for functional interrogation of ENPC and LNPC neuronal networks

Category	Agent	Concentration	Target receptor/channel
GABA modulators	Gabazine	10 µM	GABA-A receptor (competitive antagonist)
	Picrotoxin	50 µM	GABA-A chloride channel (non-competitive antagonist)
	GABA	100 µM	GABA-A receptor (agonist)
Glutamatergic modulators	Glutamate (Glu)	30 µM	Ionotropic glutamate receptors (agonist) (NMDA/AMPA)
Action potential blockade	Tetrodotoxin (TTX)	1 µM	Voltage-gated sodium channel blocker
Calcium chelation	EGTA	4 mM	Chelates extracellular calcium

2.2.3.4.3 Data analysis of calcium signal

2.2.3.4.3.1 Data processing and identifying calcium dynamics

Data analysis was performed using custom MATLAB scripts (MathWorks, Natick, MA, USA). Motion correction was applied to eliminate XY-plane drift, with the first frame used as the reference for translational registration. Identical transformations were applied to synchronously acquired Fluo-4 and Fura-Red images to ensure consistent ratioing. Regions of interest (ROIs) were detected using the Constrained Non-negative Matrix Factorisation (CNMF) algorithm implemented in the open-source CaImAn toolbox (Giovannucci et al., 2019), which estimates the spatial components of each ROI from pixels exhibiting similar fluorescence dynamics. For

each ROI, pixel coordinates were used to extract Fluo-4 and Fura-Red signals for pseudo-ratiometric analysis.

A high-pass Butterworth filter was applied to the pseudo-ratiometric traces to remove low-frequency noise before extracting spike trains. Spike trains were detected using a modified version of MATLAB's findpeaks function (Signal Processing Toolbox, MATLAB), which identified calcium events as spikes if at least one of two threshold criteria was met. To optimise these thresholds, recordings from monolayer ENPC and LNPC cultures were manually annotated by two independent users. These annotations were used to train the algorithm and define the threshold parameters. The first criterion was based on an absolute amplitude threshold, while the second required the signal amplitude to exceed a multiple of the standard deviation of the filtered baseline noise of the ratiometric trace. Typically, large-amplitude spikes satisfied the first criterion, whereas the second captured smaller, low-amplitude events. Any event meeting either criterion was classified as a true calcium spike.

A neuron was considered active if it fired at least once during the recording time, which was approximately 10.5 min for spontaneous recording; only active neurons were included in further analyses. The percentage of active neurons (number of active neurons/total number of neurons detected in the imaging field), the global synchrony index, and spike dynamics, such as rise time (s), decay time (s), and half-maximal spike width (s), were calculated using a custom script. The global synchrony index was calculated as the ratio of the total number of synchronised spikes to the total number of possible synchronised spikes across all time steps. The spike width was quantified as the full width at half maximum. The rise time was estimated as twice the duration between the half-maximum and peak; the decay time was estimated as twice the duration between the peak and the following half-maximum (Fig. 2.1).

For each recording, the mean values of all calculated parameters were averaged across all active neurons within the field of view. Three independent recordings were obtained from different culture wells (technical replicates) for each biological replicate, and the mean value across these recordings was used for statistical analysis.

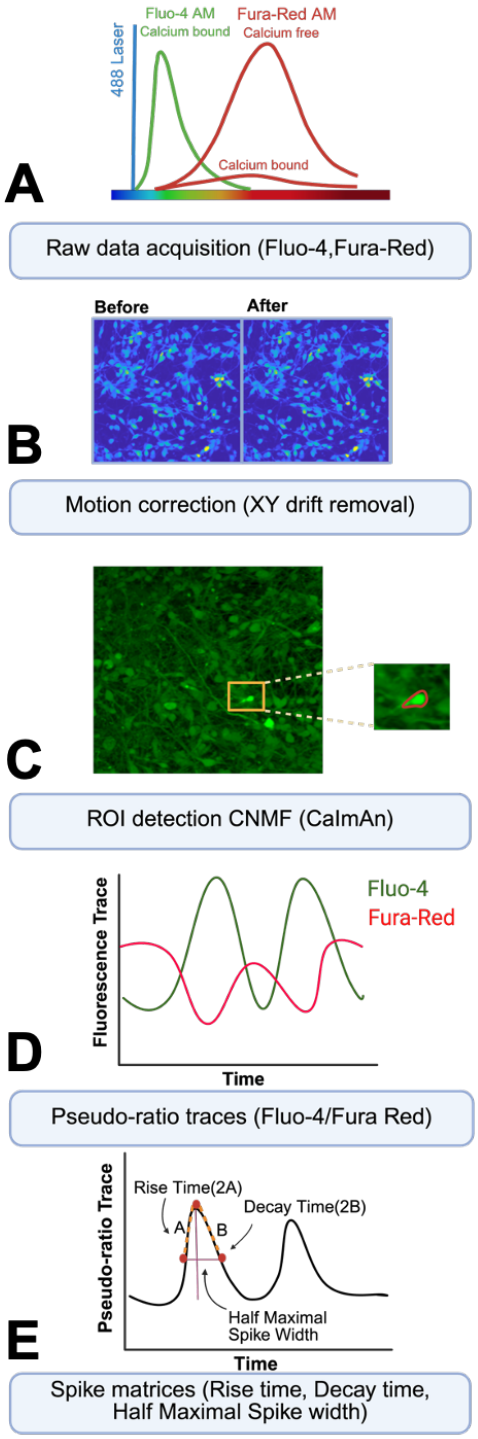

Figure 2.1 Workflow for measuring and analysis of calcium signals
(A) Raw data acquisition using the calcium indicators Fluo-4 AM and Fura-Red AM, excited with a 488 nm laser.
(B) Motion correction to remove XY-plane drift and ensure stable signal alignment across frames.
(C) ROI detection using CNMF, extracting spatial features of each ROI.
(D) Pseudo-ratiometric traces derived from Fluo-4/Fura-Red signals to minimise noise.
(E) Quantification of spike dynamics, including rise time, decay time, and half-maximal spike width from pseudo-ratiometric traces.

2.2.3.4.3.2 Functional connectivity and graph theory analysis

To evaluate the functional connectivity patterns in neurons, graph theory analysis began by computing the Pairwise Pearson correlation matrix between active neurons (Dingle et al.,

2020). A threshold of greater than 0.35 was applied to generate a weighted matrix; this threshold was selected after testing a wide range of values, identifying the optimal threshold that neither over-segmented the network nor obscured the existing network.

This analysis employed a weighted network approach, where the correlation coefficient for the paired nodes *i* and *j* represented the edge weight in the graph, and the average edge weight was calculated by averaging all edge weights across the network. Larger edge weights indicate stronger correlations between neuronal activity, reflecting tighter functional coupling, whereas lower edge weights denote weaker or more sporadic associations. The path length is inversely related to edge weight, with lower path length between connected nodes signifying more direct and efficient routes for information transfer, and longer path length reflecting reduced efficiency and weaker integration (Nelson and Bonner, 2021, Sporns, 2013).

The clustering coefficient quantifies the strength of functional connectivity among nodes in a network by assessing the extent of connections among a node's closest neighbours, represented as a ratio of actual connections to the total number of possible connections. A network with a high average clustering coefficient is better at integrating local information and is more resilient to disruptions. Modularity measures the density of edges within modules compared to the density of edges between modules. A higher modularity value indicates that the network is more strongly divided into subnetworks, with nodes more closely connected within modules than to nodes in other modules (Bullmore and Sporns, 2009, Rubinov and Sporns, 2010).

Edge weight (w_{ij}) was computed as outlined by the open script (Muldoon et al., 2016). Briefly, the edge weight between node *i* and node *j* was equal to the correlation coefficient (r) and defined as:

$$w_{ij} = r(i,j)$$

The average edge weight (W) for a network with N nodes was calculated as:

$$\mathrm{W} = \frac{1}{\mathrm{N}(\mathrm{N}-1)} \sum_{i \neq j} \mathrm{w}_{ij}$$

Path length (d_{ij}) was computed as outlined by the open script (Muldoon et al., 2016). Briefly, the distance connecting node *i* to node *j* was inversely related to the edge weight (w) and defined as:

$$d_{ij} = \frac{1}{\mathrm{w}_{ij}}$$

The average path length (PL) for a network with N nodes was calculated as:

$$\mathrm{PL} = \frac{1}{\mathrm{N}(\mathrm{N}-1)} \sum_{i \neq j} \mathrm{d}_{ij}$$

The local clustering coefficient (c_i) in a weighted graph was calculated following the method described by Onnela et al., utilising their publicly available MATLAB script (Onnela et al., 2005), which defined the clustering coefficient in a weighted graph as the intensity of triangle networks formed by triplets of nodes and calculated as:

$$c_i = \frac{1}{k_i(k_i-1)} \sum_{j,k} \frac{\sqrt[3]{\mathrm{w}_{ij}\mathrm{w}_{jk}\mathrm{w}_{ik}}}{\max(\mathrm{w})}$$

Where k_i was the number of edges connected to node *i*, and $w_{ij}$was the edge weight between *i* and *j*. The average clustering coefficient (C) for a network with N nodes was calculated as:

$$\mathrm{C} = \frac{1}{N} \sum c_i$$

Modularity (Q) was calculated using a previously published MATLAB script (Newman, 2006), which was the difference between the observed and expected fraction of edges within modules in a comparable random network. Modules (clusters) detection was performed using a previously published script (Saberi et al., 2022) that utilised an iterative Louvain community-detection algorithm (Blondel et al., 2008), which optimises the modularity function through hierarchical aggregation of nodes into modules to maximise modularity. This method efficiently identified communities in large, weighted networks by iteratively refining partitions until no further modularity improvement can be achieved. It was calculated as:

$$Q = \frac{1}{2\mathrm{w}} \sum_{i,j} \left[w_{ij} - \frac{k_i k_j}{2w} \right] \delta(xi, xj),$$

Where w_{ij} was the weight of the edge between nodes *i* and *j*. k_i was the strength of the node and was calculated as $k_i = \sum_i w_{ij}$. $2w$ was the total sum of edge weights in the networks and was calculated as $2w = \sum_{ij} w_{ij}$.

$x_i$and x_i were the community assignments of nodes *i* and j. $\delta(xi, xj)$ was equal to 1 if *i* and *j* belonged to the same community, and 0 otherwise. $\frac{k_i k_j}{2w}$ was the expected connection strength between *i* and *j* in a random network with the same strength distribution.

Networks can be classified based on their topological properties into random networks, which are highly uniform; small-world networks, which feature both high clustering and short path lengths; and regular networks or lattices, characterised by high clustering and long path lengths (Vecchio et al., 2017) (Fig. 2.2C). Small-world networks are an intermediate form of networks that exhibit a high clustering coefficient and low path lengths. Neural networks exhibit small-world properties, which enable both efficient information integration and local processing (Bassett and Bullmore, 2017). Within the neural networks, some neurons play a crucial role in connecting different parts and are known as hubs (Han et al., 2025). In our script, a neuron was defined as a hub if it had a relatively large number of intramodular connections, surpassing the 90th percentile of connections in the module.

Finally, the Fruchterman-Reingold algorithm was used to visualise inter-neuronal interactions within the module network, highlighting the topological proximity of highly connected neurons within each module (Fruchterman and Reingold, 1991). Edge length was inversely proportional to the correlation coefficient, such that shorter lines indicate stronger correlations between neuron pairs. The size of the nodes in the topology reflected hub status within each module, with centrally positioned hub neurons showing close topological proximity, consistent with their role as intramodular hubs (Fig. 2.2D).

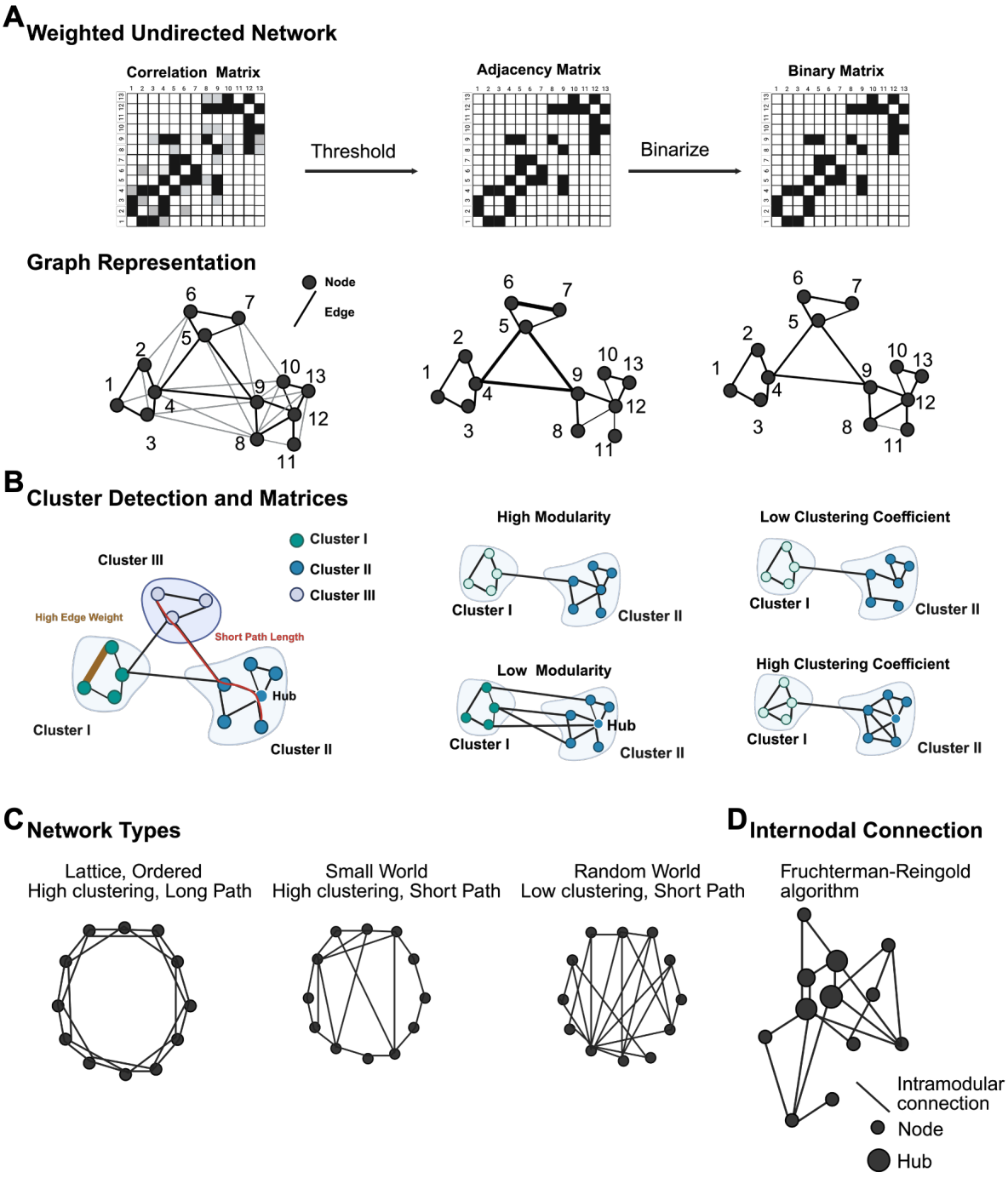

Figure 2.2 Framework for functional connectivity and graph theory analysis of neuronal networks

(A) Functional connectivity matrices are generated from pairwise correlations of pseudo-ratiometric traces of active neurons. Thresholding of the correlation matrix produces a weighted adjacency matrix, which is then converted into a binary matrix (0,1matrix). Diagrammatic illustration of a network driven by graph theory, where neurons are represented as nodes and correlation coefficients as edges connecting the nodes.

(B) The Module detection algorithm identifies modules (clusters) of highly interconnected nodes. Illustrations of different connectivity matrices, including modularity and clustering coefficient.

(C) Illustrations of different types of networks, including lattice, small world, and random world networks, are shown to highlight differences in path length and clustering coefficient.

(D) Fruchterman-Reingold Algorithm is applied to visualise internodal interactions, where node size reflects connectivity strength and hubs are prominently highlighted.

2.2.4 Intracortical injection of ENPCs and LNPCs

2.2.4.1 Experimental animals

I employed P7–P8 NOD-SCID mice (NOD.Cg-Prkdc^{scid} Il2rg^{tm1Wjl}/SzJ) for all transplantation experiments. It is a strain that combines multiple immune deficits to permit robust engraftment of human cells. The Prkdc^scid mutation on the NOD results in defective DNA-PKcs activity and a near-complete loss of T and B lymphocytes. In addition, deletion of the common γ-chain (Il2rg null allele) abolishes NK cell function, thereby impairing adaptive and innate immunity. Additional features of the NOD background contribute to tolerance of human grafts; a variant of Signal Regulatory Protein alpha (SIRPα) interacts with human CD47 at high affinity, reducing macrophage-mediated clearance, while complement C5 deficiency limits complement-driven lysis. Collectively, these features confer profound combined immunodeficiency, making them a permissive environment for the engraftment of human cell-derived grafts (DiSanto et al., 1995, Chen et al., 2022).

All procedures were approved by the local ethical review committee and conducted following the UK Animals (Scientific Procedures) Act, 1986 (ASPA), under valid Personal and Project Licences. Breeding pairs of NOD-SCID were obtained from Charles River (strain code 614). Animals were housed in individually ventilated cages under a 12-hour light/dark cycle in the Biomedical Sciences Building at the University of Oxford. Food and water were provided *ad libitum*.

2.2.4.2 Transplantation of ENPCs and LNPCs into the right motor cortex of NOD-SCID mice

Prior to surgery, instruments were autoclaved and maintained on sterile drapes throughout the procedure. ENPCs and LNPCs were passaged as described above and resuspended at a concentration of 1×10^5 cells/μL in sterile 0.1% Fast Green FCF (Sigma-Aldrich Corporation) in PBS. The suspension was loaded into a pulled glass capillary pre-filled with mineral oil (Sigma-Aldrich Corporation) and connected to a 10 μL Hamilton syringe via a Hamilton RN compression fitting (Hamilton). Pups were anaesthetised in an induction chamber using 3% isoflurane in oxygen for 3 min, then transferred to an anaesthesia maintenance mask supplied with 2% isoflurane. The body temperature of the mice was maintained with a heating pad, and the depth of anaesthesia was assessed by pedal withdrawal reflex before starting the procedure.

After disinfection of the scalp with Chlorhexidine wipes, the capillary tip was positioned above the right motor cortex (approximately +1.2 mm anterior and +1.2 mm lateral to bregma). The pipette was lowered until a slight indentation of the cortical surface was visible (defined as Z = 0), and the injection depth was set to Z = −0.5 mm from the pial surface. A total volume of 1 µl of cell suspension was injected over 2 min (0.5 µl/min) using a Stoelting Quintessential Stereotaxic Injector (QSI, Stoelting). Post-operatively, animals received a single subcutaneous injection of meloxicam (1 mg/kg) for systemic pain control. Pups were placed in a pre-warmed 37°C recovery chamber until fully recovered. They were then cleaned to remove blood traces and gently rubbed with cage bedding to mask surgical odours before being returned to the dam. On the surgery day, the pups were monitored after 2 h of surgery, and then daily for the first week after surgery, and weekly until the end of the experiment.

2.2.4.3 Brain collection and immunohistochemistry of free-floating brain sections

Animals were anaesthetised with an overdose of intraperitoneal pentobarbitone, followed by transcardial perfusion with cold 0.1 M PBS, then 4% PFA. Brains were dissected and post-fixed in 4% PFA overnight at 4°C, then transferred to 30% sucrose in 0.1M phosphate buffer (PB) and stored at 4°C for 48 h or until they sank. Brains were frozen on dry ice and coronally sectioned at 30 µm using a Leica sliding microtome. Sections were collected in 48-well plates containing cryoprotectant solution (30% Ethylene glycol, 30% Sucrose in 0.1M PB) and stored at -20°C until use. For each brain, sections were distributed sequentially across eight wells such that each well contained a representative series spanning the entire rostrocaudal extent of the brain. This ensured that each well contained a representative series of sections suitable for subsequent immunohistochemical analysis. For immunohistochemistry, free-floating sections were washed three times in PBS and blocked in PBS+ (PBS with 5% normal donkey serum and 0.3% Triton X-100) for 1 h at room temperature. Sections were incubated overnight with primary antibodies diluted in PBS+ at 4°C. The following day, sections were washed in PBS, incubated for 1.5 h with fluorescent secondary antibodies (1:500) and DAPI (1:1000) in PBS+, and then washed again before being mounted using FluorSave™ mounting medium. The primary and secondary antibodies used in this study are detailed in Tables 6.5 and 6.6.

2.2.4.4 Confocal microscopy imaging and quantitative analysis of ENPC and LNPC grafts

Neuronal differentiation and maturation of the grafts were assessed by immunohistochemistry for layer markers CTIP2 and SATB2. Each experimental group included at least three animals. From each brain, 2 coronal sections with grafts were used for analysis. For each section, three

images within the grafts were acquired, using a 40X oil-immersion objective, as a Z-stack with a 1.88 µm interval. Manual cell counting was performed using the Cell Counter plugin in ImageJ software, and the percentage of HuNu+ cells co-expressing CTIP2 or SATB2 was calculated per image. The average across the sections of each animal was calculated and represented a biological replicate (N), and this value was used for statistical analysis.

2.2.4.5 Neurolucida reconstruction of axonal projection and semi-quantitative analysis of projection density

Neurolucida software platform (MBF Bioscience) was used to trace axonal projections across serial coronal brain sections, guided by hNCAM immunostaining. Reconstructions were performed along the entire rostrocaudal axis of the brain to visualise long-range axonal trajectories and regional innervation patterns. Every eighth section along the rostrocaudal axis of the brain was used for tracing. Each section was manually outlined, and regions were delineated based on the Allen Brain Atlas.

Axonal projections were quantified using Neurolucida Explorer by dividing each section into defined cortical and subcortical regions. These included the ipsilateral cerebral cortex (layers L1–4 and L5–6), striatum, septum, thalamus, corpus callosum, internal capsule, hippocampal formation, and piriform cortex, as well as the contralateral cerebral cortex (layers L1–4 and L5–6) and corpus callosum. Within each region, the number of continuous axonal traces was recorded, and data from the ipsilateral and contralateral hemispheres relative to the implantation site were quantified separately.

Projection density within defined brain regions was scored from 0 to 3, based on estimated projection counts; 0 = no detectable projections, 1 (+) = sparse projections, fewer than 10 projections, 2 (++) = moderate projections, approximately 10–100 projections, and 3 (+++) = dense projections, more than 100 projections. This scoring system provides a relative rather than absolute quantification of axonal distribution. Each animal was scored independently, and group averages were calculated to illustrate overall projection patterns.

2.2.5 Statistical analysis

Statistical analyses were performed using GraphPad Prism 10. Data were presented as means ± SEM. Normality was assessed using the Shapiro–Wilk test. Outliers were identified using the Median Absolute Deviation (MAD) method. For group comparisons, unpaired Student *t*-test was used for two-group comparisons when data were normally distributed. For

comparisons between three or more groups, one-way ANOVA followed by Tukey's post hoc test was applied if normality was confirmed. In non-Gaussian distributions, non-parametric tests were used, including the Mann-Whitney U test for two groups and the Kruskal–Wallis test with Dunn's post hoc test for multiple groups. A paired Student *t*-test was used to assess differences in neuronal activity before and after pharmacological intervention. A p-value < 0.05 was considered statistically significant. * $p < 0.05$, ** $p < 0.01$, *** $p < 0.001$, **** $p < 0.0001$.

2.2.6 Summary of experimental pipeline, time points, and the number of replicates

The experimental groups, the number of biological experiments (n), the number of animals (N) per group, and the experimental pipeline were summarised in Table 2.12.

Table 2.12 Summary of the experimental pipeline, time points, and the number of replicates

Experiment	Time point of differentiation/ graft type	Cell type / Material	Number (n) biological replicate, Number (N) animal number
Immunocytochemistry (pluripotency, differentiation-related markers)	DIV 0	Pluripotency markers	n = 3 biological replicates except Nestin at DIV 24 and LNPCs n = 2
	DIV 9	Dorsal identity	
	DIV 24 ENPCs (DIV 45) LNPCs (DIV 70)	Cytoskeletal markers (Nestin, MAP2)	
	ENPCs (DIV 45) LNPCs (DIV 70)	Layers markers (CTIP2, SATB2)	
	ENPCs (DIV 45) LNPCs (DIV 70)	Synaptic markers (SYN1, PSD-95)	
qPCR	DIV 24 (control) ENPCs (DIV 45) LNPCs (DIV 70)	SATB2, CTIP2 MAP2, RBFOX3 (NeuN)	n = 3 biological replicates
Calcium imaging of spontaneous activity	ENPCs (DIV 45) LNPCs (DIV 70)	Spontaneous calcium activity	n = 3 biological replicates
Calcium imaging during pharmacological modulation	ENPCs (DIV 45)	EGTA	n = 3 biological replicates
		TTX	
		GABA	
		Glutamate	
		Picrotoxin/Gabazine	
Calcium imaging during pharmacological modulation	LNPCs (DIV 70)	GABA	n = 3 biological replicates
		Glutamate	
In vivo transplantation	ENPCs (DIV 45) LNPCs (DIV 70)	P7–P8 NOD-SCID mice	N = 7 animals per group
Neurolucida reconstruction of axonal projections and semi-	ENPC graft LNPC graft	Analysis at 2 MPT	N = 6 animals with ENPC grafts N = 4 animals with LNPC grafts

quantitative analysis of projection density			
Immunohistochemistry for layer-specific marker	ENPC-graft LNPC-graft	Analysis at 2 MPT	N = 3 animals per group

2.3 Results

2.3.1 Immunocytochemistry of hiPSCs and hiPSC-derived ENPCs and LNPCs

2.3.1.1 hiPSCs express pluripotency markers

The pluripotency of hiPSCs was confirmed by the expression of stemness markers, OCT4, NANOG, and SOX2, detected through immunocytochemistry (Fig. 2.3A, B). Upon neuronal induction, the expression of OCT4 and NANOG became undetectable by DIV 9, whereas SOX2 persisted (Fig. 2.4A, B), consistent with its role in maintaining neural progenitor identity during early differentiation (Graham et al., 2003).

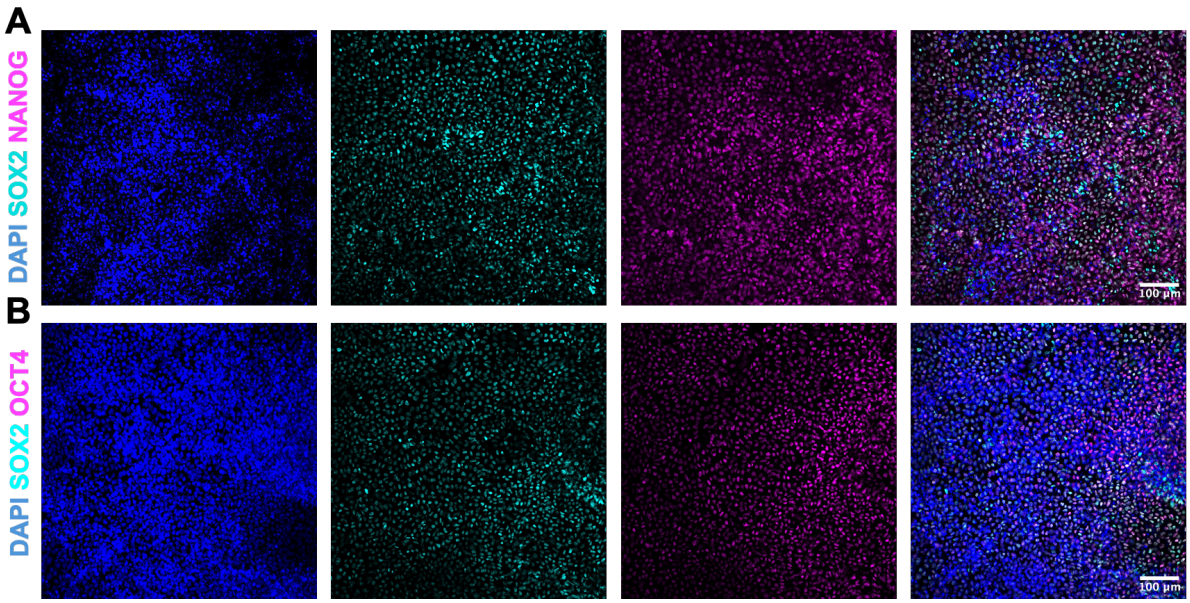

Figure 2.3 Expression of pluripotency markers in hiPSCs
(A, B) Confocal images showing NANOG, SOX2 and OCT4 expression in hiPSC monolayers. Scale bar: 100 µm.

2.3.1.2 Neural induction promotes dorsal identity

By DIV 9, neural induction produced rosette-like structures characteristic of neuroepithelial organisation. Immunostaining showed enrichment of the dorsal forebrain marker PAX6 (90.8 ± 3.15%, Fig. 2.4D), with no expression of the neural crest marker SOX10 detected (Fig. 2.4C). This indicated successful dorsal telencephalic identity without neural crest cell contamination.

Throughout the differentiation process, the cytoskeletal marker of NSCs, Nestin, was consistently detected by immunocytochemistry (Fig. 2.5), likely sustained by persistent SOX2 activity that binds to an enhancer region of the Nestin gene (Tanaka et al., 2004). In contrast, the dendritic cytoskeletal regulator MAP2 (DeGiosio et al., 2022), was detected early and increased gradually, reflecting neuronal maturation. Quantification of the percentage area

covered by cytoskeletal marker expression confirmed the progressive transition from a progenitor to a neuronal phenotype across differentiation. At DIV24, MAP2 expression levels were low (8.63 ± 0.343%, n = 3), whereas Nestin was more prominently expressed (21.12 ± 4.247%, n = 2), consistent with an early progenitor-like state. By DIV 45 (ENPCs), MAP2 expression increased markedly (35.27 ± 1.256%, n = 3), while Nestin levels decreased (17.80 ± 4.185%, n = 3), reflecting the progressive acquisition of neuronal identity. At a later stage, DIV 70 (LNPCs), MAP2 expression reached its peak (49.28 ± 1.112%, n = 3), whereas Nestin expression continued to decline (14.91 ± 3.512%, n = 2). These reciprocal changes in MAP2 and Nestin expression demonstrated the temporal maturation of the cultures, with Nestin downregulation paralleled by a sustained increase in MAP2, indicative of neuronal differentiation and dendritic development.

To further characterise the progenitor state of the differentiated cells, I analysed SOX2 expression and assessed proliferative activity using pHH3 immunostaining. SOX2+ cells were consistently detected throughout differentiation, with no significant differences between groups. At DIV 24, the percentage of SOX2+ cells was 56 ± 11%, compared with 32 ± 5.9% in ENPCs (p = 0.699) and 27 ± 7.9% in LNPCs (p = 0.158; Fig. 2.6D). Proliferative activity, as assessed by pHH3 expression, was higher at DIV 24 compared to ENPCs (3.1 ± 0.62% vs. 0.9 ± 0.22%, p = 0.0372) and LNPCs (0.98 ± 0.46%, p = 0.0430, Fig. 2.6E). These findings indicated that while both ENPCs and LNPCs contain residual progenitors, their proliferative capacity was limited, particularly at later stages of differentiation.

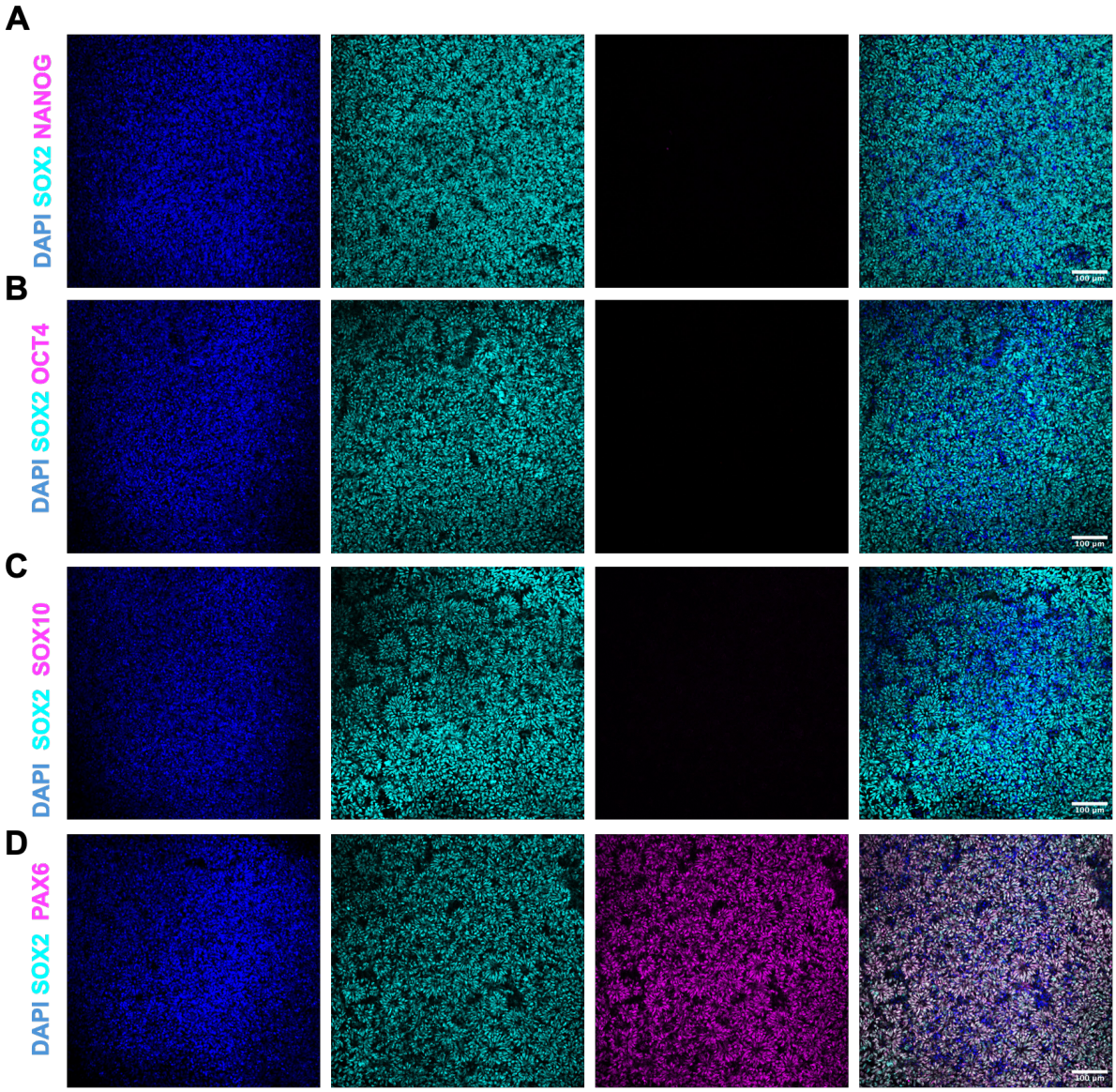

Figure 2.4 Dorsal identity of the neuroectodermal rosettes at DIV 9
(A-C) Confocal images reveal the loss of pluripotency markers NANOG and OCT4, as well as the absence of the neural crest marker SOX10, indicating a loss of pluripotency and a lack of neural crest identity.
(D) Confocal imaging demonstrates robust expression of the dorsal forebrain marker PAX6, confirming acquisition of a dorsal telencephalic identity.
Scale bar: 100 µm. n = 3 biological replicates. DIV = day *in vitro*.

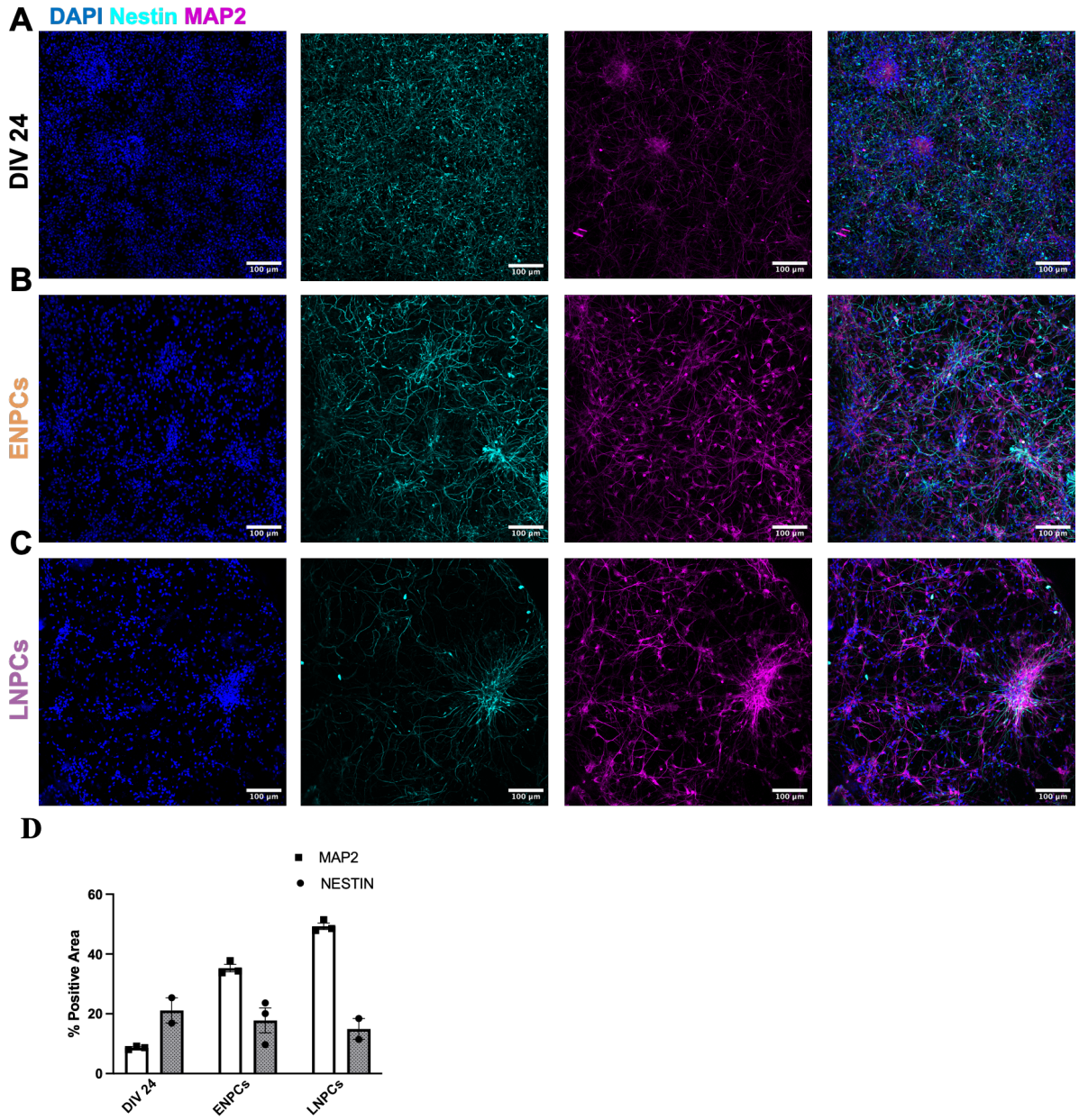

Figure 2.5 Temporal expression of cytoskeletal markers throughout neuronal differentiation
(A-C) Representative confocal images show downregulation of Nestin and upregulation of MAP2, indicating neuronal maturation.
(D) Quantification of the percentage of positive area demonstrates a decline in progenitor-associated Nestin expression and a corresponding rise in MAP2 expression. Scale bar: 100 µm. n = 3 biological replicates except for Nestin at DIV 24 and DIV 70 (LNPCs), where n = 2. DIV = day *in vitro*.

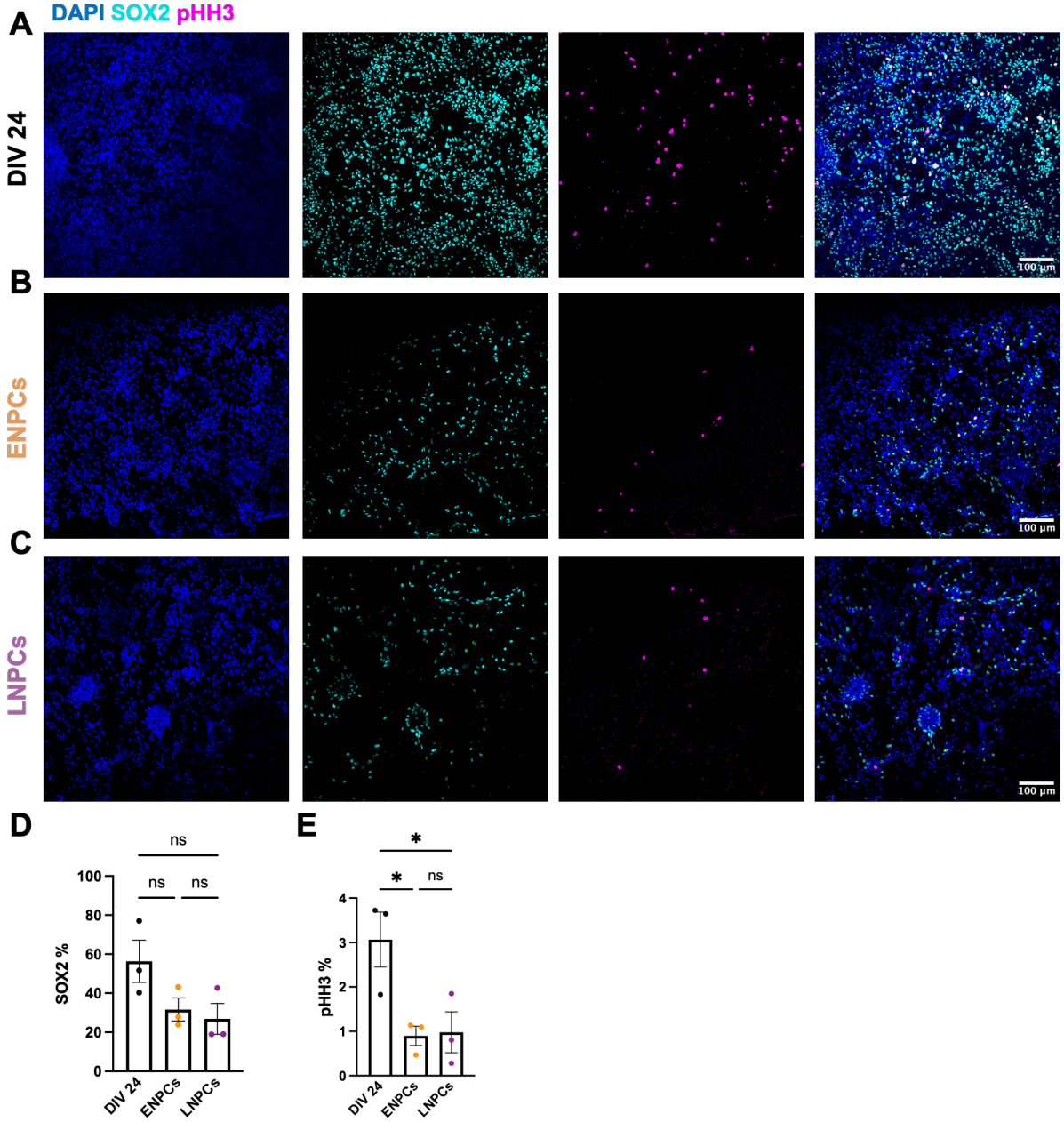

Figure 2.6 Temporal regulation of proliferative capacity throughout neuronal differentiation
(A–C) Representative confocal images of DIV 24 cells, ENPCs, and LNPCs immunostained for SOX2 and pHH3. SOX2+ and pHH3+ cells were detected across all groups, indicating persistence of progenitor identity at different stages of differentiation.
(D) Quantification reveals no significant difference in SOX2+ cells at DIV 24 compared with ENPCs ($p = 0.699$) and LNPCs ($p = 0.158$).
(E) Quantification of proliferative cells marked by pHH3 was significantly higher in DIV 24 compared with ENPCs ($p = 0.0372$) and LNPCs ($p = 0.0430$).
Scale bar: 100 µm. Data are means ± SEM. n = 3 biological replicates. DIV = day *in vitro*.

2.3.1.3 Time-dependent expression of cortical layer markers

hiPSC-derived neurons exhibited stage-specific expression of cortical layer markers, reflecting key temporal features of *in vivo* corticogenesis. The deep-layer marker CTIP2, a marker of

subcerebral PNs in layer V of the cerebral cortex, was highly expressed in ENPCs (DIV 45) and remained consistently high at later stages of differentiation. Quantification showed CTIP2 expression in 50 ± 4.6% of ENPCs (DIV 45) and 48 ± 9.0% of LNPCs (DIV 70), with no significant difference between groups (p = 0.8124, Fig. 2.7C). Additional deep-layer neurons expressing TBR1 were also detected at DIV 45, confirming enrichment of ENPCs with early-born cortical subtypes (Fig. 2.7E). The emergence of upper-layer identities was more detected in LNPCs at later stages. SATB2, a transcription factor specifying callosal PNs in layers II-IV, was significantly higher in LNPCs (38 ± 7.3%) compared with ENPCs (0.29 ± 0.29%, p = 0.05, Fig. 2.7D). Likewise, BRN2, another upper-layer marker, was expressed in LNPCs, consistent with their late-born neuronal identity (Fig. 2.7F). Layer IV marker, RORβ, was detected in ENPCs and LNPCs, with higher expression in ENPCs (63 ± 9.7%) compared to LNPCs (48 ± 5.9%, p = 0.132, Fig. 2.8C). Together, these findings demonstrated that the differentiation protocol recapitulated temporal layer specification, with ENPCs expressing deep-layer markers CTIP2 and TBR1, while LNPCs expressing SATB2 and BRN2. A partial overlap in RORβ expression was observed between both groups.

2.3.1.4 The protocol generates glutamatergic and GABAergic phenotypes

There are two neuronal phenotypes within the cerebral cortex, glutamatergic excitatory neurons and GABAergic inhibitory INs (Anderson et al., 2001). Immunostaining for the excitatory presynaptic marker VGLUT1 revealed the characteristic punctate distribution of presynaptic glutamatergic terminals in both ENPCs and LNPCs, indicating differentiation into glutamatergic phenotypes in ENPCs and LNPCs (Fig. 2.9A, B). A negative control is provided in the Supplementary Material (Fig. 6.1B), showing no signal in the channels forVGLUT1 and MAP2 channels above background.

GABAergic neurons were detected in both cultures with no significant difference (LNPCs: 22 ± 7.8%, ENPCs: 11 ± 1.9%, p = 0.183, Fig. 2.9C-E). Calbindin+ cells were detected in both ENPCs and LNPCs (Fig. 2.9F-G). These results demonstrated that both ENPCs and LNPCs could give rise to a mixed population of glutamatergic and GABAergic neurons, with a trend towards a higher, albeit non-significant, GABAergic representation in LNPCs.

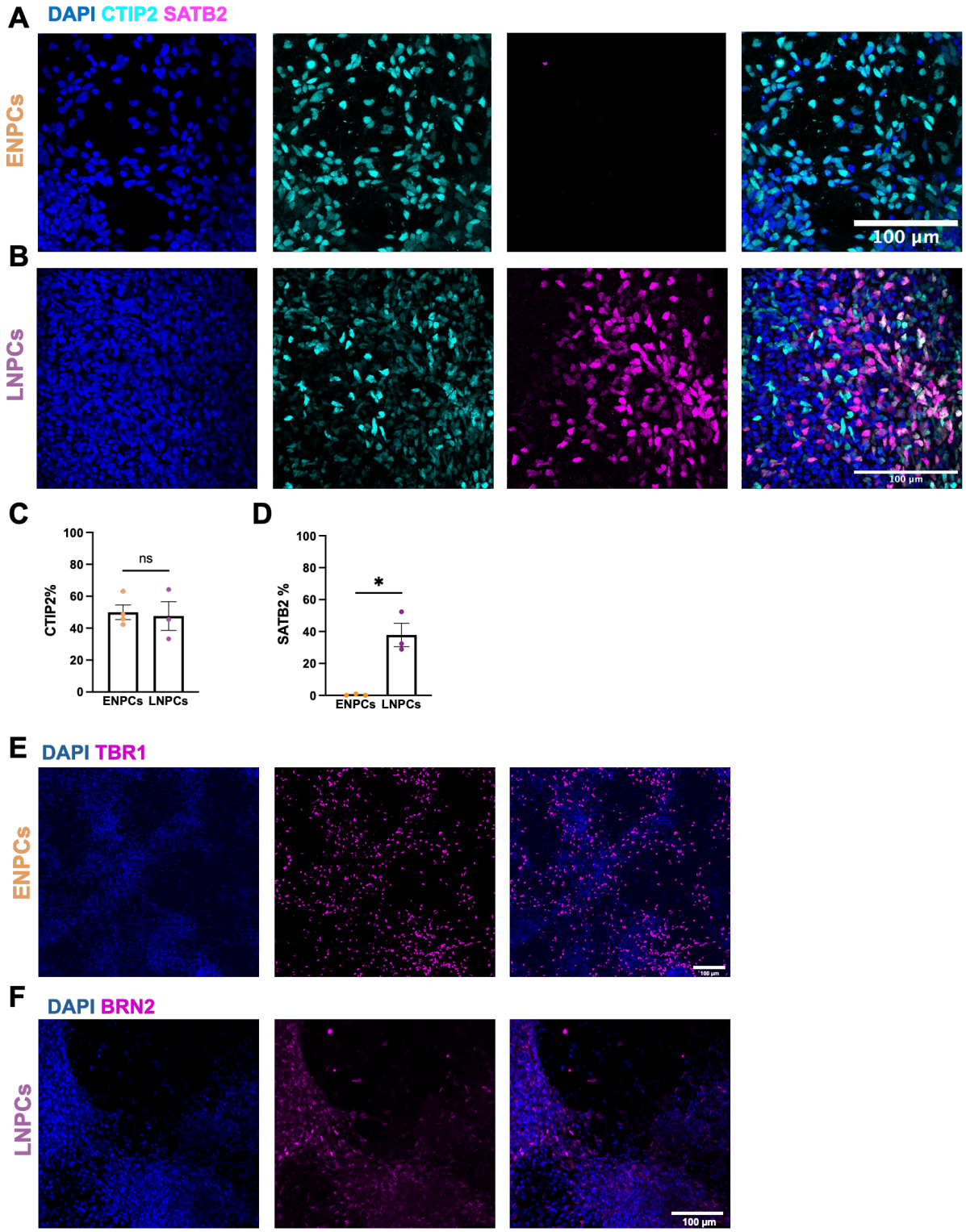

Figure 2.7 Temporal expression of cortical layer markers in ENPCs and LNPCs
(A, B) Representative confocal images showing immunostaining for the deep-layer cortical neuronal marker CTIP2 and the upper-layer cortical neuronal marker SATB2 in ENPCs and LNPCs. ENPCs were enriched in CTIP2 expression, whereas LNPCs exhibited high SATB2 expression in addition to CTIP2.
(C-D) Quantification of the percentage of CTIP2+ ($p = 0.8124$) and SATB2+ cells ($p = 0.05$) in ENCPs and LNPCs.

(E) Confocal images of ENPCs showing positive expression of TBR1, a deep-layer cortical marker.
(F) Confocal images of LNPCs showing positive expression of BRN2, an upper-layer cortical marker.
Scale bar: 100 µm. Data are presented as means ± SEM. n = 3 biological replicates.

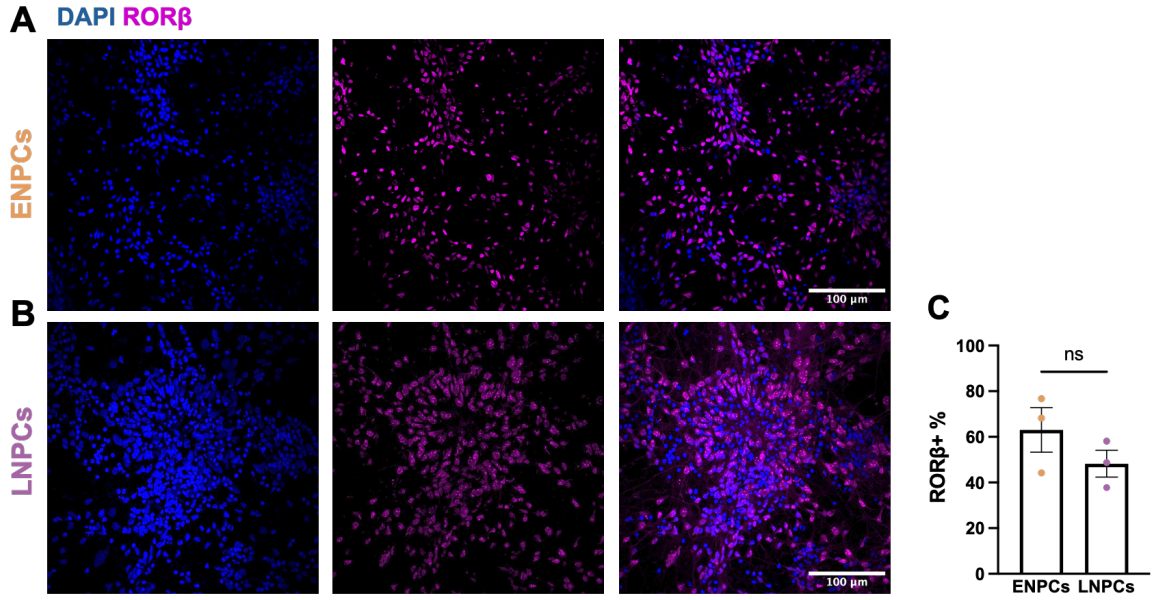

Figure 2.8 Expression of cortical layer IV marker, RORβ, in ENPCs and LNPCs
(A–B) Representative confocal images showing positive expression of the layer IV cortical marker RORβ in ENPCs and LNPCs.
(C) Quantification reveals a high percentage of RORβ+ cells in both LNPCs and ENPCs ($p = 0.132$).
Scale bar: 100 µm. Data are means ± SEM. n = 3 biological replicates.

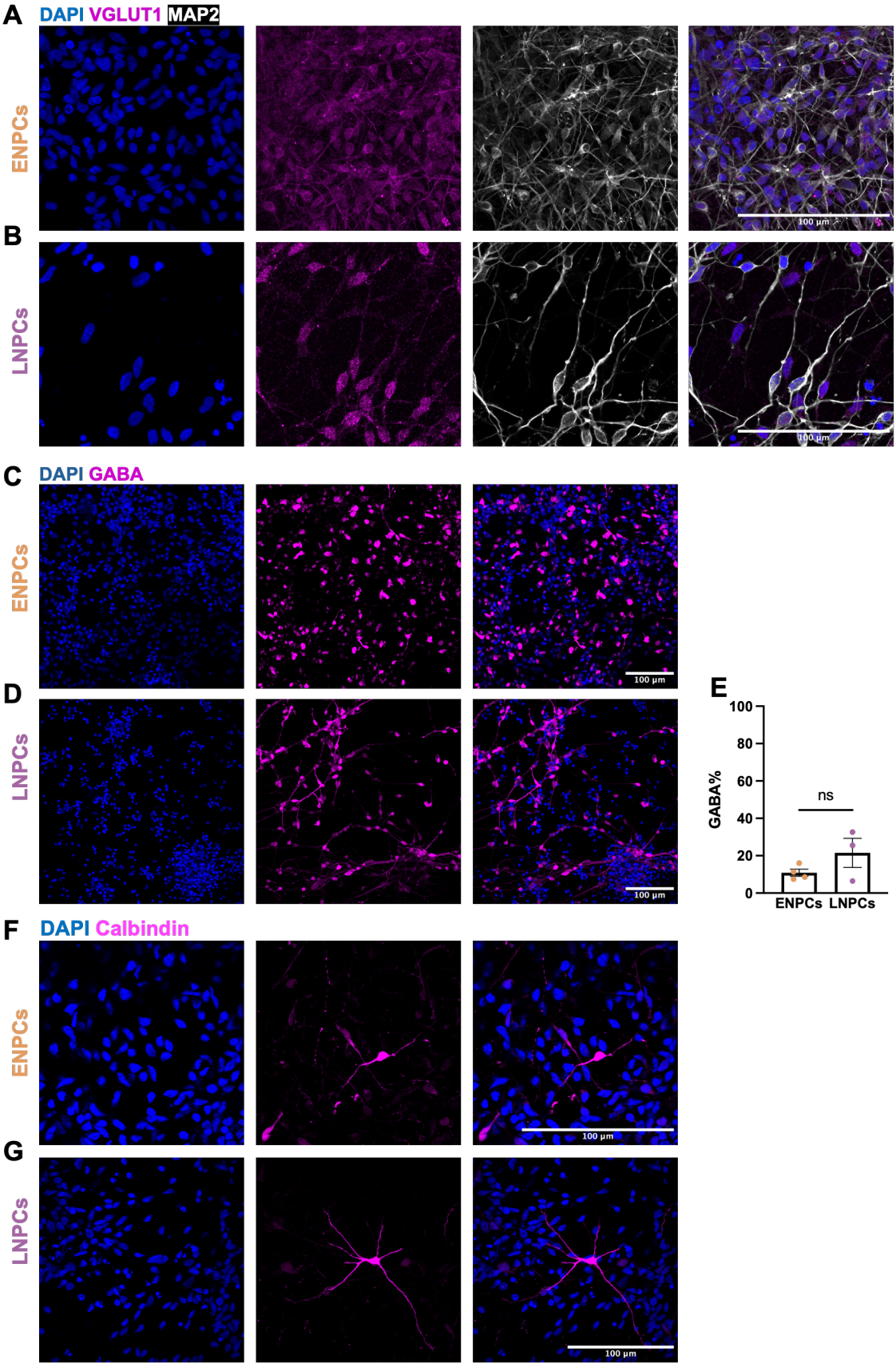

Figure 2.9 Glutamatergic and GABAergic neuronal phenotypes are generated in ENPCs and LNPCs

(A, B) Representative confocal images showing punctate expression of the excitatory presynaptic marker VGLUT1 colocalised with the cytoskeletal marker MAP2 in ENPCs and LNPCs.
(C, D) Representative confocal images of GABAergic INs in ENPCs and LNPCs.
(E) Quantification of the percentage of GABA+ neurons in ENPCs and LNPCs ($p = 0.183$).
(F, G) Representative confocal images of Calbindin+ cells in ENPCs and LNPCs.
Scale bar: 100 µm. Data are means ± SEM. n = 3 biological replicates.

2.3.1.5 hiPSC-derived cortical neurons express synaptic proteins

To investigate synapse formation, iPSC-derived ENPCs and LNPCs were immunostained for Synapsin-1 (SYN1) and PSD-95. Both ENPCs and LNPCs showed positive expression, indicating synaptogenesis and assembly into neural networks. Quantification of the presynaptic marker SYN1 showed no difference in the puncta density between ENPCs (0.22 ± 0.075 puncta/µm²) and LNPCs (0.38 ± 0.032 puncta/µm², $p = 0.056$, Fig. 2.10C). The puncta density of PSD-95 was less abundant in ENPCs (0.28 ± 0.056 puncta/µm²) than in LNPCs (0.58 ± 0.022 puncta/µm², $p = 0.0036$, Fig. 2.10D). Co-localisation of SYN1 and PSD-95 puncta demonstrated a higher density in LNPCs (0.21 ± 0.018 puncta/µm²) compared to ENPCs (0.13 ± 0.029 puncta/µm², $p = 0.0407$, Fig. 2.10E). Together, these findings suggested that hiPSC-derived ENPCs and LNPCs formed synaptic networks, with LNPCs having a denser synaptic network compared to ENPCs.

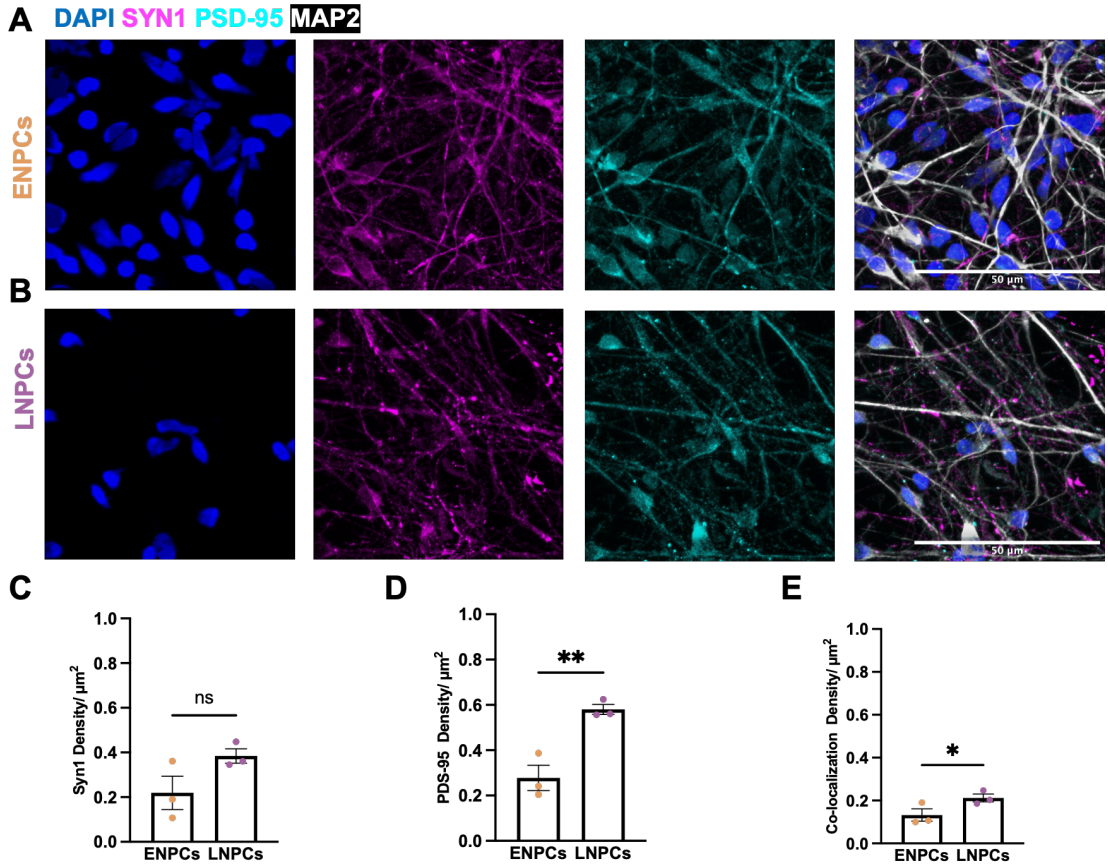

Figure 2.10 Synaptic protein expression in ENPCs and LNPCs
(A, B) Representative confocal images showing immunostaining for the presynaptic marker Synapsin-1 (SYN1) and PSD-95 in ENPCs and LNPCs.
(C-E) Quantification of puncta density, per µm², of ENPCs and LNPCs for SYN1+ ($p = 0.056$), PSD-95+ puncta ($p = 0.0036$), and SYN1+/PSD-95+ colocalised puncta ($p = 0.0407$).
Scale bar: 50 µm. Data are means ± SEM. n = 3 biological replicates.

2.3.1.6 Astrocytes are generated later in the differentiation protocol

The presence of GFAP-positive astrocytes was confirmed, although only a very small number of cells were detected in both ENPCs and LNPCs (Fig. 2.11). Astrocytes cannot be reliably identified with GFAP alone because astrocytes are highly heterogeneous and their marker expression varies with brain region, age, and brain state (Jurga et al., 2021); therefore, it is recommended to use marker panels. For general astrocyte identity, structural and membrane-associated markers can be combined, including GFAP, ALDH1L1, AQP4, EAAT1/EAAT2, S100β, and Nestin, alongside intracellular markers such as SOX9 to improve coverage across astrocyte subtypes and states (Jurga et al., 2021). For astrocyte functional profiling, marker panels should be chosen to map onto specific homeostatic pathways, for example, metabolic support via GLUT1-mediated glucose transport, synaptic glutamate clearance via EAAT1/EAAT2, glutamate–glutamine cycling via glutamine synthetase GLUL together with

the amino-acid transporters SNAT3 and SNAT5, and water and ion homeostasis via AQP4 (Jurga et al., 2021). Finally, for reactive astrogliosis, marker panels should capture reactivity-associated structural and membrane changes, including GFAP, Vimentin, Nestin, CD44, connexins Cx30 and Cx43, and S1P3 (Escartin et al., 2021).

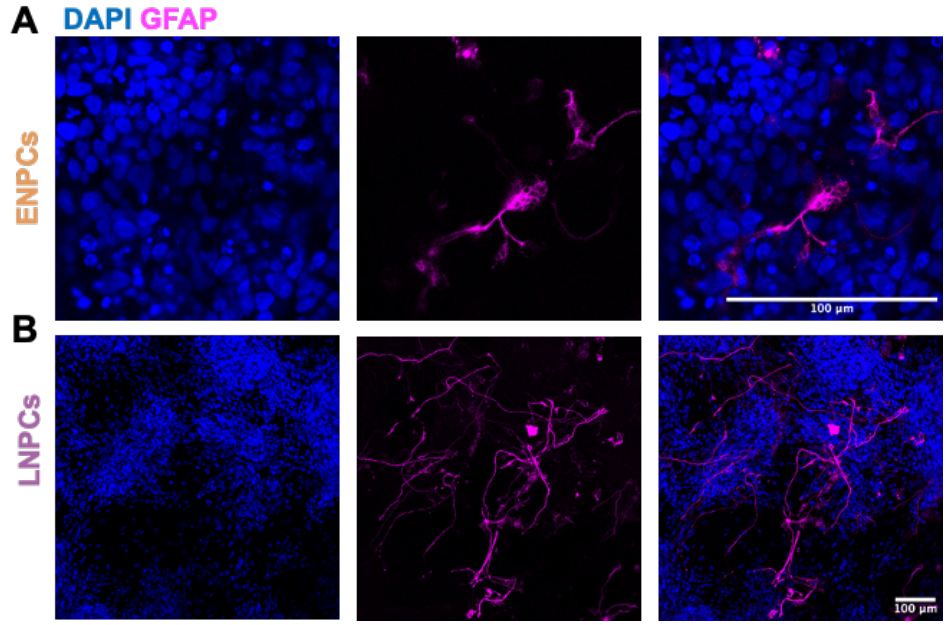

Figure 2.11 GFAP+ astrocytes are generated in ENPCs and LNPCs
(A, B) Representative confocal images showing GFAP+ astrocytes in ENPCs and LNPCs. Scale bar: 100 µm.

2.3.2 Temporal regulation of cortical layer identity and neuronal maturation (qPCR)

Expression of layer-specific markers and neuronal maturation genes was assessed at three time points: DIV24 (baseline control), DIV45 (ENPCs), and DIV70 (LNPCs). Overall, CTIP2 expression did not differ significantly from baseline: ENPCs showed a fold change of 82 ± 56 (ENPCs vs control, p = 0.3706), and LNPCs 61 ± 38 (LNPCs vs control, p = 0.5557, Fig. 2.12A). SATB2 expression showed no significant change relative to DIV24, with a fold change in ENPCs (0.87 ± 0.23, p = 0.99) and in LNPCs (3.8 ± 2.3, p = 0.69; Fig. 2.12B). In contrast, NeuN expression increased significantly over time, consistent with progressive neuronal maturation: ENPCs exhibited a fold change of 6.9 ± 0.91 (p = 0.0036) and LNPCs 5.2 ± 0.78 (p = 0.02; Fig. 2.12C). MAP2 expression fold changes also did not reach statistical significance; fold change was 2.1 ± 0.32 in ENPCs (p = 0.24) and 1.8 ± 0.48 in LNPCs (p = 0.44; Fig. 2.12D).

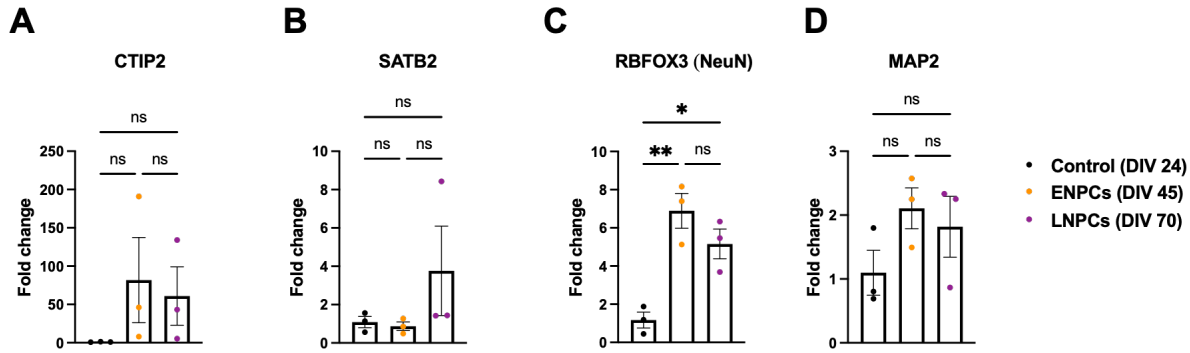

Figure 2.12 Gene expression profiling in ENPCs and LNPCs
Quantitative PCR analysis of (A) CTIP2, (B) SATB2, (C) NeuN, and (D) MAP2 in ENPCs and LNPCs. Data were normalised to the mean of DIV 24 and expressed as fold change.
(A) CTIP2 expression showed no significant difference from DIV 24 in ENPCs ($p = 0.3706$) and LNPCs ($p = 0.5557$).
(B) SATB2 expression did not differ significantly from DIV24 in ENPCs ($p = 0.87$) or LNPCs ($p = 0.99$).
(C) NeuN expression increased significantly in ENPCs ($p = 0.0036$) and LNPCs ($p = 0.02$) relative to DIV 24.
(D) MAP2 expression did not differ significantly from DIV24 (ENPCs: $p = 0.34$; LNPCs: $p = 0.56$).
Data are means ± SEM. n = 3 biological replicates. DIV = day *in vitro*. Statistical significance was assessed using one-way ANOVA.

2.3.3 Imaging calcium signalling

2.3.3.1 ENPCs and LNPCs exhibit spontaneous calcium signalling with comparable spike dynamics

hiPSC-derived ENPCs and LNPCs exhibited spontaneous calcium signals, with 88 ± 2.9% and 85 ± 4.2% of total neurons being active (i.e. at least one spike in 10.5 min) in ENPCs and LNPCs, respectively ($p = 0.2859$, Fig. 2.13B). The firing rate was comparable between the two groups (ENPCs: 103 ± 15 spikes/min; LNPCs: 101 ± 27 spikes/min; $p = 0.475$, Fig. 2.13B). LNPCs showed a modestly higher degree of synchronisation in activity, with a value of 0.54 ± 0.094, compared to 0.41 ± 0.068 in ENPCs ($p = 0.0272$, Fig. 2.13B). This indicated that although the proportion of active neurons and their firing rates were similar, LNPC networks were more temporally coordinated, suggesting stronger functional coupling between neurons at later developmental stages.

Dynamic features of calcium spikes were characterised by a rapid rise in cytosolic calcium, followed by a gradual return to baseline levels, as expected from calcium signals. The rise time was 13.54 ± 0.391 s for ENPCs and 15.44 ± 1.958 s for LNPCs ($p = 0.1986$). Decay time was 26 ± 1.2 s for ENPCs and 24 ± 1.3 s for LNPCs ($p = 0.1326$). The half maximal spike width was consistent across groups as well (ENPCs: 20 ± 0.66 s; LNPCs: 20 ± 1.5 s; $p = 0.4525$; Fig. 2.13C). These comparable kinetic parameters suggested that the underlying mechanisms of

calcium spikes may be similar between ENPCs and LNPCs, and the key difference was related to the coordination of activity across the network rather than in individual spike dynamics.

To investigate the source of calcium underlying the observed cytoplasmic spikes, activity was measured in calcium-free medium supplemented with EGTA (4 mM) to chelate extracellular calcium. This intervention rapidly suppressed spontaneous activities, indicating that calcium influx was essential for driving calcium spikes. There was a near-complete reduction in the percentage of active neurons, from 55 ± 5.7% to 1.1 ± 0.47% (p = 0.006, paired t-test), along with a decline in spike frequency (56 ± 14 to 0.32 ± 0.14 spike/min; p = 0.0284, paired t-test, Fig. 2.14A-B). Consistent with a depolarisation-driven mechanism, exposure to the voltage-gated sodium channel blocker TTX (1 μM) largely abolished activity. In ENPCs, the proportion of active neurons decreased from 46 ± 5.8% to 4.1 ± 0.8% (p = 0.0118, paired t-test), while the spike frequency declined from 78 ± 22 to 8.2 ± 0.45 spikes/min (p = 0.043, paired t-test; Fig. 2.14C–D). These findings demonstrated that spontaneous calcium spikes relied on extracellular calcium influx and voltage-gated sodium channel activity, supporting the conclusion that these spikes represented action potential–driven neuronal activity.

To further characterise the network properties of ENPCs and LNPCs in monolayers, graph theory was employed to generate metrics that describe functional neuronal connectivity. This analysis revealed distinct patterns of functional neuronal networks in ENPCs and LNPCs. The average edge weight was significantly higher in LNPCs at 0.28 ± 0.026, compared to 0.2 ± 0.016 in ENPCs (p = 0.0281, Fig. 2.15A), indicating stronger connectivity. The average path length was 2.2 ± 0.033 for ENPCs and 2.1 ± 0.08 for LNPCs (p = 0.0729, Fig. 2.15B), with no significant difference between groups.

ENPCs also showed significantly higher modularity, reflecting segregation of subnetworks with dense connections within modules but sparse connections between neurons across different modules (ENPCs: 0.38 ± 0.030, LNPCs: 0.29 ± 0.0068, p = 0.0256, Fig. 2.15C). In contrast, the clustering coefficient, which reflects local connectivity, was significantly higher in LNPCs (ENPCs: 0.62 ± 0.016, LNPCs: 0.72 ± 0.035, p = 0.0351, Fig. 2.15D). High clustering coefficients in LNPCs indicated that neurons within modules were highly interconnected, resulting in a network's robustness and resilience against random damage. Collectively, graph metrics indicated that LNPC networks were more integrated and efficiently connected, whereas ENPC networks were more modular and segregated.

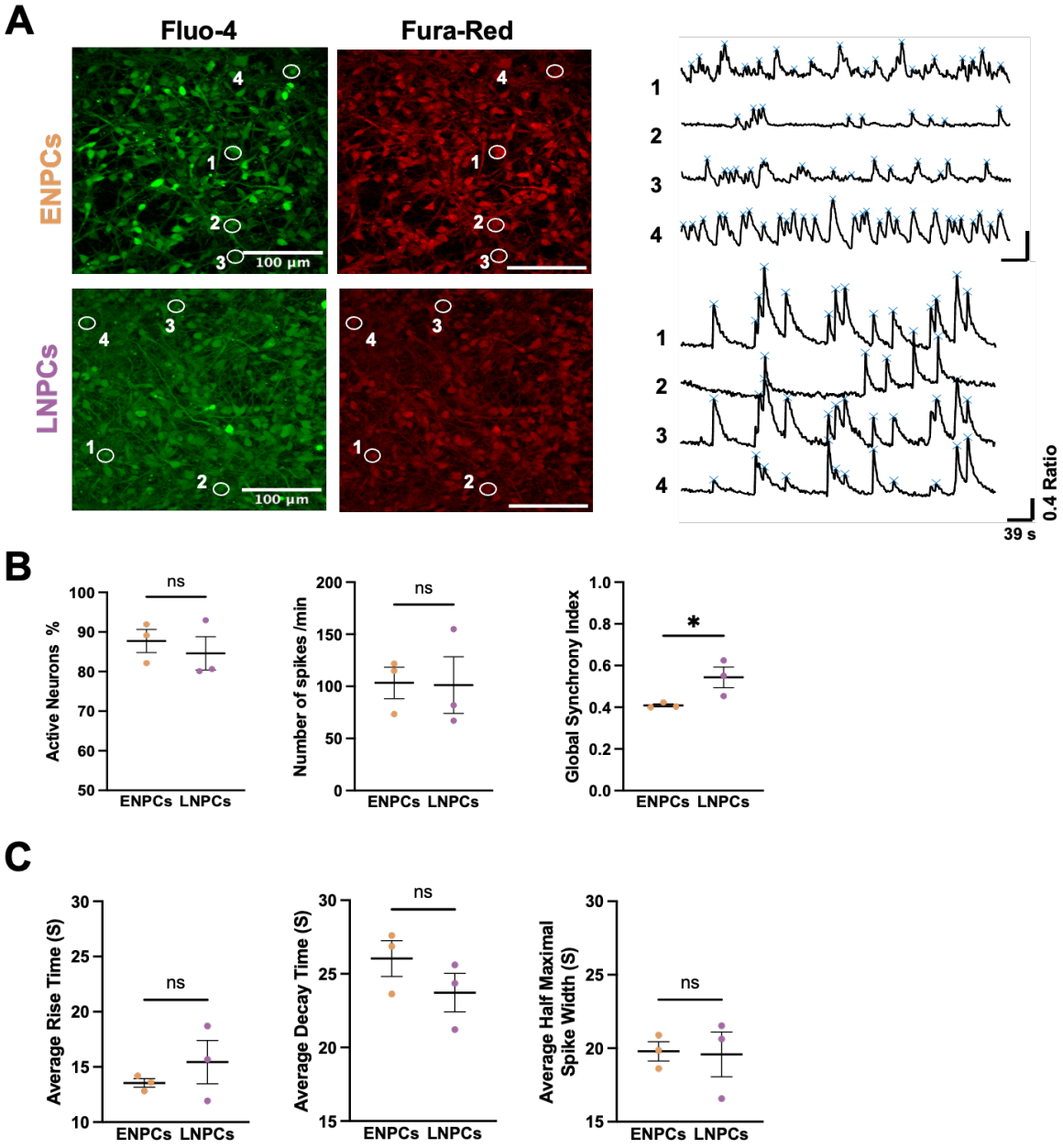

Figure 2.13 ENPCs and LNPCs exhibit spontaneous calcium activity
(A) A snapshot of the first ten recording frames of the recording. To the right, representative pseudo-ratiometric traces from four neurons are displayed, and peak activities are denoted with blue asterisks.
(B) The percentage of active neurons was comparable between ENPCs and LNPCs ($p = 0.2859$), as well as spike frequency ($p = 0.475$). LNPCs showed a higher global synchrony index than ENPCs ($p = 0.0272$).
(C) Dynamics of calcium spikes showed rapid rise and slow decay times, with comparable results between ENPCs and LNPCs, including rise time ($p = 0.1986$), decay time ($p = 0.1326$), and half maximal spike width ($p = 0.4525$). Data are means ± SEM. n = 3 biological replicates.

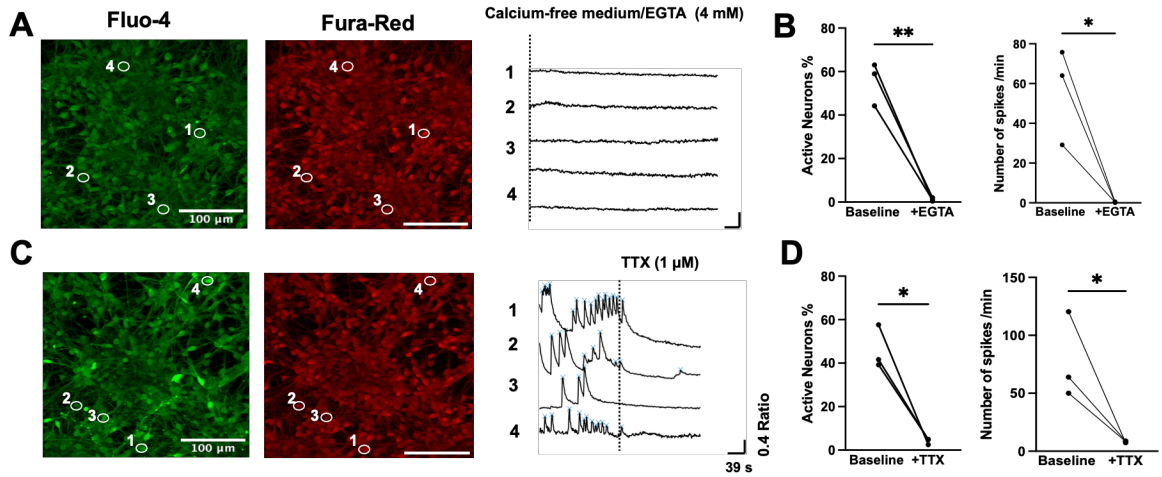

Figure 2.14 Extracellular calcium influx and sodium channel activity mediate spontaneous calcium activity

(A, B) Pseudo-ratiometric calcium imaging of ENPCs shows that chelating extracellular calcium with EGTA markedly reduced spontaneous calcium activity. Quantification reveals a significant decrease in the percentage of active neurons ($p = 0.006$, paired *t*-test) and a decrease in firing frequency ($p = 0.0284$, paired *t*-test).

(C, D) Application of the sodium channel blocker TTX largely abolished activity, reducing the proportion of active neurons ($p = 0.0118$, paired *t*-test) and spike frequency ($p = 0.043$, paired *t*-test).

Data are means ± SEM. n = 3 biological replicates.

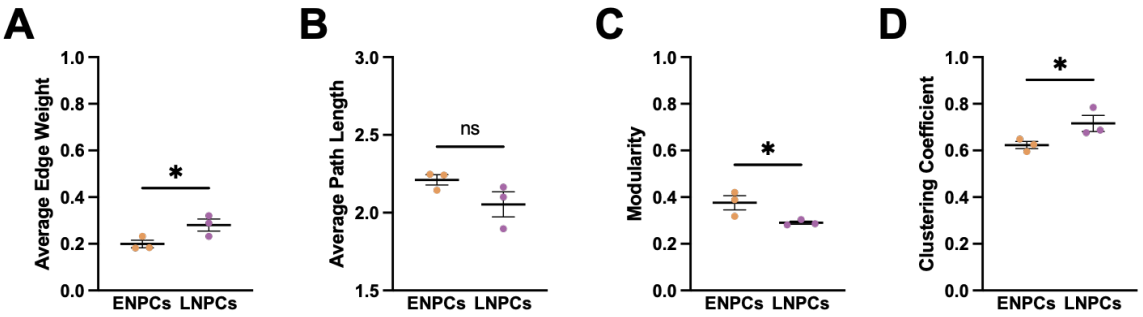

Figure 2.15 Graph theory analysis reveals distinct functional network patterns in ENPCs and LNPCs

(A) Quantification of average edge weight shows significantly stronger connections in LNPCs compared with ENPCs ($p = 0.0281$).

(B) The average path length was shorter in LNPC networks compared to ENPCs ($p = 0.0729$), indicating more efficient information transfer, although this difference did not reach statistical significance.

(C) ENPC networks exhibited significantly higher modularity than LNPCs ($p = 0.0256$), reflecting more fragmented subnetworks.

(D) The clustering coefficient, representing local connectivity, was significantly higher in LNPCs compared to ENPCs ($p = 0.0351$).

Data are means ± SEM. n = 3 biological replicates.

2.3.3.2 Pharmacological perturbation of calcium activity identifies functional glutamatergic and GABAergic receptors

To further investigate receptor activity and validate the functional excitatory and inhibitory responses, ENPCs and LNPCs were challenged with either glutamate (30 µM) or GABA (100 µM) after recording the baseline spontaneous activity (Kuijlaars et al., 2016). Glutamate treatment increased the percentage of active neurons and their firing rates in both ENPCs and LNPCs, compared to baseline activity. In ENPCs, glutamate significantly increased the percentage of active neurons (baseline: 30 ± 3.8%, glutamate: 52 ± 3.8%, $p = 0.0096$, paired *t*-test), and the firing rate (baseline: 53 ± 9.2 spikes/min, glutamate: 101 ± 18 spikes/min, $p = 0.0229$, paired *t*-test, Fig. 2.16A, B). Similarly, for LNPCs, there was a rise in percentage of active neurons (baseline: 42 ± 3.8%, glutamate: 77 ± 11%, $p = 0.0298$, paired *t*-test), accompanied by an increase in the firing rate (baseline: 71 ± 9.8 spikes/min, glutamate: 160 ± 3.8 spikes/min, $p = 0.0216$, paired *t*-test, Fig. 2.16E, F).

In contrast, the application of GABA reduced the baseline activity of the neuronal network. In GABA-treated ENPCs, the percentage of active neurons reduced (baseline: 34 ± 14%, GABA: 1.8 ± 0.51%, $p = 0.0089$, paired *t*-test). Similarly, the spike rate diminished (baseline: 67 ± 13 spikes/min, GABA: 5.3 ± 0.97 spikes/min, $p = 0.0461$, paired *t*-test, Fig. 2.16C, D). Similarly, GABA-treated LNPCs showed a significant decrease in the percentage of active neurons (baseline: 76 ± 5.8%, GABA: 67 ± 5.4%, $p = 0.007$, paired *t*-test). The recorded frequency decreased without statistical significance compared to baseline activity (baseline: 80 ± 32 spikes/min, GABA: 48 ± 13 spikes/min, $p = 0.1806$, paired *t*-test, Fig. 2.16G, H). These findings demonstrated functional glutamatergic and GABAergic signalling in both ENPC- and LNPC-derived networks, with glutamate displayed as an excitatory signal and GABA exerting an inhibitory effect.

To confirm the inhibitory effect of GABA, both gabazine, a competitive antagonist of the GABA-A receptor, and picrotoxin, a non-competitive GABA-A chloride channel blocker, were used in combination to ensure a full blockade of GABA-A receptor–mediated currents. This dual application ensured the complete inhibition, as gabazine blocked agonist binding sites while picrotoxin directly occluded the chloride channel. The baseline activity of ENPCs was first recorded, then the cells were exposed to gabazine (10 µM), followed by the co-application of gabazine (10 µM) and picrotoxin (50 µM). With gabazine alone, the proportion of active neurons was 37 ± 7.3% at baseline and 53 ± 6% with gabazine ($p = 0.1358$), while the firing

rate was 60 ± 6.2 spikes/min at baseline and 103 ± 24 spikes/min with gabazine (p = 0.1252; Fig. 2.17C). Combined gabazine and picrotoxin treatment induced a robust disinhibitory effect with a significant increase of percentage of active neurons (baseline: 37 ± 7.3%, gabazine and picrotoxin: 87 ± 2.7%, $p = 0.0054$) and the firing rate (baseline: 60 ± 6.2 spikes/min, gabazine and picrotoxin: 237 ± 61 spikes/min, $p = 0.049$, Fig. 2.17D). This finding provided evidence for intrinsic GABAergic signalling that suppressed neuronal activity and can be disinhibited by GABA-A receptor blockers.

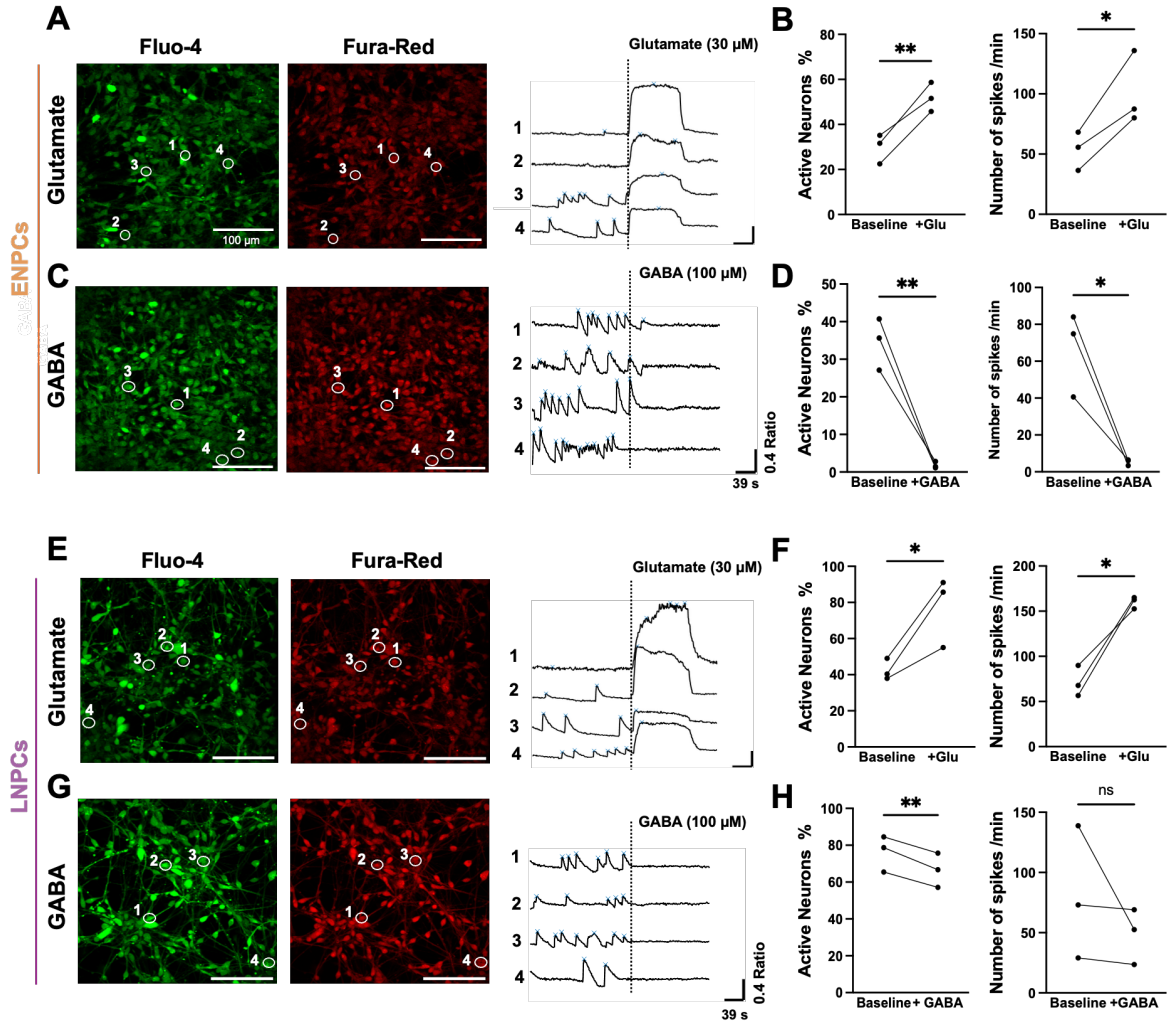

Figure 2.16 Pharmacological modulation reveals functional glutamatergic and GABAergic receptors

(A, C, E, G) The left panels display snapshots of the first ten frames, with representative pseudo-ratiometric traces from four individual neurons, where blue asterisks mark the spike activities. Vertical dotted lines denote the application of a selective neurotransmitter.

(B) In ENPCs, glutamate induced a substantial calcium influx, significantly increasing the percentage of active neurons ($p = 0.0096$, paired *t*-test) and firing rate ($p = 0.0229$, paired *t*-test), relative to baseline.

(D) In ENPCs, GABA application reduced neuronal network activity, decreasing both the percentage of active neurons ($p = 0.0089$, paired *t*-test) and firing rate ($p = 0.0461$, paired *t*-test), compared to baseline.

(F) In LNPCs, glutamate likewise triggered calcium spikes, with a significant rise in the proportion of active neurons ($p = 0.0298$, paired *t*-test) and firing rate ($p = 0.0216$, paired *t*-test), relative to baseline. (H) In LNPCs, GABA suppressed neuronal activity, reducing the percentage of active neurons ($p = 0.007$, paired *t*-test), although the decline in firing rate did not reach statistical significance ($p = 0.1806$, paired *t*-test) in comparison to baseline. Data are means ± SEM. n = 3 biological replicates.

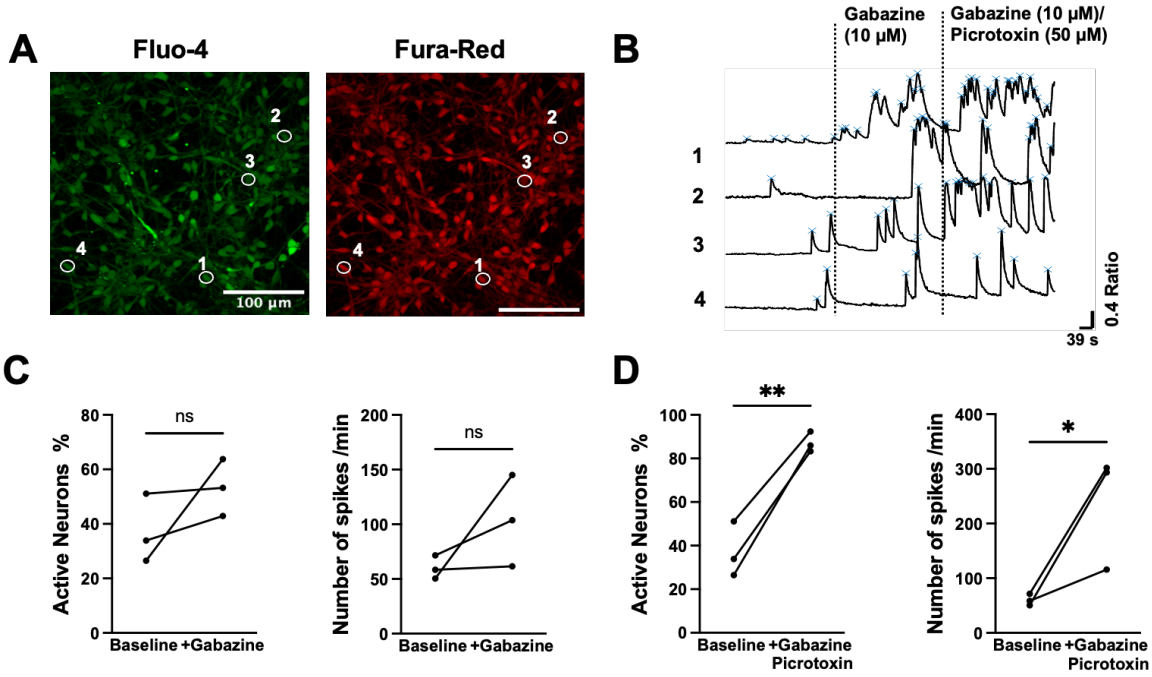

Figure 2.17 Gabazine and picrotoxin together relieve GABA-mediated inhibition
(A) Representative fluorescence images of ENPCs dual-loaded with Fluo-4 AM and Fura-Red AM. The numbered circles indicate the selected neurons, which show calcium spikes to the right.
(B) Representative pseudo-ratiometric traces from four individual neurons, where blue asterisks mark the peak activities during baseline, gabazine treatment, and combined gabazine and picrotoxin exposure. Vertical dotted lines denote the application of a selective neurotransmitter.
(C) In ENPCs treated with gabazine, the percentage of active neurons and the firing rate did not change significantly compared to baseline (p = 0.1358 and p = 0.1252, paired t-test).
(D) With gabazine and picrotoxin treatment, the percentage of active neurons significantly increased ($p = 0.0054$, paired *t*-test) and consequently the firing rate ($p = 0.049$, paired *t*-test) relative to baseline. Data are means ± SEM. n = 3 biological replicates.

2.3.4 Transplantation of hiPSC-derived ENPCs and LNPCs into the motor cortex of NOD-SCID mice

hiPSC-derived ENPCs and LNPCs were transplanted into the right motor cortex of P7-P8 NOD-SCID mice. The brains were collected at 2 MPT. Human cells were identified with immunostaining for HuNu and hNCAM to evaluate the fate of the injected cells and their potential integration into the host brain. Neurolucida tracing software was used to track axonal projections.

2.3.4.1 ENPC and LNPC grafts exhibit layer-specific identity at 2 MPT

Grafted cells were mainly detected at the injection site. Both ENPC and LNPC grafts expressed the deep-layer marker CTIP2. The percentage of CTIP2+ HuNu+ was 32 ± 11% in ENPC grafts and 43 ± 11% in LNPC grafts ($p = 0.26$; Fig. 2.18D). In contrast, SATB2 expression was higher in LNPC grafts than in ENPC grafts. The percentage of SATB2+ HuNu+ was 19 ± 6.4% in LNPC grafts and 4.0 ± 3.4% in ENPC grafts ($p = 0.05$, Fig. 2.18E). These findings indicated that ENPC grafts retained a deep-layer fate, marked by CTIP2, while LNPC grafts preserved their upper-layer identity, characterised by SATB2 expression.

2.3.4.2 Efferent projections to layer-specific targets

Neurolucida software was used to trace axonal projections across serial coronal brain sections, guided by hNCAM immunostaining. Reconstructions were performed along the entire rostrocaudal axis of the brain to visualise long-range axonal trajectories and regional innervation patterns (Fig. 2.19A).

The projection density was semi-quantified across various brain regions (Fig. 2.19C). ENPC grafts extended projections deep into the lateral cortex of the ipsilateral hemisphere (Fig. 2.20A'). Both ENPC and LNPC grafts extended projections across the corpus callosum, reaching the contralateral hemisphere (Fig. 2.20A''', C''''). Efferent projections into the thalamus, striatum, and internal capsule varied between ENPC and LNPC grafts. ENPC grafts displayed a stronger propensity for the striatum and the thalamus compared to the LNPCs (Fig. 2.19C; 2.20A'', B'') and extended projections throughout the internal capsule of the ipsilateral hemisphere (Fig. 2.19C; 2.20B'), resembling cortico-spinal projections of deep-layer cortical neurons. In contrast, LNPC grafts showed no axonal extensions within the thalamus or internal capsule and exhibited a moderate projection density within the striatum, consistent with the spatial innervation map of upper cortical neurons (Fig. 2.19C; 2.20C-D).

Collectively, tracking of axonal projections from ENPC and LNPC grafts at 2 MPT revealed stereotypical projection patterns that closely resemble the endogenous connectivity of native cortical PNs.

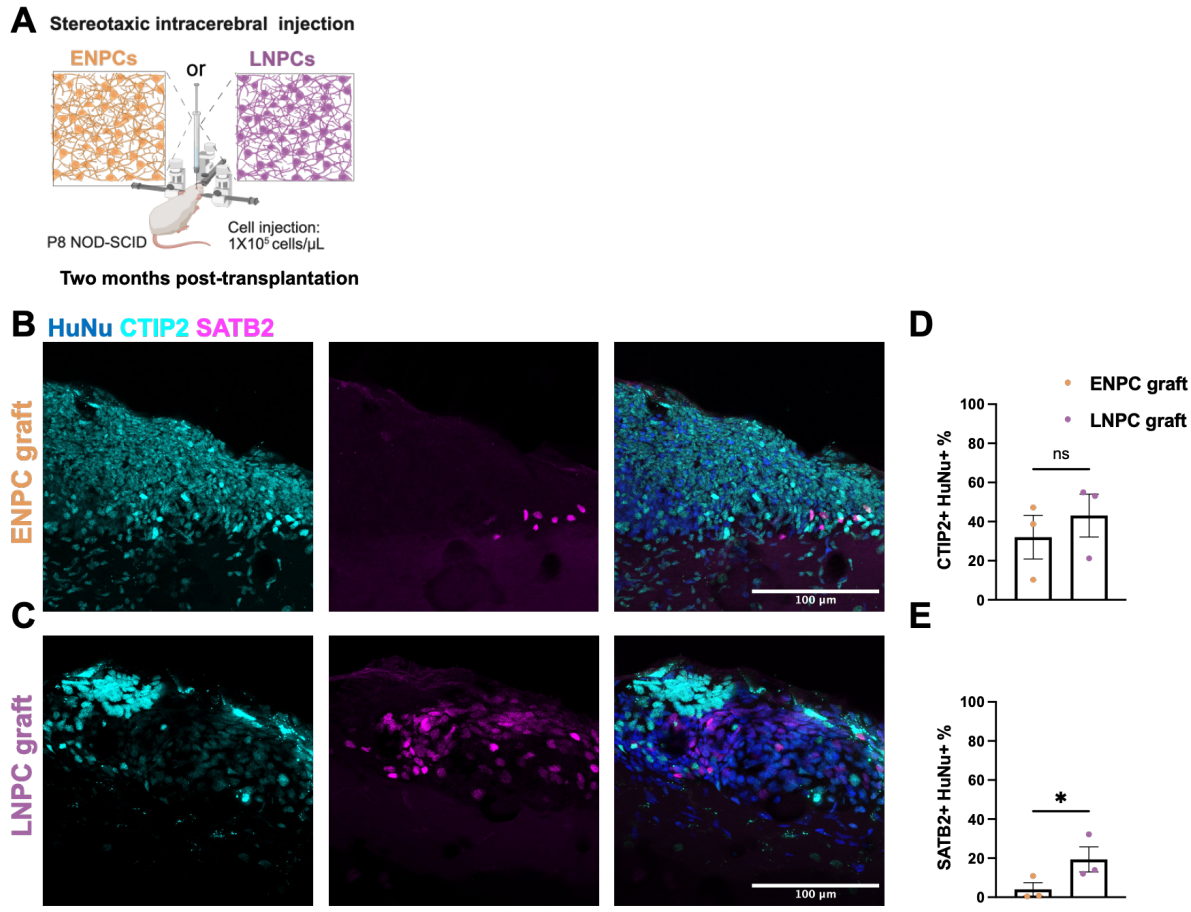

Figure 2.18 ENPC and LNPC grafts exhibit layer-specific identity at 2 MPT
(A) Schematic illustration of stereotaxic injection of ENPCs and LNPCs into the motor cortex of P7-P8 NOD-SCID mice. A total of 1 × 10^5 cells/µL were injected, and brains were collected at 2 MPT.
(B, C) Representative confocal images of ENPC and LNPC grafts. ENPC grafts exhibited CTIP2 expression but not SATB2, whereas LNPC grafts showed higher SATB2 expression in addition to CTIP2.
(D) Quantification of CTIP2+ HuNu+ of ENPC and LNPC grafts (p = 0.26).
(E) Quantification of SATB2+ HuNu+ of ENPC and LNPC grafts (p = 0.05).
Scale bar: 100 µm. Data are presented as means ± SEM; each point represents an animal (N = 3).

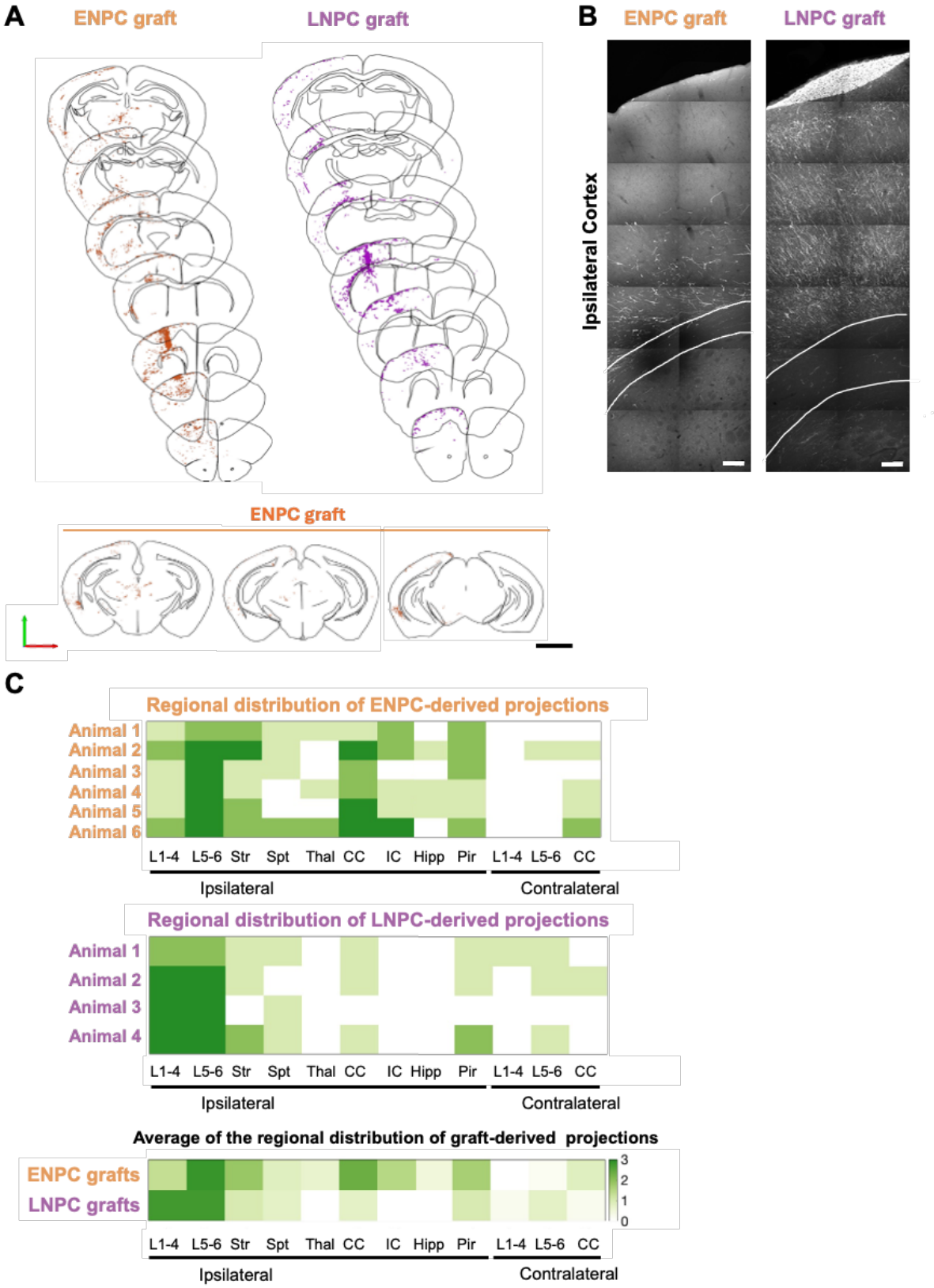

Figure 2.19 Distinct projection patterns of ENPC and LNPC grafts in the brains of NOD-SCID mice at 2 MPT

(A) Representative Neurolucida reconstructions of axonal projections across serial coronal brain sections at 2 MPT. Brain reconstructions showing the distribution of human axonal projections traced with hNCAM immunostaining.

(B) Representative stitched coronal sections illustrating projections of ENPC and LNPC grafts.
(C) Heatmaps of regional distribution of the projection density of ENPC and LNPC grafts into ipsilateral cortical layers (L 1-4, L 5-6), striatum (Str), septum (Sep), thalamus (Thal), corpus callosum (CC), internal capsule (IC), hippocampus (Hipp), and piriform cortex (Pir), and contralateral cortical layers (L 1-4, L 5-6) and corpus callosum (CC). Each row represents an individual animal (ENPC grafts: N = 6; LNPC grafts: N = 4). The bottom panel displays the average projection density across all animals within each group. Projection density was scored on a semi-quantitative scale ranging from 0 (no detectable projections) to 3 (dense projections).
Scale bar (A): 1000 µm; Scale bar (B): 100 µm.

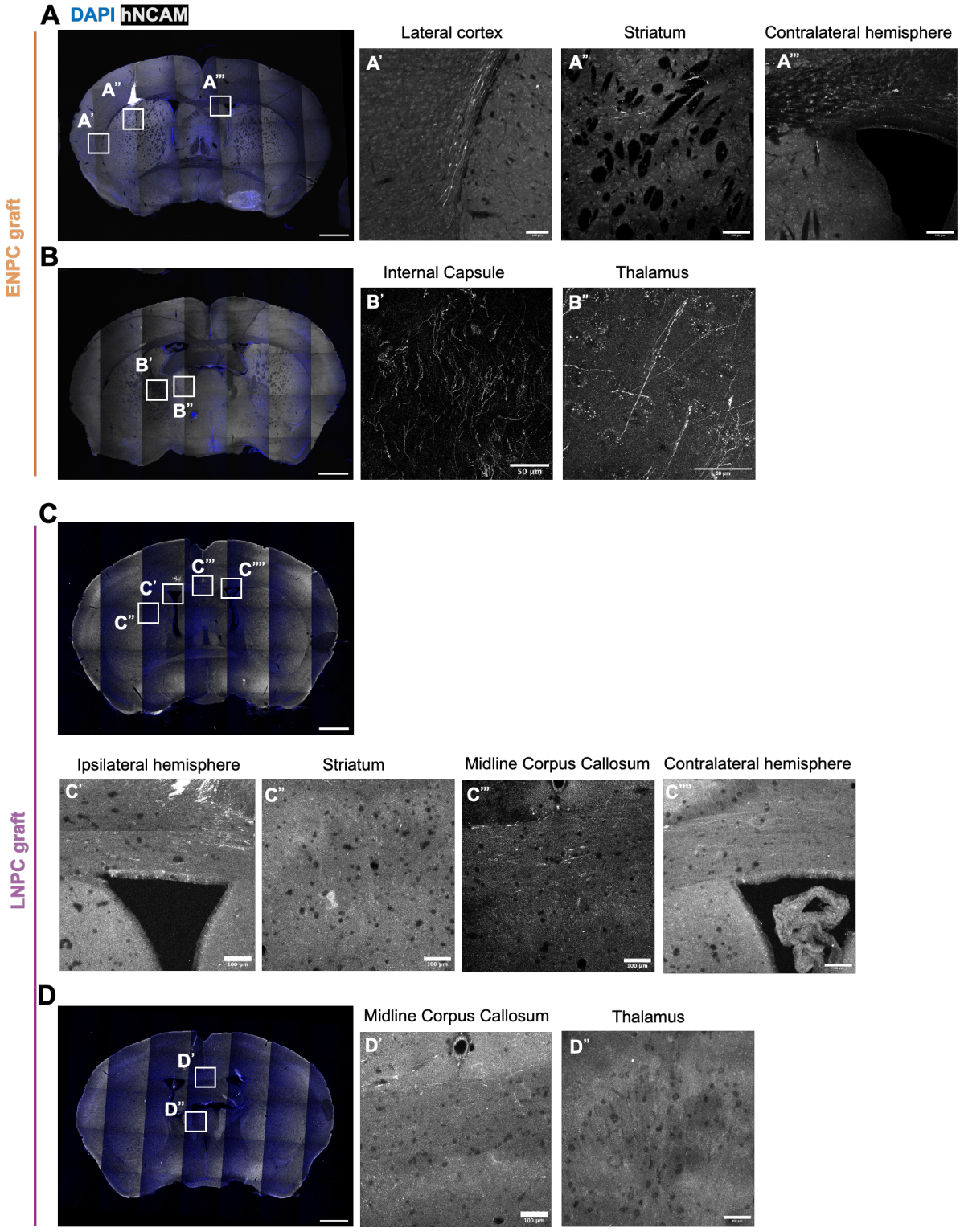

Figure 2.20 Axonal projections of ENPC and LNPC grafts in the brains of NOD-SCID mice at 2 MPT

Representative coronal brain sections of ENPC grafts (A, B) and LNPC grafts (C, D) transplanted into the motor cortex of P7-P8 NOD-SCID mice.

(A–A’’’) ENPC graft showing hNCAM+ axonal outgrowths extending into multiple brain regions. Insets highlight projections into the lateral cortex (A’), Striatum (A’’), and the contralateral hemisphere (A’’’).

(B–B’’) Representative coronal section with insets showing hNCAM+ axonal projections into the internal capsule (B’) and thalamus of the ipsilateral hemisphere (B’’).
(C–C’’’) LNPC graft, a coronal section with an inset showing the traversing hNCAM+ axonal projections from the ipsilateral hemisphere (C’) through the corpus callosum (C’’’) to the contralateral hemisphere (C’’’’).
Scale bars of coronal low-power sections counterstained with DAPI: 1000 μm; all insets in (A, C, D): 100 μm; insets in (B’, B’’): 50 μm.

2.4 Discussion

The generation of cortical neurons from hiPSCs represents a significant advance for both developmental neuroscience and regenerative medicine. Various neural differentiation protocols have been established (Shi et al., 2012b, Boissart et al., 2013, Espuny-Camacho et al., 2013, Bahmad et al., 2017, Gunhanlar et al., 2018), while relatively few have succeeded in mimicking the temporal sequence of corticogenesis with sufficient fidelity to produce laminar-specific neuronal subtypes in a reproducible manner.

In this chapter, I optimised a differentiation protocol that generated two temporally distinct populations, including ENPCs enriched in deep-layer cortical neurons and LNPCs enriched in upper-layer cortical neurons. These populations displayed distinct molecular and functional signatures consistent with their *in vivo* counterparts. Upon transplantation, they retained laminar identity and established projection patterns characteristic of their developmental stage.

2.4.1 Neural induction promotes the dorsal identity

The protocol was based on the dual-SMAD inhibition approach (Chambers et al., 2009, Shi et al., 2012a). No additional morphogens were introduced to maintain defined differentiation conditions and to avoid the variability driven by a broader array of signalling molecules. Moreover, neural induction was initiated with a confluent monolayer of hiPSCs to ensure uniform exposure to factors and to facilitate morphological monitoring.

The pluripotency of the hiPSCs was validated by the expression of OCT4 (Hansis et al., 2000), NANOG (Chambers et al., 2003), and SOX2 (Yuan et al., 1995). Following induction, OCT4 and NANOG expression became undetectable, while SOX2 persisted (Jin et al., 2022). This persistent expression of SOX2 during differentiation aligns with its dual roles in corticogenesis: during early neurogenesis, SOX2 directs cells toward a neuroectodermal fate at the expense of mesodermal and endodermal lineages (Zhao et al., 2004). Later in corticogenesis, SOX2 maintains NSC self-renewal and promotes neural maturation and arborisation (Graham et al., 2003).

By DIV 9, the neuroepithelial cells reorganised into neural rosettes exhibiting apicobasal polarity, consistent with earlier reports (Chambers et al., 2009). This rosette formation occurred earlier than typically reported with dual-SMAD inhibition, which was observed two weeks after induction (Delli Carri et al., 2013), highlighting the robustness of our induction strategy.

Dorsal telencephalic identity was confirmed by PAX6 expression, in line with its established role in specifying the dorsal identity of cortical progenitors that give rise to the PNs (Muzio et al., 2002, Molyneaux et al., 2007, Englund et al., 2005).

2.4.2 Temporal generation of deep- and upper-cortical neurons

A key strength of this protocol is its ability to recapitulate the temporal sequence of neurogenesis, consistent with previous reports (Shi et al., 2012b). During differentiation, neurons were generated in a temporal order, with deep-layer neurons generated first, followed by upper-layer neurons. It has been shown that early progenitors preferentially gave rise to CTIP2+ corticospinal and TBR1+ subplate neurons, while later progenitors produced BRN2+ and SATB2+ callosal neurons (Renner et al., 2017, Dominguez et al., 2013, Clark et al., 2020). This finding makes the protocol particularly valuable for modelling corticogenesis and laminar reconstruction, in comparison to other accelerated protocols that bypass the process of temporal corticogenesis (Zhang et al., 2013).

Ideally, LNPCs would show a temporal progression towards a more fate-restricted, late-stage cortical progenitor identity, away from the early progenitor state. However, our data showed that the LNPCs retained a substantial proportion of CTIP2-positive cells, consistent with cellular heterogeneity. This mixed progenitor state is important for interpreting the subsequent layering experiments because it implies that LNPC cultures are not purely upper-layer populations. Consequently, layer-marker readouts should be interpreted as reflecting the relative proportions of early- versus late-neuronal progenitors within each culture, rather than indicating a strict temporal switch in layer identities. Functionally, this heterogeneity could diminish the intended laminar segregation in layered neuronal tissue, leading to partial intermixing of molecular identities as well as projection and connectivity patterns upon implantation. This also suggests that stronger temporal patterning cues or additional maturation steps is necessary to obtain more clearly separated layer-specific neuron populations.

2.4.3 Generation of glutamatergic and GABAergic phenotypes

Our findings also highlighted the coexistence of glutamatergic and GABAergic phenotypes, with ENPCs and LNPCs containing VGLUT1+ glutamatergic neurons as well as GABAergic INs, consistent with prior reports (Shi et al., 2012b). This finding supported the dual origin hypothesis of human cortical INs, where both dorsal SVZ and ventral ganglionic eminence progenitors contribute (Petanjek et al., 2008, Zecevic et al., 2005). Interestingly, it has been

reported that the percentage of dorsally developed INs might be higher than that of ventrally generated INs in fate-mapping experiments of human mid-fetal slice cultures (Letinic et al., 2002). Additionally, the dorsal contribution may be specific to humans; it has been demonstrated that human RG cells isolated from the VZ/SVZ at midterm generate CalR+ INs, which is not recapitulated in mice (Yu and Zecevic, 2011). Moreover, a cellular barcoding tool has revealed that individual human cortical progenitors can generate both excitatory neurons and cortical INs (Delgado et al., 2022). The generation of GABAergic INs alongside glutamatergic neurons is considered a great benefit for cell therapy, enhancing the translational value of these cultures, given the neuroprotective and anti-epileptic properties of GABAergic grafts (Greenfield Jr, 2013). It has been reported that GABAergic transplantation into a TBI model facilitated the recovery of somatosensory function (Becerra et al., 2007) and improved memory precision (Zhu et al., 2019).

Synaptogenesis is a crucial step in the formation of functional neural networks. LNPCs expressed presynaptic and postsynaptic proteins juxtaposed along MAP2-positive dendrites, with a higher synaptic density in LNPCs. This aligns with *in vivo* observations, which show that layer II/III cortical pyramidal neurons exhibit significantly higher dendritic spine densities compared to layer V neurons (Tjia et al., 2017). In accordance with the present results, previous studies have demonstrated the formation of functional synapses *in vitro* capable of calcium-dependent glutamate release (Baldassari et al., 2022).

The presence of astrocytes has been confirmed, with a very low number of cells detected in both ENPCs and LNPCs. This indicated that astrocytic differentiation occurred later in the protocol, with neuronal lineage commitment preceding glial cell generation (Sauvageot and Stiles, 2002).

2.4.4 ENPCs and LNPCs elicit spontaneous calcium activity, with functional glutamatergic and GABAergic receptors

Both ENPCs and LNPCs exhibited spontaneous calcium activity under physiological conditions, at 37°C and in 5% CO_2 humidified atmosphere, during all imaging experiments. This approach preserved pH homeostasis and cellular metabolism, minimises drift in baseline fluorescence, and enables extended recordings without compromising viability. Thus, the observed calcium signals were more representative of *in vivo* behaviour (Lee et al., 2005). Calcium spikes were prolonged relative to the millisecond timescale of electrical action

potentials, which reflected the intrinsic calcium dynamics that operate over a wide range of temporal scales, including buffering, release from intracellular stores, and slower extrusion mechanisms (Berridge et al., 2003). This is consistent with previously published calcium imaging data that report rise times on the order of 5-20 s and decays of 10-40 s in immature human cortical cultures (Kirwan et al., 2015, Makinen et al., 2018, Cordella et al., 2022).

These spikes were typically characterised by a rapid increase in cytosolic calcium, followed by a gradual return to resting basal calcium levels, dynamics related to action potential-triggered calcium influx (Makinen et al., 2018). These spikes were largely abolished by EGTA, indicating their dependence on extracellular calcium influx, in line with previous findings (Kirwan et al., 2015). Additionally, they were mostly blocked in the presence of TTX, underscoring their dependence on depolarisation, consistent with previous reports (Kirwan et al., 2015, Pre et al., 2014, Paavilainen et al., 2018). A small subset of neurons remained active with TTX exposure, reflecting alternative depolarising mechanisms, including action potentials mediated by L-type calcium channels, which support TTX-resistant spikes and calcium-dependent firing in developing cortical neurons (Lo and Erzurumlu, 2002). Additional mechanism could include gap junction coupling (Yuste et al., 1992), or spontaneous vesicular neurotransmitter release events that occur independently of action potentials (Kavalali et al., 2011). Moreover, the coexistence of various cellular subtypes with different maturation rates within the same culture would exhibit distinct activity patterns and responses.

Glutamate treatment elicited calcium spikes in both ENPCs and LNPCs, demonstrating the existence of functional glutamatergic receptors. This finding aligns with previous studies showing that glutamate stimulation induces fast, receptor-mediated calcium spikes in hiPSC-derived cortical neurons (Cordella et al., 2022). In contrast, GABA application decreased neuronal activity, while subsequent disinhibition with dual GABA-A receptor antagonism, gabazine and picrotoxin, produced a marked increase in network activity. This response reflected the intrinsic inhibitory tone mediated by GABA-A receptors, which are abundantly expressed in cortical GABAergic INs and mediate both phasic and tonic inhibition (Farrant and Nusser, 2005). The combined application of gabazine, a competitive antagonist of the GABA-A receptor and picrotoxin, a non-competitive chloride channel blocker, produced a pronounced disinhibition of network activity, consistent with previous observations in *in vitro* hippocampal slices (Wlodarczyk et al., 2013). This reflected a developmental shift from depolarising to hyperpolarising effect of GABA (Zhang et al., 2011), resulting from the upregulation of KCC2

alongside downregulation of NKCC1 expression (Rivera et al., 2005, Virtanen et al., 2021). In the developing human cortex, a prominent upregulation of KCC2 takes place in the subplate and cortical plate prenatally, in contrast to the largely postnatal expression of KCC2 observed in rodents (Sedmak et al., 2016, Bayatti et al., 2008).

Graph theory analysis of the functional networks of ENPCs and LNPCs revealed distinct patterns of functional connectivity. The latter demonstrated stronger connectivity and more efficient information sharing in the network, as evidenced by higher edge weights, shorter path length, and clustering coefficient, consistent with the characteristics of small-world networks (Bullmore and Sporns, 2009). ENPCs, by contrast, exhibited higher modularity, a property that indicates more fragmented subnetworks with dense intra-modular connections but weaker inter-module links. These observations align with previous studies, which show the transition from random to small-world topologies during maturation of *in vitro* neuronal cultures (Downes et al., 2012) with their ability to spontaneously self-organise into modular small-world networks (Antonello et al., 2022). *In vivo*, neuronal progenitors adopt small-world functional configurations to regulate proliferation and network efficiency (Malmersjo et al., 2013). Nevertheless, the mature mammalian cortex also exhibits a weighted small-world network architecture, striking a balance between local clustering and integrative capacity (Bassett and Bullmore, 2017).

2.4.5 ENPCs and LNPCs retain their identity *in vivo*, with efferent projections innervating layer-specific targets

Following transplantation into the motor cortex, ENPCs and LNPCs preserved their laminar identity *in vivo*. ENPC grafts expressed CTIP2 and sent projections to corticospinal targets, including the internal capsule, consistent with their deep-layer fate. While LNPC grafts exhibited SATB2 expression and extended projections across the corpus callosum. Both graft types extended projections across the corpus callosum to the contralateral hemisphere, consistent with their endogenous projection programmes. Our findings align with previous reports, which demonstrated that grafted neurons adopt projection patterns characteristic of their developmental identity (Gaspard et al., 2008). Later studies extended this observation, showing that mouse ESC-derived cortical neurons with the appropriate cortical areal identity, when transplanted into the visual cortex, could participate in reconstructing damaged cortical circuits, forming reciprocal and long-range connections (Michelsen et al., 2015). Similar findings have been reported with transplantation of mouse ESC-derived cortical neurons into

both intact and lesioned cortex, where the cells integrated according to their subtype identity, further supporting the principle that laminar fate guides connectivity (Terrigno et al., 2018). However, contrasting findings show that graft connectivity is largely determined by the circuitry of the transplantation region, rather than the identity of the transplanted cells (Doerr et al., 2017).

2.4.6 Limitations

A major limitation of this study is its reliance on a single iPSC line. Previous studies have demonstrated considerable variability across pluripotent stem cell lines, with genetic background and reprogramming methods influencing differentiation potential and neuronal properties (Bock et al., 2011, Wu et al., 2007).

Comparative analyses of ESC and iPSC lines have further shown significant variation in differentiation efficiency, maturation stages and functional properties, suggesting that the robustness of our findings would be strengthened by validation across multiple lines (Hu et al., 2010). Another limitation is the protracted time course required to generate functionally post-mitotic human cortical neurons. Unlike rodent systems, the differentiation of human cortical neurons requires several weeks to months *in vitro*, making large-scale studies time-consuming and resource-intensive. This temporal mismatch not only complicates throughput but also underscores the challenge of translating such protocols into clinical screening applications. Finally, inconsistency across protocols in the use of morphogens and culture components remains a confounding factor because variability in signalling pathways can lead to divergent cellular phenotypes and functional outcomes (Engel et al., 2016). This highlights the need for more standardised, reproducible differentiation pipelines to reduce variability between studies and improve translatability.

2.5 Conclusion

In this chapter, I optimised a differentiation protocol to generate hiPSC-derived cortical neurons with distinct laminar identities, recapitulating the sequential inside-out programme of human corticogenesis. ENPCs acquired deep-layer fate and were rich in CTIP2+ subcerebral PNs, while LNPCs had upper-layer characteristics and were rich in upper-layer SATB2+ callosal PNs. Both excitatory glutamatergic and inhibitory GABAergic phenotypes were generated, reflecting the dual origin of cortical INs. Importantly, ENPCs and LNPCs expressed

synaptic proteins and displayed functional calcium activity, with LNPCs demonstrating higher network synchronisation and stronger connectivity, consistent with their advanced developmental stage.

Functional interrogation confirmed the reliance of spontaneous calcium spikes on extracellular calcium and voltage-gated sodium channels, while pharmacological manipulations highlighted the presence of functional glutamatergic and GABAergic receptors. Graph theory analysis further demonstrated that ENPCs and LNPCs established distinct functional network topologies, with LNPCs exhibiting more efficient small-world connectivity.

Finally, transplantation studies revealed that ENPCs and LNPCs preserved their laminar identity *in vivo* and extended axonal projections towards layer-specific targets in brains of NOD-SCID mice. These findings confirm that temporal identity dictates not only neuronal subtype specification but also network organisation and integration capacity.

Chapter :3 Droplet-Based Microfluidic Technique to Fabricate 3D Constructs

3.1 Introduction

The development of physiologically relevant *in vitro* models is essential not only for studying human cortical development but also for generating neural tissues for brain repair. Although conventional 2D neuronal cultures have been widely used, they do not recapitulate the spatial complexity and laminar architecture of the cerebral cortex. Additionally, the network density, structure, connectivity, and functional properties of the neurons in 2D cultures do not accurately reflect those found in living tissues (Lovett et al., 2020). In contrast, 3D cultures enable cellular interactions across multiple spatial dimensions, recapitulating the architecture and signalling dynamics of the developing brain (Ulloa Severino et al., 2016). Human brain organoids have emerged as a model for investigating various aspects of human brain development (Lancaster et al., 2017, Renner et al., 2017). However, they exhibit considerable limitations, including cell heterogeneity and the intrinsic self-organising nature that limit precise control over spatial patterning and neuronal subtype composition (Andrews and Kriegstein, 2022).

Bioprinting technologies, including droplet-based, extrusion-based, and laser-based methods, offer an alternative that enables precise spatial positioning of pre-differentiated cells in pre-designed architectures (Cadena et al., 2021). This approach allows the generation of 3D neuronal tissues with adjustable organisation and cellular composition, thereby enhancing reproducibility and improving nutrient penetration and cell survival (Bishop et al., 2017). 3D bioprinting of multi-layered brain tissues was successfully constructed by depositing the cell layers either vertically (Lozano et al., 2015b) or horizontally next to each other (Yan et al., 2024). However, bioprinting of neurons remains challenging due to the delicate nature of neurons and the difficulty in identifying a bioink that is mechanically supportive and biochemically compatible with the brain's ECM (Wang et al., 2022a).

Various bioinks have been proposed for neuronal bioprinting and tissue engineering (Aqel et al., 2023). Among these, Matrigel-based bioinks have been successfully used for bioprinting hiPSC-derived spinal neurons (Joung et al., 2018) and cortical neurons (Yan et al., 2024, Zhou

et al., 2020, Jin et al., 2023, Joung et al., 2018) with promising neuronal survival and functional maturation.

During cortical development *in vivo*, PNs populate the cerebral cortex following an inside-out pattern, where early-born neurons settle in the deeper layers, and late-born neurons migrate past them to occupy the upper layers (Rakic, 2009). This temporal patterning is accompanied by a developmental transition in calcium activity from asynchronous activity to large-scale synchronous oscillations (Garaschuk et al., 2000). While these dynamics have been described in rodent cortical slices (Corlew et al., 2004, Garaschuk et al., 2000, Allene et al., 2008) and PSC-derived neuronal cultures (Kirwan et al., 2015), their recapitulation in bioengineered human cortical tissues has not been detailed.

In the adult cortex, cortical laminae are integrated into a canonical microcircuit (D'Souza and Burkhalter, 2017). Within the cortical column, layer IV provides strong ascending excitation to layers II/III. Layers II/III integrate local network activity with long-range corticocortical inputs, projecting both horizontally within the supragranular layers and vertically to deeper layers, including layer V (Liu et al., 2024b, Weiler et al., 2008). Layers V/VI integrate inputs from both superficial layers and the thalamus, serving as the cortex's primary output channels. ,while Layer V sends most corticofugal projections to subcortical targets, and layer VI provides corticothalamic output and engages in local feedback circuits that regulate thalamocortical gain (Usrey and Sherman, 2019). Layer I is densely innervated by feedback and modulatory inputs from higher-order cortical and thalamic sources. These inputs synapse onto the apical dendritic tufts of pyramidal neurons, thereby shaping the integration of bottom-up and top-down signals (Douglas and Martin, 2004). Across areas, laminar connectivity follows a consistent pattern: feedforward corticocortical pathways arise mainly from superficial layers and preferentially terminate in middle layers, including layers III/IV, of higher-order cortex, whereas feedback pathways originate from deep layers and avoid layer IV, terminating predominantly in layer I (Markov et al., 2014).

Despite recent advances in 3D neuronal tissue engineering, no study has directly compared the functional activity of 3D ENPC and LNPC constructs, nor has it examined how the laminar arrangement of these neuronal constructs modulates network connectivity. Importantly, developing 3D ENPC and LNPC constructs extends beyond tissue modelling, representing a

translational step toward repairing cortical circuitry after implantation into TBI with a cortical lesion.

In this chapter, I addressed this by the fabrication of 3D neuronal constructs using a custom-designed droplet-based microfluidic technique with Matrigel as the bioink. hiPSCs were differentiated into ENPCs and LNPCs in monolayer culture and harvested at DIV 30 and DIV 45, respectively, to reflect early and late stages of cortical maturation. These populations were bioprinted into separate 3D constructs and either cultured individually or assembled into two-layered neuronal tissues to mimic basic features of cortical lamination. I investigated whether these constructs retain their laminar-specific identity after fabrication, using immunostaining for layer-specific markers, and examined their potential to generate different neuronal phenotypes. I investigated how the temporal identities can shape and recapitulate the pattern of *in vivo* calcium activity by recording spontaneous calcium activity, followed by graph theory analysis to reveal the connectivity patterns and functional networks. Finally, I investigated whether assembling 3D ENPC and LNPC constructs into two-layered neuronal tissues could mimic aspects of cortical lamination, with particular attention to compartmentalisation and inter-laminar connections.

3.2 Methods

3.2.1 Microfluidic technique to generate 3D neuronal constructs

3.2.1.1 Fabrication of the polydimethylsiloxane (PDMS) chip

Prefabricated master moulds featuring a T-shaped junction with a serpentine segment were used to manufacture PDMS chips. The moulds were kept in a protective case and cleaned with a nitrogen gun before use. The PDMS mixture was prepared using the Sylgard® 184 Silicone Elastomer Kit (Dow) at a 1:10 ratio, with a total of 55 grams, consisting of 5 grams of the curing agent and 50 grams of the polymer base, which were thoroughly mixed before being poured into the master mould. The mixture was degassed by placing the pre-cured PDMS in the vacuum desiccator (Fisher Scientific) for a minimum of 30 min with intermittent venting to remove trapped air bubbles. For curing, the mould was placed in a petri dish and moved to an oven, heated to 65-80°C, for 1 h. After that, a scalpel was used to make straight cuts along the edge of the master mould to detach the cured PDMS. Once all the edges were released, the PDMS was gently lifted from the bottom of the mould and placed in a clean petri dish. Two identical PDMS halves were precisely aligned to form the microfluidic chip. Two different PDMS chips with varying channel dimensions were fabricated and used to generate constructs with variable geometries. For constructs with 600 µm width, a chip featuring inlet channels of 950 µm and outlet channels of 750 µm was used. For 300 µm wide constructs, a chip with inlet channels of 750 µm and an outlet channel of 550 µm was employed. The serpentine segment in both chips was 100 mm in length (Fig. 3.1B).

3.2.1.2 Bioink preparation and fabrication of the 3D neuronal constructs

hiPSC-derived ENPCs and LNPCs were collected at DIV 30 and DIV 45, respectively. The monolayer cells were washed three times with DPBS, then incubated with 1 mL of pre-warmed Accutase for 5 min. They were resuspended in 5 mL of NMM and transferred to a 15 mL Falcon tube for centrifugation at 200 × g for 5 min. The supernatant was discarded, and if any residual supernatant remained, a second brief spin was done for 1 min. Trypan Blue staining (Thermo Fisher Scientific) was used to manually count the total number of cells and assess cell viability. The final cell pellet was resuspended in ice-cold, pre-thawed Matrigel (Matrigel® Growth Factor Reduced, Corning®) to a final density of 80-100 × 10^6 cells/mL. Matrigel was kept at 4°C throughout the procedure to prevent early polymerisation, and cell-laden Matrigel was gently mixed to ensure homogeneous cell distribution. A custom-designed cooling system was used to maintain a bioprinting temperature between 4°C and 8°C. Two syringes were

prepared and connected to polytetrafluoroethylene (PTFE) tubing; both initially filled with Fluorinert™ FC-40 (Sigma-Aldrich Corporation) to ensure continuous flow without air bubbles. One syringe was subsequently loaded at its tip with the cell-laden Matrigel, while the other remained filled with the oil to serve as the continuous oil phase. The opposite ends of the PTFE tubing were inserted into the corresponding inlets of the microfluidic chip. The syringes were mounted on syringe pumps and operated at flow rates of 2000 µL/h for the oil phase and 500 µL/h for the cell-laden Matrigel phase (Fig. 3.1A).

A third PTFE tube, 30 cm in length, was connected to the outlet of the microfluidic chip to collect droplets of cell-laden Matrigel. The inner diameter of the collecting tube was chosen to match the width of the desired constructs, of either 300 or 600 µm. Once the system was assembled, the volumes and frequencies of the formulated droplets could be adjusted by tuning the flow rate. The Matrigel droplets within the tube were spaced with oil that prevented droplet fusion, in addition to a transition of oil at the beginning and the end of the collecting tube for proper sealing. Once the collecting tube was full, it was detached from the chip and incubated at 37°C and 5% CO_2 for 2 h to allow Matrigel polymerisation. The constructs were then unloaded and cultured in ultra-low attachment plates (Merck). Consumables used for the droplet-based microfluidic technique are listed in Table 6.7.

3.2.1.3 *In vitro* culture of the 3D neuronal constructs

For the first three days post-printing (DPP), constructs were cultured in NMM supplemented with 1% Penicillin-Streptomycin (Gibco Life Technologies) and 10 µM Y-27632 ROCK inhibitor. From 3 DPP, constructs were distributed into ultra-low attachment 96-well plates, with one construct per well. Half of the medium was replaced with fresh NMM every three days throughout the culture period. ENPC constructs were cultured for an additional 15 days, and analysis was performed at DIV 45, representing an early stage of cortical development. LNPC constructs were cultured until DIV 70, corresponding to the late developmental stage. This design enabled the modelling of both early and late stages of cortical development and allowed for the generation of two-layered neuronal tissue through subsequent assembly.

3.2.1.4 Assembly of 3D ENPC and LNPC constructs into two-layered neuronal tissues

At 3 DPP, one construct of each group, 3D ENPC and LNPC constructs, was placed in a single well of a 96-well ultra-low attachment plate. They were manually positioned side by side under an inverted microscope using an insulin needle. Once positioned, the plate was returned to the

incubator carefully and left undisturbed for two days to allow spontaneous fusion. Culture medium was changed every three days by replacing half of the volume with fresh NMM.

Within the two-layered neuronal tissue, labelled LNPC constructs were used, employing two different fluorescent labelling strategies. In one approach, RFP+ iPSC-derived LNPCs were used to fabricate LNPC constructs, which were then fused with unlabelled ENPC constructs. These two-layered neuronal tissues were used for tracing inter-laminar axonal outgrowth and neuronal migration *in vitro* (Section 3.2.2.2) and for later *in vivo* implantation experiments (Chapter 4). The 300 µm-wide constructs were assembled into two-layered neuronal tissues for *in vitro* experiments, while the 600 µm-wide constructs were used to assemble the two-layered neuronal tissues that were used in implantation experiments.

In an alternative approach using 300 µm-wide constructs, Dil-labelled LNPCs were used to generate Dil-labelled LNPC constructs that were assembled with unlabelled ENPC constructs to fabricate two-layered neuronal tissues, which were then used for calcium imaging experiments. For Dil labelling (Vybrant™ DiI, Thermo Fisher Scientific), on the day of printing, the dissociated unlabelled LNPCs were incubated with 5 µM of cell tracker Dil (ex/em 549/565 nm) at 37°C for 1 h. Afterwards, excess Dil was washed away with NMM in two steps, and the cells were centrifuged into a pellet for construct fabrication, as previously described.

3.2.2 Characterisation of the 3D neuronal constructs

3.2.2.1 Live-dead assay

Cell viability after fabrication was assessed using a live-dead assay using 1 µM Calcein-AM (Cambridge Biosciences Ltd) and 100 µg/mL Propidium Iodide (PI, Sigma Aldrich). Calcein-AM is a non-fluorescent, cell-permeable molecule cleaved by intracellular esterase into green fluorescence (ex/em 494/517 nm). PI permeates the membranes of dead cells and binds to DNA by intercalating between the bases. In an aqueous solution, the dye exhibits excitation/emission maxima at 493/636 nm, respectively. Once the dye is bound to DNA, its fluorescence is enhanced 20- to 30-fold. The fluorescence excitation maximum is shifted ~30–40 nm to the red, and the fluorescence emission maximum is shifted ~15 nm to the blue, resulting in ex/em 535/617 nm. 3D constructs were incubated with dyeing solution at 37°C and 5% CO_2 for 20 min. Image acquisition was performed using confocal microscopy with a 20X objective, and Z-stacks were acquired at 15 µm intervals across 5-6 optical sections per construct.

Quantification was performed using ImageJ software. Dead cells were counted using the 3D Object Counter plugin, while live cells were manually quantified. For each construct, at least five planes were analysed. Cell viability was calculated as the percentage of Calcein-positive cells relative to the total number of counted cells (live cells + dead cells). At least three constructs were imaged at 1, 8, and 14 DPP, with three biological replicates per time point, and results were reported as mean ± SEM.

3.2.2.2 Inter-laminar neurite outgrowth and cellular migration within the two-layered neuronal tissues

To evaluate inter-laminar integration, two-layered neuronal tissues, composed of RFP+ LNPC construct and unlabelled ENPC constructs, were imaged using confocal microscopy. Z-stack images were acquired at 1 μm intervals to visualise neurite outgrowth and cell migration across the interface. For enhanced visualisation of nuclear profiles across both compartments, two-layered neuronal tissues were counterstained with 1 μg/mL Hoechst (Thermo Fisher Scientific). The same two-layered neuronal tissues were live-imaged at 2-, 6-, and 10-day post-fusion (DPF). Axonal outgrowth was quantified as the RFP+ area within the ENPC compartment, measured using ImageJ software and expressed as a percentage of the total ENPC compartment area. Migrating neurons were manually counted using ImageJ software. A cell was classified as migrated if it was RFP+, co-localised with Hoechst staining, and located within the ENPC compartment. At least three constructs were reimaged per time point across three biological replicates, and data were presented as means ± SEM. At 2 DPF, only two biological replicates were available, as the constructs were too fragile to manipulate at earlier time points.

3.2.2.3 Immunocytochemistry of the 3D neuronal constructs and two-layered neuronal tissues

3D ENPC and LNPC constructs were fixed in 4% PFA for 30 min at DIV 45 and DIV 70, respectively. Two-layered neuronal tissues were fixed after three weeks of fusion. Post-fixation, the constructs were washed three times with PBS and stored in PBS at 4°C. Immunocytochemistry was performed according to standard immunostaining protocols described in Section 2.2.3.1. The primary and secondary antibodies used for staining are listed in Tables 6.5 and 6.6. Confocal imaging with Z-stacks, captured at an interval of 1.88 μm, allowed for the analysis of marker expression, neuronal differentiation, and proliferation within the three-dimensional structure of the constructs. For synaptic development, synaptic markers were imaged using a 63X oil-immersion objective with a 1 μm interval.

For each marker, at least three fields were imaged per construct, with three constructs for each biological replicate. The cells were manually counted, and the percentage of positive cells relative to the total DAPI-positive cells was calculated. The average value for each biological replicate (n) was then calculated, and the results from the three biological replicates were used for statistical analysis. The images in the figures represent maximum intensity projections of Z-stacks.

3.2.2.4 Calcium imaging of the 3D neuronal constructs and two-layered neuronal tissues

Calcium imaging was performed using 3D ENPC and LNPC constructs at DIV 45 and DIV 70, respectively. Constructs were dual loaded with Fluo-4 AM and Fura-Red AM following the protocol described in Section 2.2.3.4, with the only modification being a 60-minute incubation period instead of 30 min to ensure the dye penetration to the centre of the constructs. Two-layered neuronal tissues, composed of Dil-labelled LNPC construct and unlabelled ENPC construct, were imaged three weeks post-fusion after loading with 5 μM Fluo-4 AM. During imaging, a 488 nm laser was used to excite Fluo-4 AM, and a 568 nm laser was used to visualise Dil-labelled LNPCs. A schematic of the workflow, from 2D expansion to microfluidic printing, assembly, and calcium imaging, is shown in Fig. 3.7A. Confocal time-lapse imaging recorded spontaneous calcium spikes of 3D constructs and two-layered neuronal tissues at a frame rate of 1.27 Hz over 800 frames.

3.2.2.5 Analysis of calcium imaging data

Data acquired from calcium imaging of 3D ENPC and LNPC constructs, as well as two-layered neuronal tissues, were analysed using custom-written algorithms in MATLAB, as described in Section 2.2.3.4.3. Functional connectivity patterns were detected using graph theory analysis (Dingle et al., 2020) as described in Section 2.2.3.4.3.2.

To investigate the inter-laminar temporal coordination of the two-layered neuronal tissues, pairwise cross-correlations were computed between Z-scored calcium traces of Dil-labelled LNPCs and ENPCs pairs. Imaging was performed at a frame rate of 1.27 Hz, corresponding to a frame duration of 0.785 s, with each recording spanning 800 frames, resulting in a total duration of ~10.5 min (T). Cross-correlation analysis was performed across a lag window of ± 5 frames (± 3.9 s). Calcium traces were Z-scored on a per-neuron basis to standardise amplitude and prevent differences in signal magnitude from biasing correlation outcomes.

For a given calcium trace x(t) of length T, the Z-scored signal Z(t) was calculated as:

$$Z(t) = (x(t) - \mu) / \sigma$$

where: $\mu = (1/T) * \Sigma x(t)$ is the mean of the trace and $\sigma = \sqrt{((1/T) \Sigma(x(t) - \mu)^2)}$ is the standard deviation.

A lag matrix was constructed where each entry represented the lag, in frames and equivalent time in seconds, at which the maximum cross correlation occurred. Positive lag indicated that the LNPC trace preceded the ENPC trace (LNPC-initiator), negative lag indicated that the ENPC trace preceded the LNPC trace (ENPC-initiator), and a lag of zero indicated simultaneous activation between ENPC and LNPC pairs (Fig. 3.9A, C).

Based on this analysis, LNPC and ENPC pairs were classified into three functional groups: LNPC-initiator, ENPC-initiator, and simultaneous pairs. The proportion of each functional group was quantified across three independent biological replicates and shown as means ± SEM.

To visualise initiator–follower dynamics at the single-neuronal level, for each initiator neuron, its Z-scored calcium trace was plotted as the initiator trace. The related follower neurons from the opposite compartment were identified based on their cross-correlation lag values. Each follower trace was Z-scored, shifted in time by the estimated lag relative to the initiator, and vertically offset. This approach allows simultaneous visualisation of an initiator's activity and the temporally aligned responses of its followers (Fig. 3.9E, G). Similarly, Z-scored traces of simultaneous pairs were also displayed (Fig. 3.9I).

To highlight group-level dynamics, the mean of calcium traces was computed for initiators and followers within each category and plotted against one another, revealing characteristic inter-laminar activity patterns (Fig. 3.9D, F). Similarly, simultaneous pairs across compartments were also displayed (Fig. 3.9H).

3.2.3 Statistical analysis

Statistical analyses were performed using GraphPad Prism version 10. Data were presented as means ± SEM. The Shapiro–Wilk test was used to assess the normality of the data. For normally distributed data, comparisons between two groups were performed using unpaired Student *t*-tests, while comparisons involving more than two groups were analysed using one-

way analysis of variance (ANOVA) followed by Tukey's post hoc test for multiple comparisons. For non-normally distributed datasets, the Mann–Whitney U test was used for pairwise comparisons, and the Kruskal–Wallis test, followed by Dunn's multiple comparison test, was applied for three or more groups. For all tests, a p-value < 0.05 was considered statistically significant. *p< 0.05, ** p < 0.01, *** p < 0.001, **** p < 0.0001.

In imaging-based experiments, biological replicates refer to independently generated constructs from independent differentiation experiments. For each biological replicate, a minimum of three constructs were analysed per time point, and at least three fields were imaged per construct. For calcium imaging, three biological replicates were used; each construct was once recorded, with at least three constructs analysed per group and time point. The average across each biological replicate was used for statistical analysis. The summary of the experimental pipeline, time points, and the number of replicates is shown in Table 3.1.

Table 3.1 Summary of the experimental pipeline, time points, and the number of replicates

Experiment	Time Point	Constructs	Number (n)
Live-dead assay	1, 8, 14 DPP	3D ENPC constructs	≥3 constructs per biological replicate, n = 4 biological replicates
		3D LNPC constructs	
Immunocytochemistry	DIV 45	3D ENPC constructs	≥3 constructs per marker, n = 3 biological replicates
	DIV 70	3D LNPC constructs	
	3 weeks post-fusion	Two-layered neuronal tissue	
Neurite outgrowth and cellular migration	2, 6, 10 DPF	Two-layered neuronal tissue (RFP+ LNPC construct and unlabelled ENPC construct)	≥3 tissues, n = 3 biological replicates at 6, 10 DPF n = 2 biological replicates at 2 DPF
Calcium imaging	DIV 45	3D ENPC constructs	≥3 constructs per biological replicate, n = 3 biological replicates
	DIV 70	3D LNPC constructs	
	3 weeks post-fusion	Two-layered neuronal tissue (Dil-labelled LNPC construct and unlabelled ENPC construct)	

3.3 Results

3.3.1 Droplet-based microfluidic technique enables reproducible generation of 3D neuronal constructs

The custom-designed droplet-based microfluidic system showed high accuracy and reproducibility. It enabled the generation of neuronal constructs in a high-throughput manner within a short timeframe with minimal post-processing, facilitating direct transition from fabrication to *in vitro* culture. This platform permitted precise control over the construct geometry within the same bioprinting session by adjusting the flow rate. Constructs with variable dimensions were successfully fabricated, including those with dimensions of approximately 300 × 600 µm and approximately 600 × 800 µm (Fig. 3.1A, B). A current limitation of the system is its inability to generate layered structures directly. When layered neuronal tissues were essential for the desired application, manual assembly became necessary, which is a time-consuming step that could be optimised in future iterations of the system.

3.3.2 Neuronal viability after fabrication of 3D neuronal constructs

To assess the impact of microfluidic printing on cell survival, viability was evaluated at three time points: 1, 8, and 14 DPP. Quantitative analysis revealed high levels of cell viability across the different time points: 75 ± 7.4% at 1 DPP, 80 ± 7.4% at 8 DPP, and 85 ± 5.4% at 14 DPP (Fig. 3.1C). These findings demonstrated that the printing process was sufficiently gentle to preserve neuronal integrity and that the culture conditions supported long-term cell survival. The sustained viability at 14 DPP indicated adequate nutrient provision, supporting the use of these constructs for downstream applications such as implantation or extended functional analysis.

3.3.3 Maturation of 3D ENPC and LNPC constructs

Immunocytochemical analysis of 3D ENPC and LNPC constructs at DIV 45 and DIV 70, respectively, showed continued neuronal maturation and acquisition of cortical neuronal identities. Expression of the deep-layer marker CTIP2 was comparable between ENPC and LNPC constructs (52 ± 14% vs. 56 ± 9.1%, $p = 0.844$, unpaired *t*-test). In contrast, the upper-layer marker SATB2 was highly expressed in LNPC constructs (39 ± 8.2%) but absent in ENPC constructs (0.0 ± 0.00%, $p = 0.004$, unpaired *t*-test, Fig. 3.2A), consistent with the advanced differentiation stage of LNPCs. GABA immunostaining confirmed the generation of GABAergic INs in both 3D ENPC and LNPC constructs (18 ± 4.2%, 15 ± 2.0%, respectively;

p = 0.232, unpaired t-test, Fig. 3.2B), indicating lineage specification into different neuronal phenotypes.

Over time, an increase in cellular density was observed (Fig. 3.1D), reflecting the preserved proliferative capacity. Ki-67+ immunolabelling demonstrated retained proliferation of ENPC and LNPC constructs (8.2 ± 0.38% and 6.8 ± 1.6%, respectively; p = 0.217, unpaired t-test, Fig. 3.2C), indicating proliferation potential of the progenitors after printing. A small fraction of apoptotic cells was detected by immunostaining for Cleaved Caspase-3 (4.5 ± 2.6% and 3.8 ± 1.1%, respectively; p = 0.5, unpaired t-test, Fig. 3.2C), supporting the viability of the constructs. SOX2+ cells were detected in both ENPC and LNPC constructs (26 ± 8.5% and 37 ± 8.0%, respectively; p = 0.214, unpaired t-test, Fig. 3.2D), consistent with the known role of SOX2 in maintaining neural progenitor identity during early differentiation and supporting aspects of neuronal maturation during later stages (Graham et al., 2003). Synaptogenesis was evidenced by immunolabelling for the SYN1 and PSD-95. Both markers exhibited punctate staining, with regions of co-localisation, suggesting the potential of synaptic formation (Fig. 3.2E). Astrocytic differentiation was confirmed by S100β expression in both ENPC and LNPC constructs (Fig. 3.2F).

3.3.4 Maturation of two-layered neuronal tissues

Two-layered neuronal tissue maintained clear anatomical lamination early post-fusion and after extended *in vitro* culture. RFP labelling revealed clear compartmental fusion, with RFP+ LNPCs primarily detected on one side and ENPCs on the other side, at 2 DPF (Fig. 3.3B). By 6 DPF, RFP+ processes extended across the interface, indicating the establishment of inter-laminar connectivity over time (Fig. 3.3B). Analysis revealed progressive inter-laminar neurite extension and neuronal migration. Quantification of inter-laminar neurite outgrowth showed a gradual expansion of the RFP+ area within the ENPC compartment, increasing from 4.0 ± 2.3% at 2 DPF to 22 ± 7.4% at 6 DPF and 35 ± 12% at 10 DPF. In parallel, an average of 25 ± 5 RFP+ neurons were detected in the ENPC compartment at 2 DPF. This average increased to 110 ± 40 at 6 DPF and reached 197 ± 30 by 10 DPF (Fig. 3.3C).

Immunocytochemistry of two-layered neuronal tissues showed preservation of spatial segregation, with SATB2 expression predominantly localised to the LNPC compartment, while CTIP2+ cells were primarily distributed in both compartments, confirming preservation of laminar identity over an extended period of *in vitro* culture (Fig. 3.3D). Proliferation potential

and astrocytic differentiation were confirmed by Ki-67 and S100β expression, respectively, in both compartments (Fig. 3.3E). These findings demonstrated that the fusion of ENPC and LNPC constructs generated a stable, two-layered neuronal tissue with maintained segregation of identity.

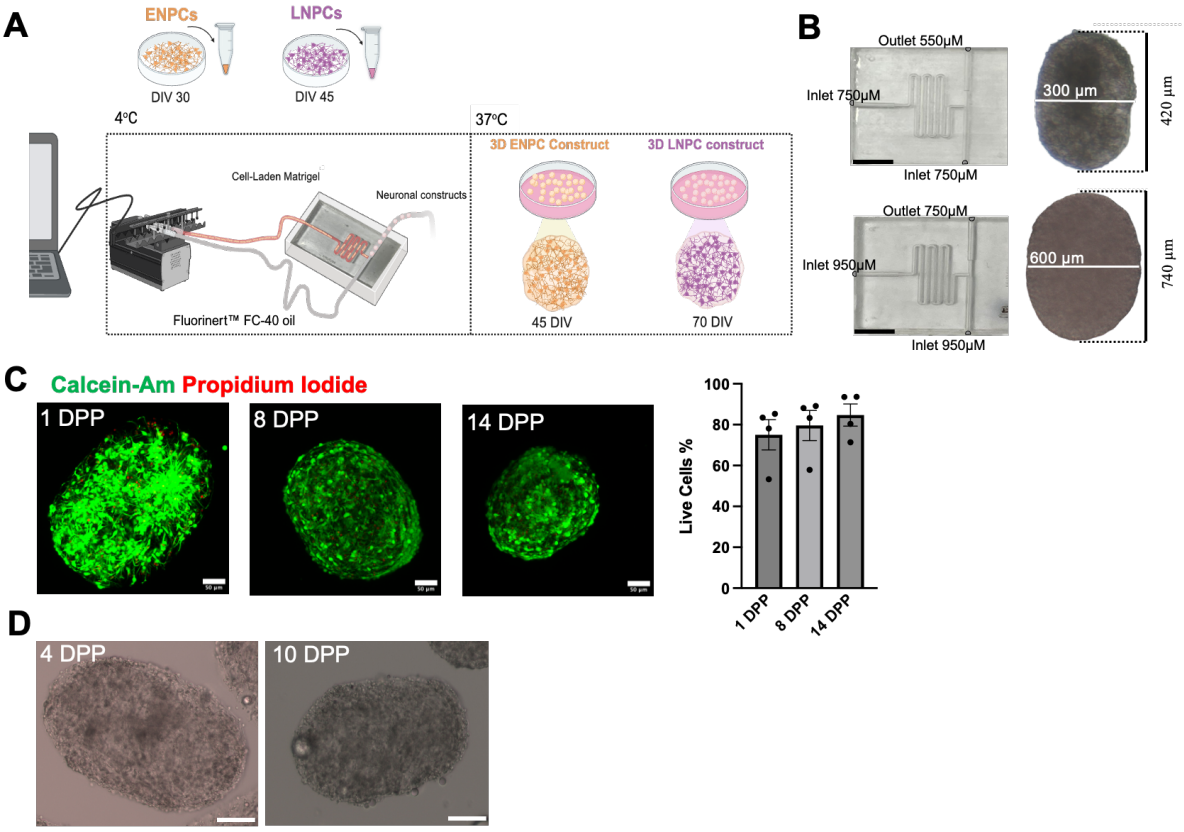

Figure 3.1 The droplet-based microfluidic technique reproducibly generates 3D constructs with high post-printing viability

(A) A schematic illustration of the droplet-based microfluidic system composed of a custom-designed PDMS microfluidic chip connected to a computer-controlled infusion pump. The microfluidic chip features two inputs, one for the oil and the other for the cell-laden Matrigel, and a single output for collecting fabricated 3D neuronal constructs.
(B) Phase-contrast images of 3D constructs with different dimensions generated using different microfluidic chips are shown to the right.
(C) Live-dead assay of 3D constructs at 1, 8, and 14 DPP, showing sustained high viability over time.
(D) Phase-contrast images of 3D constructs cultured *in vitro* at 4 and 10 DPP, showing an increase in cellular density.
Scale bar (B,): 100 mm. Scale bar (C): 50 µm. Scale bar (D): 100 µm. Results are presented as means ± SEM. n = 4 biological replicates. DPP: day post-printing.

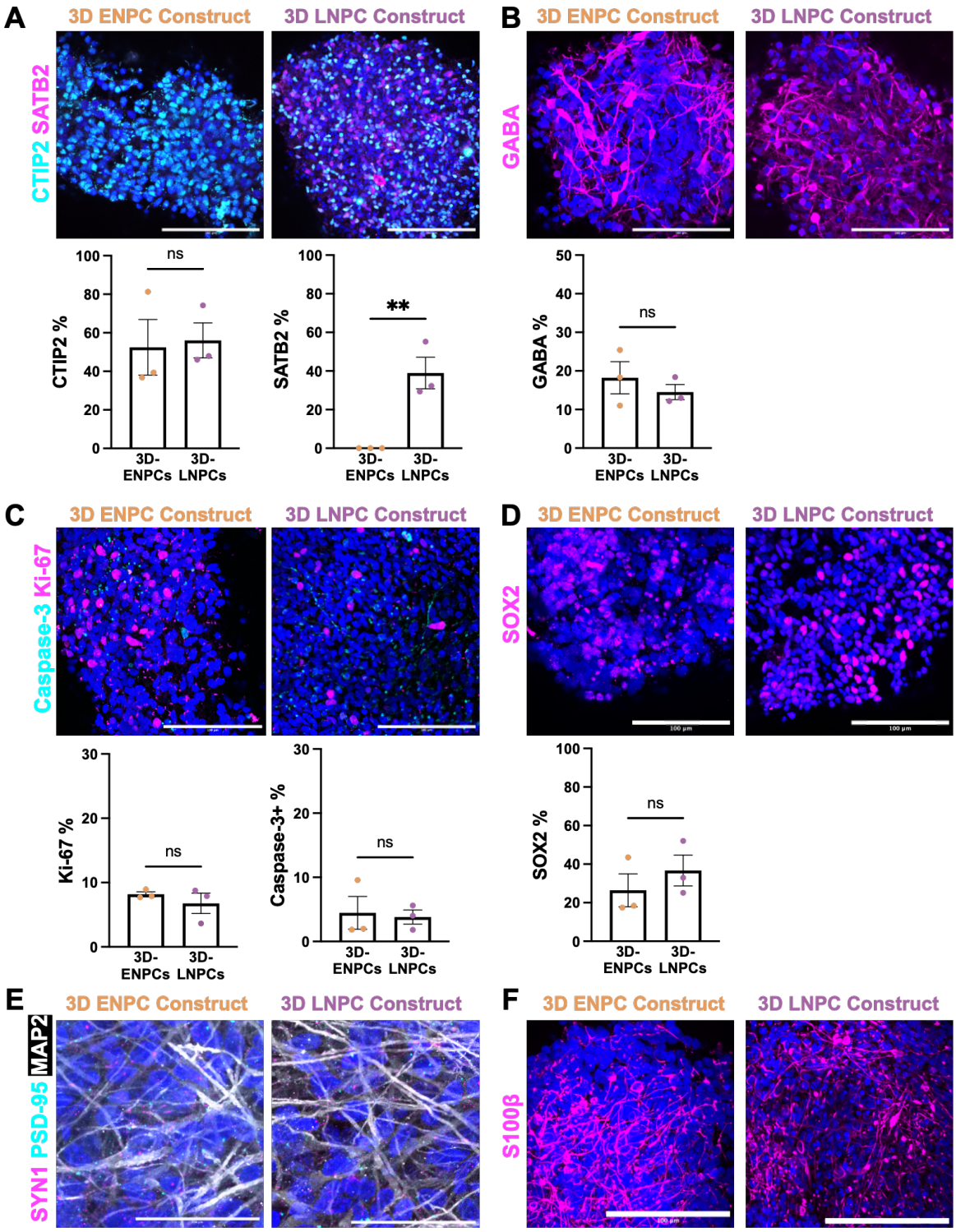

Figure 3.2 Maturation of 3D ENPC and LNPC constructs
(A) Immunostaining for cortical layer-specific markers showing CTIP2 expression in both 3D ENPC and LNPC constructs, and predominant SATB2 expression in LNPC constructs. Quantification is shown below ($p = 0.844$ for CTIP2%; $p = 0.004$ for SATB2%).
(B) GABA immunostaining indicates the presence of GABAergic INs in both ENPC and LNPC constructs; the percentage of GABA+ cells is quantified and presented below ($p = 0.232$).

(C) Immunostaining for Ki-67 and Cleaved Caspase-3 indicates continued progenitor proliferation with low levels of apoptotic cells ($p = 0.217$ for Ki-67% and $p = 0.5$ for Caspase-3%).
(D) SOX2+ expression in both constructs, with quantification revealing comparable levels between groups ($p = 0.214$).
(E) High-magnification images showing the juxtaposition of presynaptic SYN1 and the postsynaptic PSD-95, alongside MAP2-positive neurites.
(F) Immunostaining revealed positive expression for astrocytic marker S100β in both 3D ENPC and LNPC constructs.
Scale bars: (A–D, F) 100 µm; (E) 200 µm. Graphs present means ± SEM. n = 3 biological replicates.

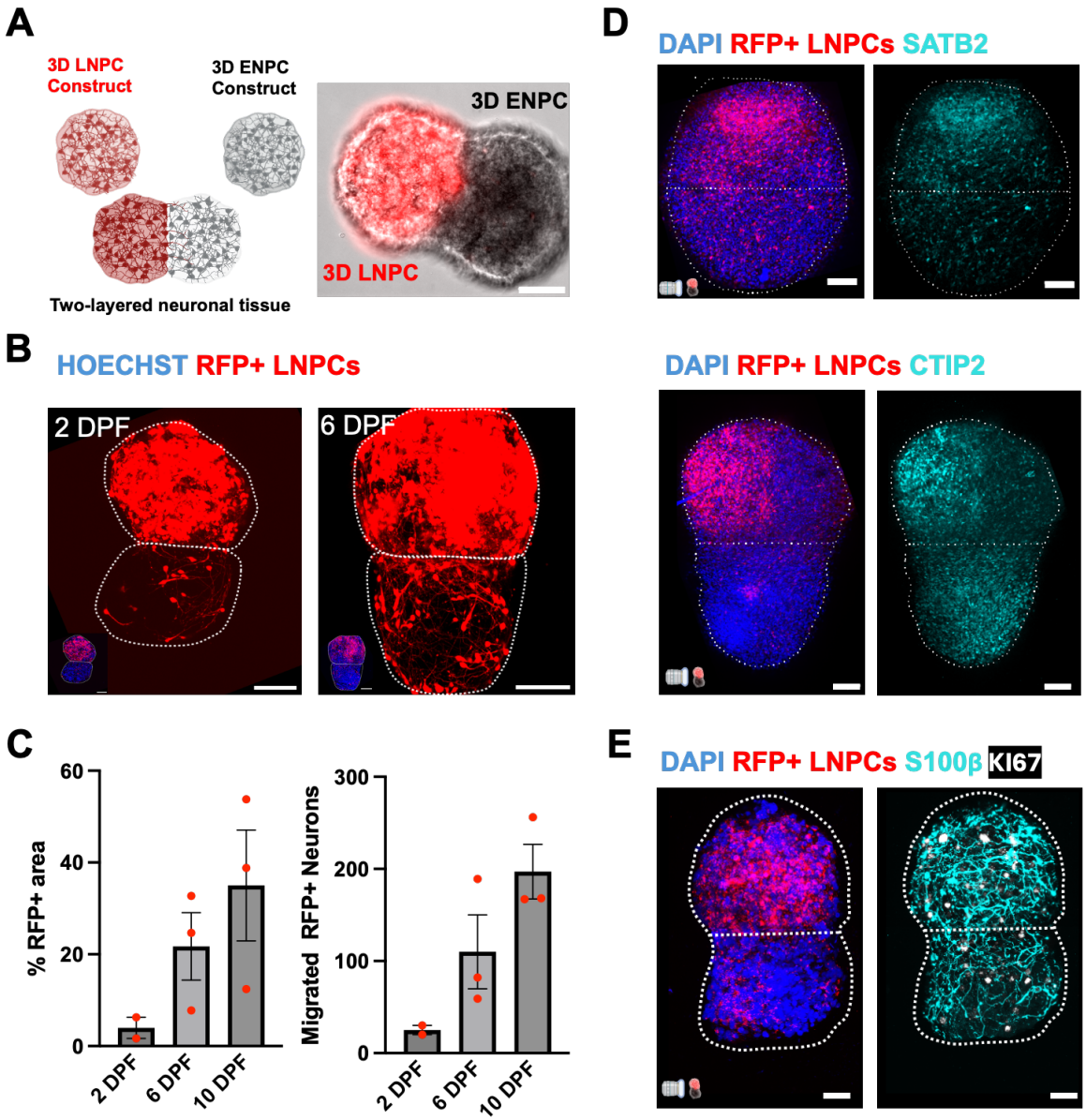

Figure 3.3 Spatial characterisation of two-layered neuronal tissues and inter-laminar connections
(A) A schematic illustration of assembling 3D ENPC and LNPC constructs into two-layered neuronal tissues. (Right) Representative fluorescence image of two-layered neuronal tissue composed of RFP+ LNPC constructs and unlabelled ENPC constructs at 2 DPF.
(B) Representative confocal images of two-layered neuronal tissue at 2 DPF and 6 DPF show progressive axonal extension and cellular migration from the RFP+ LNPC compartment into the adjacent ENPC compartment across the interface.

(C) Quantification of the % RFP+ area and the total number of migrated RFP+ neurons in the ENPC compartment.
(D) Immunofluorescence analysis three weeks post-fusion showing spatial segregation of cortical layer marker expression, with most CTIP2+ neurons localised in both compartments, while LNPC compartments were enriched with SATB2+ neurons.
(E) Immunostaining for astrocytic marker S100β and proliferation marker Ki-67, revealing potential differentiation into glial fate and ongoing proliferation within the two-layered neuronal tissue.
White dashed outlines indicate the construct's boundary.
Scale bar: 100 µm. DPF: day post-fusion. The graphs show means ± SEM. n = 3 biological replicates across time points except 2 DPF, where n = 2.

3.3.5 Spontaneous calcium activity and functional network in 3D neuronal constructs

The intrinsic activity and connectivity patterns of 3D ENPC and LNPC constructs were first characterised independently to establish their baseline functional properties. Subsequently, the influence of spatial organisation within two-layered neuronal tissues on the activity profiles and network properties of each compartment was examined. Finally, the emergence of directional interactions between compartments was analysed to determine the directionality of functional connectivity.

3.3.5.1 Distinct functional network properties in ENPC and LNPC constructs

3D ENPC and LNPC constructs exhibited spontaneous calcium activity, recruiting a high percentage of active neurons (3D ENPC: 83 ± 4.8%; 3D LNPC: 88 ± 3.5%; $p = 0.1182$, unpaired *t*-test). The mean firing rate was comparable in 3D ENPC and LNPC constructs (67 ± 13 spikes/min, 79 ± 10 spikes/min, $p = 0.2554$, unpaired *t*-test). However, 3D LNPC constructs exhibited a significantly higher global synchrony index (3D ENPC: 0.19 ± 0.019; 3D LNPC: 0.47 ± 0.10; $p = 0.0286$, unpaired *t*-test), indicating more coordinated activity and suggesting enhanced maturation of the LNPC-derived networks (Fig. 3.4C). Spike dynamics were characterised by a fast rise time and a slower decay time. 3D LNPC constructs exhibited a comparable level of rise times, 15 ± 1.8 s, in comparison to 3D ENPC 17 ± 0.59 s ($p = 0.207$, unpaired *t*-test) and significantly shorter decay times, 3D ENPC: 25 ± 0.88 s; 3D LNPC: 22 ± 0.61 s ($p = 0.0382$, unpaired *t*-test). Moreover, the half maximal width times were also shorter in 3D LNPC constructs, 19 ± 0.88 s, compared to 3D ENPC constructs, 21 ± 0.71 s ($p = 0.0571$, unpaired *t*-test), suggesting network maturation of 3D LNPC constructs (Fig. 3.4C).

Graph theory-based analysis revealed distinct patterns of connectivity. 3D LNPC constructs displayed a significantly higher average edge weight (3D ENPC: 0.24 ± 0.017; 3D LNPC: 0.50 ± 0.10; $p = 0.0286$, unpaired *t*-test), indicating stronger correlation activity. Additionally, they exhibited shorter average path length (3D ENPC: 2.1 ± 0.049; 3D LNPC: 1.7 ± 0.14;

$p = 0.0286$, unpaired *t*-test), indicating stronger and efficient functional connectivity between the LNPCs within 3D constructs. Additionally, clustering coefficients, a measure of the strength of functional connectivity among neurons, were significantly higher in 3D LNPC constructs (3D ENPC: 0.64 ± 0.033; 3D LNPC: 0.79 ± 0.046; $p = 0.0286$, unpaired *t*-test), suggesting efficient sharing of local information and being more resilient to disruptions. 3D ENPC constructs showed greater modularity (3D ENPC: 0.41 ± 0.023; 3D LNPC: 0.19 ± 0.046; $p = 0.0054$, unpaired *t*-test), suggesting more segregated subnetworks consistent with the early developmental stage represented by 3D ENPC constructs (Fig. 3.4D).

To quantify the functional connectivity, Pairwise Pearson correlation coefficients (r) were calculated between the traces of active neurons. Neuron pairs were functionally connected when r value was greater than 0.35 (section 2.2.3.4.2). In 3D ENPC constructs, the correlation matrix revealed that more than half of the neuron pairs had low r-value, while a substantial number of pairs were highly correlated (Fig. 3.5C). In contrast, most neuron pairs in 3D LNPC constructs showed high correlation, indicating high global synchrony (Fig. 3.6C). Sorting the correlation matrices based on connection density revealed that highly connected neurons had stronger connections in both 3D ENPC and LNPC constructs (Fig. 3.5D, 3.6D).

To evaluate the organisation of functional subnetworks, I applied the Louvain community-detection algorithm. In 3D ENPC constructs, two distinct modules were identified with sparse intermodular connectivity, consistent with a more fragmented network (Fig. 3.5F). Within each module, the neurons were interconnected in a hierarchical topology, with a few hub neurons with a high number of connections, and more peripheral neurons at the outer edges of the network topology (Fig. 3.5G). In the 3D LNPC constructs, two modules were identified, exhibiting strong intermodular connections, indicating rich interconnectivity within the 3D constructs (Fig. 3.6F). Within each module, the neurons were interconnected in a hierarchical topology, with more centralised neurons and fewer peripheral neurons at the outer edges of the network topology, compared to the 3D ENPC construct topology (Fig. 3.6G). Taken together, 3D LNPC constructs exhibited efficient, interconnected networks capable of generating synchronous oscillatory activity, while 3D ENPC constructs organised into more segregated and less synchronous subnetworks. These findings demonstrated that functional connectivity in 3D constructs was influenced by both neuronal identity and maturity stage.

3.3.5.2 Enhanced functional connectivity of two-layered neuronal tissues

The functional network activity of two-layered neuronal tissues was assessed using calcium imaging conducted three weeks after assembly. The representative mean calcium traces and heatmaps demonstrated spontaneous activity in both compartments of the two-layered neuronal tissue, with highly temporally coordinated activity profiles (Fig. 3.7C-E). To evaluate whether the laminar arrangement alters the intrinsic activity profiles, the calcium dynamics of the ENPC and LNPC compartments of the two-layered neuronal tissue were compared to those of their respective single 3D ENPC and LNPC constructs. The firing frequency in the two-layered tissues averaged 73 ± 6.1 spikes/min in the ENPC compartment and 84 ± 22 spikes/min in the LNPC compartment, values comparable to those recorded in single 3D ENPC constructs (67 ± 13 spikes/min) and in single 3D LNPC constructs (79 ± 10 spikes/min, Fig. 3.7F), suggesting that lamination did not markedly alter the intrinsic firing frequency of either neuronal population.

Calcium transient kinetics, including rise time, decay time, and half maximal spike width, were also comparable between ENPC and LNPC compartments of two-layered neuronal tissues and their counterparts, single 3D constructs. In the two-layered neuronal tissues, the ENPC and LNPC compartments exhibited a rise time of 15 ± 1.6 s and 15 ± 1.3 s, respectively, compared to 17 ± 0.59 s in single 3D ENPC constructs and 15 ± 1.8 s in single 3D LNPC constructs (Fig. 3.7G). Decay times measured 23 ± 1.5 s in the ENPC compartment and 23 ± 1.4 s in the LNPC compartment, closely matching values of 25 ± 0.88 s in single 3D ENPC constructs and 22 ± 0.61 s in single 3D LNPC constructs (Fig. 3.7H). The half maximal spike width was 19 ± 1.5 s in the ENPC compartment and 19 ± 1.4 s in the LNPC compartment, compared to 21 ± 0.71 s and 19 ± 0.88 s in single 3D ENPC and LNPC constructs, respectively (Fig. 3.7I). These findings suggested that the lamination within the two-layered neuronal tissue did not significantly affect the calcium dynamics in either neuronal population.

Pairwise correlation analysis revealed highly coordinated activity between active neuron pairs in two-layered neuronal tissues (Fig. 3.8A). Louvain algorithm detected two modules, and reordering of the correlation matrices to group neurons of the same module highlighted the presence of strong intramodular and intermodular network connections (Fig. 3.8B–C). Spatial overlays of neuron maps revealed the distribution of active neurons assigned to two functionally defined modules within the two compartments of the two-layered neuronal tissue. The inset highlights hub neurons identified in both ENPC and LNPC compartments, indicating

inter-laminar connectivity and integration (Fig. 3.8D). Graph layouts were visualised using the Fruchterman–Reingold algorithm and highlighted dense intramodular connections with highly connected central hub nodes (Fig. 3.8E).

The two-layered neuronal tissue exhibited a high global synchrony index of 0.57 ± 0.039, with the ENPC and LNPC compartments showing similar values of 0.57 ± 0.026 and 0.58 ± 0.047, respectively. In contrast, single 3D ENPC constructs had a significantly lower index of 0.19 ± 0.019, whereas single 3D LNPC constructs reached 0.47 ± 0.10 (Fig. 3.8F). These findings suggested that a laminar arrangement enhanced the overall synchrony, particularly in ENPC networks.

Graph theory matrices further supported this conclusion. The average edge weight of the two-layered neuronal tissues was 0.47 ± 0.048, with the ENPC compartment measuring 0.50 ± 0.051 and the LNPC compartment 0.48 ± 0.043. Single 3D ENPC constructs had a markedly lower edge weight of 0.24 ± 0.017, while single 3D LNPC constructs matched layered values at 0.50 ± 0.10 (Fig. 3.8G). The average path length of the two-layered neuronal tissues was 1.6 ± 0.057, with values of 1.4 ± 0.12 in the ENPC compartment and 1.3 ± 0.13 in the LNPC compartment, compared to high values of 2.1 ± 0.049 in single 3D ENPC constructs and 1.7 ± 0.14 in single 3D LNPC constructs (p = 0.0466 between LNPC compartments and 3D ENPC constructs, one-way ANOVA, Fig. 3.8H). These data suggested that the lamination supported stronger functional connectivity in the ENPC compartment compared to single 3D ENPC constructs, potentially due to network integration with the LNPC compartments.

The clustering coefficient was highest in the two-layered neuronal tissue, at 0.95 ± 0.021, and reached 1.0 ± 0.017 and 1.0 ± 0.041 in the ENPC and LNPC compartments, respectively. This was compared to 0.64 ± 0.033 in single 3D ENPC constructs and 0.79 ± 0.046 in single 3D LNPC constructs (p = 0.0269 between ENPC compartments and 3D ENPC constructs, one-way ANOVA, Fig. 3.8I). The modularity of the two-layered neuronal tissue was 0.24 ± 0.049, with ENPC and LNPC compartments both exhibiting similar values of 0.24 ± 0.045 and 0.24 ± 0.046, respectively (Fig. 3.8J). Modularity showed clear differences between single 3D ENPC and LNPC constructs. It was 0.41 ± 0.023 and 0.19 ± 0.046 in 3D ENPC and LNPC constructs, respectively. These findings suggested that two-layered neuronal tissue facilitated network connectivity between the two compartments and enhanced functional coupling

between the compartments while preserving their intrinsic properties, as evidenced by modulating the graph-theory-based matrices.

3.3.5.3 Inter-laminar temporal coordination in the two-layered neuronal tissues

The spatially segregated architecture of the two-layered neuronal tissue enabled laminar and inter-laminar analysis. The dynamics of inter-laminar coordination were revealed by applying temporal cross-correlation analysis between LNPC and ENPC compartments. This approach identified three functional groups, including LNPC-initiator, ENPC-initiator, and simultaneous pairs (Fig. 3.9A). Temporal functional analysis revealed coordinated activity across compartments, consistent with bidirectional interactions. This supports the hypothesis that hub-like activity in one compartment can entrain network activity in the adjacent compartment.

Quantitative analysis across three independent biological replicates revealed that the ENPC-initiator accounted for 36 ± 2.0%, followed closely by the LNPC-initiator at 34 ± 1.8%. Simultaneous pairs were less frequent, representing 30 ± 3.7% (Fig. 3.9B). These proportions suggested that both compartments actively contributed to inter-laminar activity, with a slight predominance of events led by ENPCs. Temporal lag analysis within a ± 5-frame window (± 3.9 s), between LNPC and ENPC compartments, revealed a positive lag in LNPC-initiators, confirming the delayed recruitment of ENPCs following LNPCs activation, while a negative lag in ENPC-initiators confirmed the recruitment of LNPCs after ENPCs activation. To visualise both LNPC-initiator and ENPC-initiator categories, Z-scored traces from one initiator and the corresponding follower neurons were temporally aligned according to their lag values (Fig. 3.9E, G). Z-scored traces of simultaneous pairs were also displayed (Fig. 3.9H). The mean fluorescence traces for each functional group, including LNPC-initiator, ENPC-initiator, and simultaneous pairs, were calculated and plotted separately (Fig. 3.9D, F, H).

Taken together, these findings demonstrated that the two-layered neuronal tissues preserved coordinated inter-laminar coupling. While cross-correlation analysis cannot establish causality, the observed temporal lead–lag relationships highlighted the potential of both LNPC and ENPC populations to contribute dynamically to inter-laminar network activity.

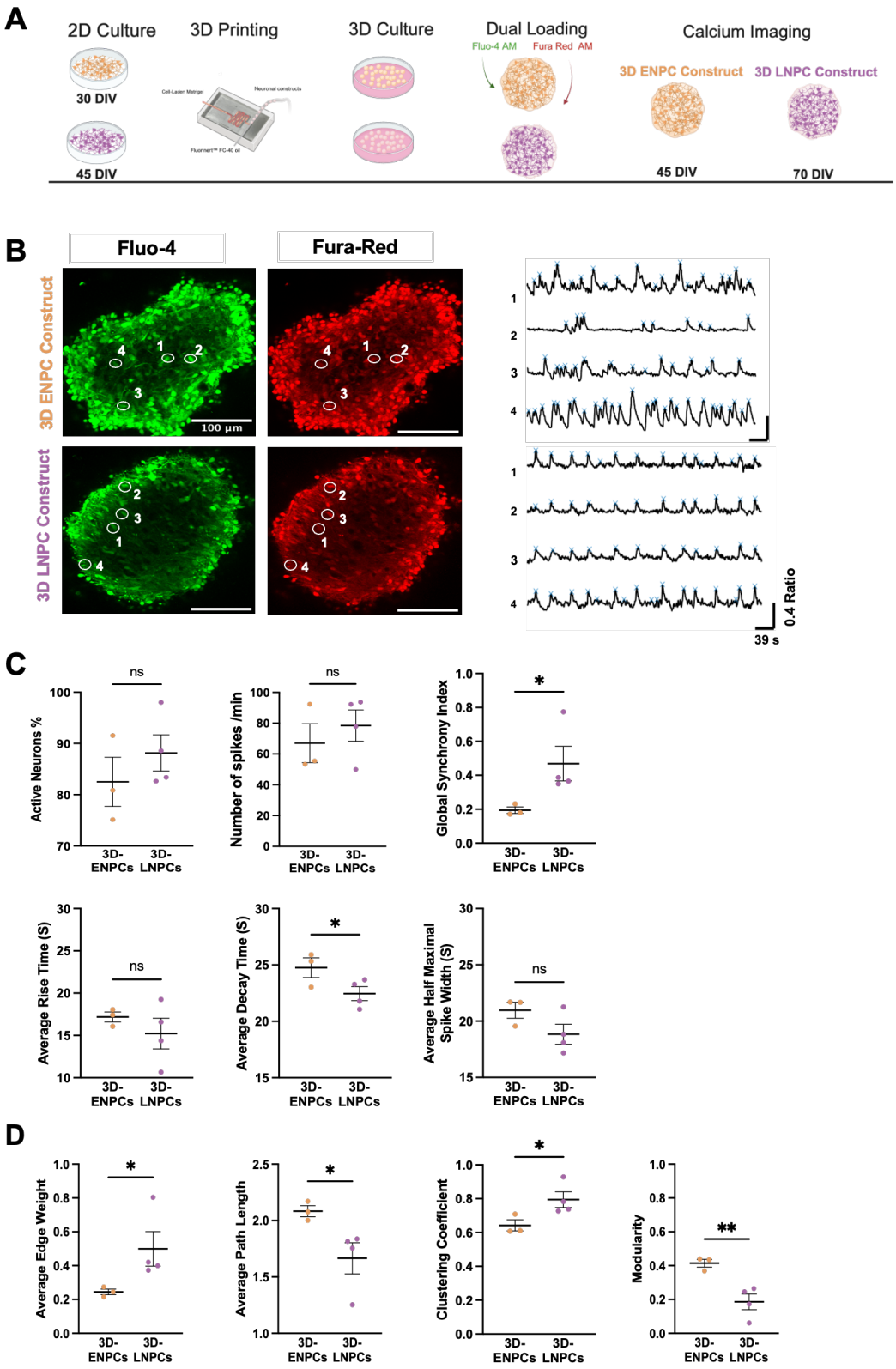

Figure 3.4 3D ENPC and LNPC constructs exhibit spontaneous calcium activity with distinct functional neuronal networks

(A) A schematic illustration showing the generation of 3D ENPC and LNPC constructs using a droplet-based microfluidic technique. These constructs were matured *in vitro*, and calcium activity was captured after dual-labelling with Fluo-4 AM and Fura-Red AM.

(B) Representative fluorescence images displaying 3D ENPC and LNPC constructs loaded with Fluo-4 and Fura-Red.
To the right, representative pseudo-ratiometric traces from four neurons are shown. Each row represents a single-neuron calcium trace, with detected spikes marked by blue asterisks.
(C) Quantitative analysis of percentage of active neurons, firing frequency, global synchrony index, and temporal dynamics of calcium spikes (rise time (s), decay time (s), and half maximal spike width (s)). 3D LNPC constructs displayed a significantly higher global synchrony index ($p = 0.0286$) and a shorter decay time ($p = 0.0382$).
(D) Graph theory analysis reveals that 3D LNPC constructs exhibited significantly higher average edge weights ($p = 0.0286$) and lower average path length ($p = 0.0286$). 3D LNPC constructs also displayed higher clustering coefficient ($p = 0.0286$), and significantly lower modularity ($p = 0.0054$).
Scale bar: 100 µm. Results are means ± SEM; each dot represents one independent biological replicate.

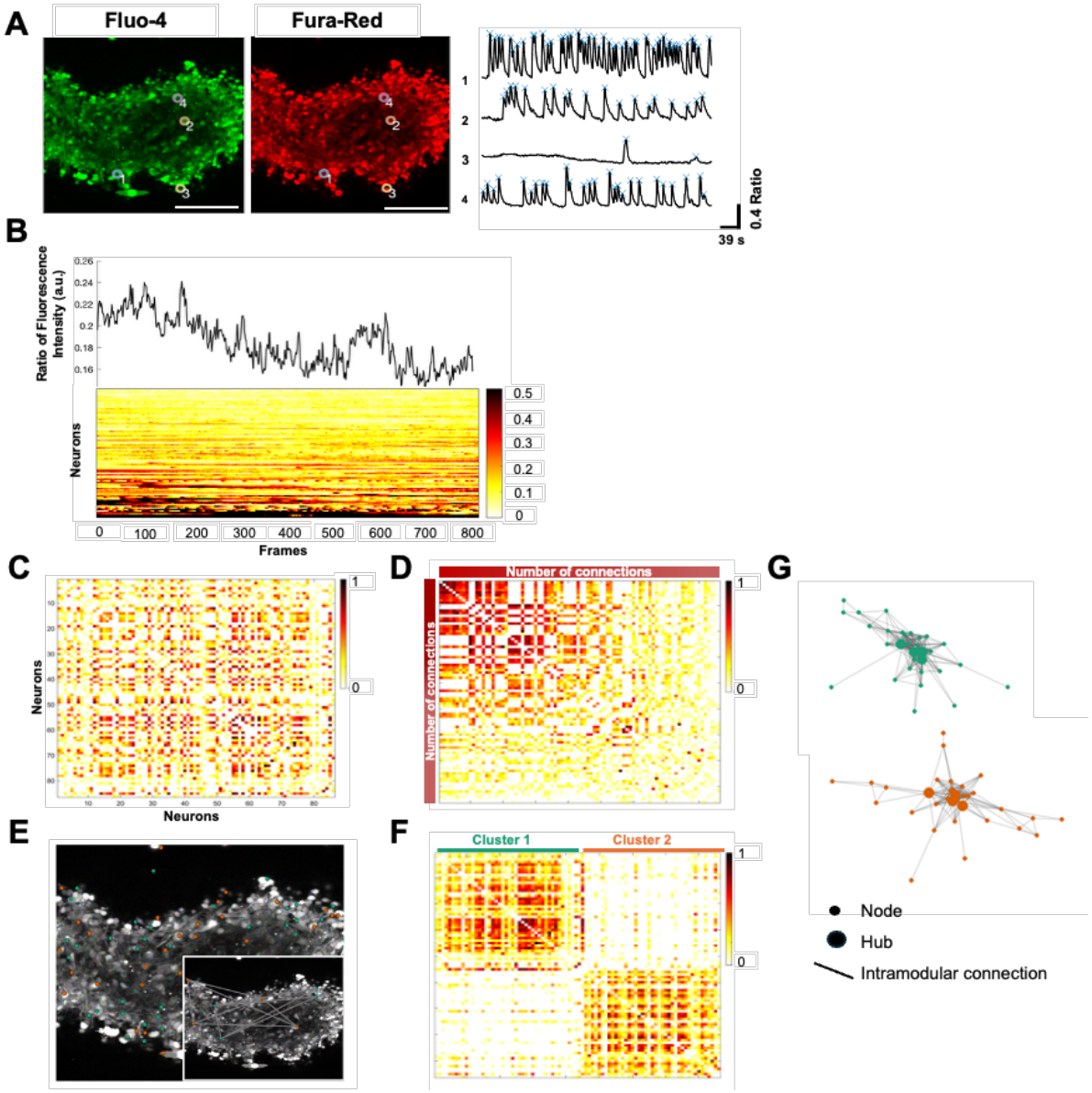

Figure 3.5 Functional neuronal network of 3D ENPC constructs reveals high modularity with low intermodular connections
(A) A snapshot from Fluo-4 and Fura-Red fluorescence channels overlaid with four neurons. The corresponding single-neuron pseudo-ratiometric traces are shown to the right, with asterisks indicating the detected spikes.
(B) Heatmap of calcium imaging activity, with every row representing a single neuron. The top trace shows the mean of pseudo-ratiometric traces across active neurons.
(C) Pairwise correlation matrix of calcium traces of 90 active neurons. Each entry represents the Pearson correlation coefficient (r-value) between pairs of neurons. Two neurons are considered functionally connected when the correlation coefficient (r-value) > 0.35.
(D) The same correlation matrix as in (C), reordered based on the density of their functional connections.
(E) Spatial distribution of colour-coded neurons belonging to two modules. The inset shows the hub neurons, defined as those with intra-module connections exceeding the 90th percentile. The cross-module hub connections are represented by grey lines.
(F) Clustered correlation matrix; Louvain algorithm revealed the presence of two modules. The correlation matrix is reordered to group neurons belonging to the same module. The low density of cross-module correlations indicates weak inter-module connectivity.
(G) Topological representation of intra-module connectivity visualised using the Fruchterman–Reingold algorithm. Edge length is inversely proportional to the correlation coefficient, such that shorter lines indicate stronger correlations between neuron pairs. The size reflects hub status within each module, with centrally positioned hub neurons showing close topological proximity, consistent with their role as intramodular hubs.

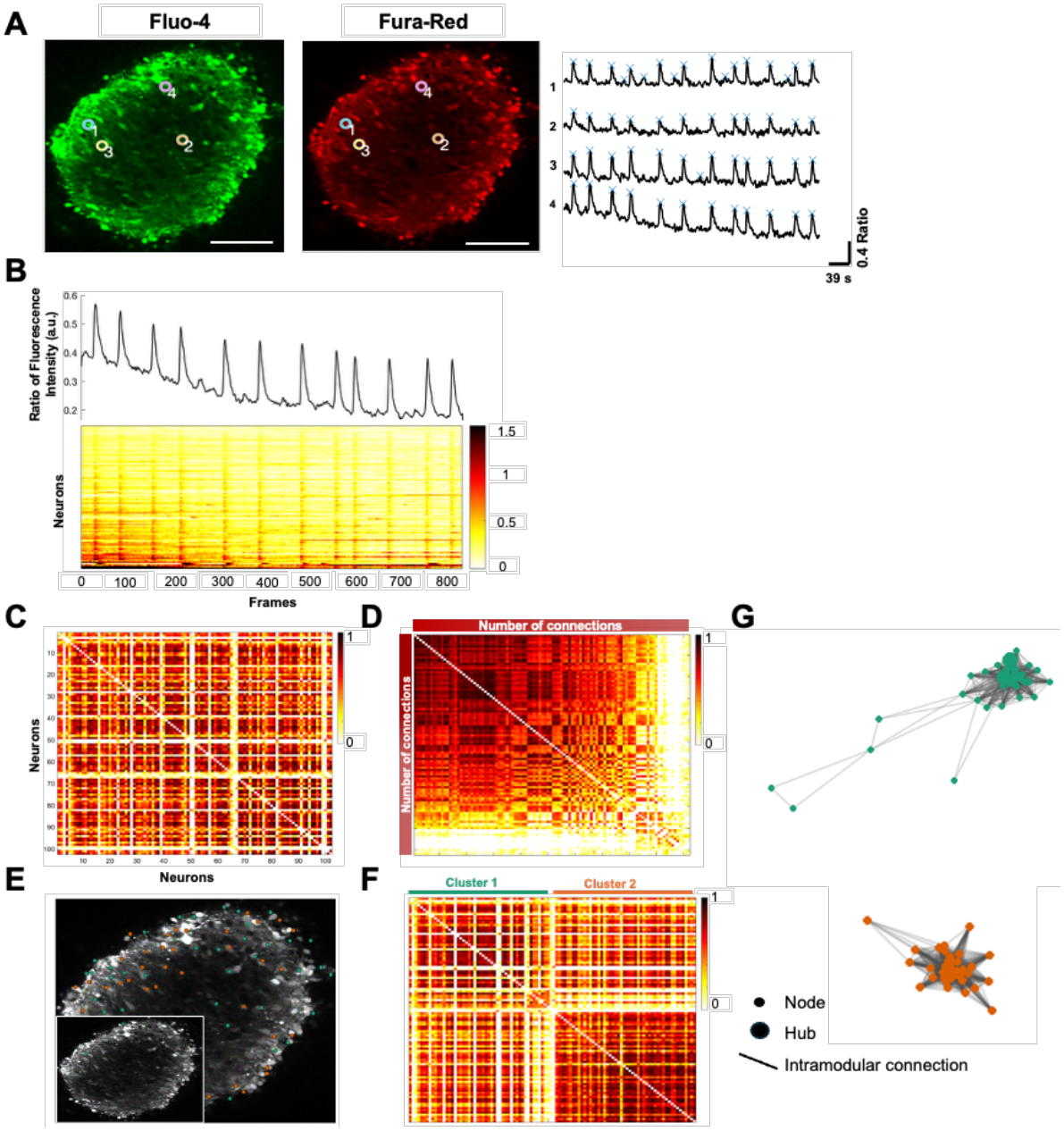

Figure 3.6 Functional neuronal network of 3D LNPC constructs shows high intermodular and intramodular connectivity

(A) Representative Fluo-4 and Fura-Red fluorescence images overlaid with four highlighted neurons. Corresponding single-neuron pseudo-ratiometric traces are shown to the right, with asterisks marking detected spikes.

(B) Heatmap of calcium activity, with each row representing a single neuron; the top trace shows the mean of pseudo-ratiometric traces across active neurons.

(C) Pairwise correlation matrix of calcium spikes from 100 active neurons, with functional connections defined as correlation coefficient (r-value) > 0.35.

(D)The same correlation matrix as in (C), with the neurons sorted based on the density of their functional connections.

(E) The spatial localisation of colour-coded neurons that belong to two modules. The inset shows the hub neurons, and the cross-module hub connections are represented by grey lines.

(F) Clustered correlation matrix groups neurons of the same module. The high density of cross-module correlation indicates strong inter-module correlations and extensive hub connectivity between modules.

(G) Fruchterman–Reingold visualisation of intra-module connectivity networks. Hub neurons are represented in larger sizes and are centrally positioned.
Scale bar: 100 µm.

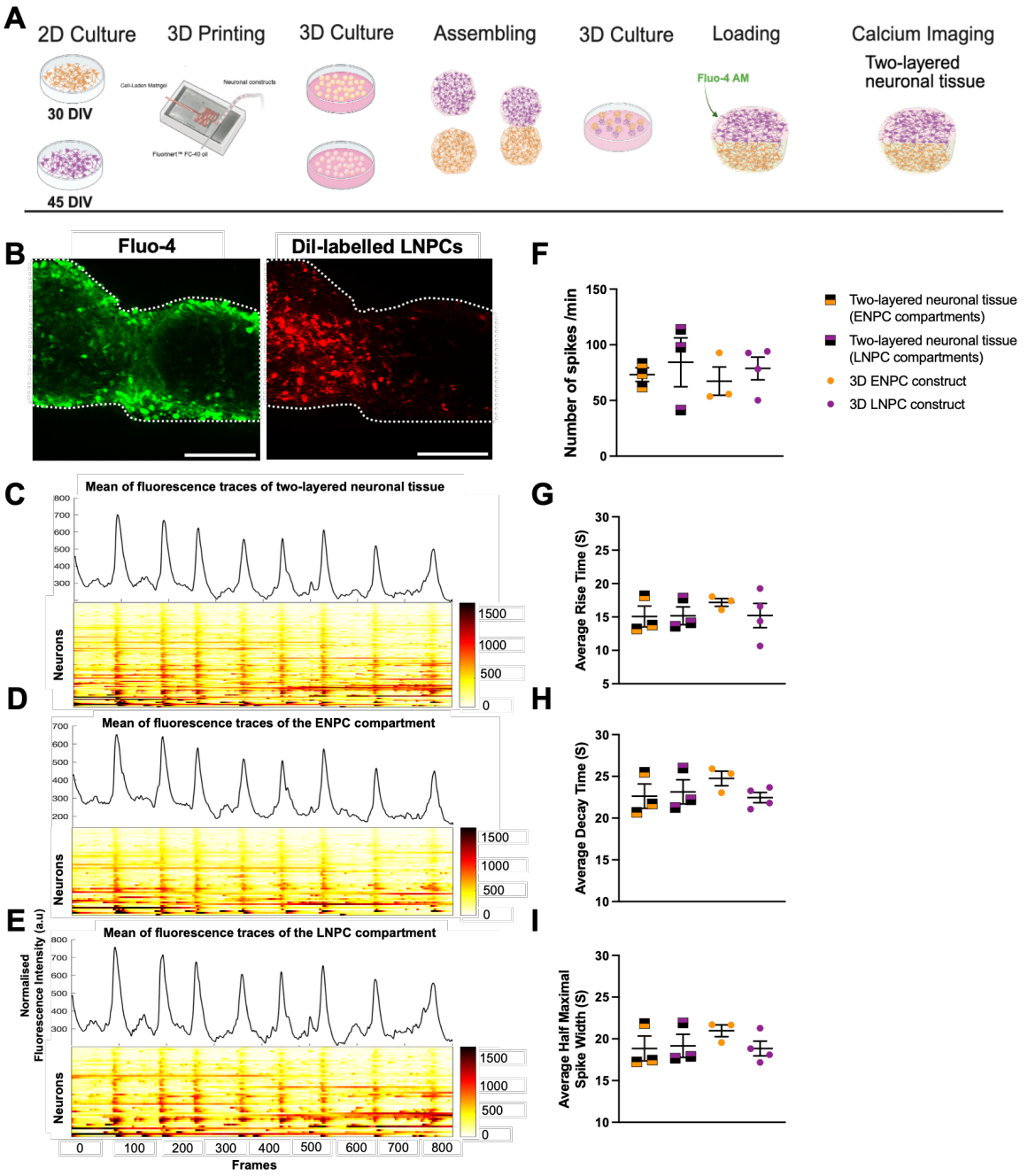

Figure 3.7 Two-layered neuronal tissue exhibits spontaneous calcium activity with highly correlated activity across the compartments
(A) Schematic illustration showing the methodology and experimental timeline. ENPCs and LNPCs were bioprinted at DIV 30 and 45, respectively. The constructs were assembled and cultured *in vitro* for three weeks before being loaded with Fluo-4 AM for calcium imaging.
(B) Confocal images of two-layered neuronal tissue showing distinct ENPC and LNPC compartments loaded with Fluo-4 and LNPCs labelled with DiI. White dashed outlines indicate the boundary of the two-layered neuronal tissue.

(C) Mean fluorescence trace of active neurons of the two-layered neuronal tissue and the corresponding heatmap reveal spontaneous calcium spikes with synchronous bursting, with every row representing a single neuron.
(D–E) Mean traces and corresponding heatmaps of active neurons in the ENPC compartment (D) and the LNPC compartment (E).
(F–I) Quantification of calcium spike matrices in LNPC and ENPC compartments within two-layered neuronal tissues compared with their respective single 3D LNPC and ENPC constructs; (F) spike frequency, (G) rise time (s), (H) decay time (s), and (I) half maximal spike width (s).
Scale bar: 100 µm. Results are means ± SEM; each dot represents one independent biological replicate. Only significant results are presented with an asterisk.

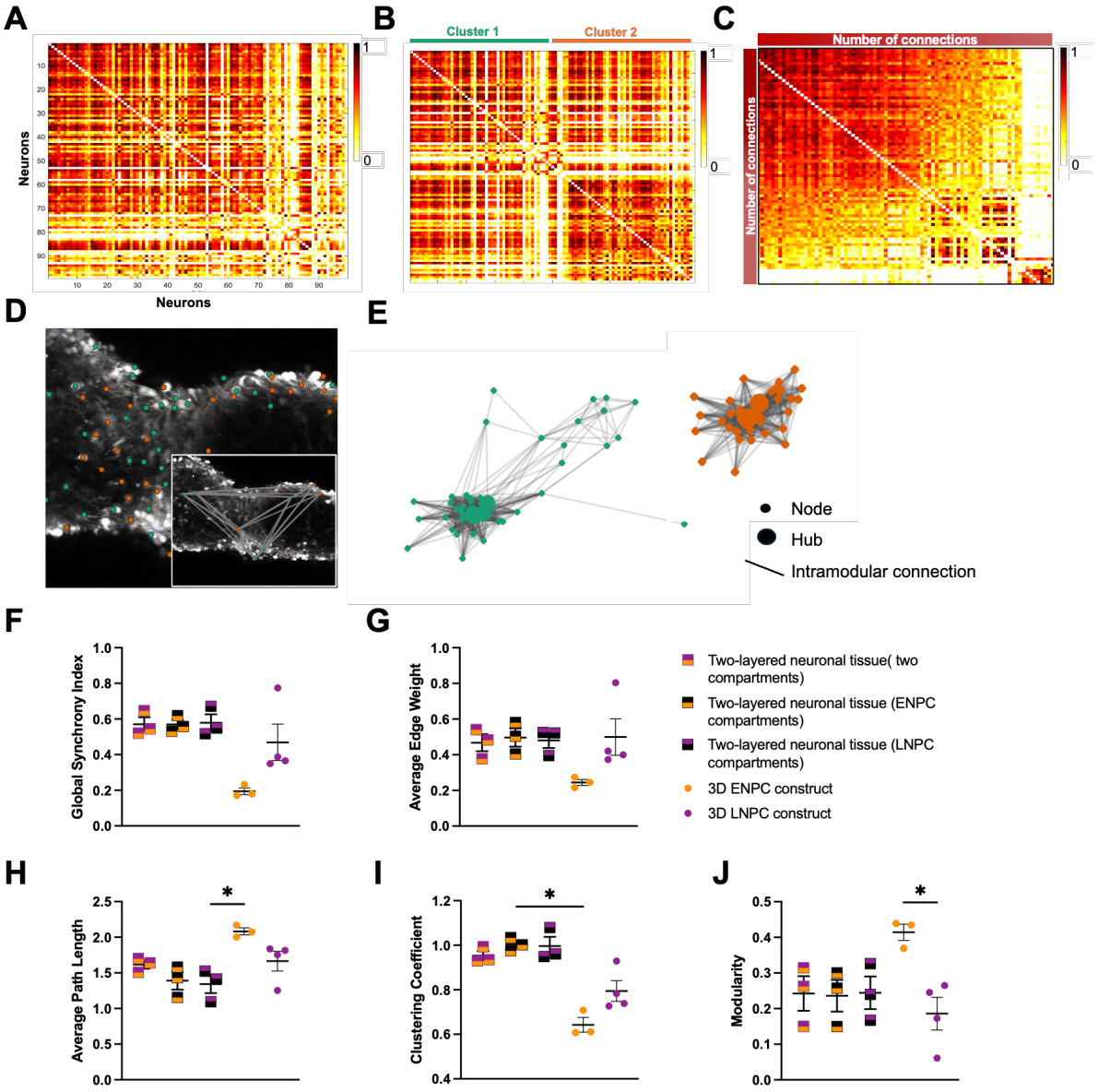

Figure 3.8 Functional connectivity mapping of two-layered neuronal tissue shows recruitment of both compartments in modules with hubs located in both compartments
(A) Pairwise correlation matrix of calcium traces from active neurons in both compartments. Neurons are considered functionally connected when the correlation coefficient (r-value) > 0.35.
(B) Clustered correlation matrix reordered to group neurons within the same module, revealing strong intra- and inter-modular correlations.

(C)The same correlation matrix as in B, but with the neurons sorted based on the density of their functional connections.
(D) The spatial localisation of colour-coded neurons that belong to two modules. The inset shows the hub neurons, and the cross-module hub connections are represented by grey lines.
(E) Topological representation of the intra-module functional connectivity networks. Each module network is visualised using the Fruchterman–Reingold algorithm, where the length of the lines connecting the neurons is inversely proportional to the r-value.
(F-J) Quantification of graph theory matrices for two-layered neuronal tissue, the ENPC compartment, and the LNPC compartment, compared with their counterpart single 3D constructs. Parameters include: (F) global synchrony index, (G) average edge weight, (H) average path length, (I) clustering coefficient, and (J) modularity. Only significant results are presented with an asterisk. Graphs show means ± SEM; each point represents a biological replicate.

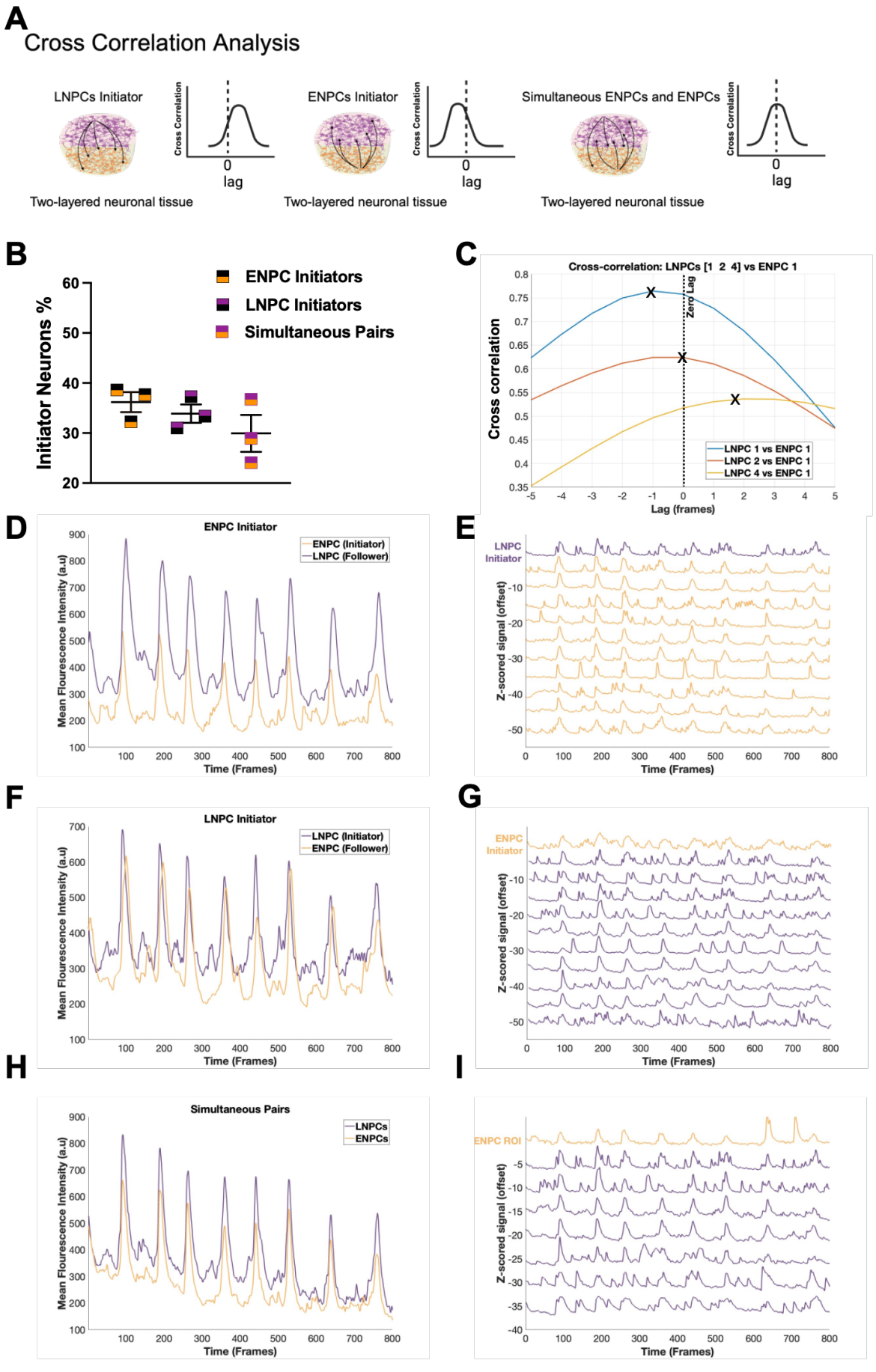
A
Cross Correlation Analysis
LNPCs Initiator
Cross Correlation
0
lag
Two-layered neuronal tissue
ENPCs Initiator
Cross Correlation
0
lag
Two-layered neuronal tissue
Simultaneous ENPCs and ENPCs
Cross Correlation
0
lag
Two-layered neuronal tissue
B
Initiator Neurons %
ENPC Initiators
LNPC Initiators
Simultaneous Pairs
C
Cross-correlation: LNPCs [1 2 4] vs ENPC 1
Cross correlation
Zero Lag
LNPC 1 vs ENPC 1
LNPC 2 vs ENPC 1
LNPC 4 vs ENPC 1
Lag (frames)
D
ENPC Initiator
ENPC (Initiator)
LNPC (Follower)
Mean Flourescence Intensity (a.u)
Time (Frames)
E
LNPC Initiator
Z-scored signal (offset)
Time (Frames)
F
LNPC Initiator
LNPC (Initiator)
ENPC (Follower)
Mean Flourescence Intensity (a.u)
Time (Frames)
G
ENPC Initiator
Z-scored signal (offset)
Time (Frames)
H
Simultaneous Pairs
LNPCs
ENPCs
Mean Flourescence Intensity (a.u)
Time (Frames)
I
ENPC ROI
Z-scored signal (offset)
Time (Frames)

Figure 3.9 Cross-correlation reveals inter-laminar coordinated activity in the two-layered neuronal tissues
(A) Diagram illustrating the cross-correlation workflow across two-layered neuronal tissues. Cross-correlation was computed for LNPC-ENPC pairs, and the lag at the peak correlation was used to classify pairs as LNPC-initiators (positive lag), ENPC-initiators (negative lag), and simultaneous pairs (lag = 0).
(B) Proportion of functional groups; ENPC-initiators, LNPC-initiators, and simultaneous pairs across cross-correlated pairs.
(C) Representative cross-correlogram from three pairs of neurons. The normalised correlation coefficient is plotted as a function of lag (± 5 frames). Black crosses mark the peak cross correlation and corresponding lag. Example pairs include: ENPC (2) leading LNPC (1) by one frame (blue), simultaneous activity of LNPC (2) and ENPC (1) (red), and LNPC (1) leading ENPC (4) by two frames (yellow).
(D-F-H) Mean fluorescence traces of leader–follower pairs:
(D) Mean fluorescence traces of the ENPC-initiators with the corresponding LNPC followers, showing a consistent delay in ENPC response, (F) Mean fluorescence traces of LNPC-initiators and their ENPC followers, exhibiting reversed timing profiles, and (H) Mean fluorescence traces of simultaneous pairs of ENPC and LNPC.
(E-G-I) Aligned individual Z-scored calcium traces from representative neurons, (E) Multiple ENPC followers aligned to a single LNPC-initiator, (G) Traces from multiple LNPC followers aligned to an ENPC-initiator, and (I) Traces from simultaneous pairs.
Neurons of LNPC and ENPC compartments are colour-coded for visual clarity.

3.4 Discussion

This chapter demonstrated that the droplet-based microfluidic platform could reproducibly generate 3D ENPC and LNPC constructs that maintained high viability, matured into distinct cortical subtypes, and displayed functional calcium dynamics reflective of their developmental stage. When assembled into two-layered neuronal tissue, these constructs preserved lamination and developed inter-laminar anatomical and functional interconnections. While earlier research has created two-layered human neuronal tissue and detected spontaneous calcium activity (Jin et al., 2023), this study was the first to integrate laminar-specific calcium imaging with graph theory and cross-correlation analyses to reveal network connectivity and map temporal coordination between compartments.

3.4.1 Reproducible generation of 3D neuronal constructs

The droplet-based microfluidic platform enabled reproducible and precise control of construct geometry, facilitating rapid fabrication of constructs without the need for extensive post-processing. Compared to conventional bioprinting techniques, the platform was expected to operate under lower shear stress, which has been associated with improved preservation of cell integrity and long-term viability (Bishop et al., 2017). Fluorinert™ FC-40 oil was selected as carrier oil due to its lower cytotoxicity and ability to maintain stable droplets (Budharaju et al., 2024). Matrigel was used as a bioink because of its compatibility with neural cultures and its support for neuronal survival and functional maturation (Yan et al., 2024, Zhou et al., 2020, Jin et al., 2023, Joung et al., 2018). However, its xenogeneic nature and batch variability limit its clinical application (Kleinman and Martin, 2005). Recent studies have highlighted the promise of decellularised ECM-based hydrogels as alternative bioinks for hiPSC-derived neural constructs (Sood et al., 2019, Zamponi et al., 2023, Sood et al., 2016).

Following fabrication of the constructs, they demonstrated high viability and proliferation with low levels of apoptosis, consistent with previous findings after bioprinting of hiPSC-derived neural progenitors (Salaris et al., 2019, Joung et al., 2018, Abelseth et al., 2019).

The constructs, measuring approximately 600–800 μm in height, were designed to match the thickness of the mouse neocortex around P7, which is the time window for implantation. At this stage, the neocortex is laminated, and the motor cortex has already received

thalamocortical input, providing a structurally organised host environment (Vitalis et al., 2018, Fenlon et al., 2015).

3.4.2 Laminar identity and functional maturation of 3D neuronal constructs

The constructs retained laminar-specific cortical identity, with ENPC constructs enriched in CTIP2+ deep-layer PNs and LNPC constructs expressing SATB2, a marker of upper-layer neurons. These expression profiles align with prior studies on *in vitro* corticogenesis using hiPSCs (Jin et al., 2023, Pasca et al., 2015, Kadoshima et al., 2013). Both constructs contained GABA+ INs, which are essential components for establishing excitatory–inhibitory balance in cortical networks (Warm et al., 2021). Evidence of synaptogenesis was provided by co-localisation of SYN1 and PSD-95, indicating the capacity to form functional synapses.

Calcium imaging and graph theory analysis revealed distinct patterns of activity in 3D ENPC and LNPC constructs. 3D ENPC constructs exhibited less synchronous activity, while 3D LNPC constructs displayed frequent, highly coordinated spikes, consistent with the transition from early asynchronous activity to synchronised network bursts during *in vivo* corticogenesis (Luhmann et al., 2016, Wu et al., 2024). The activity pattern in 3D LNPC constructs was consistent with observations in *ex vivo* cortical slices (Corlew et al., 2004, Garaschuk et al., 2000, Allene et al., 2008), primary cell cultures (Opitz et al., 2002, Voigt et al., 2001), and hiPSC-derived cortical neurons (Kirwan et al., 2015).

Oscillatory network activity in developing circuits can be driven by distinct mechanisms, including glutamatergic synaptic transmission, GABAergic signalling, or gap junction–mediated electrical coupling (Blankenship and Feller, 2010). Garaschuk et al., demonstrated that spontaneous calcium waves necessitate glutamatergic receptor activation, and their postnatal cessation coincides with the developmental shift of GABAergic signalling from depolarising to hyperpolarising (Garaschuk et al., 2000). Two-photon calcium imaging further revealed the role of depolarising GABAergic transmission in eliciting synchronous network activity; as the depolarising action of GABA-A decreased, the network activity in lateral cortex cultures transitioned from stereotypical bursting to more clustered and asynchronous activity patterns (Baltz et al., 2010, Opitz et al., 2002). Additionally, electrical coupling via dendrodendritic gap junction contributes to network synchrony rather than excitatory synaptic transmission, suggesting a glutamate-independent mechanism of synchronisation (Peinado, 2001).

The scarcity of human tissue at these developmental stages and the limited viability of acute brain slices over extended culture periods make hiPSC-derived cortical neurons a valuable alternative model for studying the neuronal network. It has been shown that hiPSC-derived cortical neurons can recapitulate the temporal transitions in activity patterns that are driven by AMPA and NMDA receptor-mediated glutamatergic signalling (Kirwan et al., 2015). Furthermore, GABAergic modulation of glutamatergic neurons has been shown to contribute to synchronous bursting in hiPSC-derived networks (Sakaguchi et al., 2019).

3.4.3 Calcium dynamics and connectivity patterns

Graph-theory analysis highlighted the role of temporal maturation in shaping the functional properties of networks. While both 3D ENPC and LNPC constructs demonstrated spontaneous calcium activity, the 3D LNPC constructs exhibited a more efficient network topology compared to 3D ENPC constructs. They exhibited increased edge weight, indicating stronger functional correlation, and a reduced average path length for information to travel across the network. Moreover, they had a higher clustering coefficient, making the network more resilient even if some connections are lost. Such topology is known to promote efficient information transfer and robustness to node loss, features commonly found in biological, small-world neural networks (Bullmore and Sporns, 2009). Conversely, 3D ENPC constructs exhibited higher modularity, indicating greater segregation and fragmentation into subnetworks, with limited global integration. This higher modularity suggested an immature stage, where circuits are still forming local subnetworks rather than participating in globally integrated communication (Nelson and Bonner, 2021).

3.4.4 Inter-laminar structural and functional connectivity across two-layered neuronal tissues

Structural integration was evident with inter-laminar neurite outgrowth and neuronal migration, along with the maintenance of anatomical lamination and spatial marker expression for weeks *in vitro*, consistent with earlier research on 3D bioprinted cortical tissue (Jin et al., 2023). Functionally, the two-layered neuronal tissue displayed widespread synchronous activity spanning both compartments, with subsets of neurons acting as pacemaker-like initiators that propagated activity to neighbouring cells in the opposite compartment. Similar pacemaker properties have been identified in neonatal mouse cortical slice cultures, where synchronised spontaneous activity originates at either of two homologous pacemakers in the temporal region and propagates rapidly across the cortex (Lischalk et al., 2009).

Temporal cross-correlation was applied to examine inter-laminar coordination (Narayanan and Laubach, 2009, Adhikari et al., 2010). This analysis revealed that activity in one compartment was frequently associated with temporally shifted activity in the other, consistent with inter-laminar reciprocal interactions. While cross-correlation cannot establish anatomical connectivity or causal directionality, the presence of both LNPC-leading and ENPC-leading events suggests that activity can propagate in either direction across the compartments. Such reciprocal dynamics are consistent with feedforward and feedback signalling between laminae within the cortical column of the cerebral cortex (Douglas and Martin, 2004).

From a developmental perspective, deep-layer neurons emerge and mature earlier, establishing local circuits which later incorporate upper-layer neurons (Lodato et al., 2015). In vivo, transient developmental circuits originate in subplate neurons and travel upward into the immature cortical layers, a phenomenon unique to early developmental stages when such transient layers are present (Luhmann et al., 2016). The slight predominance of ENPC-initiated events *in vitro* is consistent with this developmental sequence, while the presence of LNPC-initiated events may suggest early reciprocal loop formation.

Taken together, these findings confirm that the bioprinted 3D constructs not only supported the survival and maturation of neurons but also facilitated the emergence of functional activity patterns that resemble *in vivo* developmental trajectories. The ability to build layered cortical tissues in a controlled and reproducible manner offered new opportunities to study the inter-laminar circuitry and early cortical circuit assembly. In regenerative contexts, pre-patterned constructs with preserved laminar identity may integrate effectively after implantation into TBI with a cortical lesion, an approach explored further in Chapter 4.

3.4.5 Limitations and future directions

This study has certain limitations that also inform future directions. Manual assembly of 3D constructs is labour-intensive. Future platforms should incorporate automated, multi-laminar tissue fabrication to improve reproducibility and scalability. Furthermore, while Matrigel is experimentally beneficial as a bioink, its xenogeneic origin raises concerns for clinical translation, including the potential for antigenicity and a risk of contamination. Previous reports have identified viral contamination, particularly with lactate dehydrogenase-elevating virus (LDHV), in animal-derived ECM products such as Matrigel (Liu et al., 2011, Peterson, 2008). Furthermore, inconsistencies between batches or even within the same batch in biochemical

(Vukicevic et al., 1992, Hughes et al., 2010) and mechanical properties limit its reproducibility (Reed et al., 2009). Therefore, future efforts should focus on replacing Matrigel with clinically compliant ECM analogues that are biocompatible and have mechanical and biochemical properties that match those of the brain ECM (Cadena et al., 2021, Sensharma et al., 2017).

Although calcium imaging provided valuable insights into spontaneous activity dynamics and different connectivity patterns, it lacks temporal resolution to capture fast-spiking events or synaptic currents. Incorporating patch-clamp recordings would enable direct assessment of action potentials and circuit excitability at higher temporal resolution.

Furthermore, the constructs were primarily composed of excitatory cortical PNs and GABAergic INs, with limited representation of astrocytes, and lacked both microglia and oligodendrocytes. Supplying the constructs with different cell types, such as astrocytes, microglia, and oligodendrocytes, would enhance physiological relevance and tissue integration for translational applications.

3.5 Conclusion

Through this chapter, I optimised the use of a droplet-based microfluidic platform for generating physiologically relevant 3D neuronal constructs. The droplet-based microfluidic technique enabled the reproducible generation of 3D constructs with high post-printing viability, preserved neurogenic potential, and functional maturation. Both 3D ENPC and LNPC constructs retained laminar-specific molecular profiles, generated GABAergic INs, and established synaptic networks. When assembled into two-layered neuronal tissues, lamination was maintained with underlying inter-laminar structural integration. Calcium imaging revealed spontaneous activity related to the temporal identity of the 3D constructs. ENPC constructs displayed lower synchrony activity, while LNPC constructs exhibited highly coordinated oscillatory activity. In the two-layered neuronal tissue, cross-correlation analysis revealed temporal coordination between the two layers, consistent with reciprocal interactions, but it did not confirm bidirectional connectivity. Collectively, these findings established a method for generating physiologically relevant, laminar-specific human cortical constructs *in vitro*, thereby recapitulating aspects of both developmental and mature cortical dynamics. From a translational perspective, the next chapter will investigate the *in vivo* integration of 3D neuronal constructs derived from ENPCs and LNPCs following implantation into TBI with a cortical lesion.

Chapter :4 Implantation of 3D Constructs into TBI Model

4.1 Introduction

TBI is a critical clinical condition that affects millions worldwide each year, standing as the leading cause of mortality and morbidity among young people (Maas et al., 2022). Despite advances in pharmacological and surgical interventions, current treatment modalities cannot achieve complete restoration of injured brain function (Pearn et al., 2017).

This limitation has driven growing interest in stem cell-based therapies as a potential avenue for brain repair. Stem cells possess anti-inflammatory, anti-apoptotic, pro-angiogenic, and neurotrophic properties, making them promising candidates for TBI treatment at various stages of pathophysiology (Song et al., 2018).

Cell-based therapy of TBI aims to restore damaged neural tissues and modulate the post-injury microenvironment (Chrostek et al., 2019). Various sources of stem cells have been explored, including ESCs, iPSCs, and PSCs from fetal and adult brain tissue, to target different regions of the brain and address various types of damage (Schantz et al., 2025b). Grafted cells have demonstrated the ability to integrate into the host brain circuitry and improve functional outcomes, including enhanced motor function and cognitive abilities (Somaa et al., 2017, Yu et al., 2019, Andreoli et al., 2020, Xiong et al., 2021). The integration of grafts and the successful restoration of function were influenced by the identity and maturation stage of the transplanted neurons. Studies have consistently shown that neurons with region-specific identities, particularly those matching the host cortical area, exhibit superior integration and contribute more effectively to circuit reconstruction (Michelsen et al., 2015, Linaro et al., 2019, Espuny-Camacho et al., 2013, Terrigno et al., 2018).

While most preclinical work has involved xenotransplantation into rodent models, a recent allograft study demonstrated that hiPSC-derived cortical progenitors transplanted into adult human cortical tissue can survive and differentiate into mature cortical neurons exhibiting electrophysiological and ultrastructural properties characteristic of functional human neurons, further supporting the potential of translational therapy (Grønning Hansen et al., 2020).

To further improve graft survival, maturation, and circuit reconstruction, 3D neural tissues have emerged as an alternative to dissociated cell injections. Organoid implantation offers several

advantages. They are considered a niche of diverse cell types that can restore lost cells after TBI. The organoid microenvironment provides effective support for the implanted cells, making them less susceptible to inflammation-induced cell death compared to traditional cell suspension injection (Daviaud et al., 2018).

Multiple preclinical studies have demonstrated the capacity of human brain organoids to integrate structurally and functionally into host brains following TBI (Shen and Kokaia, 2025). Wang et al., showed that when hESC-derived cerebral organoids were implanted into an acute cortical lesion, the cells migrated along white-matter tracts, colonising distant brain regions, including the thalamus, hippocampus, and contralateral cortex (Wang et al., 2020b). Similarly, Bao et al., implanted hESC-derived cortical organoids into the sensorimotor cortex 7 days after CCI. The neurons not only differentiated into various neuronal subtypes but also extended long projections into the ipsilateral and contralateral hemispheres (Bao et al., 2021). To explore circuit-specific integration, Jgamadze et al., implanted forebrain organoids into the visual cortex of rats and reported extensive, bidirectional, reciprocal connections (Jgamadze et al., 2023). The reported structural integrations with organoid implantation were associated with improvements in functional outcomes, including motor coordination (Wang et al., 2020b) and cognitive abilities (Bao et al., 2021, Kim et al., 2022). A major challenge in successful brain tissue engrafts is establishing vascularisation within the graft that connects to the host's vasculature, which is essential for the graft's survival and maturation (Huang et al., 2022). Strikingly, transplanted organoids have been shown to integrate with the host vasculature across various studies (Daviaud et al., 2018, Wang et al., 2020b, Jgamadze et al., 2023, Bao et al., 2021).

While cerebral organoids offer promising avenues for brain repair, several limitations currently restrict their therapeutic application. Their structural and functional maturation is limited by *in vitro* culture conditions, which impair their ability to integrate effectively with host brain following implantation. The absence of a functional microvasculature restricts the delivery of nutrients and oxygen, thereby limiting their survival. Furthermore, they lack the immune cells, which are critical for tissue repair following TBI. Their cellular heterogeneity can lead to off-target projections, thereby reducing the specificity in circuit reconstruction. Finally, variability in organoid differentiation can lead to inconsistencies across batches, which complicates the standardisation and comparisons between studies (Andrews and Kriegstein, 2022).

To address these challenges, this study established a robust microfluidic system to generate physiologically relevant, 3D neuronal constructs. The droplet-based microfluidic platform enabled the reproducible generation of 3D constructs using pre-differentiated hiPSC-derived ENPCs and LNPCs, with high post-printing viability. The fabrication process enabled precise control over construct dimensions and cell density, ensuring the uniform diffusion of nutrients and oxygen throughout the tissue. When ENPC and LNPC constructs were assembled into two-layered neuronal tissues, lamination was maintained with underlying inter-laminar structural and functional integration.

I hypothesised that, following TBI, implantation of 3D neuronal constructs derived from temporally specified ENPCs and LNPCs would enhance implant survival and enable identity-dependent integration with the host cortex. Furthermore, the implantation of two-layered neuronal tissue that mimics cortical lamination could facilitate the reconstruction of cortical columnar circuits by promoting both local and long-range connectivity.

The chapter focused on evaluating the structural integration of implants with the host brain and the reconstruction of cortical architecture. The primary objective was to investigate how laminar identity influences projection patterns, synaptic connectivity, and glial responses in vivo. It also evaluated whether spatially patterned two-layered neuronal tissues could survive and integrate when implanted into an aspiration-induced TBI model in P7–P8 NOD-SCID mice.

To achieve this, 3D RFP+ NPC constructs were implanted, and brains were collected and analysed at 2 WPI and 2 MPI. Key endpoints included the evaluation of cell survival (Ki-67, Cleaved Caspase-3), neuronal differentiation (CTIP2, SATB2), vascularisation (CD31), and glial responses (Iba1, GFAP), alongside Neurolucida reconstructions of axonal projections. To investigate how laminar identity influences projection patterns, 3D ENPC and LNPC constructs were implanted, and brain tissues were collected at 2 MPI. The structural integration of layer-specific 3D ENPC and LNPC constructs was then compared. This involved mapping axonal projections using Neurolucida and immunostaining for human-specific Synaptophysin (hSYP) and the postsynaptic PSD-95. Finally, the potential of anatomical integration of two-layered neuronal tissues into the host brains was investigated through reconstruction of compartment-specific projections using Neurolucida.

4.2 Methods

4.2.1 3D neuronal constructs used for implantation

3D neuronal constructs were generated as described in Chapter 3. The viability was assessed using a live-dead assay to ensure batch quality before proceeding with implantation. The constructs used for implantation were cultured for a week after fabrication before being implanted. All the constructs used for implantation were 600 μm-wide, including 3D RFP+ NPC constructs, 3D ENPC and LNPC constructs. Additionally, the two-layered neuronal tissues used for implantation were assembled using RFP+ LNPC constructs and unlabelled 3D ENPC constructs, both were 600 μm-wide.

4.2.2 Implantation of 3D neuronal constructs

4.2.2.1 Experimental animals

Strain details were described in section 2.2.4.3.

4.2.2.2 Implantation of 3D neuronal constructs following TBI

Postnatal mice were anaesthetised in an induction chamber using 3% isoflurane in oxygen for 3 min, then transferred to an anaesthesia maintenance mask supported with 2% isoflurane. The body temperature of the mice was maintained with a heating pad, and the depth of anaesthesia was assessed by pedal withdrawal reflex before starting the procedure. The surgical site was disinfected, and a midline skin incision was made to expose the skull. The right motor cortex was identified, and a 3-sided cranial window of approximately 1 × 1 mm was created using a fine scissor (Fine Science Tools).

A focal cortical lesion of approximately 1 mm^3 was created in the motor cortex by gentle aspiration using a fine glass pipette connected to a vacuum line. The glass pipette had been flame-pulled to achieve a narrow, smooth tip, allowing precise removal of cortical tissue to a depth of approximately 1 mm, reaching just above the corpus callosum. Immediately after lesioning, a single 3D construct of either 3D RFP+ NPC construct, 3D LNPC construct or 3D ENPC construct was placed into the lesion cavity using a pipette tip. The two-layered neuronal tissues, composed of RFP+ LNPC constructs and unlabelled ENPC constructs, were implanted following the same steps. To identify the spatial orientation of the two-layered neuronal tissue, fluorescent images of the two-layered neuronal tissues were taken and used as a reference to identify the shape and orientation of the two-layered neuronal tissues during implantation. The

bone flap was repositioned and sealed with tissue adhesive, followed by skin closure using the same tissue adhesive. In the TBI group, the procedure was identical, except that no construct was implanted. Post-operatively, animals received a single subcutaneous injection of meloxicam (1 mg/kg) for systemic pain control. The pups were placed in a heated recovery chamber until they were fully awake, and then they were returned to the dam. On the day of surgery, animals were monitored 2 h post-operatively and subsequently monitored daily for one week. Animals implanted with RFP+ NPC constructs were survived for 2 WPI and 2 MPI for histological analysis. Animals implanted with 3D ENPC constructs or 3D LNPC constructs were maintained for 2 MPI for electrophysiological recording and histological examination. Finally, animals implanted with two-layered neuronal tissues were evaluated at 2 MPI for histological studies.

4.2.3 Brain collection and tissue processing for immunohistochemistry on free-floating brain sections

Procedures were performed as described in Section 2.2.4.3.

4.2.4 Confocal microscopy imaging and quantitative analysis

Immunohistochemical analyses were performed on coronal sections of brains implanted with RFP+ NPC constructs collected at 2 WPI and 2 MPI, and on the coronal sections of brains implanted with 3D ENPC and LNPC constructs, and two-layered neuronal tissue collected at 2 MPI.

The glial reaction was evaluated using Iba1 immunoreactivity to identify microglia and infiltrating macrophages, and GFAP to label reactive astrocytes. Each group included at least three animals, with 2–3 coronal sections analysed per animal. From each section, four confocal images were acquired as Z-stacks of ten optical planes at 1.88 µm intervals using a 40X oil-immersion objective. Each image included a transitional zone showing both the implant region and the surrounding host cortex, with two regions imaged on each side of the implant (Fig. 4.7D). Z-stacks were flattened using ImageJ software, and quantification was performed using QuPath software (version 0.6.0). Iba1+ cells were manually counted in the peri-implant HuNu-negative region and normalised to the analysed area. GFAP reactivity was calculated as the percentage of GFAP-positive area relative to the total HuNu-negative area surrounding the implant.

Neuronal differentiation and maturation were assessed by immunohistochemistry for CTIP2 and SATB2. Each experimental group included at least three animals. From each brain, 2–3 coronal sections were used for analysis. For each section, three to five fields of view within the implants were acquired, using a 63X oil-immersion objective, as a Z-stack with a 1.88 µm interval. Manual cell counting was performed using the Cell Counter plugin in ImageJ software, and the percentage of HuNu+ cells co-expressing CTIP2 or SATB2 was calculated per image.

Proliferation and apoptosis potential within the implants were assessed by immunostaining for Ki-67 and Cleaved Caspase-3, respectively. The same sampling strategy was applied, with a minimum of three images per section acquired using a 63X oil-immersion objective. The percentage of Ki-67+ or Cleaved Caspase-3+ cells was calculated as the number of marker-positive nuclei divided by the total number of DAPI+ nuclei per image.

To quantify CD31+ vascularisation within the implants, Z-stack images were processed in ImageJ. The CD31 signal was enhanced by subtracting a blurred background (Gaussian Blur, radius = 10) from a lightly smoothed version of the original image (radius = 2). The resulting image was further smoothed (radius = 5) and thresholded using the Moments algorithm to segment vascular structures. The vascularised area was measured and expressed as a percentage of the total construct area in the same section.

For all histological quantifications of glial reaction, neuronal differentiation, proliferation, apoptosis, and CD31+ vascularisation data were pooled per animal and expressed as means ± SEM across the group.

Synaptogenesis following the implantation of 3D ENPC and LNPC constructs was evaluated using immunohistochemistry for human-specific Synaptophysin (hSYP) and PSD-95 to identify pre- and postsynaptic puncta, respectively. Confocal images were acquired using a 63X oil-immersion objective and a 1X digital zoom, with Z-stacks at 1 µm intervals. Image processing was performed using ImageJ software.

4.2.5 Neurolucida reconstruction of axonal projection and semi-quantitative analysis of projection density

Procedures were performed as described in Section 2.2.4.5.

Axon projections were quantified using the Neurolucida Explorer software by partitioning each section into cortical and subcortical anatomical regions, including the striatum, piriform, thalamus, hypothalamus, corpus callosum, corticospinal tract, and hippocampal formation, and recording the number of continuous traces in each region. Symmetric regions, ipsilateral and contralateral to the implant site, were quantified separately.

4.2.6 Neurolucida reconstruction and volumetric quantification of the implants

The implanted 3D RFP+ NPC, 3D LNPC, and 3D ENPC constructs were reconstructed using Neurolucida software, followed by volume quantification. Every eighth section (30 μm thick) along the rostrocaudal axis of the brain was used for analysis. Areas of HuNu+ regions were manually traced and aligned to generate a 3D model of the implant. The total volume of the implant was calculated from the aligned areas and section thicknesses, and the results were expressed in mm^3.

4.2.7 Electrophysiological recordings from acute brain slices implanted with 3D ENPC and LNPC constructs at 2 MPI

Spontaneous extracellular activity was recorded using an MEA system from acute brain slices implanted with 3D ENPC and LNPC constructs at 2 MPI to assess the functional activity of the host brain after implantation of constructs. Additional recordings were performed from slices from non-implanted TBI and age-matched uninjured control brains to provide comparative reference data. Data were collected with a Maxwell device (MaxOne, Maxwell Biosystems, Zürich, Switzerland). The MaxOne features 26,400 electrodes within a large sensing area of 3.85 × 2.10 mm^2. Simultaneous recording can be done of 1024 electrodes (Muller et al., 2015).

4.2.7.1 Slice preparation and MEA recording

Prior to the experiment, dissection instruments were prepared, and a fresh razor blade (Scientific Laboratory Supplies Limited) was installed into the vibratome (Leica VT1200S). The slice storage chamber was filled with artificial cerebrospinal fluid (ACSF); the compositions of the ACSF are illustrated in Table 6.9. All solutions used in the experiment were saturated with 95% O2 and 5% CO2.

Following decapitation, a midline incision from the foramen magnum to the front end of the skull was made, and the two skull segments were folded to the sides. The brain was quickly

and gently removed using a spatula and transferred to a petri dish filled with ice-cold N-methyl-D-glucamine (NMDG) solution, which enhances neuronal preservation (Ting et al., 2018). The compositions of the NMDG solution are illustrated in Table 6.9.

The cerebellum, posterior cortex, and olfactory bulbs were trimmed. The brain was glued using super glue (cyanoacrylate, Loctite) onto the vibratome platform with the posterior side down and then mounted in the vibratome. Then, the vibratome chamber was filled with crushed, ice-cold NMDG solution and continuously bubbled. Coronal sections of 300 µm thickness were sliced through the implanted cortical area using a high blade oscillation and slow advance speed. Typically, 3-4 slices containing implants were collected per animal. Slices were washed in cold NMDG solution, then in ACSF, before being placed in an interface storage chamber. They were incubated for 1.5 h at room temperature until recording.

The MEA system was initialised, and the MaxOne chip was superfused with ACSF at 3 mL/min to flush air bubbles from the system. Then, the brain slice was positioned directly over the sensing area of the MaxOne chip with a drop of ACSF. Once settled, the extra ACSF was removed to ensure adequate contact between the slice and the underlying electrodes. The slice grid was then placed on top of the slice to provide stability when the superfusion was restored. The superfusion was continued for 10 min as an equilibration period before the actual recording began. Spontaneous activity was recorded at a sampling rate of 20 kHz. Three recordings were obtained from each slice, each lasting 5 min, with a one-minute interval. During the recording, ACSF was supplemented with 200 µM 4-aminopyridine (4-AP, Abcam) and heated to 32°C using a feedback heating block in series with the superfusion system line.

4.2.7.2 Data analysis

Electrophysiological data were analysed using a custom MATLAB pipeline developed to assess spiking activity and oscillatory dynamics.

4.2.7.2.1 Data metrics

Raw electrophysiological data were acquired from high-density MEA recordings and stored in HDF5 format. Due to the large file size, the data were processed in two sequential chunks. Raw signals were converted from digital units to electrode voltage and corrected for the amplifier gain. These steps ensured accurate signal preprocessing for subsequent filtering and spike detection.

Two digital filters were applied to prepare the signals for further analysis: a second-order Butterworth notch filter to remove 50 Hz noise and a high-pass Butterworth filter with a passband starting at 1 Hz to eliminate slow drifts. The filtered signals were then downsampled by a factor of 20 to reduce computational load while retaining relevant frequency content, and a sampling frequency of 1 kHz was assumed throughout.

High-pass-filtered voltage traces were denoised using a median filter prior to spike detection. Spikes were identified using MATLAB's findpeaks function, applying a threshold of 5 times the median absolute deviation (MAD) of the signal. Spike timestamps were visualised using raster plots, with each row representing an electrode and each dot indicating a detected spike.

The spike frequency (spikes/s) for each electrode was calculated as the number of action potentials per second. Similarly, for each electrode, mean and maximum spike amplitudes (μV), and inter-spike intervals (ISIs) were calculated. Bursts were defined as sequences of spikes with ISIs <100 ms. For each electrode, matrices were computed and then averaged across all electrodes and across the three recordings obtained per slice. A total of 3–4 slices were analysed for each animal. Three animals per group were recorded. Averages from slices were plotted as means ± SEM.

Spectral properties of neural activity were analysed using Welch's method (pwelch function) applied to low-pass-filtered signals. The power spectral density (PSD) was computed and integrated across five canonical frequency bands: gamma (30–100 Hz), beta (12–30 Hz), delta (0.5–4 Hz), theta (4-8 Hz), and alpha (8–12 Hz). PSD was aggregated to compute per-slice averages with a total of 3-4 slices per animal.

PSD across canonical frequency bands indexes distinct aspects of network function in vivo. Gamma (30–100 Hz) supports higher-order cortical computations, including attention and working memory, whereas beta power (12–30 Hz) is associated with sensorimotor control (Medithe and Nelakuditi, 2016). Delta activity (0.5–4 Hz) is a hallmark of non-REM sleep and has been linked to sleep-dependent memory processes, serving as a marker of low-frequency, large-scale synchrony (Nir et al., 2011). Theta (4–8 Hz) is closely associated with hippocampal-dependent memory operations and navigation, and coordinates information processing via theta–gamma coupling (Kragel et al., 2020). Finally, alpha rhythms (8–12 Hz) dominate awake, eyes-closed Electroencephalography (EEG) and are implicated in attentional suppression-sensory gating and access to stored information (Foxe and Snyder, 2011).

4.2.8 Statistical analysis

Statistical analyses were performed using GraphPad Prism 10. Data were presented as means ± SEM; the number of animals (N) involved in each experiment is presented in Table 4.1. Normality was assessed using Shapiro–Wilk test. Outliers were identified using MAD method and excluded from subsequent analysis. When data were normally distributed, unpaired *t*-tests were used for two-group comparisons and a one-way ANOVA followed by Tukey's post hoc test was applied for comparisons between three or more groups. In non-normal distributions, nonparametric tests were used, including the Mann-Whitney U test for two groups or the Kruskal-Wallis test with Dunn's post hoc test for multiple groups. A p-value < 0.05 was considered statistically significant. *$p < 0.05$, **$p < 0.01$, ***$p < 0.001$, ****$p < 0.0001$.

4.2.9 Summary of animals employed across experimental groups

The experimental groups, the number of animals per group, and the experimental pipeline were summarised in Table 4.1.

Table 4.1 Summary of experimental groups, time points, and number of animals (N) in each experimental pipeline

Group	Construct Type	Time Point	Analysis Pipeline	Markers/Tools	No. of Animals (N)
3D RFP+ NPC implants	RFP+ hiPSC-derived ENPCs	2 WPI	Axonal tracing	Neurolucida	1
			Neuronal subtype	CTIP2, SATB2	3
			Glial response	GFAP, Iba1	3
			Proliferation/apoptosis	Ki-67, Caspase-3	3
			Volume reconstruction	Neurolucida	4
			Vascularisation	CD31	4
3D RFP+ NPC implants	RFP+ hiPSC-derived ENPCs	2 MPI	Axonal tracing	Neurolucida	1
			Neuronal subtype	CTIP2, SATB2	3
			Glial response	GFAP, Iba1	3
			Proliferation/apoptosis	Ki-67, Caspase-3	3
			Volume reconstruction	Neurolucida	3
			Vascularisation	CD31	3
3D ENPC implants	Unlabelled hiPSC-derived ENPCs	2 MPI	Axonal tracing	Neurolucida	2
			Synaptic integration	hSYP, PSD-95	2
			Volume reconstruction	Neurolucida	5
			Glial response	GFAP, Iba1	3
3D LNPC implants	Unlabelled hiPSC-derived LNPCs	2 MPI	Axonal tracing	Neurolucida	2
			Synaptic integration	hSYP, PSD-95	2
			Volume reconstruction	Neurolucida	4
			Glial response	GFAP, Iba1	3
		2 MPI	Axonal tracing	Neurolucida	1

Two-layered neuronal tissue	RFP+ LNPC constructs + Unlabelled ENPC constructs		Compartment-specific tracing	hNCAM	3
TBI brains	None	2 MPI	Glial response	GFAP, Iba1	3

4.3 Results

4.3.1 RFP+ NPC implants integrate into the host brains and differentiate after implantation

To evaluate survival, differentiation, and integration of the RFP+ NPC implants, coronal brain sections were analysed at 2 WPI and 2 MPI (Fig. 4.1A). Human cells were identified based on the co-expression of RFP and human-specific markers, including HuNu and hNCAM.

4.3.1.1 RFP+ NPC implants extend long-range projections at 2 WPI and 2 MPI

Neurolucida software was used to trace axonal outgrowth across serial coronal brain sections, guided by the fluorescence of RFP+ NPCs. Reconstruction was performed along the entire rostrocaudal axis of the brain to visualise long-range axonal projections and regional innervation patterns (Fig. 4.1B). At both post-implantation time points, dense projection bundles were observed emerging from the implant and projecting locally into adjacent cortical layers (Fig. 4.1B). Additionally, long-range projections were observed at early and late time points, crossing the midline via the corpus callosum into contralateral cortical regions (Fig. 4.2A, C; 4.3A, D). Moreover, another long-range projection can be detected extending along the ipsilateral lateral cerebral cortex to the piriform area of the ventral cortex at 2WPI and 2 MPI (Fig. 4.2B’’; 4.3B’’’’). Subcerebral projections were also evident, with projections descending through the internal capsule, indicating potential targeting of deep brain structures and long-range connectivity (Fig. 4.2B’; 4.3B’’’).

At 2 MPI, axonal projections were markedly enhanced, exhibiting widespread and organised trajectories. In addition to callosal projections, RFP+ projections were observed traversing the anterior commissure, an interhemispheric white matter pathway that links the bilateral temporal lobes across the cerebral hemispheres (Hsu et al., 2020), highlighting its role in interhemispheric connectivity. Beyond cortical targets, axonal projections reached subcortical nuclei, including the hypothalamus and thalamus (Fig. 4.3B’, B’’). RFP+ axonal projections within the hippocampus were only observed at 2 MPI, suggesting ongoing axonal growth and

delayed integration with specific brain regions (Fig. 4.3C'). These findings demonstrated that axonal projections from implanted human constructs followed known anatomical white matter tracts in the mouse host, supporting the notion of appropriate guidance and alignment with host neuronal architecture.

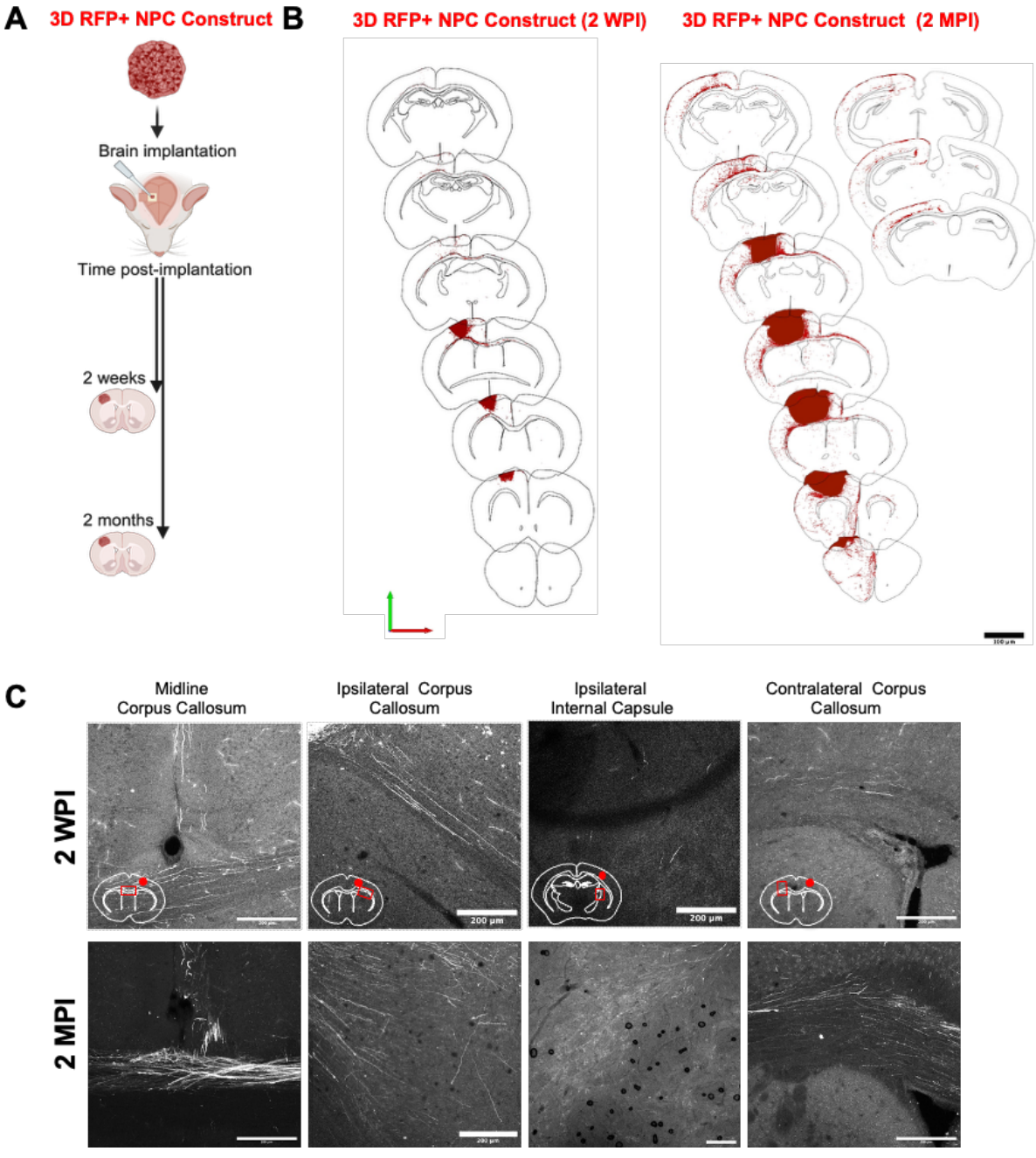

Figure 4.1 3D RFP+ NPC implants extend long-range projections at 2 WPI and 2 MPI
(A) Schematic representation of the experimental design. RFP+ NPC constructs were implanted into the right motor cortex of P7-P8 in NOD-SCID mice. Brains were collected at 2 WPI and 2 MPI. (B) Representative Neurolucida reconstructions of axonal projections across serial coronal brain sections at 2 WPI and 2 MPI. At 2 MPI, axonal projections were remarkably dense and detected in various cortical and subcortical regions and along different white matter tracts; N=1.

(C) Confocal images of representative brain regions reveal axonal projections from the implants into different brain regions. At 2 WPI and 2 MPI, projections were observed in the midline corpus callosum, ipsilateral corpus callosum and internal capsule, in addition to contralateral corpus callosum, with denser and more widespread projections at 2 MPI.
Scale bar (B): 1000 µm, Scale bar (C): 200 µm. WPI: weeks post-implantation; MPI: months post-implantation.

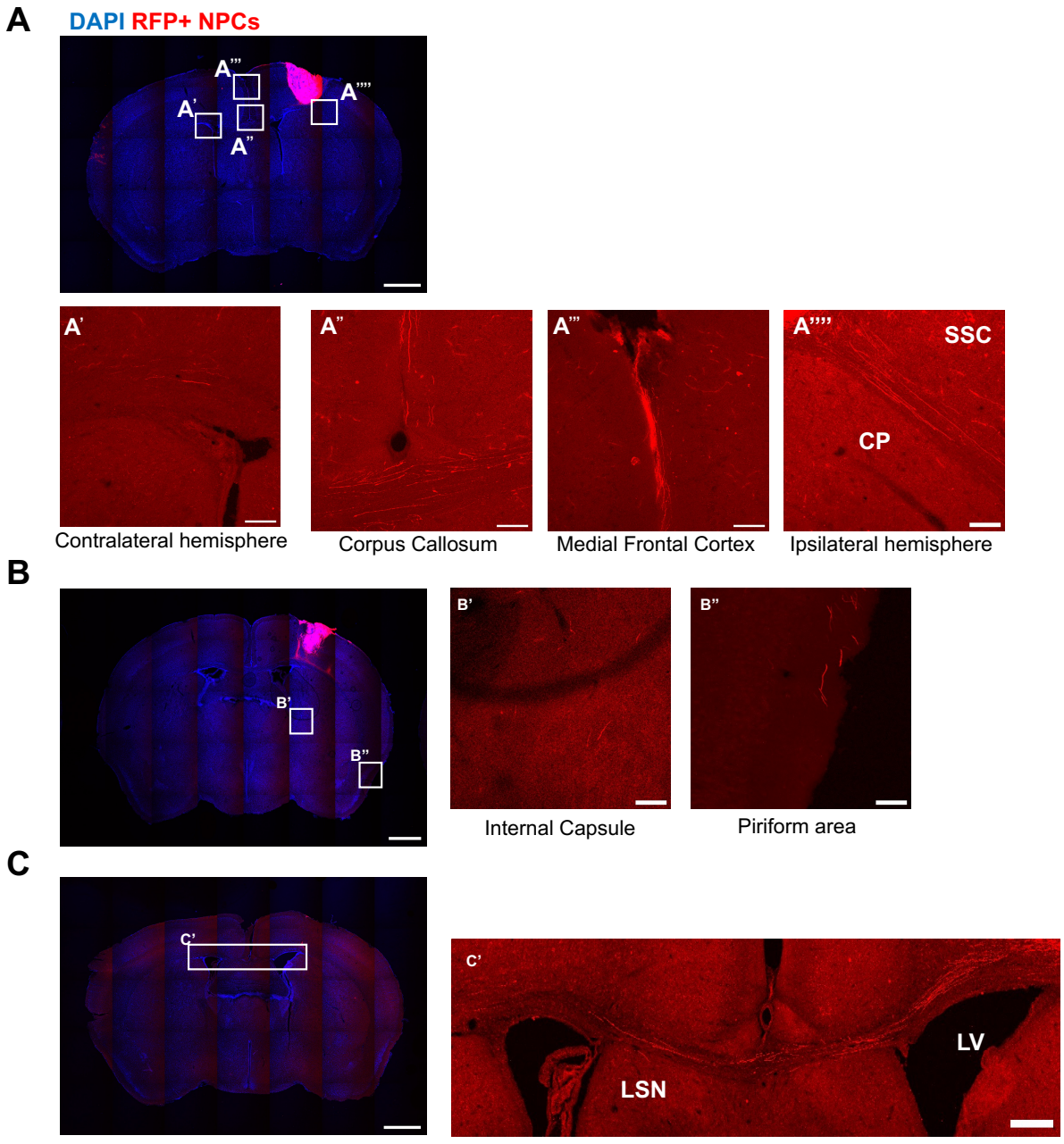

Figure 4.2 3D RFP+ NPC implants send axonal projections to the ipsilateral and contralateral hemispheres at 2 WPI
(A) Representative coronal section showing RFP+ projections extending from the implant into various brain regions. Insets highlight axonal projections within the contralateral hemisphere (A'), the midline corpus callosum (A''), the medial frontal cortex (A'''), and the ipsilateral hemisphere (A''''). (B) Representative coronal section with insets showing RFP+ projections into the internal capsule (B') and the Piriform area (B'').

(C) Another coronal section with an inset showing the traversing long-range axonal projections through the corpus callosum (C') to the contralateral hemisphere.
Scale bars of coronal low-power sections counterstained with DAPI: 1000 µm; all insets (A'-B''): 100 µm; (C'): 200 µm.
Abbreviations: WPI: weeks post-implantation; CP: caudoputamen; SSC: somatosensory cortex; LV: lateral ventricle; LSN: lateral septal nucleus.

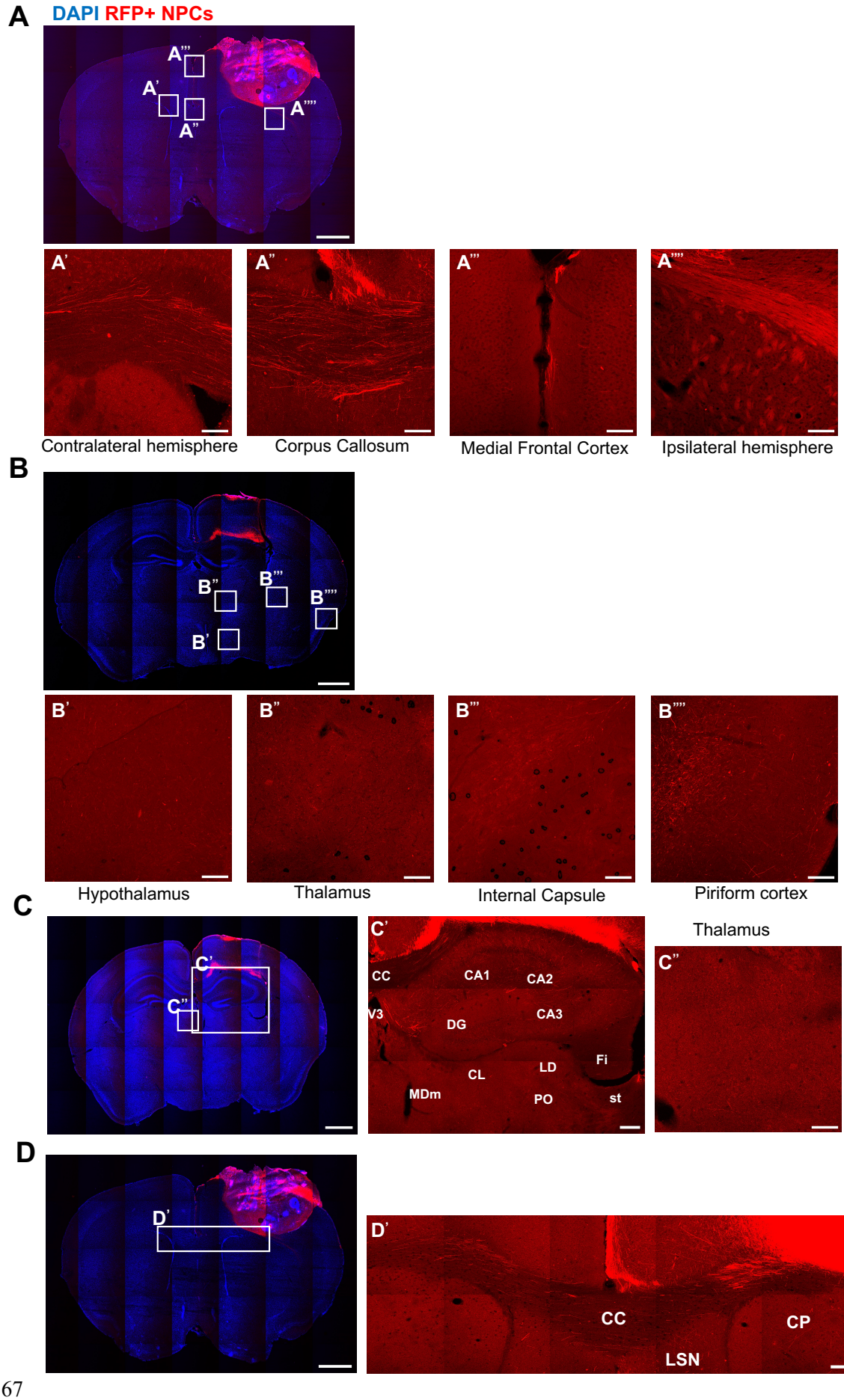
A
DAPI RFP+ NPCs
A'''
A'
A''
A''''
A'
A''
A'''
A''''
Contralateral hemisphere
Corpus Callosum
Medial Frontal Cortex
Ipsilateral hemisphere
B
B''
B'''
B''''
B'
B'
B''
B'''
B''''
Hypothalamus
Thalamus
Internal Capsule
Piriform cortex
C
C'
C''
C'
CC
CA1
CA2
V3
DG
CA3
CL
LD
Fi
MDm
PO
st
Thalamus
C''
D
D'
D'
CC
CP
LSN

Figure 4.3 Axonal projections from 3D RFP+ NPC implants across cortical and subcortical regions at 2 MPI
(A) Representative coronal section showing the RFP+ implants sending projections towards various brain regions. High-magnification insets illustrate RFP+ projections within the contralateral hemisphere (A'), the midline corpus callosum (A''), the medial frontal cortex (A'''), and the ipsilateral hemisphere(A'''').
(B) Coronal section highlighting axonal projections into ipsilateral subcortical brain regions and white matter tracts. White boxes highlighted the brain regions shown in higher magnification: (B') hypothalamus, (B'') thalamus, (B''') internal capsule, and (B'''') Piriform cortex.
(C) Axonal projections in the hippocampus and thalamus. (C') Overview of hippocampal innervation, with labelled subregions (CA1, CA2, CA3, DG) and nearby thalamic nuclei (CL, MDm, LD, PO). (C'') shows axonal projections within the thalamus.
(D) Coronal section showing implant-derived axonal projections traversing the corpus callosum towards the contralateral hemisphere. (D') High magnification confocal image showing long-range axonal projections through the corpus callosum (CC) to the contralateral hemisphere and into the ipsilateral and contralateral lateral septal nucleus (LSN) and caudoputamen (CP).
Scale bars of coronal low-power sections counterstained with DAPI: 1000 μm; all insets (A'-C''): 100 μm; (D'): 200 μm.
Abbreviations: CL: central lateral nucleus; MDm: mediodorsal nucleus, medial part; LD: lateral dorsal nucleus; PO: posterior nucleus; Fi: fimbria; DG: dentate gyrus; st: stria terminalis; CP: caudoputamen.

4.3.1.2 Progressive differentiation of 3D RFP+ NPC implants into upper- and deep-layer cortical neurons

The 3D RFP+ NPC implants exhibited a time-dependent increase in the expression of cortical layer-specific markers. The percentage of SATB2+HuNu+ neurons increased significantly from 0.29 ± 0.08% at 2 WPI to 31 ± 9.5% at 2 MPI ($p = 0.0153$, unpaired *t*-test, Fig. 4.4A), suggesting progressive maturation into upper-layer callosal PNs. The proportion of CTIP2+ HuNu+ neurons was comparable at 2 and 4 MPI (76 ± 2.9% vs 87 ± 4.3%; $p = 0.0584$, unpaired t-test; Fig. 4.4B). These findings suggested that the implants continued to differentiate into deep- and upper layers over time.

4.3.1.3 Temporal changes in cell proliferation and apoptosis within the 3D RFP+ NPC implants

To determine whether the observed expansion in construct volume was associated with cellular proliferation, 3D RFP+ NPC implants were analysed for expression of the proliferation marker Ki-67 and the apoptotic marker Cleaved Caspase-3 at 2 WPI and 2 MPI. At 2 WPI, proliferative Ki-67+ cells were primarily localised within neuroepithelial niches of neuronal rosette-like structures. In contrast, by 2 MPI, Ki-67+ cells appeared sparsely distributed throughout the implant (Fig. 4.5A). Quantification revealed a significant decrease in the percentage of Ki-67+ cells from 8.4 ± 1.5% at 2 WPI to 2.0 ± 0.39% at 2 MPI ($p = 0.0064$, unpaired *t*-test, Fig. 4.5B).

A low percentage of Cleaved Caspase-3+ apoptotic cells was observed, with no significant difference between the two time points. The percentage of Cleaved Caspase-3+ cells was 0.27 ± 0.07% at 2 WPI and 0.17 ± 0.03% at 2 MPI (p = 0.1107, unpaired t-test, Fig. 4.5B). In summary, these data suggested that implant overgrowth was driven by high early-stage proliferation, and the minimal apoptosis did not significantly contribute to post-implantation volume dynamics.

4.3.1.4 Volumetric expansion of the 3D RFP+ NPC implants occurs between two weeks and two months post-implantation

Volumetric reconstruction and quantification using Neurolucida software revealed a remarkable increase in the volume of the 3D RFP+ NPC implants between 2 WPI and 2 MPI (Fig. 4.6). Quantitative analysis showed that the average volume of RFP+ NPC implants increased from 0.51 ± 0.22 mm^3 at 2 WPI to 5 ± 1.5 mm^3 at 2 MPI (p = 0.0286, unpaired t-test), confirming a statistically significant expansion during the first two months following implantation. In some brains, the overgrown implants extended over the cerebral surface of the surrounding tissue. Despite this expansion, there was no evidence of compression of adjacent structures, ventricular displacement, or midline shift on coronal sections, indicating that implant growth was accommodated without disrupting the surrounding host anatomy (Fig. 4.6A). This may be attributed to the fact that the growth rates of the implants and the developing postnatal brain were within a comparable range, allowing spatial integration without exerting compressive effects.

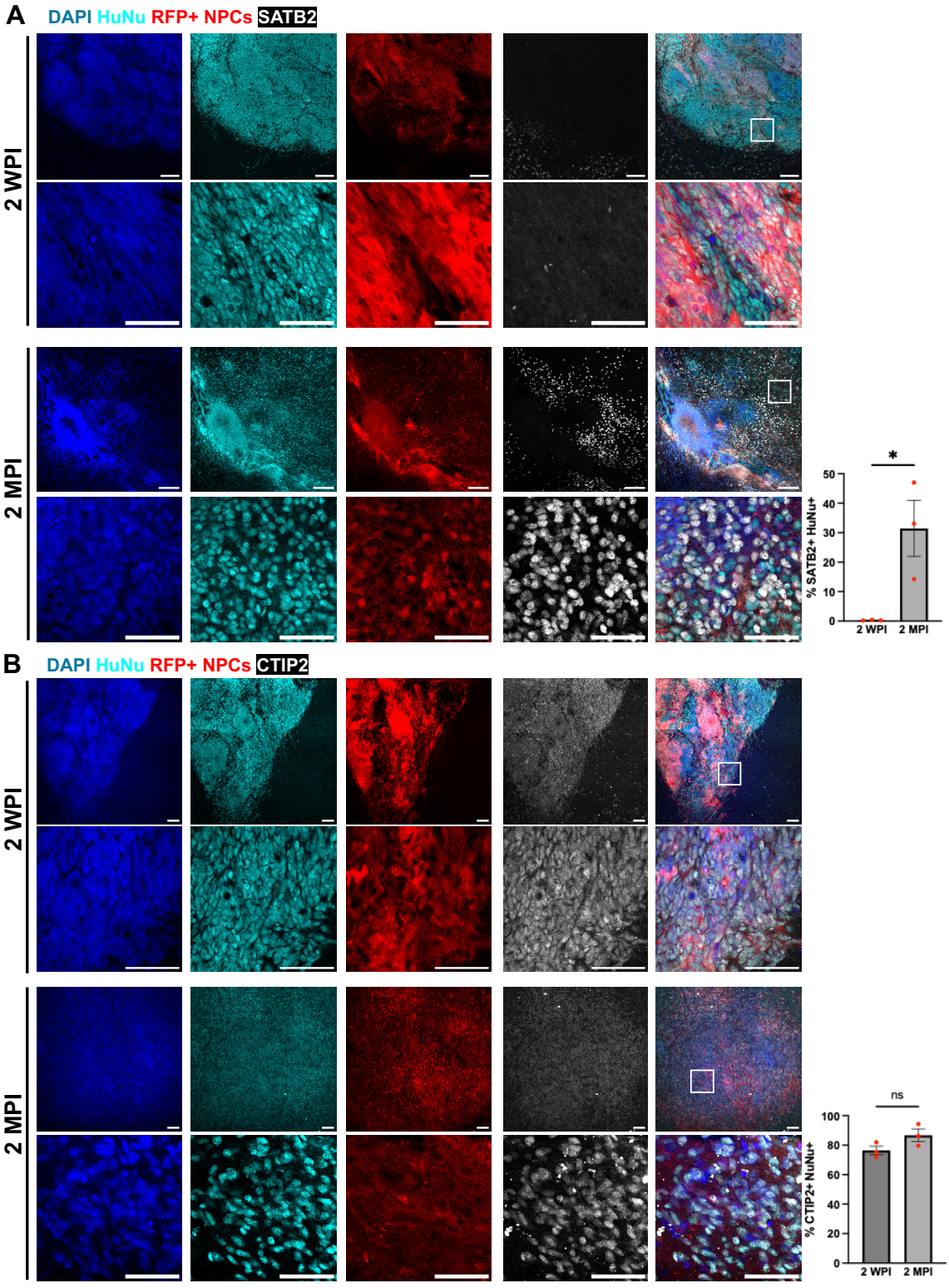

Figure 4.4 Differentiation of 3D RFP+ NPC implants into deep- and upper-layer cortical neurons

(A) Representative confocal images of 3D RFP+ NPC implants at 2 WPI and 2 MPI. Right panel: quantification of the percentage of SATB2+ HuNu+ neurons reveal that the percentage of positive neurons was more abundant at 2 MPI ($p = 0.0153$, unpaired t-test).

(B) Confocal images showing expression of CTIP2+HuNu+ neurons within the implants at 2 WPI and 2 MPI. Quantification shows a non-significant difference in the percentage of CTIP2+ HuNu+ (p = 0.0584, unpaired t-test).
Scale bar: 50 µm. WPI: weeks post-implantation; MPI: months post-implantation, ns = non-significant. Results are presented as means ± SEM; N = 3.

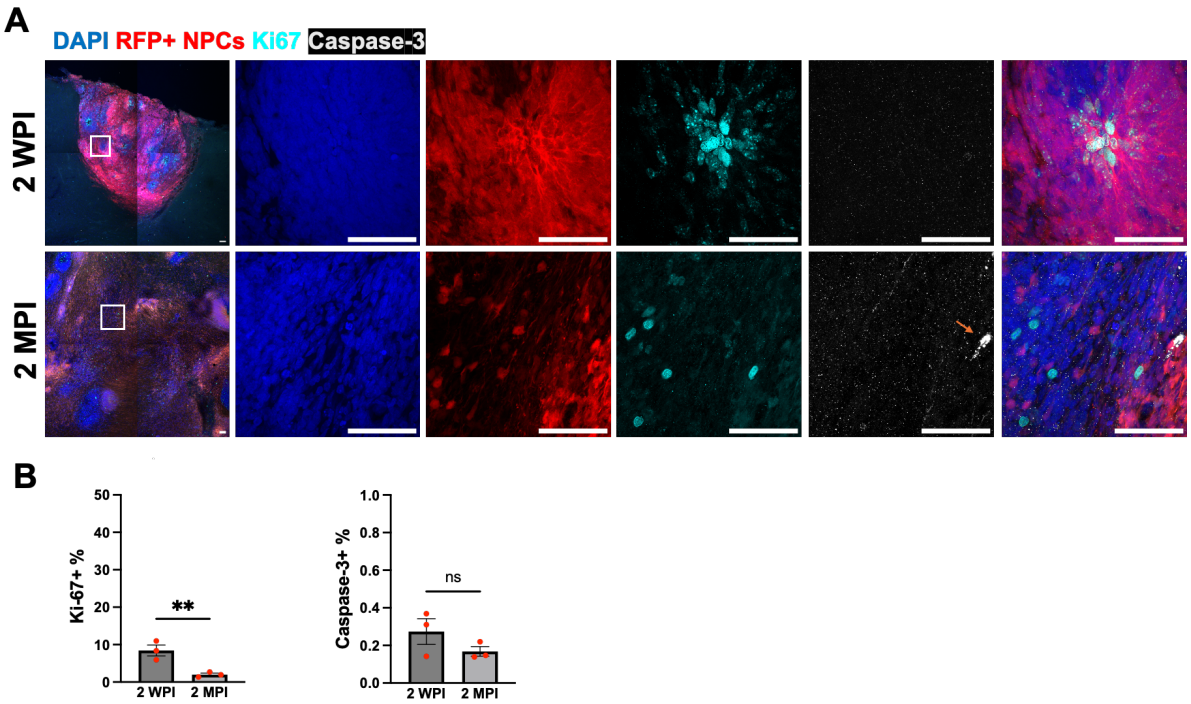

Figure 4.5 Temporal changes in cell proliferation and apoptosis within the 3D RFP+ NPC implants
(A) Representative confocal images of RFP+ NPC implants at 2 WPI and 2 MPI immunostained for Ki-67 and Cleaved Caspase-3. At 2 WPI, Ki-67+ proliferative cells were primarily localised within the neuroepithelial niche of rosettes, while at 2 MPI, Ki-67 expression was sparsely distributed. Caspase-3+ apoptotic cells (indicated by orange arrow) were present at both time points, but in reduced numbers at 2 MPI.
(B) The percentage of Ki-67+ cells significantly decreases from 2 WPI to 2 MPI (p = 0.0064, unpaired t-test), whereas the reduction in Caspase-3+ cell percentage was not statistically significant (p = 0.1107).
Scale bars for all panels: 50 µm. WPI: weeks post-implantation; MPI: months post-implantation, ns: non-significant. Results are presented as means ± SEM; N = 3.

4.3.1.5 Diffuse and stable vascularisation of the 3D RFP+ NPC implants

Vascularisation is essential for graft viability and integration. To assess the vascularisation of the implanted constructs over time, brain sections were immunostained for an endothelial marker, CD31 (Lertkiatmongkol et al., 2016). CD31+ endothelial cells were observed throughout the implants as early as 2 WPI, indicating early vasculature infiltration. By 2 MPI, the CD31+ vascular network remained widely distributed throughout the growing implants. These vessel-like structures appeared to branch and scale within the expanded implant, indicating stable vascular integration alongside the implant's expansion. Quantitative analysis

revealed that the total CD31+ area (µm^2) within the implants and the percentage of CD31+ area relative to the total implant area remained stable between 2 WPI and 2 MPI (Fig. 4.6C). Quantitative analysis of implant vascularisation revealed that both the absolute and relative vascularised areas remained stable between early and late post-implantation time points. At 2 WPI, the mean CD31+ area within the implant was 5960 ± 387 µm², corresponding to 4.1% ± 0.95 of the total implant area (N = 4). By 2 MPI, the CD31+ area measured 5625 ± 789 µm², representing 1.9% ± 0.35 of the implant area (N = 3). While there was a trend toward reduced vascular coverage over time, the differences were not statistically significant for either the absolute CD31+ area ($p = 0.3643$) or the percentage of CD31+ area ($p = 0.0527$). These findings suggested that vascularisation was established early after implantation and maintained over time. However, the origin of the vasculature was not determined in this study. Moreover, the presence of structural vasculature does not necessarily indicate stable blood perfusion.

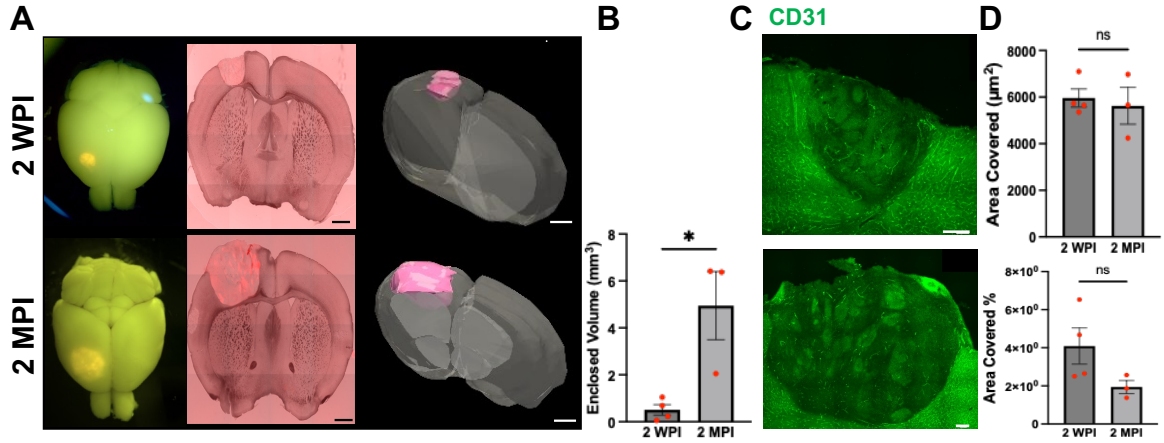

Figure 4.6 Volumetric expansion and vascularisation of the 3D RFP+ NPC implants over time
(A) Volumetric reconstruction of RFP+ NPC implants at 2 WPI and 2 MPI. Left: Fluorescence imaging of the whole brain, showing the fluorescent implants within the motor cortex. Middle: corresponding coronal sections showing the spatial relationship of the implant within the host cortex. Right: 3D reconstruction of the implants using Neurolucida software across coronal sections. Scale bar: 1000 µm.
(B) Quantification reveals a significant increase in implants' volume between 2 WPI and 2 MPI ($p = 0.0286$, unpaired *t*-test).
(C) Representative confocal images of RFP+ NPC implants immunostained for CD31, a marker of endothelial cells, showing vascular infiltration at both time points.
(D) Bar graphs show no significant difference in either the CD31+ area (µm^2) ($p = 0.3643$) or percentage of the CD31+ area ($p = 0.0527$) between 2 WPI and 2 MPI.
Scale bar: 200 µm. WPI: weeks post-implantation; MPI: months post-implantation, ns: non-significant. Results are presented as means ± SEM; N (2 WPI) = 4; N (2 MPI) = 3.

4.3.1.6 Remodelling of glial reaction two months after implantation of RFP+ NPC constructs

Quantitative analysis revealed a significant reduction in the density of Iba1+ microglia surrounding the implants between 2 WPI and 2 MPI. The density of Iba1+ microglia decreased from 0.00071 ± 0.00015 cells / μm² to 0.00040 ± 0.00004 cells / μm² ($p = 0.0125$). Reactive microglia observed within the implants did not colocalise with HuNu, indicating host origin (Fig. 4.7C). Microglial morphology varied according to spatial distribution. At the host-implant interface, Iba1+ microglia displayed hypertrophic cell bodies and thickened, retracted processes indicative of reactive, activated microglia (Fig. 4.7A'). Iba1+ microglia located distant from the implants exhibited a more ramified morphology, consistent with the resting state (Fig. 4.7 A''''). Microglia infiltrating the implants exhibited an amoeboid or rod-like morphology, characteristic of phagocytic function (Fig. 4.7A'', A'''). Further quantitative analyses are required to validate these morphological observations.

GFAP immunostaining revealed a pronounced astrocytic response at the host–implant interface, with dense accumulation of hypertrophied astrocytes insulating the implant. GFAP+ astrocytes were also distributed throughout the central regions of the implants. The proportion of GFAP+ area within the peri-implant zone significantly reduced from $64 \pm 8.5\%$ at 2 WPI to $44 \pm 1.5\%$ at 2 MPI ($p = 0.0410$), indicating a progressive attenuation of astrocytic reactivity (Fig. 4.7C). Collectively, these findings suggested dynamic remodelling of the glial response over time, with a trend towards stabilisation of the local inflammatory microenvironment by 2 MPI.

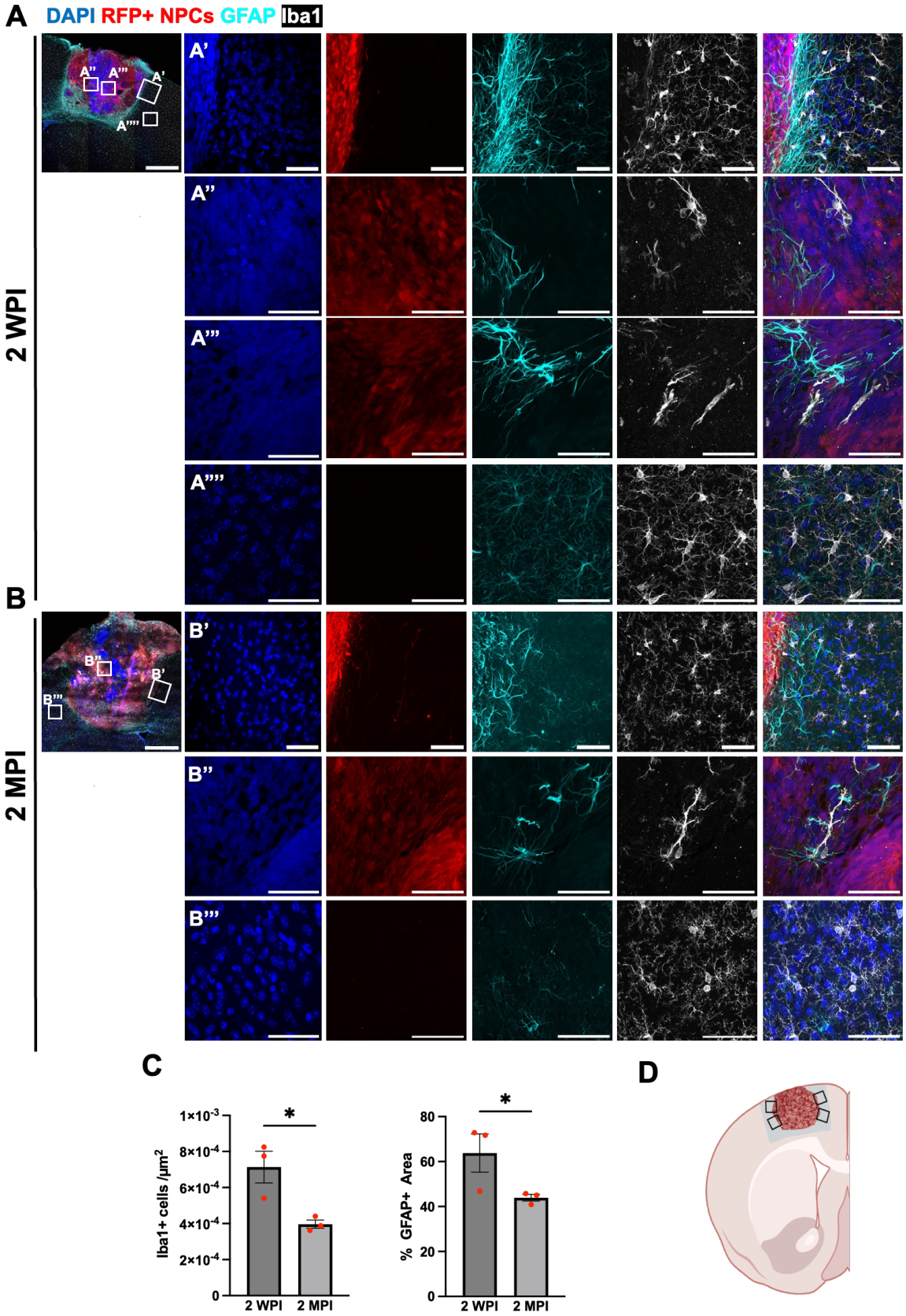

Figure 4.7 Remodelling of host glial response following implantation of RFP+ NPC constructs
Representative confocal images of coronal brain sections at 2 WPI and 2 MPI illustrate the host glial response to the implants.

(A, B) Low-magnification confocal images illustrate implant location and selected regions for higher magnification, marked in white boxes.
(A', B') Insets highlight the host–implant interface, where dense astrocytic and microglial reactivity were evident. Iba1+ microglia displayed hypertrophic cell bodies and thickened, retracted processes indicative of activation. Astrocytes exhibited a hypertrophic morphology, with prominent, thickened primary processes.
(A'', A''') insets showing reactive microglia and hypertrophied reactive astrocytes occupying the implant. (A'') insets show the ameboid morphology of the microglia with phagocytic features, and (A''') show rod-shaped microglia.
(A'''') Higher magnification of the area surrounding the construct shows ramified microglia and branched non-reactive astrocytes, indicating a homeostatic phenotype.
(B'') Insets showing reactive ameboid microglia and hypertrophied astrocytes invading the implants at 2 MPI.
(B''') Higher magnification of the area surrounding the construct shows ramified microglia and non-reactive astrocytes.
(C) Quantification reveals a significant reduction in the percentage of GFAP+ area (left) and Iba1+ cell density (right) in the peri-implant region between 2 WPI and 2 MPI ($p = 0.0410$ and $p = 0.0125$, respectively; unpaired *t*-test).
(D) The schematic illustration of the host-implant interface on both sides of the implant used for analysis.
Scale bar: 500 µm (main panels), 50 µm (insets). Results are presented as means ± SEM; N = 3.
WPI: weeks post-implantation; MPI: months post-implantation.

4.3.2 3D ENPC and LNPC implants exhibit distinct integration and connectivity

Brains implanted with single 3D ENPC or LNPC constructs were collected at 2 MPI (Fig. 4.8A). The 3D implants accommodated the lesion cavity and integrated with the host tissue. To assess the integration of implanted cortical constructs, human cells were identified by immunostaining for HuNu and hNCAM.

4.3.2.1 Distinct efferent projections and regional targeting of 3D ENPC and LNPC implants

The Neurolucida software system was used to track axonal projections across serial coronal sections, guided by the hNCAM signal (Fig. 4.8B). Axon projections were quantified using the Neurolucida Explorer software by partitioning each section into cortical and subcortical anatomical regions, including the striatum, piriform, thalamus, hypothalamus, corpus callosum, corticospinal tract, and hippocampal formation. Symmetric regions, ipsilateral and contralateral to the implant site, were quantified separately.

Both 3D ENPC and LNPC implants sent dense axonal projections into adjacent cortical layers; however, they exhibited distinct axonal targeting and distribution patterns across various brain regions. In ENPC implants, projections were more broadly distributed and extended to multiple subcortical regions, with higher densities observed in the ipsilateral and contralateral striatum, thalamus and hypothalamus. Moderate densities were detected in the CST and hippocampal

formation. This widespread projection pattern suggested that 3D ENPC implants retained the characteristics of deep-layer corticofugal neurons, which can extend long-range projections toward subcortical and descending pathways (Fig. 4.8C). In contrast, 3D LNPC implants exhibited more restricted and locally concentrated projections, predominantly targeting the cortex and corpus callosum, with limited extension into deeper subcortical regions. Moderate density was detected in the striatum, but the overall density was lower than that observed for 3D ENPC implants. No projections detected in the thalamus and hippocampal formation. This projection profile is consistent with the callosal and associative connectivity pattern of upper-layer cortical neurons (Fig. 4.8C).

When averaged across animals, 3D ENPC implants displayed higher efferent density in subcortical and descending pathways, whereas 3D LNPC implants showed preferential intracortical and commissural connectivity, indicating an identity-dependent integration pattern.

4.3.2.2 Synaptic integration of the implant-derived projections with host cortical circuits

Adequate neural replacement requires not only survival and axonal projections but also the formation of functional synaptic connections with host brain circuits. To assess synaptogenesis, brain sections were immunostained for human-specific Synaptophysin (hSYP), a marker of human-specific presynaptic terminals, and for PSD-95, a postsynaptic density marker.

Confocal imaging revealed a dense network of hSYP puncta surrounding host neurons. Many of these presynaptic terminals were closely opposed to PSD-95 puncta, suggesting synaptogenesis. High-resolution analysis identified individual synaptic sites marked by co-localisation of hSYP and PSD-95, supporting the synaptogenesis between implant-derived projections and host circuitry (Fig. 4.9).

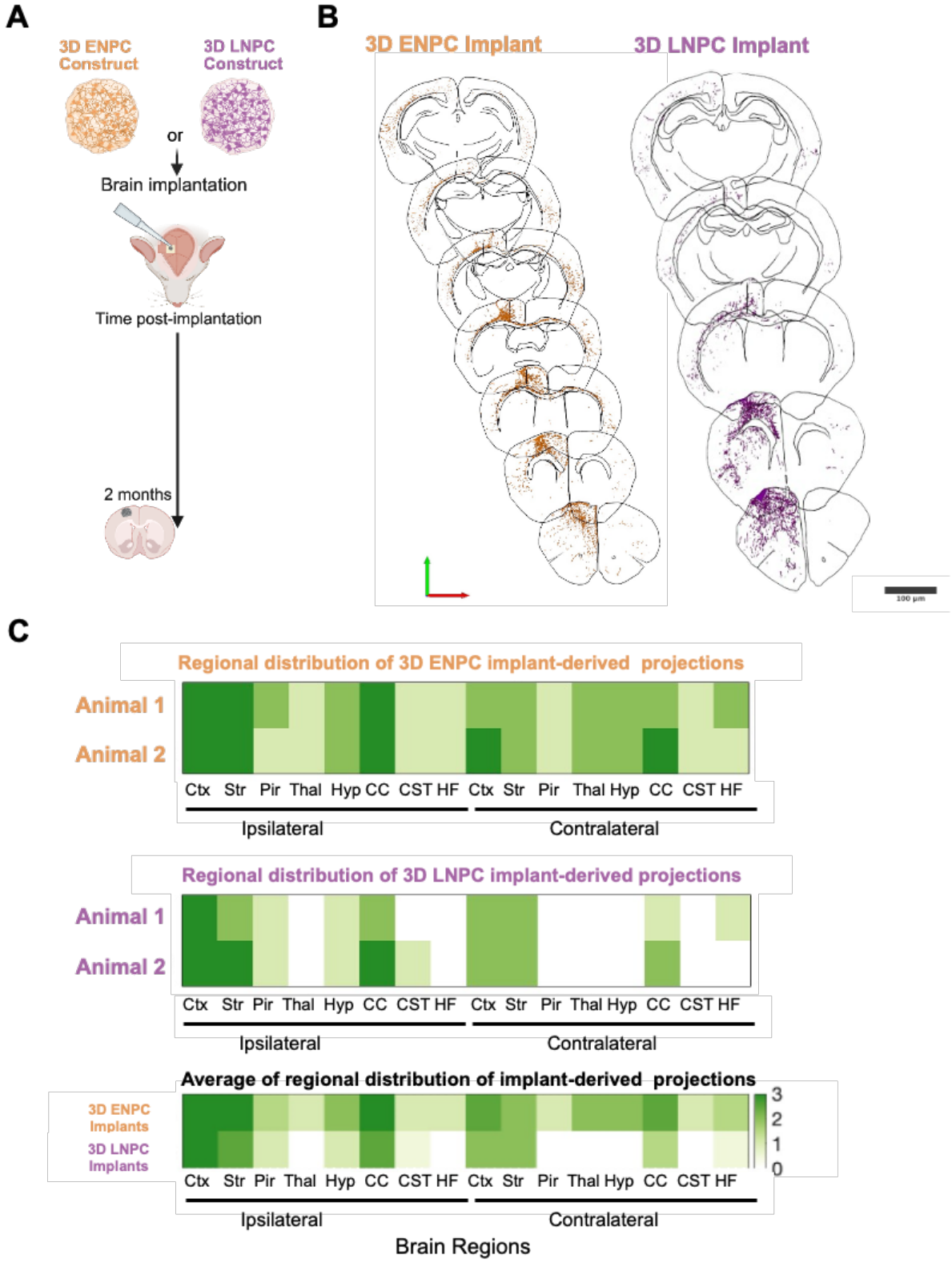

Figure 4.8 3D ENPC and LNPC implants show distinct axonal projection patterns
(A) Schematic timeline illustrating the implantation of 3D ENPC and LNPC constructs into the right motor cortex of P7-P8 in NOD-SCID mice. Brains were collected and processed at 2 MPI.
(B) Representative Neurolucida reconstructions of axonal projections of 3D ENPC and LNPC implants across serial coronal brain sections at 2 MPI.

(C) Heatmaps of regional distribution of the projection density of 3D ENPC and LNPC implants into distinct ipsilateral and contralateral cortical regions, including cerebral cortex (Ctx), striatum (Str), piriform (Pir), thalamus (Thal), hypothalamus (Hyp), corpus callosum (CC), corticospinal tract (CST) and hippocampus formation (HF). Each row represents an individual animal.
The bottom panel displays the average projection density across all animals within each group. Projection density was scored on a semi-quantitative scale, ranging from 0 (no detectable projections) to 3 (dense projections). Scale bar (B): 1000 µm; N=2.

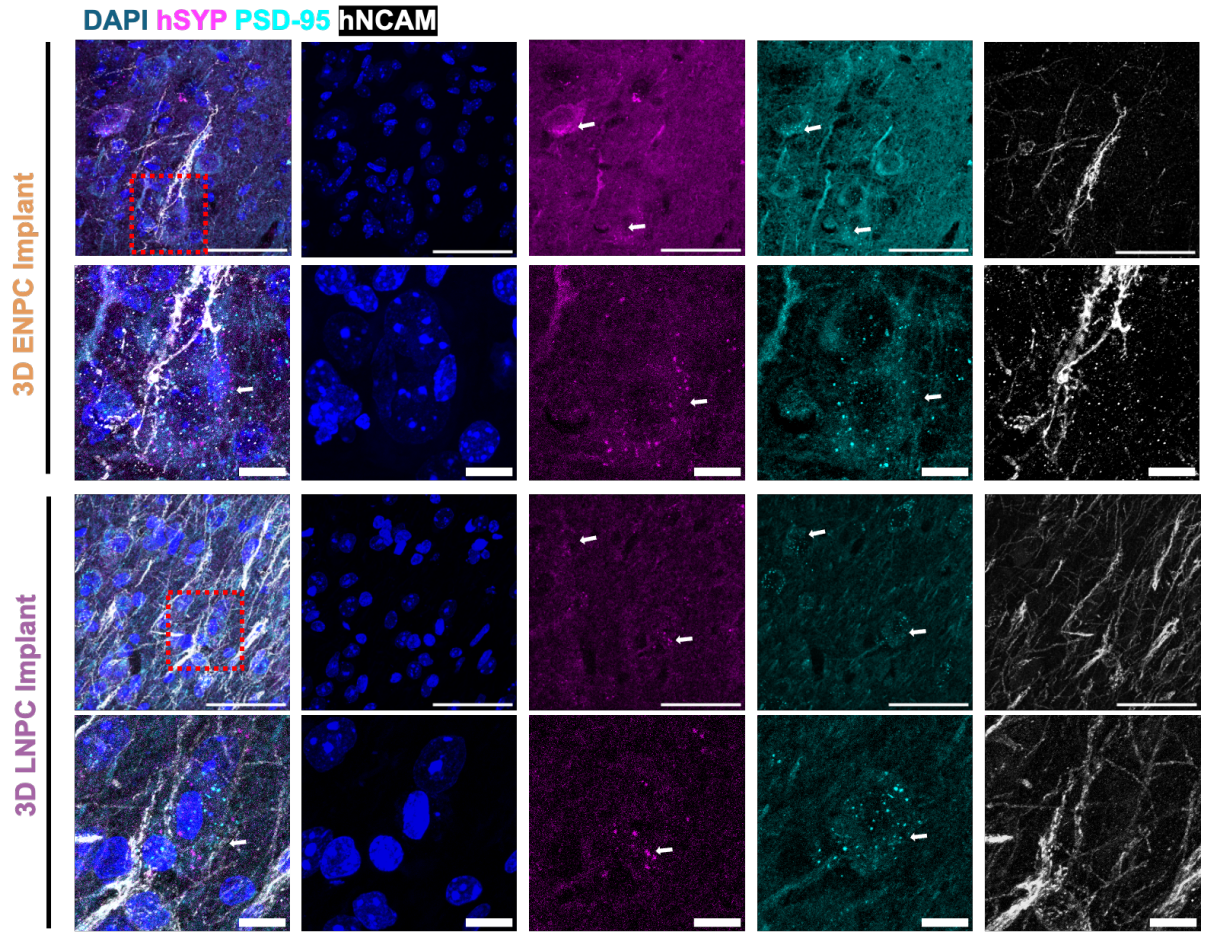

Figure 4.9 3D ENPC and LNPC implants exhibit human-host synaptic formation
High-magnification confocal images showing the juxtaposition of the presynaptic human-specific Synaptophysin (hSYP) and the postsynaptic marker PSD-95, indicated by white arrows.
Scale bar: 50 µm (main panels), 10 µm (insets). MPI: months post-implantation; N=2.

4.3.2.3 3D reconstruction and quantification of the implant volume

The volumes of the 3D ENPC and LNPC implants were reconstructed and quantified using Neurolucida software (Fig. 4.10B). Volumetric quantification demonstrated comparable volumes in the ENPC and LNPC implants, with no statistically significant difference. The average of reconstructed volume of 3D ENPC implants was 0.060 ± 0.010 mm^3 and was 0.051 ± 0.021 mm^3 for 3D LNPC implants (p = 0.3619, unpaired t-test, Fig. 4.10C). These findings suggested that the differences observed in the anatomical integration patterns of the 3D ENPC and LNPC implants were primarily due to differences in cell identity rather than volume.

4.3.2.4 Glial reactivity to 3D ENPC and LNPC implants in comparison to TBI brains

To evaluate the host immune response to 3D ENPC and LNPC implants and whether the implants had immunomodulatory effects, glial reactivity in brains with 3D ENPC or 3D LNPC implants was compared with that in TBI brains. Quantification of Iba1+ microglial density in the peri-lesional or peri-implant regions revealed higher values in brains with 3D ENPC implants (0.00055 ± 0.0001 cells/µm²) and 3D LNPC implants ($0.00047 \pm 5.0 \times 10^{-5}$ cells/µm²), relative to the TBI brains ($0.00040 \pm 4.1 \times 10^{-5}$ cells/µm², Fig. 4.11B). These differences did not reach statistical significance (ENPC implants vs. LNPC implants: $p = 0.72$; ENPC implants vs. TBI brains: $p = 0.34$; LNPC implants vs. TBI brains: $p = 0.75$; one-way ANOVA). Astrocytic reactivity, quantified as the percentage of GFAP-positive area relative to the total peri-implant HuNu-negative area, was highest in TBI brains ($70 \pm 8.2\%$). Brains with ENPC implants exhibited an intermediate level of GFAP coverage ($51 \pm 13\%$), while LNPC implants elicited the lowest astrocytic response ($37 \pm 0.27\%$, Fig. 4.11C). Group comparisons did not reveal statistically significant differences (ENPC implants vs. LNPC implants, p = 0.671; ENPC implants vs. TBI brains, p = 0.441; LNPC implants vs. TBI brains, p = 0.111; one-way ANOVA). Together, these results indicated that the 3D ENPC and LNPC implants did not significantly exacerbate the host glial response compared to TBI brains.

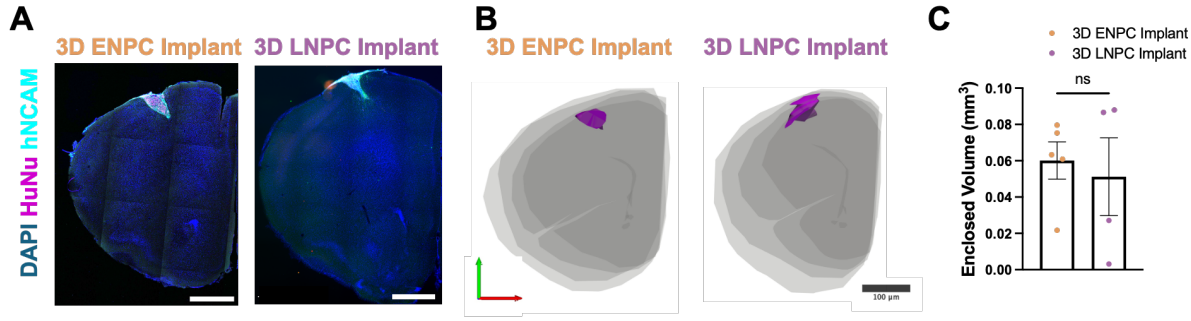

Figure 4.10 Volumetric reconstruction of 3D ENPC and LNPC implants at 2 MPI
(A) Representative coronal brain sections of brains with 3D ENPC and LNPC implants imaged at 2 MPI.
(B)Volumetric reconstructions of 3D ENPC and LNPC implants were conducted using serial coronal sections.
(C) Quantitative analysis shows no statistically significant difference in the volume of 3D ENPC and LNPC implants at 2 MPI ($p = 0.3619$, unpaired *t*-test).
Scale bar (A, B): 1000 µm. MPI: months post-implantation, ns: non-significant. Results are presented as means ± SEM; N (Animals with ENPC implants) = 5; N (Animals with LNPC implants) = 4.

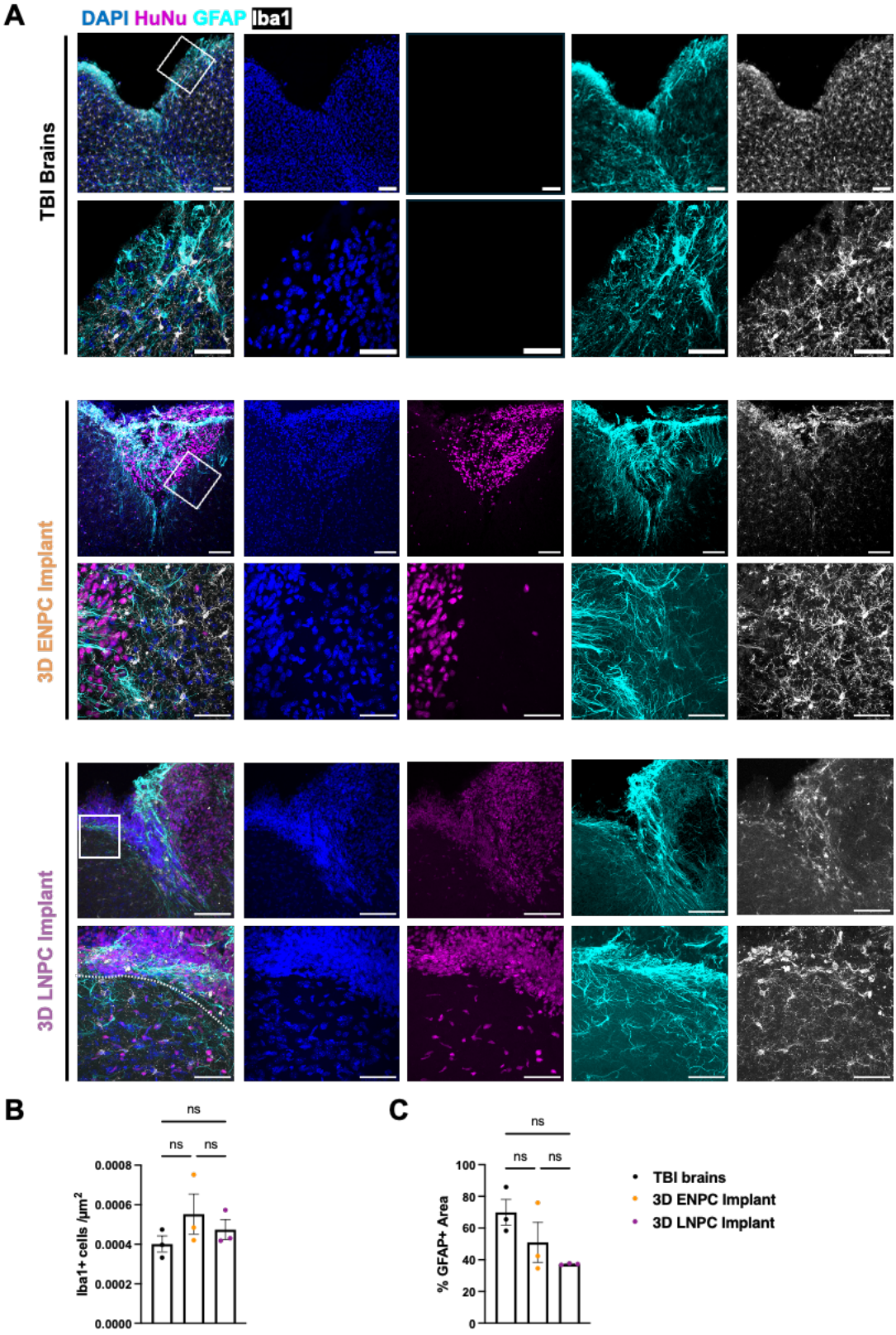

Figure 4.11 Glial reactivity to 3D ENPC and LNPC implants at 2MPI
(A) Representative confocal images showing GFAP+ astrocytes and Iba1+ microglia in coronal sections from TBI brains at 2 months post-injury and brains with 3D ENPC and 3D LNPC implants at 2 MPI.

(B) Quantification of peri-lesional or peri-implant Iba1+ microglial density reveals no statistical significance across groups (cells/µm²) (ENPC implants vs. LNPC implants: $p = 0.72$; ENPC implants vs. TBI brains: $p = 0.34$; LNPC implants vs. TBI brains: $p = 0.75$; one-way ANOVA),
(C) Quantification of the percentage of GFAP+ area reveals no statistical significance across groups (ENPC implants vs. LNPC implants: $p = 0.671$; ENPC implants vs. TBI brains: $p = 0.441$; LNPC implants vs. TBI brains: $p = 0.111$; one-way ANOVA).
Scale bar: 100 µm (main panels); 50 µm (insets). MPI: months post-implantation; ns: non-significant. Results are presented as means ± SEM; N = 3.

4.3.2.5 Electrophysiological assessment of cortical network activity of brains with 3D ENPC and LNPC implants compared to TBI and control brains

Spontaneous extracellular activity was recorded using the MEA system from acute brain slices with 3D ENPC and LNPC implants at 2 MPI to assess the functional activity of the host brain after implantation. Additional recordings were performed from slices from non-implanted TBI and age-matched uninjured control brains to provide comparative reference data. There was no significant difference in spike frequency (spikes/s) between groups. Control brains exhibited a frequency of 0.073 ± 0.0029 (Number of Slices, NS = 12). TBI brains had a frequency of 0.072 ± 0.0023 (NS = 11). Brains with 3D ENPC implants and 3D LNPC implants recorded (0.074 ± 0.00090, NS = 13) and (0.066 ± 0.0031, NS = 12, Fig. 4.12B), respectively. Dunn's multiple comparisons test revealed no significant differences between any of the groups.

Total burst number was slightly higher in the control group (0.77 ± 0.10, NS = 11), compared to TBI brains (0.47 ± 0.049, NS = 11), brains with 3D ENPC implants (0.51 ± 0.020, NS = 13), and brains with 3D LNPC implants (0.45 ± 0.055, NS =12, Fig. 4.12B). Dunnett's T3 post hoc tests revealed no statistically significant differences.

Median ISI (ms) was significantly prolonged in brains with 3D LNPC implants compared to the TBI brains. Median ISI values were as follows: control brains, 13323 ± 352 ms (NS =11); TBI brains, 12046 ± 323 ms (NS =12); brains with 3D ENPC implants, 12890 ± 196 ms (NS =13, Fig. 4.12C); and brains with 3D LNPC implants, 14292 ± 543 ms (NS =12). Only the comparison between the TBI brains and brains with 3D LNPC implants reached statistical significance ($p = 0.0081$).

Similarly, the mean ISI (ms) was highest in brains with 3D LNPC implants (19352 ± 667 ms, NS =12), compared to control brains (18245 ± 437 ms, NS =12), brains with 3D ENPC implants (17548 ± 246 ms, NS =13), and TBI brains (16508 ± 430 ms, NS =11). Only the comparison between TBI brains and brains with 3D LNPC implants showed statistical significance ($p = 0.0045$), indicating a delay in spiking activity.

Mean spike amplitude was significantly increased in brains with 3D LNPC implants (12 ± 1.3 μV, NS =12), compared to control brains (9.2 ± 0.096 μV, NS =12), TBI brains (9.1 ± 0.089 μV, NS =12), and brains with 3D ENPC implants (9.1 ± 0.037 μV, NS =13). Statistical analysis revealed significant differences between brains with 3D LNPC implants and all other groups (Control brains vs. brains with 3D LNPC implants: $p = 0.0186$; TBI brains vs. brains with 3D LNPC implants: $p = 0.0014$; brains with 3D ENPC implants vs. brains with 3D LNPC implants: $p = 0.0419$, Fig. 4.12C).

Maximum spike amplitude was significantly elevated in brains with 3D LNPC implants (14 ± 1.5 μV, NS =12), compared to control brains (11 ± 0.41 μV, NS =12), TBI brains (11 ± 0.18 μV, NS =11), and brains with 3D ENPC implants (11 ± 0.039 μV, NS =13). Dunn's multiple comparisons test indicated significant differences for control brains vs. brains with 3D LNPC implants ($p = 0.0351$), TBI brains vs. brains with 3D LNPC implants ($p = 0.0202$), brains with 3D ENPC implants vs. brains with 3D LNPC implants ($p = 0.0043$, Fig. 4.12D), highlighting the greater peak signal output in brains with 3D LNPC implants.

Table 4.2 Summary of statistical *p*-values for the spike parameters comparing control brains (Control), TBI brains (TBI), brains with 3D ENPC implants (ENPC), and brains with 3D LNPC implants (LNPC)

Parameter	Statistical Test (multiple comparison)	Control vs TBI	Control vs ENPC	Control vs LNPC	TBI vs ENPC	TBI vs LNPC	ENPC vs LNPC
Frequency	Dunn's	>0.9999	>0.9999	0.5616	>0.9999	>0.9999	0.3679
Burst Number	Dunnett's T3	0.1010	0.1621	0.0748	0.9375	0.9998	0.8157
Median ISI	Dunn's	0.2255	>0.9999	>0.9999	>0.5676	0.0081**	0.6159
Mean ISI	Dunn's	0.1236	>0.9999	>0.9999	>0.5986	0.0045**	0.4035
Mean Spike Amplitude	Dunn's	>0.9999	>0.9999	0.0186*	>0.9999	0.0014**	0.0419*
Max Spike Amplitude	Dunn's	>0.9999	>0.9999	0.0350*	>0.9999	0.0202*	0.0043**

* $p < 0.05$, ** $p < 0.01$, *** $p < 0.001$, **** $p < 0.0001$.

Power spectral analysis revealed significant group differences in gamma band activity. The mean gamma power was highest in the TBI brains ($1.1 \times 10^{-9} \pm 1.0 \times 10^{-10}$, NS =12) and in brains with LNPC implants ($1.1 \times 10^{-9} \pm 2.4 \times 10^{-10}$, NS =12), compared to the control brains ($8.3 \times 10^{-10} \pm 1.0 \times 10^{-10}$, NS =12). In contrast, brains with ENPC implants exhibited the lowest gamma power ($5.2 \times 10^{-10} \pm 5.1 \times 10^{-12}$, NS =13, Fig. 4.13B). Statistical comparisons using Dunn's multiple comparisons test revealed significantly lower gamma power in brains with

ENPC implants compared to both the TBI brains ($p < 0.0001$) and the control brains ($p = 0.009$).

Analysis of beta frequency power (12-30 Hz) revealed differential activity across groups. Brains with LNPC implants showed the highest beta PSD values ($1.2 \times 10^{-9} \pm 2.5 \times 10^{-10}$, NS = 11), followed by control brains ($7.2 \times 10^{-10} \pm 1.6 \times 10^{-11}$, NS = 9), TBI brains ($6.8 \times 10^{-10} \pm 2.3 \times 10^{-11}$, NS = 11), and lastly those brains with ENPC implants ($5.7 \times 10^{-10} \pm 4.8 \times 10^{-12}$, NS = 13, Fig. 4.13B). Dunn's multiple comparisons test revealed significantly lower beta power in brains with ENPC implants compared to control ($p = 0.0025$) and TBI brains ($p = 0.0309$). Brains with LNPC implants also showed non-significant difference relative to control ($p = 0.0798$).

PSD analysis of the delta frequency band (0.5-4 Hz) revealed differences across the experimental groups. The mean delta power was highest in the TBI brains ($7.9 \times 10^{-9} \pm 1.2 \times 10^{-9}$, NS = 12), followed by brains with LNPCs implants ($4.0 \times 10^{-9} \pm 9.6 \times 10^{-10}$, NS = 11), control brains ($2.5 \times 10^{-9} \pm 8.6 \times 10^{-11}$, NS = 8), and brains with 3D ENPC implants ($2.3 \times 10^{-9} \pm 2.6 \times 10^{-10}$, NS = 10, Fig. 4.13C). Dunn's multiple comparisons test indicated no significant differences between the control and other groups. However, brains with ENPC implants and those with LNPC implants showed significantly reduced delta power compared to TBI brains (TBI brains vs. brains with ENPC implants: $p = 0.0007$; TBI brains vs. brains with LNPC implants: $p = 0.0025$), suggesting a potential reduction of low-frequency oscillatory activity following the implantation of these constructs.

Analysis of theta band power (4-8 Hz) revealed that control brains exhibited the highest power ($2.8 \times 10^{-9} \pm 9.4 \times 10^{-10}$, NS = 12), followed by TBI brains ($1.8 \times 10^{-9} \pm 2.0 \times 10^{-10}$, NS = 12), brains with 3D LNPC implants ($1.6 \times 10^{-9} \pm 3.6 \times 10^{-10}$, NS = 11), and those with 3D ENPC implants ($8.5 \times 10^{-10} \pm 1.7 \times 10^{-11}$, NS = 13, Fig. 4.13C). Dunn's multiple comparisons test showed a significant reduction in theta power in brains with 3D ENPC implants compared to both control ($p = 0.0096$) and TBI brains ($p = 0.0035$). No other pairwise comparisons reached significance. These findings indicated that 3D ENPC implants may suppress theta-range activity more than other groups.

Alpha band power **(**8-12 Hz) exhibited group-dependent variations. Control brains showed the highest alpha PSD ($7.8 \times 10^{-10} \pm 1.9 \times 10^{-10}$, NS = 12), followed by brains with 3D LNPC implants ($6.8 \times 10^{-10} \pm 1.5 \times 10^{-10}$, NS = 11), TBI brains ($5.0 \times 10^{-10} \pm 3.5 \times 10^{-11}$, NS = 12),

and brains with 3D ENPC implants ($3.4 \times 10^{-10} \pm 3.9 \times 10^{-12}$, NS = 13, Fig. 4.13C). Dunn's multiple comparisons test revealed that ENPC constructs exhibited significantly reduced alpha power compared to both control (p = 0.0022) and TBI brains (p = 0.0069), while LNPC implants showed no significant difference from other groups. These data suggested that 3D ENPC implants suppressed alpha oscillatory activity to a greater extent than 3D LNPC implants.

Table 4.3 Summary of statistical *p*-values for PSD comparisons across frequency bands between control brains (control), TBI brains (TBI), brains with 3D ENPC implants (ENPC), and brains with 3D LNPC implants (LNPC)

PSD	Statistical Test (multiple comparison)	Control vs TBI	Control vs ENPC	Control vs LNPC	TBI vs ENPC	TBI vs LNPC	ENPC vs LNPC
Gamma	Dunn's	>0.9999	0.009**	>0.9999	<0.0001****	0.1374	0.3317
Beta	Dunn's	>0.9999	0.0025**	0.0798	0.0309*	0.5241	>0.9999
Delta	Dunn's	>0.1935	0.9472	>0.9999	0.0007***	0.0025**	>0.9999
Theta	Dunn's	>0.9999	0.0096**	0.1227	0.0035**	0.0578	>0.9999
Alpha	Dunn's	>0.9999	0.0022**	0.0791	0.0069**	0.1759	>0.9999

*$p < 0.05$, **$p < 0.01$, ***$p < 0.001$, ****$p < 0.0001$.

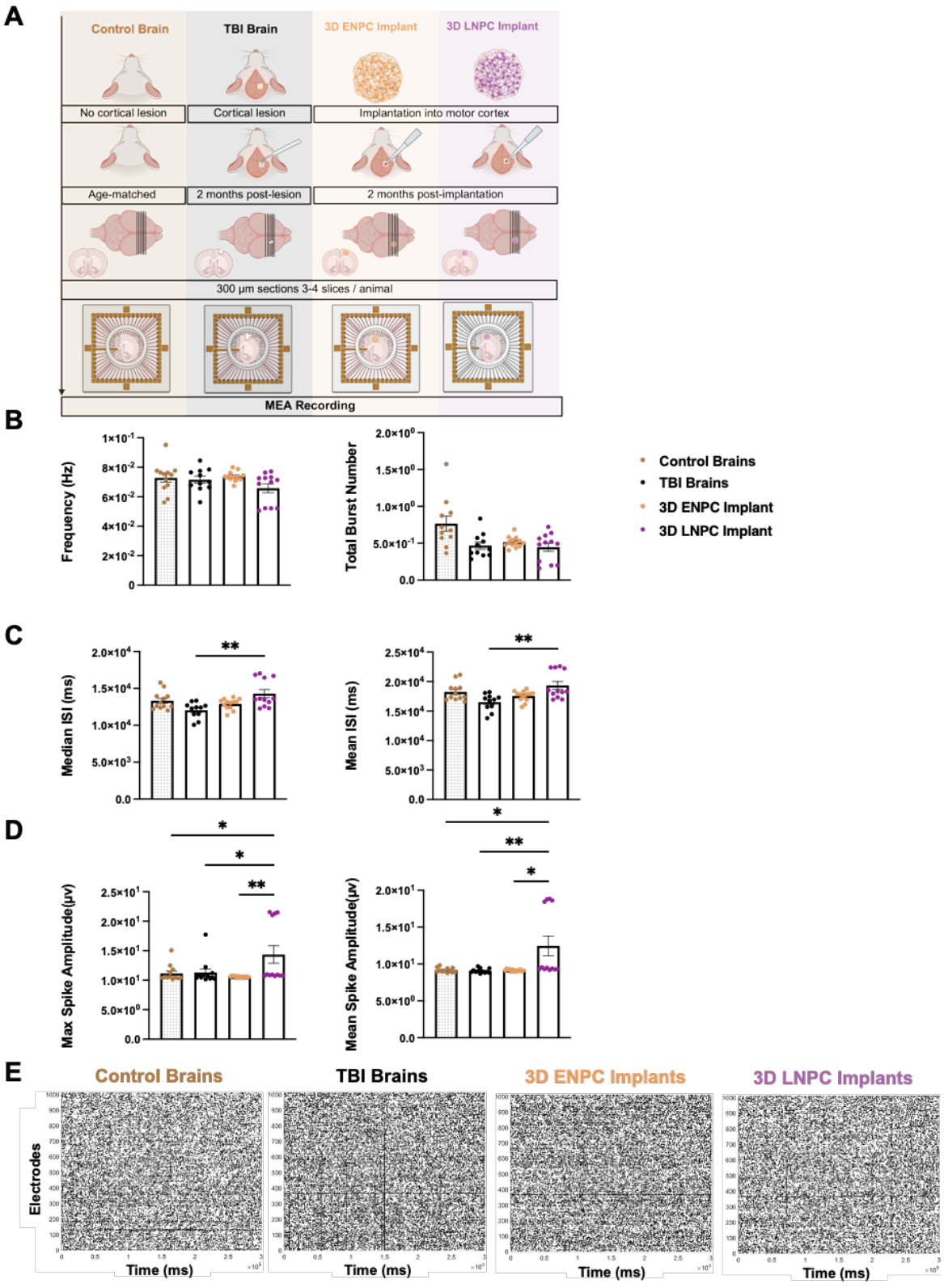

Figure 4.12 Electrophysiological assessment of cortical network activity of brains with 3D ENPC and LNPC implants compared to TBI and control brains
(A) Experimental workflow comprising control brains, TBI brains, and brains implanted with 3D ENPC or 3D LNPC constructs.

At 2 MPI/post-lesion, acute coronal slices 300 µm thick, with 3-4 slices per animal, were prepared, and spontaneous activity was recorded using high-density MEA.
(B –D) Quantification of electrophysiological parameters across groups. Parameters include:
(B) spike frequency (spikes/s), total burst number per 5-minute epoch,
(C) median inter-spike interval (ms) and mean inter-spike interval (ms),
(D) mean spike amplitude (µV) and maximum spike amplitude (µV).
(E) Representative raster plots of spontaneous spiking activity from control brains, TBI brains and brains with 3D ENPC and 3D LNPC implants. Each row corresponds to an electrode's activity, and each dot represents a detected spike.
Data represent means ± SEM; each dot represents an average recording from a slice (NS = 11-13). Non-significant results are not shown for better visualisation.

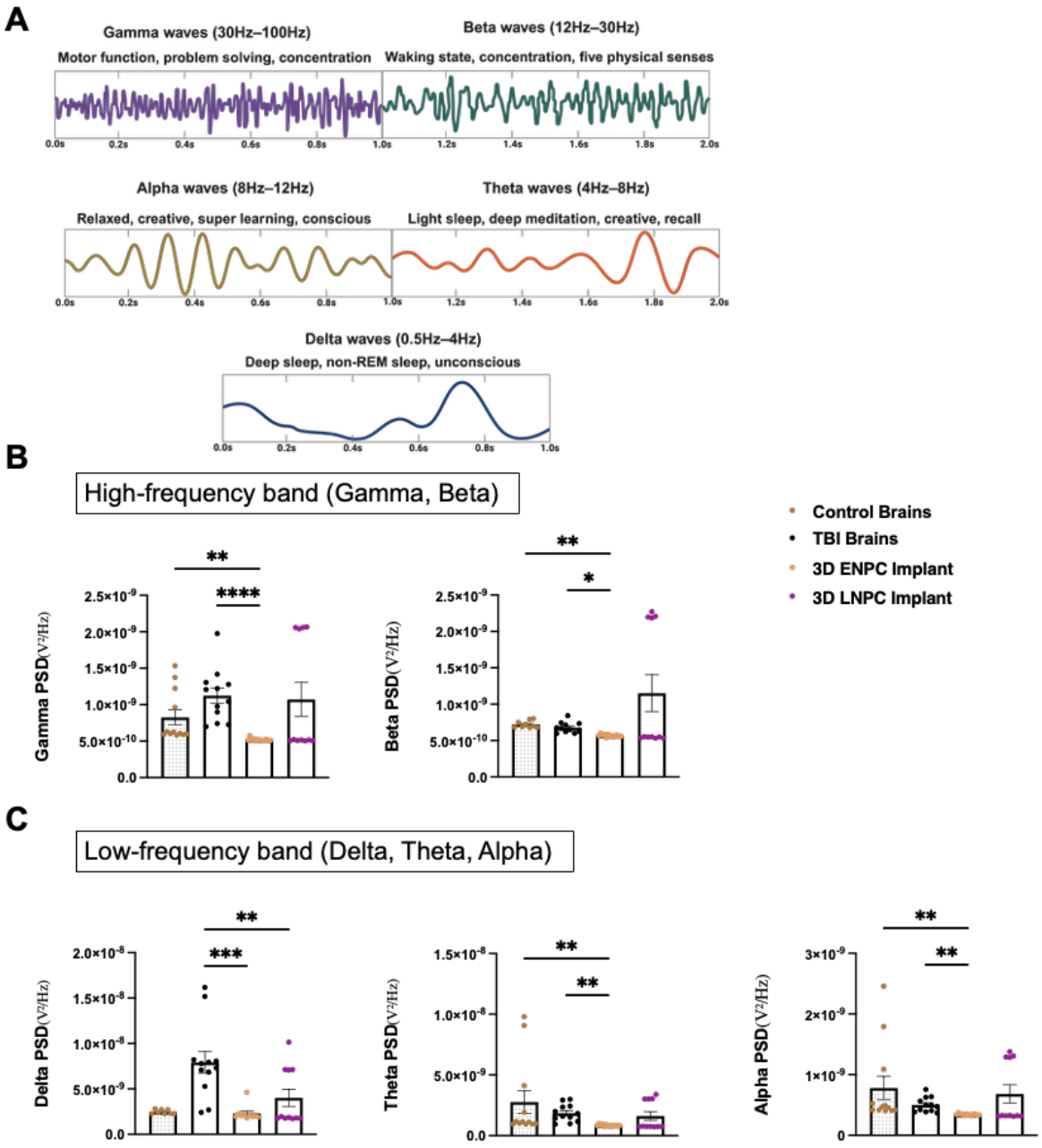

Figure 4.13 Frequency of band-specific power of brains with 3D ENPC and LNPC implants compared to TBI and control brains
(A) Illustration of traces of canonical brain rhythms: gamma (30–100 Hz), beta (12–30 Hz), alpha (8–12 Hz), theta (4–8 Hz), and delta (0.5–4 Hz). Each frequency band is shown with example oscillatory waveforms and associated cognitive and physiological functions.
(B) Quantification of PSD of high-frequency bands across groups.
(left) gamma power, brains with 3D ENPC implants vs. TBI brains ($p < 0.0001$), brains with 3D ENPC implants vs. control brains ($p = 0.009$).
(right) beta power, brains with 3D ENPC implants vs. control brains ($p = 0.0025$), brains with ENPC implants vs. TBI brains ($p = 0.0309$), brains with 3D LNPC implants vs. control brains ($p = 0.0798$).
(C) Quantification of PSD of high frequency across groups
(left) delta power, TBI brains vs. brains with 3D ENPC implants ($p = 0.0007$), TBI brains vs. brains with LNPC implants ($p = 0.0025$).
(middle) theta power, brains with 3D ENPC implants vs. control brains ($p = 0.0096$), brains with 3D ENPC implants vs. TBI brains ($p = 0.0035$).
(right) alpha power, brains with 3D ENPC implants vs. control brains ($p = 0.0022$), brains with 3D ENPC implants vs. TBI brains ($p = 0.0069$).
Data represent means ± SEM; each dot represents an average recording from a slice (NS = 9-13). Non-significant results are not shown for better visualisation.

4.3.3 Two-layered neuronal tissue recapitulates local and long-range cortical projections

Following implantation of two-layered neuronal tissue, brains were collected 2 MPI for anatomical analysis. The Neurolucida software system was used to track axonal projections across serial coronal sections, along the entire rostrocaudal axis of the brain to visualise axonal trajectories. Axonal projections of the LNPC compartment were guided by red fluorescence of RFP+ LNPCs, whereas the axonal projections of the ENPC compartment were guided by hNCAM-positive staining of unlabelled ENPCs. Two distinct colours were used to distinguish the axonal projections of the compartments during tracing, revealing distinct integration patterns across various brain regions (Fig. 4.14B). ENPC compartment exhibited broad axonal projections into multiple cortical and subcortical regions, including the striatum, thalamus, and internal capsule (Fig. 4.14B). In contrast, axonal projections from the LNPC compartment were more spatially restricted, predominantly confined to adjacent cortical layers surrounding the implantation site (Fig. 4.14B, Fig. 4.15). Semiquantitative analysis of the total projections from delineated regions revealed that the implanted two-layered neuronal tissues sent dense axonal projections into the ipsilateral cortical layers and corpus callosum, with moderate representation in the contralateral cortical layers and corpus callosum. Additionally, projections extended to multiple subcortical regions, including the striatum, thalamus, and hypothalamus. Furthermore, moderate density was detected in the CST. This widespread projection pattern suggested that two-layered neuronal tissue could recapitulate both the

connectivity of deep-layer corticofugal neurons as well as upper-layer callosal and associative cortical neurons.

However, these observations upon tracing using Neurolucida were derived from a single brain implanted with a two-layered neuronal tissue and should therefore be interpreted cautiously. Moreover, the anatomical projections were not complemented by electrophysiological recordings to confirm functional connectivity. Therefore, further experiments involving combined structural-functional analyses will be required to draw definitive conclusions about the integrative potential of the two-layered neuronal tissue.

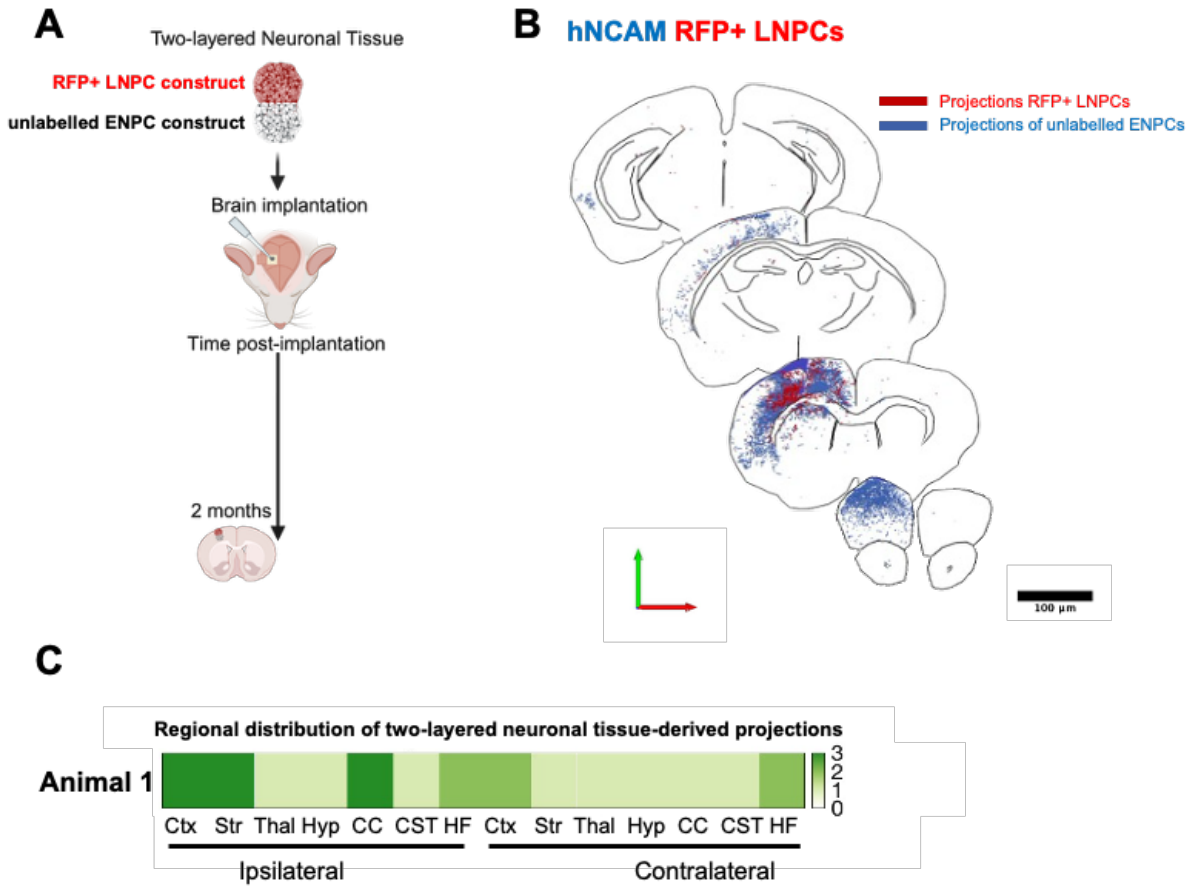

Figure 4.14 Anatomical integration of two-layered neuronal tissue at 2 MPI
(A) Schematic timeline illustrating the implantation of 3D two-layered neuronal tissue into the right motor cortex of P7-P8 NOD-SCID mice. Brains were collected at 2 MPI.
(B) Representative Neurolucida reconstructions of axonal projections across serial coronal brain sections at 2 MPI. The ENPC compartment showed dense axonal projections to various cortical and subcortical regions, as well as along white matter tracts. The LNPC compartment displayed more localised, regional distribution projections across the different layers of the cerebral cortex.

(C) Heatmap of regional distribution of the projection density of two-layered neuronal tissue into distinct ipsilateral and contralateral cortical regions, including cerebral cortex (Ctx), striatum (Str), thalamus (Thal), hypothalamus (Hyp), corpus callosum (CC), corticospinal tract (CST) and hippocampus formation (HF). Each row represents an individual animal (N = 1). Projection density was scored on a semi-quantitative scale ranging from 0 (no detectable projections) to 3 (dense projections); N=1.

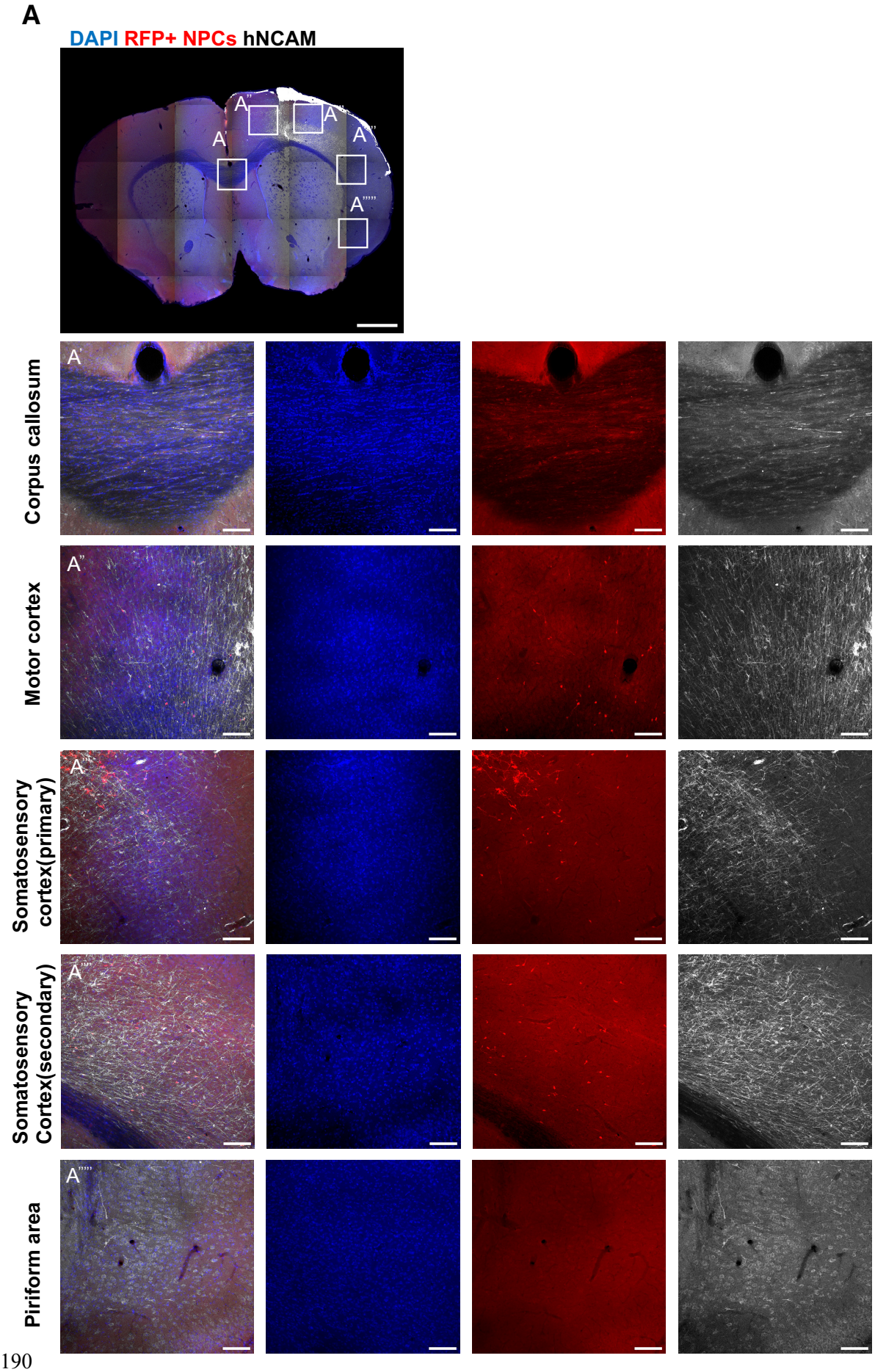
A
DAPI RFP+ NPCs hNCAM
A'
A''
A'''
A''''
A'''''
Corpus callosum
Motor cortex
Somatosensory cortex(primary)
Somatosensory Cortex(secondary)
Piriform area

Figure 4.15 Local and long-range axonal projections of the implanted two-layered neuronal tissues

(A) Representative confocal images of the brain implanted with two-layered neuronal tissue, immunostained for hNCAM to visualise the total axonal projections of unlabelled ENPCs and RFP+ LNPCs, relative to RFP+ axonal projections of RFP+ LNPCs in different brain regions. White boxes indicate regions shown in high-magnification panels A'- A''''.

High-magnification confocal images reveal the axonal distribution in selected brain regions at increasing distances from the implant site on both sides, (A') corpus callosum, (A'') motor cortex, (A''') primary somatosensory cortex, (A'''') secondary somatosensory cortex and (A''''') piriform area. Scale bar (A): 1000 μm. Scale bar (A'–A'''''): 100 μm.

4.4 Discussion

Advances in stem cell research highlight the potential of cell-based therapy as a promising therapeutic approach for TBI (Adugna et al., 2022). I hypothesised that, following TBI, implantation of 3D neuronal constructs derived from temporally specified ENPCs and LNPCs would enhance implant survival and enable identity-dependent integration with the host cortex. Furthermore, the implantation of two-layered neuronal tissue that mimics key aspects of cortical lamination could facilitate the reconstruction of cortical columnar circuits by promoting both local and long-range connectivity.

In this study, I differentiated hiPSCs into ENPCs and LNPCs, representing deep- and upper-cortical neurons, respectively. Next, I employed a droplet-based microfluidic technique to generate 3D ENPC and LNPC constructs, which were subsequently assembled into a two-layered neuronal tissue that resembled the basic aspects of the cortical lamination.

To investigate the therapeutic potential of 3D neuronal constructs in TBI, RFP+ NPC constructs were implanted into P7–P8 in NOD-SCID mice following an aspiration-induced cortical lesion. Brains were collected at 2 WPI and 2 MPI. The results demonstrated robust cell survival, progressive neuronal maturation, robust vascularisation, immune response modulation, and structural integration with the host brain. Subsequently, 3D ENPC or 3D LNPC constructs were implanted into the same TBI model and evaluated at 2 MPI. They displayed distinct axonal projection patterns that matched their neuronal identities. Finally, two-layered neuronal tissue can recapitulate key aspects of the cortical connectome, combining the corticofugal output of deep-layer neurons with the callosal and associative connectivity of upper-layer cortical neurons.

Various preclinical models exist for modelling TBI (Fesharaki-Zadeh and Datta, 2024). In this study, I employed a focal aspiration lesion targeting the motor cortex, which resulted in substantial cortical tissue loss, BBB disruption, and intracerebral haemorrhage, representing a severe form of TBI. By removing a defined brain region while sparing surrounding tissue, the aspiration model provided a reproducible cavity suitable for studying implant integration in a controlled environment.

In this study, NOD-SCID mice were used to minimise immune-mediated rejection of human xenografts, owing to impaired innate and adaptive immune status, with no additional

pharmacological immunosuppressants required (Shultz et al., 1995). However, given this relatively short endpoint, the use of a profoundly immunodeficient strain may not have been necessary for addressing the outcomes of the current study. In similar short-term transplantation paradigms, immunocompetent hosts maintained under continuous immunosuppression for the study duration have been used as an alternative strategy to support graft survival while preserving a more clinically relevant immune context (Feng et al., 2024). An alternative effective approach in this study is to use an immunocompetent model under the influence of immunosuppressive agents for the entire duration of the study (Diehl et al., 2017).

Age and the timing of implantation are key determinants of implant survival and integration. In this study, postnatal mice were selected for implantation to capitalise on the highly permissive neuroplastic environment at this postnatal developmental stage (Marzola et al., 2023). At this stage (P7-P8), the neocortex is already fully laminated, and the motor cortex has already received thalamocortical input, providing a structurally organised host environment (Vitalis et al., 2018, Fenlon et al., 2015). Immediate implantation of 3D constructs was performed following the induction of a cortical lesion. Although delaying organoid implantation by a week after cortical lesioning studies is more clinically relevant and has shown significant enhancement of implant survival and axonal outgrowth (Kitahara et al., 2020), immediate implantation offers distinct advantages. It allows the lesion cavity to be sealed before significant infiltration by inflammatory cells occurs, thereby preserving the local tissue environment and mitigating the secondary inflammatory cascade.

The three-dimensional nature of the constructs provides a major advantage over traditional cell suspension injections. Unlike dissociated cells, which lack spatial organisation, 3D constructs resembles the native architecture of neural tissue, enabling neurons to interact within a structured and physiologically relevant environment (Ulloa Severino et al., 2016). Encapsulation within Matrigel droplets protected the cells from mechanical and shear stress during implantation. This ECM also offered a supportive niche that promoted neuronal survival, structural organisation, and functional maturation. Additionally, the incubation period following fabrication allowed the neuronal network to recover and stabilise before implantation. Local implantation of 3D constructs into the cortical lesion helped overcome key challenges associated with peri-lesional injection of cell suspension, including limited cell migration and the presence of a glial scar barrier that impedes integration and survival. These combined advantages are consistent with previous studies demonstrating enhanced implant

survival and improved functional outcomes following implantation of 3D neuronal tissue (Carlson et al., 2016, Francis et al., 2020).

Different cortical regions have distinct physical properties, necessitating consideration of scaffold material and microenvironmental compatibility during the design of implantable neuronal constructs. A range of biomaterials with different compositions is available for bioprinting applications (Cadena et al., 2021, Gungor-Ozkerim et al., 2018). In this study, Matrigel was used as a scaffold material due to its supportive properties for survival and maturation of NSC (Wang et al., 2020a, Uemura et al., 2010). Consistent with previous reports on implantation of 3D brain organoid (Mansour et al., 2018, Kitahara et al., 2020, Jgamadze et al., 2023) and other engineered neuronal tissue (Latchoumane et al., 2021, Carlson et al., 2016, Tate et al., 2002), the implanted constructs demonstrated robust long-term survival for up to 2 MPI.

4.4.1 Neuroregenerative and neuromodulation properties of RFP+ NPC implants

The RFP+ NPC implants established long-range axonal projections along major white matter tracts, including the corpus callosum and internal capsule. Moreover, axonal terminals were identified in cortical and subcortical structures. These findings support the potential of these neurons to contribute to circuit reconstruction in TBI. Consistent with our findings, prior studies have demonstrated that transplanted hiPSC-derived cortical neurons in cell suspension can establish extensive, long-range projections across significant white matter tracts, reaching both ipsilateral and contralateral hemispheres (Palma-Tortosa et al., 2020). Similarly, hESC-derived cortical organoids implanted into SCID with CCI of the sensorimotor cortex extended long projections into the ipsilateral and contralateral hemispheres, with evidence of synapse formation (Bao et al., 2021).

The anatomical reconstruction was accompanied by time-dependent terminal differentiation into cortical neuronal subtypes, including SATB2+ callosal PNs and CTIP2+ subcortical PNs. The cumulative percentage of marker-positive cells exceeded 100%, which likely reflected the presence of double-positive cells, which could not be resolved due to the use of single-marker staining protocols. Similar observation of co-expression of CTIP2 and SATB2 occurs during a brief window of time postnatally in specific cortical regions as a part of dynamic refinement of neuronal identities, shortly after that vast majority of cells expressing either SATB2 or CTIP2, but not both (Alcamo et al., 2008, Harb et al., 2016).

Multilineage differentiation of transplanted cells into mature neurons, astrocytes, and oligodendrocytes has been reported (Haus et al., 2016), while another study reported lineage bias towards oligodendroglia but not neurons or astrocytes (Koutsoudaki et al., 2016). In the present study, differentiation into non-neuronal lineages was not assessed; therefore, the extent of fate potential of the implanted cells into glial lineage remains undetermined.

The balance between proliferation and maturation within the implants evolved. At 2 WPI, a higher proliferative index was observed, leading to early implant expansion. This was followed by a stabilisation phase in which neuronal differentiation and host integration became predominant. Despite the significant volumetric expansion, there was no evidence of tissue compression or midline shift, indicating that the growth was well accommodated within the injured cortical cavity and that the implant's growth rate matched that of the host brain.

4.4.1.1 Vascularisation of RFP+ NPC implants detected at 2 WPI and 2 MPI

A key challenge in achieving successful brain tissue engraftment is the establishment of a functional and stable blood perfusion, which is essential for neuronal differentiation and neurogenesis (Shen et al., 2004). In our study, widespread vascularisation was observed throughout the implants, as evidenced by CD31+ endothelial cells as early as 2 WPI and up to 2 MPI. This observation aligns with previous studies reporting host-derived vascular integration into implanted organoids in TBI models (Daviaud et al., 2018, Wang et al., 2020b). In a more recent study, progressive host-derived vascularisation of implanted organoid supported volume maintenance and reduced apoptosis (Jgamadze et al., 2023). However, the precise origin of the vasculature was not determined in this study.

The timing of vascularisation and implant expansion is an intriguing aspect to explore. A previous study reported a reduction in implant volume during the first two weeks before the establishment of vascular networks (Daviaud et al., 2018). This suggests that delayed vascularisation initially constrains implant growth, followed by an expansion phase once vascular support is established. Our observation of increased implant volume between 2 WPI and 2 MPI is consistent with this trajectory. Evaluating early post-implantation time is necessary for a more detailed understanding of early vascular dynamics.

Vascularisation may be facilitated by astrocytes that surrounded and occupied the implants. Astrocytes are known to have an angiogenic effect through VEGF secretion (Rosenstein and Krum, 2004). Additionally, they exhibit neurotrophic and neuroprotective effects (Barkho et

al., 2006) via the secretion of BDNF and NGF (Schwartz et al., 1994). These trophic effects may support the continued differentiation and proliferation of NPCs within the implants, highlighting the role of astrocytes in implant survival and integration.

4.4.1.2 Remodelling of glial reaction at two months after implantation of RFP+ NPC constructs

While most studies emphasise the angiogenic and neuroregenerative effects of stem cell-based therapies, their immunomodulatory properties remain underexplored. Nonetheless, growing evidence suggests that immune modulation may be a key mechanism underlying the therapeutic benefits of cell-based therapy for TBI. In this study, peri-implant microglial and astrocyte reactivity significantly declined by 2 MPI, reflecting an evolving immune environment consistent with the therapeutic effect of neural stem cell-based therapy (Pluchino and Martino, 2008, Fainstein et al., 2013). This finding aligns with previous studies that showed reduced glial scarring after organoid implantation (Kim et al., 2022, Bao et al., 2021).

Microglia are among the first cells to respond to CNS injuries (Donat et al., 2017, Nespoli et al., 2024). Early post-implantation, host Iba1+ microglial activation was prominent, consistent with previous reports on organoid implantation (Mansour et al., 2018, Daviaud et al., 2018). These infiltrating microglia play a crucial role in implant integration and the regenerative process. When M1-polarised microglia1 cells secrete various pro-inflammatory cytokines (Zhao et al., 2025), M2-polarised microglia promote repair through the release of neurotrophic factors, including NGF, BDNF, and GDNF, thereby facilitating angiogenesis, neuronal survival, and remyelination (Hu et al., 2015).

At 2 WPI, there were abundant reactive astrocytes in the peri-implant cortex, consistent with glial reaction to injury (Nespoli et al., 2024). The fundamental role of reactive astrocytosis after brain injury is to maintain homeostasis in the CNS through creating a physical barrier between damaged and healthy tissues (Silver and Miller, 2004, Cieri and Ramos, 2025), increasing the BBB integrity (Faulkner et al., 2004), clearing excess extracellular glutamate (Zou et al., 2010), and stabilising extracellular fluid and ion balance (Sofroniew and Vinters, 2010).

4.4.2 Cortical identity-guided integration of 3D ENPC and LNPC implants

Effective brain repair requires specificity in circuit reconstruction and the avoidance of off-target connections that can disrupt brain function. This specificity can be achieved by employing neurons with pre-defined identities. 3D ENPC implants, enriched in CTIP2+ PNs,

extended long-range axonal projections targeting both cortical and subcortical regions, in addition to CST, supporting their functional identity as deep-layer PNs (Leone et al., 2008). Prior work has shown that CTIP2-enriched organoids generate extensive axonal projections along the host CST by 12 WPI (Kitahara et al., 2020).

In contrast, 3D LNPC constructs**,** enriched in SATB2+ neurons, exhibited corticocortical projection profiles. Their axons were primarily confined to adjacent cortical regions, consistent with their role in intracortical signalling (Leone et al., 2008). These distinct patterns supported the notion that the intrinsic identity of the implants strongly influenced the eventual projection pattern and structural integration. In conjunction with the long- and short-range axonal projections exhibited by 3D ENPC and LNPC implants, respectively, synaptogenesis was evidenced by the juxtaposition of hSYP and PSD-95, supporting the potential of functional integration. Similar observations of synaptogenesis have been reported with organoid implantation (Wang et al., 2020b, Bao et al., 2021).

In addition to their distinct projection patterns, 3D ENPC and LNPC implants elicited differential host glial responses, suggesting that neuronal identity may also influence immune modulation post-implantation. GFAP was quantified in predefined regions at the graft–host interface, as this boundary provides the relevant information for assessing reactive astrogliosis that could affect graft survival, neurite outgrowth, and host–implant interactions. To minimise sampling bias, regions of interest were positioned using a pre-defined, standardised approach across all sections and groups, sampling approximately two-thirds peri-implant host tissue and one-third implant tissue, rather than being selected on the basis on GFAP signal intensity. The lateral edges of each implant were systematically sampled, with two regions per side imaged. The dorsal surface of the implants was excluded due to disproportionately high GFAP staining, likely reflecting meningeal effects that are not directly comparable to the parenchymal interface and could therefore skew between-group comparisons (Moumdjian et al., 1991). This standardised approach effectively accounted for the distribution of GFAP and enabled robust, anatomically matched comparisons between experimental groups.

Quantitative analysis of astrocytes and microglia within peri-implant regions revealed that brains with 3D LNPC implants exhibited the lowest astrocytic reactivity, while Iba1+ microglial density was also slightly reduced compared with 3D ENPC implants. These results suggested that 3D LNPC implants, which integrated more locally, provoked a milder glial

response than 3D ENPC implants, which exhibited broader subcortical projections. These findings suggested that neuronal subtype influenced not only anatomical and functional integration but also the local inflammatory environment, a critical factor in long-term graft acceptance.

Collectively, 3D ENPC and LNPC implants demonstrated comparable survival and volume expansion but exhibited distinct integration patterns and differential glial response. These differences in axonal targeting and potential network reconstruction highlight the importance of matching cell type with therapeutic goals.

4.4.3 Electrophysiological profiles of cortical slices at 2 MPI after 3D ENPC or LNPC implantation

There was no difference in the spontaneous firing rate between the control and TBI cortices recorded from *in vitro* slices. This aligns with cortical reports showing no change in the incidence of spontaneous firing after TBI (Feng et al., 2021). Similarly, there was no significant difference in bursts across groups recorded from the cortical areas, consistent with previous reports indicating that the cortex is less prone to significant changes in spontaneous activity, including rate and duration, than the hippocampus (Kang and Morrison, 2015).

Despite similar firing rates, TBI brains exhibited shorter ISIs than those implanted with LNPC constructs, suggesting neural hyperexcitability after TBI. This finding is consistent with previous reports of focal somatosensory cortical injury, which causes a suppression of cortical responses followed by an imbalance in excitation and inhibition in the chronic post-injury phase, manifesting as hyperexcitability (Ding et al., 2011). This hyperexcitability is attributed to a decline in GABA release, likely due to the loss of superficial inhibitory INs (Yang et al., 2007). The lengthening of the ISI in brains with LNPC implants relative to TBI brains aligns with previously published data on increased inhibitory tone and suppression of hyperexcitability after the integration of grafted cortical progenitor cells (Zhu et al., 2023). Although I have not implanted pure INs, the implants contained a mixture of glutamatergic and GABAergic INs, as discussed before in Chapter 2.

PSD of gamma waves is associated with higher-level cognitive tasks, such as information processing and brain connectivity, as recorded by EEG (Medithe and Nelakuditi, 2016). In chronic TBI, gamma power findings are heterogeneous across modalities; some cohorts show increased resting gamma, others report reduced gamma synchrony (Huang et al., 2020, Vakorin

et al., 2016). Magnetoencephalograms (MEG) studies of chronic human TBI reported a marked increase in resting gamma, which associates with poorer executive performance and visuospatial processing (Huang et al., 2020). Similarly, in a preclinical study, global increases in absolute EEG power were observed across most frequency bands, including gamma, delta, theta, alpha, and beta at chronic time points following injury (May et al., 2023).

Conversely, other studies reported reduced network connectivity in gamma frequency ranges within 3 months of injury, as observed in resting-state MEG from adults with TBI (Vakorin et al., 2016). Our MEA data align with this complexity; TBI brains showed no significant differences in gamma power at 2 MPI compared to the control brains. The brains with ENPC implants exhibited the lowest gamma power, while brains with LNPC implants and TBI brains had levels comparable to the control brains. This difference highlights the methodological dependence and the distinction between *in vivo* and *in vitro* recording of brain waves. In acute brain slices, long-range feedback and feedforward projections are severed, altering the absolute band power. Moreover, a cautious interpretation of the high-frequency data is warranted in this context because slices lack the different state transitions, such as sleep, arousal, and locomotion, that strongly reshape the *in vivo* power spectral density.

Brains with 3D LNPC implants showed a non-significant increase in gamma power relative to brains with ENPC implants and levels comparable to those of the control and TBI brains. This increase in gamma may reflect better local circuit integration of LNPC implants with the host brain. It has previously been demonstrated that gamma oscillations can be modulated by treatment. In cases where TBI reduces gamma oscillations, 40 Hz Blue LED therapy restores reduced cortical gamma activity and significantly improves performance on the modified neurological severity score (Yang et al., 2022). Similarly, in clinical trials, transcranial direct current stimulation (tDCS) combined with cognitive training has been shown to positively influence neuroplasticity and functional connectivity in prefrontal regions and to be associated with increased gamma power detected by EEG (Afsharian et al., 2024).

The levels of beta power after TBI were comparable to those in control brains, while brains with 3D ENPC implants exhibited reduced beta power relative to both control and TBI brains. In brains with 3D LNPC implants, beta power was comparable to control brains, with a non-significant difference. An increase in beta power has been previously reported in association

with therapeutic interventions and improvements in cognitive performance in clinical trials (Afsharian et al., 2024).

In this study, Delta power was highest in TBI brains, and brains with 3D ENPC and LNPC implants had significantly lower delta power than TBI brains. This finding partially aligns with previous reports where TBI rats exhibited a trend toward increased delta power compared to sham rats (Mountney et al., 2021). Alpha or theta power in TBI brains did not differ significantly from controls. Clinical studies showed that patients with post-injury syndrome displayed a decrease in alpha frequency as recorded by EEG (Kadri and Apriani, 2022) and other reports have shown a reduced alpha-band power bilaterally in the frontal lobes, as measured by MEG, following TBI (Popescu et al., 2016). Additionally, rats with LFPI demonstrated deficits in hippocampal theta activity, characterised by a significant attenuation of theta power (Fedor et al., 2010).

The reduction in delta power in brains with 3D ENPC and LNPC implants may indicate some modulation in cortical network, consistent with a shift away from post-injury cortical slowing and towards functional reorganisation associated with implant integration. This aligns with previously published data that associates recovery and improved cognition with decreased delta power, measured with EEG in the medial frontal cortex following transcranial magnetic stimulation (Durbin et al., 2023). The lower bands, alpha and theta, were lowest in brains with 3D ENPC implants, whereas brains with 3D LNPC implants exhibited levels close to those of control brains. This increase in alpha and theta power with LNPC implants is consistent with previous reports of increases with therapeutic intervention and improvement in cognitive function (Afsharian et al., 2024). Similarly, in a clinical study, tDCS has been shown to beneficially modulate cortical excitability, with EEG results indicating a decrease in delta activity and an increase in alpha activity, alongside cognitive benefits (Ulam et al., 2015).

Collectively, at 2 MPI, 3D LNPC implants were found to have a more positive impact on cortical network dynamics than 3D ENPC implants. 3D LNPC implants were associated with prolonging the inter-spike intervals, increasing spike amplitudes, and reducing delta power, while bringing alpha, theta, and beta activity closer to normal levels. Additionally, gamma power in brains with LNPC implants was comparable to that in control and TBI brains and higher than in brains with 3D ENPC implants but did not reach statistical significance. On the other hand, 3D ENPC implants seemed to generally suppress oscillatory activity across various

frequency bands, and this suppression didn't lead to improvements in spike timing or amplitude. This might indicate weaker local synaptic engagement of the 3D implants.

The 3D LNPC implants group showed consistently higher values across several readouts, giving the visual impression that this dataset skewed the group distribution. Importantly, this recording was not formally classified as an outlier and therefore was retained in the analysis. This pattern reflects a common feature of acute ex vivo MEA recordings, in which multiple technical and biological factors can introduce substantial variance between slices, including electrode–tissue contact, subtle differences in slice thickness, and the extent and location of the implant relative to the array. To ensure that the group-level conclusions were not dependent on a single dataset, future studies should increase cohort size to better capture the true variance in implant-driven network activity.

4.4.4 Two-layered neuronal tissues reconstruct local and long-range cortical connections

Anatomical mapping of axonal trajectories of implanted two-layered neuronal tissue revealed distinct integration patterns between the ENPC and LNPC compartments. Consistent with their developmental origins, ENPC compartments exhibited extensive projections extending into both cortical and subcortical regions, including the striatum, thalamus, and internal capsule, indicative of a deep-layer corticofugal phenotype (Molyneaux et al., 2007). In contrast, LNPC compartments displayed more confined projections to adjacent cortical layers and the corpus callosum, aligning with the connectivity pattern of upper-layer callosal and associative neurons (Britanova et al., 2008). These projections, together, reconstruct local and long-range cortical connections

This widespread projection pattern suggested that two-layered neuronal tissue can reestablish aspects of cortical lamination and associated connectivity, with ENPC compartments exhibiting long-range efferent pathways and LNPC compartments supporting local and interhemispheric communication. However, these observations were derived from a single implanted brain, and the conclusions remain preliminary. This anatomical integration provides the potential of host-implant integration, and electrophysiological recordings are needed to confirm functional connectivity.

During implantation of the 3D ENPC and LNPC constructs, the ideal scenario is to align the construct with the corresponding cortical lamina. This alignment enables investigating how

layer-specific cues influence graft differentiation and integration. However, precisely placing 3D constructs into either superficial or deep cortical laminae is technically challenging, even with standardisation of lesion size. Deeper placement typically requires traversing more superficial tissue, which may itself alter the local microenvironment and confound interpretation of layer-dependent effects.

Implantation of two-layered neuronal tissues introduces an additional challenge: maintaining precise orientation. Here, fluorescence imaging was employed to distinguish superficial from deep compartments, providing a practical guide for surgical alignment. Nonetheless, some degree of rotation or misalignment can occur during placement and wound closure. Such misorientation is important to consider, as it may expose each compartment to an unintended microenvironment, potentially influencing survival, maturation, and host innervation patterns independently of the original ENPC/LNPC identity.

To address this limitation, future experiments should incorporate explicit orientation controls, such as an inverted double-layer group in which the ENPC/LNPC order is deliberately reversed. These controls would clarify whether observed outcomes are driven primarily by cell identity or by superficial–deep positioning and would enable systematic assessment of how compartment-lamina mismatches influence graft integration.

4.4.5 Limitations and future directions

While this study demonstrated the integrative potential of 3D neuronal constructs, still limitations that should be acknowledged, and future directions can be identified to further advance this work.

One of the limitations of the study is the age of the mice used for modelling TBI and further implantation, which was P7–P8. Cross-species neurodevelopmental benchmarking aligns rodent P7–P8 with a human late-preterm period, ~30–34 gestational weeks, rather than the mature brain (Semple et al., 2013). At this stage, the rodent brain is undergoing rapid growth and circuit assembly with ongoing glial proliferation, early myelination, and an evolving E/I balance that can be disrupted by injury, yielding pathophysiology that is not directly comparable to that of adolescent and adult TBI (Delage et al., 2021a). Therefore, this model is very relevant to immature perinatal brain injury; this developmental mismatch should be recognised as a limitation, as it does not reflect the age distribution of TBI in humans (Lele, 2022). To strengthen translational interpretation, future work should investigate key outcomes

in older injury models to test whether graft survival, differentiation, and integration patterns are conserved across developmental stages.

Incorporating additional cell types such as GABAergic INs, astrocytes, oligodendrocytes, or endothelial cells could further enhance circuit complexity, support synaptic integration, promote myelination, and improve vascularisation, thereby advancing the functional maturation of the constructs *in vitro* and improving outcomes following *in vivo* implantation. In a parallel experimental study, we are exploring the incorporation of murine astrocytes into 3D constructs containing hiPSC-derived NPCs. Astrocyte-NPC implants exhibited enhanced neuronal maturation *in vitro* with promising results upon implantation, including robust axonal growth and evidence of astrocyte coupling to blood vessels within the implants compared to NPC-only implants. These findings underscore the pivotal role of astrocytes in facilitating neuronal tissue integration.

Another direction that can be investigated is comparing *in vivo* 3D implants with their *in vitro* counterparts at equivalent stages of maturation to assess whether the host environment accelerates or modifies neural circuit development of the constructs. This study did not directly address this question, but they are critical for understanding the influence of host environment on construct maturation after implantation.

Moreover, injury-scaffold matching may improve anatomical compatibility and integration. Advances in imaging and biofabrication, such as MRI-guided 3D printing, offer the possibility of tailoring scaffold geometry to the exact dimensions of cortical lesions (Fu et al., 2017). The feasibility of applying this approach to variable lesion sizes or multi-site injuries remains an open question that warrants further exploration.

Two-layered neuronal tissue offers a promising strategy for re-establishing cortical columnar circuitry following TBI. However, the lack of cellular polarity is an important limitation to acknowledge. The apical dendrites of deep-compartment PNs have not observed to traverse the overlying LNPC compartment to reach the pial surface of the brain, thereby limiting the formation of canonical cortical microcircuits. In the intact cortex, the dendrites of pyramidal cells of layer V cluster and ascend through layer IV, reaching layer I along with other dendrites from layers II and III (Molnár and Rockland, 2020). The apical dendrite orientation and interactions with upper-layer neurons are critical for input integration and cortical computation (Spruston, 2008). Therefore, future strategies should aim to generate laminated neuronal tissue

with preserved cellular polarity to better recapitulate the functional organisation of the cerebral cortex.

At the time of thesis submission, analysis of the two-layer neuronal tissue cohort was limited to a single animal. This work was conducted collaboratively, and the remaining samples could not be processed to the same analytical standard before submission. Progress on the remaining work was further delayed by equipment failure, a broken microscope, which prevented the acquisition of additional imaging datasets. As a result, only one animal provided complete and analysable imaging data at submission. This limitation is fully acknowledged, and the results for two-layered neuronal tissues were presented as preliminary and descriptive rather than as a powered group-level comparison.

In summary, this study provides strong evidence for the viability and integrative potential of 3D neuronal constructs following implantation into a TBI model. These findings support the concept of using developmentally patterned, layered cortical tissues to reconstruct disrupted cortical column circuits. Future work should focus on optimising implant composition, refining transplantation strategies, modulating host responses, and evaluating long-term functional outcomes to advance the clinical translation of this approach.

4.5 Conclusion

Implantation of RFP+ NPC constructs into the postnatal TBI model demonstrated robust survival, progressive neuronal differentiation, and anatomical integration. The implants grew without disrupting surrounding brain structures, exhibited early and stable vascularisation, and showed a temporal decline in proliferation and apoptosis. Implant-derived projections extended across major white matter tracts, reaching cortical, subcortical, and subcerebral targets. These findings provide strong evidence that NPCs within a supportive 3D microenvironment can survive *in vivo* and may contribute to *in vivo* circuit repair.

Implantation of 3D ENPC and LNPC constructs further highlighted the importance of developmental origin in shaping projection patterns and host integration. 3D ENPC implants preferentially targeted subcortical regions and white matter pathways, consistent with their deep-layer CTIP2+ identity, while 3D LNPC implants exhibited localised cortical projections aligned with their SATB2+ upper-layer identity. Both implant types displayed stable volumes but diverged in the spatial targeting of axons. These findings support the rationale for using

regionally specified neuronal subtypes to achieve targeted reconstruction of cortical circuits. The MEA data indicated that 3D LNPC implants led to longer ISIs, higher spike amplitudes, decreased delta power compared to TBI brains, and helped restore alpha, theta, and beta activity toward normal levels, suggesting enhanced local network dynamics. In contrast, ENPC implants broadly suppressed oscillatory activity across frequency bands without improving spike timing or amplitude under our recording conditions.

The layered organisation offers a promising strategy for approximating aspects of cortical connectivity after implantation. The two-layered neuronal tissue, composed of assembled ENPC and LNPC constructs, successfully mimicked certain aspects of the laminar architecture of the cerebral cortex and exhibited a widespread projection profile. The ENPC compartment projected to distant subcortical targets, while the LNPC compartment maintained local cortical projections.

Together, these results provide compelling evidence that 3D neuronal constructs, implanted into TBI, can survive, mature, vascularise, and integrate into the host brain. The distinct projection patterns driven by cell identity reinforce the importance of matching neuronal subtype to therapeutic goals. Nevertheless, this study provides the first attempt to generate the fundamental units of cerebral cortical tissue, providing a foundation for personalised, anatomically guided neural repair strategies following cortical injury.

Chapter :5 General Discussion

5.1 General findings

In this DPhil project, I developed a platform to generate human cortical neuronal progenitors and assemble them into 3D engineered neural tissues. hiPSCs were differentiated into ENPCs and LNPCs, which broadly align with deep- and upper-layer cortical projection neuron identities, and these populations were then biofabricated using a droplet-based microfluidic approach to produce 3D ENPC and LNPC constructs. These constructs were additionally assembled into simplified two-layer neuronal tissues to approximate key aspects of cortical lamination. The hypothesis underlying this work was that implanting 3D neuronal constructs derived from temporally specified ENPCs and LNPCs would improve implant survival and enable integration with the host cortex based on cell identity. Additionally, implanting two-layered neuronal tissue could facilitate the reconstruction of cortical columnar circuits by promoting both local and long-range connectivity. This work shows that temporal patterning shaped not only marker expression but also network behaviour in 2D culture and 3D cortical tissues. In vivo, implanting 3D ENPC and LNPC constructs into an aspiration lesion model showed that these engineered tissues can survive, mature, and form distinct projection patterns within the injured brain based on cell identity, supporting the feasibility of transplanting 3D neuronal constructs. Building on this, the two-layer constructs also offered a preliminary platform that replicates the complementary behaviours of deep and upper layers in vivo.

Collectively, the current findings support the therapeutic potential of identity-specified, 3D neuronal constructs for cortical circuit reconstruction following TBI. To advance this approach toward clinical translation, several key stages must be addressed within a structured framework for cell-therapy development.

5.2 Limitations and future directions

While these findings demonstrate feasibility, important biological, technical, and translational challenges remain. Below, I critically evaluate these limitations and suggest future directions.

5.2.1 Cell source

In this study, I utilised human iPSCs, which bypass ethical concerns associated with ESCs and hold potential for autologous transplantation (Takahashi et al., 2007). Nevertheless, several

challenges remain. A key issue is genomic instability, along with the associated risk of tumourigenesis (Yamanaka, 2020). The tumourigenic potential is strongly influenced by the reprogramming approach. Using c-MYC transgenes and integrating vectors, whether retroviral or lentiviral, increases the risk of insertional mutagenesis. In contrast, non-integrating methods, such as Sendai RNA virus, adenovirus, or episomal plasmids, substantially mitigate this risk (Schlaeger et al., 2015). Although autologous transplantation is theoretically achievable with iPSC-derived grafts, a major translational concern is the potential for immunogenicity. De novo mtDNA mutations can arise during reprogramming or long-term culture, generating immunogenic neoepitopes that elicit immune responses even in genetically matched, autologous settings (Deuse et al., 2019). This highlights the importance of screening for genetic and mitochondrial integrity in iPSC-derived neurons before clinical use.

Establishing patient-specific autologous iPSC lines remains time-consuming and costly, limiting their clinical scalability. Two alternative strategies have been proposed to overcome this challenge. The first involves genetic modification to generate universal donor cell lines with reduced expression of human leukocyte antigens (HLA). The second is the development of iPSC haplobanks, where selected homozygous lines for common HLA haplotypes are stored. From these, HLA-matched therapeutic products can be derived for a broad proportion of the population (Turner et al., 2013, Sullivan et al., 2020). Both approaches have the potential to enhance scalability, lower manufacturing costs, and improve the clinical applicability of iPSC-based therapies.

A limitation of this study is the use of a single iPSC line (AH016-3). It is well established that ESC and iPSC lines exhibit significant variation in differentiation efficiency, maturation stages, and functional properties, suggesting that the robustness of our findings would be strengthened by validation across multiple lines (Hu et al., 2010). Only a single hiPSC line was used for the core experiments in this thesis to minimise biological and technical variability while establishing the feasibility of the differentiation and biofabrication pipeline. iPSC lines can differ substantially in baseline epigenetic state and differentiation propensity, meaning that incorporating multiple lines would introduce additional variance and require a much larger experimental design to distinguish true biological effects from line-to-line effects. Within the scope of this project, prioritising one well-characterised line allowed optimisation of the protocol, consistent production of ENPC and LNPC populations, and systematic evaluation of 3D construct formation and implantation outcomes under controlled conditions. This choice is

therefore a pragmatic limitation; although it strengthens internal consistency, it restricts the immediate generalisability of the findings across genetic backgrounds.

To address this limitation, parts of the workflow were repeated using hESCs, providing preliminary evidence that the approach is not strictly confined to a single hiPSC line. However, these hESC experiments were not designed as a direct comparative study and were therefore not included in the thesis as a formal line-to-line evaluation. Future work should extend the analysis to multiple hiPSC lines with direct comparisons to quantify robustness and identify any line-dependent effects on neuronal subtype specification, construct behaviour, and in vivo integration.

Another limitation involves the characterisation of the ENPCs and LNPCs used in this study. I used only a few layer-specific markers to define laminar identity, which do not fully reflect the molecular diversity of upper- and deep-layer neuronal populations. Moreover, I did not directly compare these cells with human in vivo–derived upper- and deep-layer cortical neurons at comparable developmental stages. As a result, it is uncertain to what extent the cells mimic the complete transcriptional and functional profiles of native cortical neurons. Future research should incorporate more comprehensive molecular profiling, such as single-cell transcriptomics, alongside electrophysiological studies, compared with primary human tissue.

5.2.2 Stage of differentiation and composition of the implants

hiPSC-derived ENPCs and LNPCs expressed layer-specific markers, yet retained proliferative capacity, indicating the persistence of progenitor cells. Thus, the implants represented a heterogeneous composition rather than a pure population of post-mitotic neurons. A more precise quantification of the ratio between progenitors and different neuronal phenotypes would provide important insights into how cellular composition influences laminar identity and functional outcomes after implantation. Therefore, single-cell transcriptomics of the constructs should be compared with single-cell atlases of the developing human cortices at various stages of maturation.

The stage of neuronal differentiation significantly influences implant outcome. NPCs and NSCs are widely favoured for transplantation because of their scalability and plasticity (Ottoboni et al., 2017). However, their fate and integration are largely dictated by host environmental cues, which reduces the degree of experimental control (Ludwig et al., 2018). In contrast, post-mitotic neurons are less plastic and more fragile, making dissociation and

implantation a technically challenging process (Ottoboni et al., 2017). A mixed population of progenitors and differentiated neurons may therefore offer an optimal balance. Progenitors can provide trophic and structural support while gradually maturing in vivo, whereas differentiated neurons can integrate immediately into host circuitry and shape the differentiation trajectory of neighbouring progenitors (Chau et al., 2016, Revah et al., 2022). In principle, this mixed population could deliver both rapid and sustained therapeutic benefits.

Cells can be genetically engineered to enhance their neuroprotective and immunomodulatory functions. For example, MSCs engineered to overexpress IL-10 have been shown to improve functional recovery in TBI models by reducing inflammation (Peruzzaro et al., 2019). Similarly, Genetic modification of transplanted NSPCs, whether by overexpressing neurotrophins such as NGF or BDNF, or transcriptional regulators like CEND1, enhanced survival, neuronal fate commitment, and synaptic integration with functional recovery (Ma et al., 2012, Wang et al., 2022b, Makri et al., 2010, Philips et al., 2001). Collectively, these findings underscore the therapeutic potential of augmenting cell-based therapies through genetic modification to enhance their anti-inflammatory and neurotrophic properties. However, further systematic studies are required to refine optimal targets and assess long-term safety.

5.2.3 Bioink and scaffold considerations

My study did not directly investigate the effects of various bioinks and the impact of the ECM on development, differentiation, and integration. While Matrigel offers considerable experimental utility as a bioink, its xenogeneic origin raises substantial barriers to clinical translation. Key concerns include antigenicity and the potential risk of pathogen transmission (Liu et al., 2011, Peterson, 2008). Furthermore, inconsistencies between batches or even within the same batch in biochemical and mechanical properties challenge the reproducibility (Vukicevic et al., 1992, Hughes et al., 2010, Reed et al., 2009), further limiting its translational potential. Therefore, future efforts should focus on replacing Matrigel with clinically compliant ECM analogues that are biocompatible, pathogen-free, xeno-free, and capable of recapitulating the structural and biochemical features of the native ECM. Such alternatives must also be scalable, consistent, and suitable for supporting the functional integration of engineered neural tissues in therapeutic applications (Cadena et al., 2021, Sensharma et al., 2017).

In my study, I successfully generated two-layered neuronal tissues that recapitulated some basic elements of cortical lamination. A next step would be the fabrication of more complex

multilayered tissues incorporating diverse neuronal and glial populations, thereby providing a close approximation of native cortical organisation. Achieving this will require greater precision in both cell differentiation and spatial positioning, which in turn may benefit from advanced bioprinting strategies with higher spatial resolution and more accurate cell patterning.

5.2.4 Implantation paradigm and peri-operative care

In this study, constructs were implanted one week after fabrication, a timeframe that was likely sufficient for initial cellular recovery but may have been inadequate for progenitors to fully establish layer-specific identities *in vitro*. The effect of different pre-implantation timeframes was not studied; therefore, future studies should explore the optimisation of the interval between construct generation and implantation to balance graft viability with the acquisition of laminar fate.

In this study, I employed NOD-SCID mice for the host model because they lack adaptive immunity and NK cells, providing a permissive environment for human graft survival (DiSanto et al., 1995, Chen et al., 2022). However, the innate immune system remains intact, with resident microglia and astrocytes still functional, and can elicit local inflammation in response to the surgical injury and the grafts. Thus, NOD-SCID mice serve as a model for optimising implant survival and preventing rejection; however, they do not recapitulate the full complexities of the immune system.

From a translational perspective, the use of immunocompetent hosts in combination with immunosuppressive regimens is more clinically relevant. However, careful optimisation is essential, since inappropriate drug choice or dosing may compromise implant viability. *In vitro*, it has been demonstrated that Cyclosporine A and Mycophenolate Mofetil (MPA) exert strong anti-proliferative and pro-apoptotic effects, while also suppressing neurogenesis at clinically relevant concentrations. In contrast, Everolimus and Prednisolone cause minimal apoptosis and only modest effects on proliferation and differentiation at therapeutic doses (Skardelly et al., 2013). In vivo, an immunosuppressive cocktail consisting of Tacrolimus, methylprednisolone, and MPA effectively prevented immune rejection and enabled robust hNSCs survival and long-term engraftment up to 16 WPT (Spurlock et al., 2017). Conversely, hMSCs promoted comparable structural protection and functional recovery in both immunosuppressed and immunocompetent mice, independent of immunosuppression (Pischiutta et al., 2014). Taken

together, these findings underscore the importance of tailoring immunosuppressive protocols to the type of implant and the recipient's immune status in future experiments.

All surgical procedures were performed on postnatal mice, when the neocortex is laminated (Vitalis et al., 2018, Fenlon et al., 2015), allowing constructs to be implanted into a structurally organised yet highly plastic environment (Marzola et al., 2023). However, this age does not recapitulate the pathological complexity of adult TBI (Semple et al., 2013) and does not accurately reflect the epidemiology of TBI in the population (Lele, 2022). To enhance translational relevance, future studies should include adolescents, adults, and the geriatric TBI models to capture the age-dependent variability.

In this study, implantation was performed during the acute phase of injury, immediately after lesioning the cortex, to seal the lesion cavity before extensive inflammatory infiltration, aiming to preserve the local environment and mitigate secondary inflammatory cascades (Shang et al., 2022). Although transplantation of NSCs within the acute window can enhance motor recovery and increase synaptic plasticity (Xiong et al., 2018, Ma et al., 2012), the subacute phase is widely considered the favourable window for transplantation (Shang et al., 2022). Additionally, cell therapy in the chronic phase of TBI offers opportunities for neuronal differentiation and modulation of glial responses (Shang et al., 2022). From a clinical perspective, delayed therapeutic interventions could also benefit patients who do not receive treatment within the narrow early neuroprotection window. Future studies should therefore directly compare acute, subacute, and chronic implantation protocols in matched models to define the optimal therapeutic window for clinical translation.

I have utilised the aspiration model of TBI, which provides a controlled method for generating a precise focal cortical lesion, but it lacks the mechanical forces and diffuse axonal injury characteristic of clinical TBI (Xiong et al., 2013). As a result, this model does not capture the full cascade of excitotoxicity, neuroinflammation, and secondary injury that influence patient outcomes. While aspiration lesions are useful for studying cortical reconstruction, their translational relevance is limited, and the use of other injury models better recapitulates the multifactorial nature of TBI.

Implantation and handling of 3D constructs are technically demanding, making standardisation of surgical parameters essential for comparability and safety. Critical variables include the choice of surgical instruments that delicately handle the engineered tissue without damaging

it, which may require the development of new surgical tools for this empirical step. Additionally, the time interval between handling of the 3D construct and implantation must be considered and validated, as abrupt transitions from culture to the brain environment can impose significant stress on the implants (Gobbel et al., 2010). Further complexity arises with the implantation of patterned neuronal tissues, where correct orientation is critical to preserve laminar architecture. In stereotactic implantation, multiple parameters directly influence implant viability and integration, including needle gauge, tip geometry, infusion rate, carrier viscosity, and post-implantation dwell time (Kondziolka et al., 2011). The needle must be appropriately sized for the implant and designed with materials and linings that minimise friction. Flow rates should be carefully balanced, sufficiently strong to advance the implant, yet delicate enough to avoid excessive shear stress or compression of the surrounding tissue. Likewise, the choice of carrier vehicle is crucial, as an appropriate medium can reduce mechanical damage and facilitate smooth delivery of the implants.

Developing effective post-operative care is essential for both optimising surgical outcomes and enabling early detection of adverse effects. In this study, animals were monitored daily during the first post-operative week and then weekly until the end of the experiment, allowing for the detection of both acute and chronic complications while ensuring animal welfare. Beyond surgical management, combining cell therapy with pharmacological agents may promise to enhance therapeutic efficacy. It has been shown that when BM-MSCs transplantation was combined with the inhibition of Calpain, one of the earliest pro-inflammatory mediators upregulated after neurotrauma, it reduced neuroinflammation and graft apoptosis, improved cell survival, and ultimately enhanced functional recovery compared with untreated controls (Hu et al., 2019).

It is also important to recognise that standalone cell therapy, as tested in preclinical trials, does not reflect the multidrug treatment protocols commonly employed in clinical TBI management. Clinical management of TBI frequently involves the concurrent use of multiple drugs for comorbidities or complications of multi-trauma. Moreover, the impact of multidrug regimens on grafted cells at sites where the BBB is compromised is poorly understood, particularly for highly sensitive, culture-derived neurons. Preclinical studies are therefore necessary to evaluate the safety and efficacy of combination regimens under conditions that more closely mirror the clinical setting.

Although anatomical integration and synaptic marker expression were observed in this study, definitive evidence of functional implant-host communication will require electrophysiological validation via patch-clamp analysis or calcium imaging. In parallel, behavioural testing using motor and cognitive assays in TBI models will be necessary to determine whether implanted constructs contribute to functional recovery. Developing approaches for the targeted activation and inactivation of integrated implant-host circuits, such as optogenetic approaches, alongside behavioural testing, will be essential to provide the functional contribution of the implants.

In the present study, infiltrating cells were not comprehensively studied beyond the glial reaction at the host-implant interface; therefore, the cellular composition of infiltrates, including recruited macrophages and microglia, and the presence of oligodendroglia lineage remains to be defined in future work using lineage- and origin-resolved markers. Several transplantation studies showed that implant-derived axons can become myelinated in vivo. Strong proof-of-principle that human pluripotent stem cell–derived cortical grafts can generate myelinating oligodendrocytes was shown in a rat stroke model, where grafted human iPSC-derived cortical neurons extended long-range axons, and immuno-electron microscopy demonstrated myelin ensheathment of graft-derived axons (Palma-Tortosa et al., 2020). In the same study, MBP-positive fibres close to the graft could be co-labelled with human-specific markers, consistent with functional donor-derived oligodendroglia contribution (Palma-Tortosa et al., 2020). Complementing this, a subsequent study using a cortically patterned human iPSC-derived NPCs showed that grafts can generate mature, myelinating oligodendrocytes with EM evidence of graft-associated myelin in vivo and in human cortical organotypic cultures (Martinez-Curiel et al., 2023). Importantly, the detection of oligodendrocyte-lineage markers; such as OLIG2 or PDGFRα, in or around a graft does not demonstrate functional myelination; this requires direct evidence of myelin sheaths ensheathing axons, ideally supported by myelin protein localisation around axons and ultrastructural confirmation by electron microscopy. Mansour et al. detected OLIG2-positive oligodendrocyte-lineage cells in grafted cerebral organoids, but did not report MBP staining consistent with myelination (Mansour et al., 2018). Conversely, Dong et al. reported that a small subset of STEM121-positive human cells co-expressed MBP after cerebral organoid transplantation, suggesting that human-derived myelination may occur, but likely at low levels (Dong et al., 2021).

Beyond local circuit engagement, functional recovery after TBI also depends on the restoration of distributed network dynamics, including interhemispheric communication through the corpus callosum. One well-established physiological readout of interhemispheric coupling is interhemispheric inhibition (IHI). In the intact brain, IHI is a physiological process where one hemisphere sends signals that suppress the activity of the corresponding area in the opposite hemisphere, often referred to as transcallosal inhibition (Ni et al., 2009). Functionally, this inhibitory coupling helps maintain hemispheric balance and support selective unilateral motor control (Hubers et al., 2008). IHI can be demonstrated with paired-pulse Transcranial Magnetic Stimulation (PP-TMS); a conditioning stimulus over one M1 suppresses the motor-evoked potential (MEP) produced over the opposite M1 at interstimulus intervals typically in the ~5–15 ms range (Ferbert et al., 1992, Daskalakis et al., 2002).

After TBI, diffuse axonal injury can affect interhemispheric pathways, including the callosal communication and inhibition. In individuals with a history of sport-related concussion, studies report altered transcallosal inhibition with impaired interhemispheric inhibitory signalling (Davidson and Tremblay, 2016). Similar findings have been reported in adolescents after concussion, where delayed onset of transcallosal inhibition has been observed during the typical symptomatic period (Schmidt et al., 2021). Mechanistically, these physiological changes are consistent with IHI's dependence on intact callosal pathways, supporting the idea that callosal vulnerability in TBI can contribute to altered interhemispheric balance (Li et al., 2013). A key question is whether implant-derived callosal projections could support restoration of interhemispheric coupling and rebalance interhemispheric dynamics. Given the association of SATB2 with callosal projection neuron identity, LNPC-derived neurons may be particularly relevant to this restoration (Alcamo et al., 2008). However, because the functional role of interhemispheric inhibition cannot be inferred from anatomy alone, future work should therefore test whether donor-derived transcallosal projections form functional synapses in contralateral cortex and whether they normalise interhemispheric interactions.

5.2.5 Long-term monitoring and imaging

While this study assessed outcomes up to 2 MPI, longer-term evaluations are required to monitor implant stability, vascularisation, and immune response over extended periods because histological data obtained at early time points do not correlate with long-term outcomes. To support long-term studies, non-invasive or minimally invasive imaging modalities, such as MRI and Positron emission tomography (PET), can be combined to evaluate different aspects

of implants in vivo. MRI offers multiparametric options, including structural MRI, which can track lesion evolution; perfusion MRI techniques to monitor cerebral blood flow and BBB permeability; and functional MRI, which enables network-level assessments (Dijkhuizen, 2011). PET imaging has been utilised to monitor metabolic recovery after stem cell transplantation in models of cerebral ischemia, revealing enhanced glucose uptake at graft sites that correlates with improved neurological function (Wang et al., 2013a).

Additional minimally invasive modalities, such as ultrasound and photoacoustic imaging, enable high-temporal-resolution vascular and perfusion monitoring at the bedside, while electrophysiological techniques provide complementary functional data (Hu et al., 2022). In non-human primate studies and clinical pipelines, multiparametric MRI combined with PET offer a robust framework for translating studies. Importantly, applying these modalities to our 3D implants would enable longitudinal visualisation of implants, thus strengthening the translational impact of our work.

Rodent models have been invaluable for establishing proof of concept in cell therapy for TBI, demonstrating long-term survival and migration (Pischiutta et al., 2021). However, their predictive value for clinical outcomes is limited by fundamental species differences in brain size and cortical organisation (Ardesch et al., 2022). The rodent cortex lacks the extensive gyrification, expanded association areas, and complex laminar circuitry characteristic of the human neocortex (Ventura-Antunes et al., 2013). As a result, many therapies effective in rodents fail to translate to humans (Loane and Faden, 2010). To improve translational relevance, promising interventions should be validated in large-animal models with neuroanatomical and functional features more comparable to those of the human brain before advancing to clinical trials.

Establishing a robust preclinical foundation for the clinical translation of cell therapies necessitates meticulous study design. This includes using both male and female animals, covering a range of different ages, incorporating models with comorbidities, applying randomisation and blinding, calculating appropriate sample sizes, exploring dose-response effects, and evaluating transplanted cells in multiple animal models across various research sites.

5.3 Concluding remarks

This work represents an initial step toward reconstructing the fundamental cellular and functional components of the cerebral cortex. The findings demonstrate that hiPSC-derived 3D cortical constructs, including RFP+ NPC, ENPC, LNPC, and two-layered neuronal tissues, can survive and integrate into the injured rodent brain. The vascularisation and host immune responses observed in the RFP+ implants indicate active implant–host interactions that may support implant maintenance and integration. Importantly, the distinct projection patterns shaped by neuronal identity underscore the necessity to align implant composition with specific therapeutic goals. These results provide a foundational platform for advancing targeted neural repair therapies, where implant composition and structural organisation can be tailored to the anatomical and clinical requirements of individual patients.

REFERENCES

ABELSETH, E., ABELSETH, L., DE LA VEGA, L., BEYER, S. T., WADSWORTH, S. J. & WILLERTH, S. M. 2019. 3D Printing of Neural Tissues Derived from Human Induced Pluripotent Stem Cells Using a Fibrin-Based Bioink. *ACS Biomater Sci Eng,* 5**,** 234-243.

ADHIKARI, A., SIGURDSSON, T., TOPIWALA, M. A. & GORDON, J. A. 2010. Cross-correlation of instantaneous amplitudes of field potential oscillations: a straightforward method to estimate the directionality and lag between brain areas. *Journal of neuroscience methods,* 191**,** 191-200.

ADUGNA, D. G., ARAGIE, H., KIBRET, A. A. & BELAY, D. G. 2022. Therapeutic Application of Stem Cells in the Repair of Traumatic Brain Injury. *Stem Cells and Cloning: Advances and Applications,* 15**,** 53.

AFSHARIAN, F., ABADI, R. K., TAHERI, R. & SARAJEHLOU, S. A. 2024. Transcranial direct current stimulation combined with cognitive training improves two executive functions: Cognitive flexibility and information updating after traumatic brain injury. *Acta Psychol (Amst),* 250**,** 104553.

AHMAD, R., WOLBER, W., ECKARDT, S., KOCH, P., SCHMITT, J., SEMECHKIN, R., GEIS, C., HECKMANN, M., BRÜSTLE, O. & MCLAUGHLIN, J. K. 2012. Functional neuronal cells generated by human parthenogenetic stem cells.

ALCAMO, E. A., CHIRIVELLA, L., DAUTZENBERG, M., DOBREVA, G., FARIÑAS, I., GROSSCHEDL, R. & MCCONNELL, S. K. 2008. Satb2 regulates callosal projection neuron identity in the developing cerebral cortex. *Neuron,* 57**,** 364-377.

ALLENE, C., CATTANI, A., ACKMAN, J. B., BONIFAZI, P., ANIKSZTEJN, L., BEN-ARI, Y. & COSSART, R. 2008. Sequential generation of two distinct synapse-driven network patterns in developing neocortex. *J Neurosci,* 28**,** 12851-63.

AMER, M. H., ROSE, F., SHAKESHEFF, K. M., MODO, M. & WHITE, L. J. 2017. Translational considerations in injectable cell-based therapeutics for neurological applications: concepts, progress and challenges. *NPJ Regen Med,* 2**,** 23.

AMIRBEKYAN, M., ADHIKARLA, V., CHENG, J. P., MOSCHONAS, E. H., BONDI, C. O., ROCKNE, R. C., KLINE, A. E. & GUTOVA, M. 2023. Neuroprotective potential of intranasally delivered L-myc immortalized human neural stem cells in female rats after a controlled cortical impact injury. *Sci Rep,* 13**,** 17874.

ANDERSON, J. M. & JONES, J. A. 2007. Phenotypic dichotomies in the foreign body reaction. *Biomaterials,* 28**,** 5114-20.

ANDERSON, J. M., RODRIGUEZ, A. & CHANG, D. T. 2008. Foreign body reaction to biomaterials. *Semin Immunol,* 20**,** 86-100.

ANDERSON, S. A., MARÍN, O., HORN, C., JENNINGS, K. & RUBENSTEIN, J. 2001. Distinct cortical migrations from the medial and lateral ganglionic eminences. *Development,* 128**,** 353-363.

ANDREOLI, E., PETRENKO, V., CONSTANTHIN, P. E., CONTESTABILE, A., BOCCHI, R., EGERVARI, K., QUAIRIAUX, C., SALMON, P. & KISS, J. Z. 2020. Transplanted Embryonic Neurons Improve Functional Recovery by Increasing Activity in Injured Cortical Circuits. *Cereb Cortex,* 30**,** 4708-4725.

ANDREU, M., MATTI, N., BRAMLETT, H. M., SHI, Y., GAJAVELLI, S. & DIETRICH, W. D. 2023. Dose-dependent modulation of microglia activation in rats after penetrating traumatic brain injury (pTBI) by transplanted human neural stem cells. *PLoS One,* 18**,** e0285633.

ANDREWS, M. G. & KRIEGSTEIN, A. R. 2022. Challenges of Organoid Research. *Annu Rev Neurosci,* 45**,** 23-39.

ANLAR, B. & GUNEL-OZCAN, A. 2012. Tenascin-R: Role in the central nervous system. *International Journal of Biochemistry and Cell Biology,* 44**,** 1385-1389.

ANTOINE, E. E., VLACHOS, P. P. & RYLANDER, M. N. 2014. Review of collagen I hydrogels for bioengineered tissue microenvironments: characterization of mechanics, structure, and transport. *Tissue Eng Part B Rev,* 20**,** 683-96.

ANTONELLO, P. C., VARLEY, T. F., BEGGS, J., PORCIONATTO, M., SPORNS, O. & FABER, J. 2022. Self-organization of in vitro neuronal assemblies drives to complex network topology. *Elife,* 11.

AQEL, S., AL-THANI, N., HAIDER, M. Z., ABDELHADY, S., AL THANI, A. A., KOBEISSY, F. & SHAITO, A. A. 2023. Biomaterials in Traumatic Brain Injury: Perspectives and Challenges. *Biology (Basel),* 13.

ARDESCH, D. J., SCHOLTENS, L. H., DE LANGE, S. C., ROUMAZEILLES, L., KHRAPITCHEV, A. A., PREUSS, T. M., RILLING, J. K., MARS, R. B. & VAN DEN HEUVEL, M. P. 2022. Scaling Principles of White Matter Connectivity in the Human and Nonhuman Primate Brain. *Cereb Cortex,* 32**,** 2831-2842.

ARJUN MCKINNEY, A., PETROVA, R. & PANAGIOTAKOS, G. 2022. Calcium and activity-dependent signaling in the developing cerebral cortex. *Development,* 149.

ARLOTTA, P., MOLYNEAUX, B. J., CHEN, J., INOUE, J., KOMINAMI, R. & MACKLIS, J. D. 2005. Neuronal subtype-specific genes that control corticospinal motor neuron development in vivo. *Neuron,* 45**,** 207-221.

ASSINGER, A., VOLF, I. & SCHMID, D. 2015. A novel, rapid method to quantify intraplatelet calcium dynamics by ratiometric flow cytometry. *PLoS One,* 10**,** e0122527.

AUGUSTYNIAK, J., LENART, J., LIPKA, G., STEPIEN, P. P. & BUZANSKA, L. 2019. Reference Gene Validation via RT-qPCR for Human iPSC-Derived Neural Stem Cells and Neural Progenitors. *Mol Neurobiol,* 56**,** 6820-6832.

AUTAR, K., GUO, X., RUMSEY, J. W., LONG, C. J., AKANDA, N., JACKSON, M., NARASIMHAN, N. S., CANEUS, J., MORGAN, D. & HICKMAN, J. J. 2022. A functional hiPSC-cortical neuron differentiation and maturation model and its application to neurological disorders. *Stem Cell Reports,* 17**,** 96-109.

BADNER, A., REINHARDT, E. K., NGUYEN, T. V., MIDANI, N., MARSHALL, A. T., LEPE, C. A., ECHEVERRIA, K., LEPE, J. J., TORRECAMPO, V., BERTAN, S. H., TRAN, S. H., ANDERSON, A. J. & CUMMINGS, B. J. 2021. Freshly Thawed Cryobanked Human Neural Stem Cells Engraft within Endogenous Neurogenic Niches and Restore Cognitive Function after Chronic Traumatic Brain Injury. *J Neurotrauma,* 38**,** 2731-2746.

BAE, M., HWANG, D. W., KO, M. K., JIN, Y., SHIN, W. J., PARK, W., CHAE, S., LEE, H. J., JANG, J., YI, H. G., LEE, D. S. & CHO, D. W. 2021. Neural stem cell delivery using brain-derived tissue-specific bioink for recovering from traumatic brain injury. *Biofabrication,* 13.

BAHMAD, H., HADADEH, O., CHAMAA, F., CHEAITO, K., DARWISH, B., MAKKAWI, A.-K. & ABOU-KHEIR, W. 2017. Modeling human neurological and neurodegenerative diseases: from induced pluripotent stem cells to neuronal differentiation and its applications in neurotrauma. *Frontiers in Molecular Neuroscience,* 10**,** 50.

BALDASSARI, S., CERVETTO, C., AMATO, S., FRUSCIONE, F., BALAGURA, G., PELASSA, S., MUSANTE, I., IACOMINO, M., TRAVERSO, M. & CORRADI, A. 2022. Vesicular Glutamate Release from Feeder-FreehiPSC-Derived Neurons. *International journal of molecular sciences,* 23**,** 10545.

BALTZ, T., DE LIMA, A. D. & VOIGT, T. 2010. Contribution of GABAergic interneurons to the development of spontaneous activity patterns in cultured neocortical networks. *Front Cell Neurosci,* 4**,** 15.

BANERJEE, J., SHI, Y. & AZEVEDO, H. S. 2016. In vitro blood–brain barrier models for drug research: state-of-the-art and new perspectives on reconstituting these models on artificial basement membrane platforms. *Drug discovery today,* 21**,** 1367-1386.

BAO, Z., FANG, K., MIAO, Z., LI, C., YANG, C., YU, Q., ZHANG, C., MIAO, Z., LIU, Y. & JI, J. 2021. Human Cerebral Organoid Implantation Alleviated the Neurological Deficits of Traumatic Brain Injury in Mice. *Oxidative medicine and cellular longevity,* 2021.

BARKER, R. A., BARRETT, J., MASON, S. L. & BJORKLUND, A. 2013. Fetal dopaminergic transplantation trials and the future of neural grafting in Parkinson's disease. *Lancet Neurol,* 12**,** 84-91.

BARKER, R. A., LAO-KAIM, N. P., GUZMAN, N. V., ATHAUDA, D., BJARTMARZ, H., BJORKLUND, A., CHURCH, A., CUTTING, E., DAFT, D., DAYAL, V., DUNNETT, S., EVANS, A., GREALISH, S., HANNAWAY, N., HE, X., HEWITT, S., KEFALOPOULOU, Z., MAHLKNECHT, P., MARTIN-BASTIDA, A., FARRELL, K., MOORE, S., BULSTRODE, H., NAKORNCHAI, T., NELANDER-WAHLESTEDT, J., ROUPE, L., PAUL, G., PEALL, K., ROSSER, A., ROCA-FERNANDEZ, A., ROWLANDS, S., MCGORRIAN, A. M., SCHERF, C., VINH, N. N., ROBERTON, V., KELLY, C., LELOS, M., TORRES, E., SHIRES, K., HILLS, R., WILLIAMS, D., ROUSSAKIS, A. A., SIBLEY, K., TYERS, P., WIJEYEKOON, R., WILLIAMS-GRAY, C., FOLTYNIE, T., PICCINI, P., MORRIS, R., LAZIC, S. E., LINDVALL, O., PARMAR, M., WIDNER, H. & TRANSEURO, C. 2025. The TransEuro open-label trial of human fetal ventral mesencephalic transplantation in patients with moderate Parkinson's disease. *Nat Biotechnol*.

BARKHO, B. Z., SONG, H., AIMONE, J. B., SMRT, R. D., KUWABARA, T., NAKASHIMA, K., GAGE, F. H. & ZHAO, X. 2006. Identification of astrocyte-expressed factors that modulate neural stem/progenitor cell differentiation. *Stem cells and development,* 15**,** 407-421.

BARON-VAN EVERCOOREN, A., KLEINMAN, H. K., OHNO, S., MARANGOS, P., SCHWARTZ, J. P. & DUBOIS-DALCQ, M. E. 1982. Nerve growth factor, laminin, and fibronectin promote neurite growth in human fetal sensory ganglia cultures. *Journal of neuroscience research,* 8**,** 179-193.

BASSETT, D. S. & BULLMORE, E. T. 2017. Small-World Brain Networks Revisited. *Neuroscientist,* 23**,** 499-516.

BAYATTI, N., MOSS, J. A., SUN, L., AMBROSE, P., WARD, J. F., LINDSAY, S. & CLOWRY, G. J. 2008. A molecular neuroanatomical study of the developing human neocortex from 8 to 17 postconceptional weeks revealing the early differentiation of the subplate and subventricular zone. *Cereb Cortex,* 18**,** 1536-48.

BECERRA, G., TATKO, L., PAK, E., MURASHOV, A. & HOANE, M. 2007. Transplantation of GABAergic neurons but not astrocytes induces recovery of sensorimotor function in the traumatically injured brain. *Behavioural brain research,* 179**,** 118-125.

BEDI, S. S., WALKER, P. A., SHAH, S. K., JIMENEZ, F., THOMAS, C. P., SMITH, P., HETZ, R. A., XUE, H., PATI, S., DASH, P. K. & COX, C. S., JR. 2013. Autologous bone marrow mononuclear cells therapy attenuates activated microglial/macrophage response and improves spatial learning after traumatic brain injury. *J Trauma Acute Care Surg,* 75**,** 410-6.

BELLAIL, A. C., HUNTER, S. B., BRAT, D. J., TAN, C. & VAN MEIR, E. G. 2004. Microregional extracellular matrix heterogeneity in brain modulates glioma cell invasion. *International Journal of Biochemistry and Cell Biology,* 36**,** 1046-1069.

BERRIDGE, M. J., BOOTMAN, M. D. & RODERICK, H. L. 2003. Calcium signalling: dynamics, homeostasis and remodelling. *Nat Rev Mol Cell Biol,* 4**,** 517-29.

BERRY, C., LEY, E. J., TILLOU, A., CRYER, G., MARGULIES, D. R. & SALIM, A. 2009. The effect of gender on patients with moderate to severe head injuries. *Journal of Trauma and Acute Care Surgery,* 67**,** 950-953.

BIGNAMI, A., HOSLEY, M. & DAHL, D. 1993. Hyaluronic acid and hyaluronic acid-binding proteins in brain extracellular matrix. *Anat Embryol (Berl),* 188**,** 419-33.

BIREY, F., ANDERSEN, J., MAKINSON, C. D., ISLAM, S., WEI, W., HUBER, N., FAN, H. C., METZLER, K. R. C., PANAGIOTAKOS, G., THOM, N., O'ROURKE, N. A., STEINMETZ, L. M., BERNSTEIN, J. A., HALLMAYER, J., HUGUENARD, J. R. & PAŞCA, S. P. 2017. Assembly of functionally integrated human forebrain spheroids. *Nature,* 545**,** 54-59.

BISHOP, E. S., MOSTAFA, S., PAKVASA, M., LUU, H. H., LEE, M. J., WOLF, J. M., AMEER, G. A., HE, T.-C. & REID, R. R. 2017. 3-D bioprinting technologies in tissue engineering and regenerative medicine: Current and future trends. *Genes & diseases,* 4**,** 185-195.

BLAESER, A., DUARTE CAMPOS, D. F., PUSTER, U., RICHTERING, W., STEVENS, M. M. & FISCHER, H. 2016. Controlling Shear Stress in 3D Bioprinting is a Key Factor to Balance Printing Resolution and Stem Cell Integrity. *Adv Healthc Mater,* 5**,** 326-33.

BLANKENSHIP, A. G. & FELLER, M. B. 2010. Mechanisms underlying spontaneous patterned activity in developing neural circuits. *Nat Rev Neurosci,* 11**,** 18-29.

BLAYA, M. O., TSOULFAS, P., BRAMLETT, H. M. & DIETRICH, W. D. 2015. Neural progenitor cell transplantation promotes neuroprotection, enhances hippocampal neurogenesis, and improves cognitive outcomes after traumatic brain injury. *Exp Neurol,* 264**,** 67-81.

BLONDEL, V. D., GUILLAUME, J.-L., LAMBIOTTE, R. & LEFEBVRE, E. 2008. Fast unfolding of communities in large networks. *Journal of statistical mechanics: theory and experiment,* 2008**,** P10008.

BOCK, C., KISKINIS, E., VERSTAPPEN, G., GU, H., BOULTING, G., SMITH, Z. D., ZILLER, M., CROFT, G. F., AMOROSO, M. W., OAKLEY, D. H., GNIRKE, A., EGGAN, K. & MEISSNER, A. 2011. Reference Maps of human ES and iPS cell variation enable high-throughput characterization of pluripotent cell lines. *Cell,* 144**,** 439-52.

BOISSART, C., POULET, A., GEORGES, P., DARVILLE, H., JULITA, E., DELORME, R., BOURGERON, T., PESCHANSKI, M. & BENCHOUA, A. 2013. Differentiation from human pluripotent stem cells of cortical neurons of the superficial layers amenable to psychiatric disease modeling and high-throughput drug screening. *Translational psychiatry,* 3**,** e294-e294.

BOOTMAN, M. D. & BULTYNCK, G. 2020. Fundamentals of cellular calcium signaling: a primer. *Cold Spring Harbor perspectives in biology,* 12**,** a038802.

BOSMAN, C. A. & ABOITIZ, F. 2015. Functional constraints in the evolution of brain circuits. *Frontiers in neuroscience,* 9**,** 303.
BRAMLETT, H. M. & DIETRICH, W. D. 2001. Neuropathological protection after traumatic brain injury in intact female rats versus males or ovariectomized females. *J Neurotrauma,* 18**,** 891-900.
BREVINI, T. A. & GANDOLFI, F. 2008. Parthenotes as a source of embryonic stem cells. *Cell Prolif,* 41 Suppl 1**,** 20-30.
BRITANOVA, O., DE JUAN ROMERO, C., CHEUNG, A., KWAN, K. Y., SCHWARK, M., GYORGY, A., VOGEL, T., AKOPOV, S., MITKOVSKI, M. & AGOSTON, D. 2008. Satb2 is a postmitotic determinant for upper-layer neuron specification in the neocortex. *Neuron,* 57**,** 378-392.
BUDHARAJU, H., SUNDARAMURTHI, D. & SETHURAMAN, S. 2024. Embedded 3D bioprinting–An emerging strategy to fabricate biomimetic & large vascularized tissue constructs. *Bioactive Materials,* 32**,** 356-384.
BULLMORE, E. & SPORNS, O. 2009. Complex brain networks: graph theoretical analysis of structural and functional systems. *Nat Rev Neurosci,* 10**,** 186-98.
CADENA, M., NING, L., KING, A., HWANG, B., JIN, L., SERPOOSHAN, V. & SLOAN, S. A. 2021. 3D Bioprinting of Neural Tissues. *Adv Healthc Mater,* 10**,** e2001600.
CAKIR, B., XIANG, Y., TANAKA, Y., KURAL, M. H., PARENT, M., KANG, Y. J., CHAPETON, K., PATTERSON, B., YUAN, Y., HE, C. S., RAREDON, M. S. B., DENGELEGI, J., KIM, K. Y., SUN, P., ZHONG, M., LEE, S., PATRA, P., HYDER, F., NIKLASON, L. E., LEE, S. H., YOON, Y. S. & PARK, I. H. 2019. Engineering of human brain organoids with a functional vascular-like system. *Nat Methods,* 16**,** 1169-1175.
CAMINITI, R., GHAZIRI, H., GALUSKE, R., HOF, P. R. & INNOCENTI, G. M. 2009. Evolution amplified processing with temporally dispersed slow neuronal connectivity in primates. *Proc Natl Acad Sci U S A,* 106**,** 19551-6.
CARLSON, A. L., BENNETT, N. K., FRANCIS, N. L., HALIKERE, A., CLARKE, S., MOORE, J. C., HART, R. P., PARADISO, K., WERNIG, M., KOHN, J., PANG, Z. P. & MOGHE, P. V. 2016. Generation and transplantation of reprogrammed human neurons in the brain using 3D microtopographic scaffolds. *Nat Commun,* 7**,** 10862.
CHAMBERS, I., COLBY, D., ROBERTSON, M., NICHOLS, J., LEE, S., TWEEDIE, S. & SMITH, A. 2003. Functional expression cloning of Nanog, a pluripotency sustaining factor in embryonic stem cells. *Cell,* 113**,** 643-655.
CHAMBERS, S. M., FASANO, C. A., PAPAPETROU, E. P., TOMISHIMA, M., SADELAIN, M. & STUDER, L. 2009. Highly efficient neural conversion of human ES and iPS cells by dual inhibition of SMAD signaling. *Nat Biotechnol,* 27**,** 275-80.
CHAU, M., ZHANG, J., WEI, L. & YU, S. P. 2016. Regeneration after stroke: Stem cell transplantation and trophic factors. *Brain Circ,* 2**,** 86-94.
CHEN, J., LIAO, S., XIAO, Z., PAN, Q., WANG, X., SHEN, K., WANG, S., YANG, L., GUO, F., LIU, H. F. & PAN, Q. 2022. The development and improvement of immunodeficient mice and humanized immune system mouse models. *Front Immunol,* 13**,** 1007579.
CHEN, P., CESCON, M. & BONALDO, P. 2015. The role of collagens in peripheral nerve myelination and function. *Molecular neurobiology,* 52**,** 216-225.
CHEN, Z., LU, X. C., SHEAR, D. A., DAVE, J. R., DAVIS, A. R., EVANGELISTA, C. A., DUFFY, D. & TORTELLA, F. C. 2011. Synergism of human amnion-derived multipotent progenitor (AMP) cells and a collagen scaffold in promoting brain wound recovery: pre-clinical

studies in an experimental model of penetrating ballistic-like brain injury. *Brain Res,* 1368**,** 71-81.
CHROSTEK, M. R., FELLOWS, E. G., GUO, W. L., SWANSON, W. J., CRANE, A. T., CHEERAN, M. C., LOW, W. C. & GRANDE, A. W. 2019. Efficacy of cell-based therapies for traumatic brain injuries. *Brain sciences,* 9**,** 270.
CIERI, M. B. & RAMOS, A. J. 2025. Astrocytes, reactive astrogliosis, and glial scar formation in traumatic brain injury. *Neural Regen Res,* 20**,** 973-989.
CLARK, E. A., RUTLIN, M., CAPANO, L. S., AVILES, S., SAADON, J. R., TANEJA, P., ZHANG, Q., BULLIS, J. B., LAUER, T. & MYERS, E. 2020. Cortical RORβ is required for layer 4 transcriptional identity and barrel integrity. *Elife,* 9**,** e52370.
CORDELLA, F., FERRUCCI, L., D'ANTONI, C., GHIRGA, S., BRIGHI, C., SOLOPERTO, A., GIGANTE, Y., RAGOZZINO, D., BEZZI, P. & DI ANGELANTONIO, S. 2022. Human iPSC-Derived Cortical Neurons Display Homeostatic Plasticity. *Life (Basel),* 12.
CORLEW, R., BOSMA, M. M. & MOODY, W. J. 2004. Spontaneous, synchronous electrical activity in neonatal mouse cortical neurones. *J Physiol,* 560**,** 377-90.
COX, C. S., JR. 2018. Cellular therapy for traumatic neurological injury. *Pediatr Res,* 83**,** 325-332.
COX, C. S., JR., BAUMGARTNER, J. E., HARTING, M. T., WORTH, L. L., WALKER, P. A., SHAH, S. K., EWING-COBBS, L., HASAN, K. M., DAY, M. C., LEE, D., JIMENEZ, F. & GEE, A. 2011. Autologous bone marrow mononuclear cell therapy for severe traumatic brain injury in children. *Neurosurgery,* 68**,** 588-600.
COX, C. S., JR., HETZ, R. A., LIAO, G. P., AERTKER, B. M., EWING-COBBS, L., JURANEK, J., SAVITZ, S. I., JACKSON, M. L., ROMANOWSKA-PAWLICZEK, A. M., TRIOLO, F., DASH, P. K., PEDROZA, C., LEE, D. A., WORTH, L., AISIKU, I. P., CHOI, H. A., HOLCOMB, J. B. & KITAGAWA, R. S. 2017. Treatment of Severe Adult Traumatic Brain Injury Using Bone Marrow Mononuclear Cells. *Stem Cells,* 35**,** 1065-1079.
COX JR, C. S., HETZ, R. A., LIAO, G. P., AERTKER, B. M., EWING-COBBS, L., JURANEK, J., SAVITZ, S. I., JACKSON, M. L., ROMANOWSKA-PAWLICZEK, A. M. & TRIOLO, F. 2017. Treatment of severe adult traumatic brain injury using bone marrow mononuclear cells. *Stem Cells,* 35**,** 1065-1079.
COX JR, C. S., NOTRICA, D. M., JURANEK, J., MILLER, J. H., TRIOLO, F., KOSMACH, S., SAVITZ, S. I., ADELSON, P. D., PEDROZA, C. & OLSON, S. D. 2024. Autologous bone marrow mononuclear cells to treat severe traumatic brain injury in children. *Brain,* 147**,** 1914-1925.
D'SOUZA, R. D. & BURKHALTER, A. 2017. A Laminar Organization for Selective Cortico-Cortical Communication. *Front Neuroanat,* 11**,** 71.
DASKALAKIS, Z. J., CHRISTENSEN, B. K., FITZGERALD, P. B., ROSHAN, L. & CHEN, R. 2002. The mechanisms of interhemispheric inhibition in the human motor cortex. *J Physiol,* 543**,** 317-26.
DAVIAUD, N., FRIEDEL, R. H. & ZOU, H. 2018. Vascularization and Engraftment of Transplanted Human Cerebral Organoids in Mouse Cortex. *eNeuro,* 5.
DAVIDSON, T. W. & TREMBLAY, F. 2016. Evidence of alterations in transcallosal motor inhibition as a possible long-term consequence of concussions in sports: a transcranial magnetic stimulation study. *Clinical Neurophysiology,* 127**,** 3364-3375.

DEGIOSIO, R. A., GRUBISHA, M. J., MACDONALD, M. L., MCKINNEY, B. C., CAMACHO, C. J. & SWEET, R. A. 2022. More than a marker: potential pathogenic functions of MAP2. *Frontiers in Molecular Neuroscience,* 15.

DELAGE, C., TAIB, T., MAMMA, C., LEROUET, D. & BESSON, V. C. 2021a. Traumatic Brain Injury: An Age-Dependent View of Post-Traumatic Neuroinflammation and Its Treatment. *Pharmaceutics,* 13.

DELAGE, C., TAIB, T., MAMMA, C., LEROUET, D. & BESSON, V. C. 2021b. Traumatic brain injury: an age-dependent view of post-traumatic neuroinflammation and its treatment. *Pharmaceutics,* 13**,** 1624.

DELGADO, R. N., ALLEN, D. E., KEEFE, M. G., MANCIA LEON, W. R., ZIFFRA, R. S., CROUCH, E. E., ALVAREZ-BUYLLA, A. & NOWAKOWSKI, T. J. 2022. Individual human cortical progenitors can produce excitatory and inhibitory neurons. *Nature,* 601**,** 397-403.

DELLI CARRI, A., ONORATI, M., CASTIGLIONI, V., FAEDO, A., CAMNASIO, S., TOSELLI, M., BIELLA, G. & CATTANEO, E. 2013. Human pluripotent stem cell differentiation into authentic striatal projection neurons. *Stem Cell Rev Rep,* 9**,** 461-74.

DEUSE, T., HU, X., AGBOR-ENOH, S., KOCH, M., SPITZER, M. H., GRAVINA, A., ALAWI, M., MARISHTA, A., PETERS, B. & KOSALOGLU-YALCIN, Z. 2019. De novo mutations in mitochondrial DNA of iPSCs produce immunogenic neoepitopes in mice and humans. *Nature Biotechnology,* 37**,** 1137-1144.

DIEHL, R., FERRARA, F., MULLER, C., DREYER, A. Y., MCLEOD, D. D., FRICKE, S. & BOLTZE, J. 2017. Immunosuppression for in vivo research: state-of-the-art protocols and experimental approaches. *Cell Mol Immunol,* 14**,** 146-179.

DIJKHUIZEN, R. M. 2011. Advances in MRI-Based Detection of Cerebrovascular Changes after Experimental Traumatic Brain Injury. *Transl Stroke Res,* 2**,** 524-32.

DING, M. C., WANG, Q., LO, E. H. & STANLEY, G. B. 2011. Cortical excitation and inhibition following focal traumatic brain injury. *J Neurosci,* 31**,** 14085-94.

DINGLE, Y. L., LIAUDANSKAYA, V., FINNEGAN, L. T., BERLIND, K. C., MIZZONI, C., GEORGAKOUDI, I., NIELAND, T. J. F. & KAPLAN, D. L. 2020. Functional Characterization of Three-Dimensional Cortical Cultures for In Vitro Modeling of Brain Networks. *iScience,* 23**,** 101434.

DISANTO, J. P., MULLER, W., GUY-GRAND, D., FISCHER, A. & RAJEWSKY, K. 1995. Lymphoid development in mice with a targeted deletion of the interleukin 2 receptor gamma chain. *Proc Natl Acad Sci U S A,* 92**,** 377-81.

DISCHER, D. E., JANMEY, P. & WANG, Y. L. 2005. Tissue cells feel and respond to the stiffness of their substrate. *Science,* 310**,** 1139-1143.

DITYATEV, A., SCHACHNER, M. & SONDEREGGER, P. 2010. The dual role of the extracellular matrix in synaptic plasticity and homeostasis. *Nat Rev Neurosci,* 11**,** 735-46.

DIXON, C. E., CLIFTON, G. L., LIGHTHALL, J. W., YAGHMAI, A. A. & HAYES, R. L. 1991. A controlled cortical impact model of traumatic brain injury in the rat. *Journal of neuroscience methods,* 39**,** 253-262.

DOERR, J., SCHWARZ, M. K., WIEDERMANN, D., LEINHAAS, A., JAKOBS, A., SCHLOEN, F., SCHWARZ, I., DIEDENHOFEN, M., BRAUN, N. C., KOCH, P., PETERSON, D. A., KUBITSCHECK, U., HOEHN, M. & BRUSTLE, O. 2017. Whole-brain 3D mapping of human neural transplant innervation. *Nat Commun,* 8**,** 14162.

DOMINGUEZ, M. H., AYOUB, A. E. & RAKIC, P. 2013. POU-III transcription factors (Brn1, Brn2, and Oct6) influence neurogenesis, molecular identity, and migratory destination of upper-layer cells of the cerebral cortex. *Cereb Cortex,* 23**,** 2632-43.

DONAT, C. K., SCOTT, G., GENTLEMAN, S. M. & SASTRE, M. 2017. Microglial Activation in Traumatic Brain Injury. *Front Aging Neurosci,* 9**,** 208.

DONG, X., XU, S. B., CHEN, X., TAO, M., TANG, X. Y., FANG, K. H., XU, M., PAN, Y., CHEN, Y., HE, S. & LIU, Y. 2021. Human cerebral organoids establish subcortical projections in the mouse brain after transplantation. *Mol Psychiatry,* 26**,** 2964-2976.

DOUGLAS, R. J. & MARTIN, K. A. 2004. Neuronal circuits of the neocortex. *Annu Rev Neurosci,* 27**,** 419-51.

DOWNES, J. H., HAMMOND, M. W., XYDAS, D., SPENCER, M. C., BECERRA, V. M., WARWICK, K., WHALLEY, B. J. & NASUTO, S. J. 2012. Emergence of a small-world functional network in cultured neurons. *PLoS Comput Biol,* 8**,** e1002522.

DUNKERSON, J., MORITZ, K. E., YOUNG, J., PIONK, T., FINK, K., ROSSIGNOL, J., DUNBAR, G. & SMITH, J. S. 2014. Combining enriched environment and induced pluripotent stem cell therapy results in improved cognitive and motor function following traumatic brain injury. *Restor Neurol Neurosci,* 32**,** 675-87.

DURBEEJ, M. 2010. Laminins. *Cell and tissue research,* 339**,** 259-268.

DURBIN, K. A., MARDER, K. G., WILSON, A. C., NGO, T. D., CORLIER, J., VINCE-CRUZ, N., BILDER, R., VESPA, P., TADAYONNEJAD, R. & LEE, J. C. 2023. Low frequency transcranial magnetic stimulation for cognitive recovery after traumatic brain injury: A case report. *Psychiatry Research Case Reports,* 2**,** 100173.

ECONOMO, M. N., VISWANATHAN, S., TASIC, B., BAS, E., WINNUBST, J., MENON, V., GRAYBUCK, L. T., NGUYEN, T. N., SMITH, K. A. & YAO, Z. 2018. Distinct descending motor cortex pathways and their roles in movement. *Nature,* 563**,** 79-84.

EIRAKU, M., WATANABE, K., MATSUO-TAKASAKI, M., KAWADA, M., YONEMURA, S., MATSUMURA, M., WATAYA, T., NISHIYAMA, A., MUGURUMA, K. & SASAI, Y. 2008. Self-organized formation of polarized cortical tissues from ESCs and its active manipulation by extrinsic signals. *Cell Stem Cell,* 3**,** 519-32.

ELKIN, B. S., AZELOGLU, E. U., COSTA, K. D. & MORRISON III, B. 2007. Mechanical heterogeneity of the rat hippocampus measured by atomic force microscope indentation. *Journal of Neurotrauma,* 24**,** 812-822.

ENGEL, M., DO-HA, D., MUNOZ, S. S. & OOI, L. 2016. Common pitfalls of stem cell differentiation: a guide to improving protocols for neurodegenerative disease models and research. *Cell Mol Life Sci,* 73**,** 3693-709.

ENGLER, A. J., SEN, S., SWEENEY, H. L. & DISCHER, D. E. 2006. Matrix Elasticity Directs Stem Cell Lineage Specification. *Cell,* 126**,** 677-689.

ENGLUND, C., FINK, A., LAU, C., PHAM, D., DAZA, R. A., BULFONE, A., KOWALCZYK, T. & HEVNER, R. F. 2005. Pax6, Tbr2, and Tbr1 are expressed sequentially by radial glia, intermediate progenitor cells, and postmitotic neurons in developing neocortex. *J Neurosci,* 25**,** 247-51.

ESCARTIN, C., GALEA, E., LAKATOS, A., O'CALLAGHAN, J. P., PETZOLD, G. C., SERRANO-POZO, A., STEINHAUSER, C., VOLTERRA, A., CARMIGNOTO, G., AGARWAL, A., ALLEN, N. J., ARAQUE, A., BARBEITO, L., BARZILAI, A., BERGLES, D. E., BONVENTO, G., BUTT, A. M., CHEN, W. T., COHEN-SALMON, M., CUNNINGHAM, C., DENEEN, B., DE STROOPER, B., DIAZ-CASTRO, B., FARINA, C., FREEMAN, M., GALLO, V., GOLDMAN, J. E., GOLDMAN,

S. A., GOTZ, M., GUTIERREZ, A., HAYDON, P. G., HEILAND, D. H., HOL, E. M., HOLT, M. G., IINO, M., KASTANENKA, K. V., KETTENMANN, H., KHAKH, B. S., KOIZUMI, S., LEE, C. J., LIDDELOW, S. A., MACVICAR, B. A., MAGISTRETTI, P., MESSING, A., MISHRA, A., MOLOFSKY, A. V., MURAI, K. K., NORRIS, C. M., OKADA, S., OLIET, S. H. R., OLIVEIRA, J. F., PANATIER, A., PARPURA, V., PEKNA, M., PEKNY, M., PELLERIN, L., PEREA, G., PEREZ-NIEVAS, B. G., PFRIEGER, F. W., POSKANZER, K. E., QUINTANA, F. J., RANSOHOFF, R. M., RIQUELME-PEREZ, M., ROBEL, S., ROSE, C. R., ROTHSTEIN, J. D., ROUACH, N., ROWITCH, D. H., SEMYANOV, A., SIRKO, S., SONTHEIMER, H., SWANSON, R. A., VITORICA, J., WANNER, I. B., WOOD, L. B., WU, J., ZHENG, B., ZIMMER, E. R., ZOREC, R., SOFRONIEW, M. V. & VERKHRATSKY, A. 2021. Reactive astrocyte nomenclature, definitions, and future directions. *Nat Neurosci,* 24**,** 312-325.

ESPUNY-CAMACHO, I., MICHELSEN, K. A., GALL, D., LINARO, D., HASCHE, A., BONNEFONT, J., BALI, C., ORDUZ, D., BILHEU, A. & HERPOEL, A. 2013. Pyramidal neurons derived from human pluripotent stem cells integrate efficiently into mouse brain circuits in vivo. *Neuron,* 77**,** 440-456.

FAINSTEIN, N., EINSTEIN, O., COHEN, M. E., BRILL, L., LAVON, I. & BEN-HUR, T. 2013. Time limited immunomodulatory functions of transplanted neural precursor cells. *Glia,* 61**,** 140-9.

FARACE, E. & ALVES, W. M. 2000. Do women fare worse: a metaanalysis of gender differences in traumatic brain injury outcome. *Journal of neurosurgery,* 93**,** 539-545.

FARRANT, M. & NUSSER, Z. 2005. Variations on an inhibitory theme: phasic and tonic activation of GABA(A) receptors. *Nat Rev Neurosci,* 6**,** 215-29.

FAULKNER, J. R., HERRMANN, J. E., WOO, M. J., TANSEY, K. E., DOAN, N. B. & SOFRONIEW, M. V. 2004. Reactive astrocytes protect tissue and preserve function after spinal cord injury. *Journal of neuroscience,* 24**,** 2143-2155.

FEDOR, M., BERMAN, R. F., MUIZELAAR, J. P. & LYETH, B. G. 2010. Hippocampal theta dysfunction after lateral fluid percussion injury. *J Neurotrauma,* 27**,** 1605-15.

FEENEY, D. M., BOYESON, M. G., LINN, R. T., MURRAY, H. M. & DAIL, W. G. 1981. Responses to cortical injury: I. Methodology and local effects of contusions in the rat. *Brain research,* 211**,** 67-77.

FENG, S., ZHANG, T., HE, Z., ZHANG, W., CHEN, Y., YUE, C. & JING, N. 2024. Continuous immunosuppression is required for suppressing immune responses to xenografts in non-human primate brains. *Cell Regen,* 13**,** 8.

FENG, Y., LI, K., ROTH, E., CHAO, D., MECCA, C. M., HOGAN, Q. H., PAWELA, C., KWOK, W. M., CAMARA, A. K. S. & PAN, B. 2021. Repetitive Mild Traumatic Brain Injury in Rats Impairs Cognition, Enhances Prefrontal Cortex Neuronal Activity, and Reduces Pre-synaptic Mitochondrial Function. *Front Cell Neurosci,* 15**,** 689334.

FENLON, L. R., LIU, S., GOBIUS, I., KURNIAWAN, N. D., MURPHY, S., MOLDRICH, R. X. & RICHARDS, L. J. 2015. Formation of functional areas in the cerebral cortex is disrupted in a mouse model of autism spectrum disorder. *Neural development,* 10**,** 10.

FERBERT, A., PRIORI, A., ROTHWELL, J. C., DAY, B. L., COLEBATCH, J. G. & MARSDEN, C. D. 1992. Interhemispheric inhibition of the human motor cortex. *J Physiol,* 453**,** 525-46.

FESHARAKI-ZADEH, A. & DATTA, D. 2024. An overview of preclinical models of traumatic brain injury (TBI): relevance to pathophysiological mechanisms. *Front Cell Neurosci,* 18**,** 1371213.
FISCHER, U. M., HARTING, M. T., JIMENEZ, F., MONZON-POSADAS, W. O., XUE, H., SAVITZ, S. I., LAINE, G. A. & COX JR, C. S. 2009. Pulmonary passage is a major obstacle for intravenous stem cell delivery: the pulmonary first-pass effect. *Stem cells and development,* 18**,** 683-692.
FISHELL, G. 2007. Perspectives on the developmental origins of cortical interneuron diversity. *Novartis Found Symp,* 288**,** 21-35; discussion 35-44, 96-8.
FLIERL, M. A., STAHEL, P. F., BEAUCHAMP, K. M., MORGAN, S. J., SMITH, W. R. & SHOHAMI, E. 2009. Mouse closed head injury model induced by a weight-drop device. *Nature protocols,* 4**,** 1328-1337.
FOXE, J. J. & SNYDER, A. C. 2011. The Role of Alpha-Band Brain Oscillations as a Sensory Suppression Mechanism during Selective Attention. *Front Psychol,* 2**,** 154.
FRANCIS, N. L., ZHAO, N., CALVELLI, H. R., SAINI, A., GIFFORD, J. J., WAGNER, G. C., COHEN, R. I., PANG, Z. P. & MOGHE, P. V. 2020. Peptide-Based Scaffolds for the Culture and Transplantation of Human Dopaminergic Neurons. *Tissue Eng Part A,* 26**,** 193-205.
FREED, C. R., GREENE, P. E., BREEZE, R. E., TSAI, W. Y., DUMOUCHEL, W., KAO, R., DILLON, S., WINFIELD, H., CULVER, S., TROJANOWSKI, J. Q., EIDELBERG, D. & FAHN, S. 2001. Transplantation of embryonic dopamine neurons for severe Parkinson's disease. *N Engl J Med,* 344**,** 710-9.
FRISCHKNECHT, R. & GUNDELFINGER, E. D. 2012. The brain's extracellular matrix and its role in synaptic plasticity. *Advances in Experimental Medicine and Biology,* 970**,** 153-171.
FRUCHTERMAN, T. M. & REINGOLD, E. M. 1991. Graph drawing by force-directed placement. *Software: Practice and experience,* 21**,** 1129-1164.
FU, F., QIN, Z., XU, C., CHEN, X. Y., LI, R. X., WANG, L. N., PENG, D. W., SUN, H. T., TU, Y., CHEN, C., ZHANG, S., ZHAO, M. L. & LI, X. H. 2017. Magnetic resonance imaging-three-dimensional printing technology fabricates customized scaffolds for brain tissue engineering. *Neural Regen Res,* 12**,** 614-622.
FUMADO NAVARRO, J., CRILLY, S., CHAN, W. K., BROWNE, S., MASON, J. O., VALLEJO-GIRALDO, C., PANDIT, A. & LOMORA, M. 2025. Cerebral Organoids with Integrated Endothelial Networks Emulate the Neurovascular Unit and Mitigate Core Necrosis. *Adv Sci (Weinh)***,** e07256.
GAO, J., GRILL, R. J., DUNN, T. J., BEDI, S., LABASTIDA, J. A., HETZ, R. A., XUE, H., THONHOFF, J. R., DEWITT, D. S., PROUGH, D. S., COX, C. S., JR. & WU, P. 2016. Human Neural Stem Cell Transplantation-Mediated Alteration of Microglial/Macrophage Phenotypes after Traumatic Brain Injury. *Cell Transplant,* 25**,** 1863-1877.
GAO, J., PROUGH, D. S., MCADOO, D. J., GRADY, J. J., PARSLEY, M. O., MA, L., TARENSENKO, Y. I. & WU, P. 2006. Transplantation of primed human fetal neural stem cells improves cognitive function in rats after traumatic brain injury. *Experimental neurology,* 201**,** 281-292.
GARASCHUK, O., LINN, J., EILERS, J. & KONNERTH, A. 2000. Large-scale oscillatory calcium waves in the immature cortex. *Nat Neurosci,* 3**,** 452-9.
GASPARD, N., BOUSCHET, T., HOUREZ, R., DIMIDSCHSTEIN, J., NAEIJE, G., VAN DEN AMEELE, J., ESPUNY-CAMACHO, I., HERPOEL, A., PASSANTE, L. & SCHIFFMANN, S. N. 2008. An

intrinsic mechanism of corticogenesis from embryonic stem cells. *Nature,* 455**,** 351-357.
GELMAN, D. M., MARTINI, F. J., NÓBREGA-PEREIRA, S., PIERANI, A., KESSARIS, N. & MARÍN, O. 2009. The embryonic preoptic area is a novel source of cortical GABAergic interneurons. *Journal of Neuroscience,* 29**,** 9380-9389.
GHAFFARPASAND, F., RAZMKON, A. & DEHGHANKHALILI, M. 2013. Glasgow Coma Scale Score in Pediatric Patients with Traumatic Brain Injury; Limitations and Reliability. *Bull Emerg Trauma,* 1**,** 135-6.
GILBERT, C. D. 1983. Microcircuitry of the visual cortex. *Annual review of neuroscience,* 6**,** 217-247.
GIORDANO, K. R., ROJAS-VALENCIA, L. M., BHARGAVA, V. & LIFSHITZ, J. 2020. Beyond binary: influence of sex and gender on outcome after traumatic brain injury. *Journal of neurotrauma,* 37**,** 2454-2459.
GIOVANNUCCI, A., FRIEDRICH, J., GUNN, P., KALFON, J., BROWN, B. L., KOAY, S. A., TAXIDIS, J., NAJAFI, F., GAUTHIER, J. L., ZHOU, P., KHAKH, B. S., TANK, D. W., CHKLOVSKII, D. B. & PNEVMATIKAKIS, E. A. 2019. CaImAn an open source tool for scalable calcium imaging data analysis. *Elife,* 8.
GOBBEL, G. T., KONDZIOLKA, D., FELLOWS-MAYLE, W. & URAM, M. 2010. Cellular transplantation for the nervous system: impact of time after preparation on cell viability and survival. *J Neurosurg,* 113**,** 666-72.
GOPARAJU, S., KOHDA, K., IBATA, K., SOMA, A., NAKATAKE, Y., AKIYAMA, T., WAKABAYASHI, S., MATSUSHITA, M., SAKOTA, M. & KIMURA, H. 2017. Rapid differentiation of human pluripotent stem cells into functional neurons by mRNAs encoding transcription factors. Sci Rep 7: 42367.
GORSKI, J. A., TALLEY, T., QIU, M., PUELLES, L., RUBENSTEIN, J. L. & JONES, K. R. 2002. Cortical excitatory neurons and glia, but not GABAergic neurons, are produced in the Emx1-expressing lineage. *Journal of Neuroscience,* 22**,** 6309-6314.
GRADE, S. & GOTZ, M. 2017. Neuronal replacement therapy: previous achievements and challenges ahead. *NPJ Regen Med,* 2**,** 29.
GRAHAM, V., KHUDYAKOV, J., ELLIS, P. & PEVNY, L. 2003. SOX2 functions to maintain neural progenitor identity. *Neuron,* 39**,** 749-765.
GREENFIELD JR, L. J. 2013. Molecular mechanisms of antiseizure drug activity at GABAA receptors. *Seizure,* 22**,** 589-600.
GRIENBERGER, C. & KONNERTH, A. 2012. Imaging calcium in neurons. *Neuron,* 73**,** 862-885.
GRØNNING HANSEN, M., LATERZA, C., PALMA-TORTOSA, S., KVIST, G., MONNI, E., TSUPYKOV, O., TORNERO, D., UOSHIMA, N., SORIANO, J. & BENGZON, J. 2020. Grafted human pluripotent stem cell-derived cortical neurons integrate into adult human cortical neural circuitry. *Stem cells translational medicine,* 9**,** 1365-1377.
GROVE, E. A. & FUKUCHI-SHIMOGORI, T. 2003. Generating the cerebral cortical area map. *Annual review of neuroscience,* 26**,** 355-380.
GU, Q., TOMASKOVIC-CROOK, E., LOZANO, R., CHEN, Y., KAPSA, R. M., ZHOU, Q., WALLACE, G. G. & CROOK, J. M. 2016. Functional 3D Neural Mini-Tissues from Printed Gel-Based Bioink and Human Neural Stem Cells. *Adv Healthc Mater,* 5**,** 1429-38.
GUNGOR-OZKERIM, P. S., INCI, I., ZHANG, Y. S., KHADEMHOSSEINI, A. & DOKMECI, M. R. 2018. Bioinks for 3D bioprinting: an overview. *Biomater Sci,* 6**,** 915-946.

GUNHANLAR, N., SHPAK, G., VAN DER KROEG, M., GOUTY-COLOMER, L., MUNSHI, S., LENDEMEIJER, B., GHAZVINI, M., DUPONT, C., HOOGENDIJK, W. & GRIBNAU, J. 2018. A simplified protocol for differentiation of electrophysiologically mature neuronal networks from human induced pluripotent stem cells. *Molecular psychiatry,* 23**,** 1336-1344.

HAENSELER, W., SANSOM, S. N., BUCHRIESER, J., NEWEY, S. E., MOORE, C. S., NICHOLLS, F. J., CHINTAWAR, S., SCHNELL, C., ANTEL, J. P. & ALLEN, N. D. 2017. A highly efficient human pluripotent stem cell microglia model displays a neuronal-co-culture-specific expression profile and inflammatory response. *Stem cell reports,* 8**,** 1727-1742.

HAN, Y. K., ZHANG, H. J., CHEN, Y. J., LIU, C., ZHANG, Y. H., ZHANG, Z. J., JING, R. T., GUO, L., LI, D. & CHU, W. Y. 2025. Small-world network and neuroscience. *Brain-X,* 3**,** e70025.

HANAFY, S., XIONG, C., SUTTON, M., ESCOBAR, M., COLANTONIO, A. & MOLLAYEVA, T. 2021. Comorbidity in traumatic brain injury and functional outcomes: a systematic review. *European journal of physical and rehabilitation medicine,* 57**,** 535.

HANSIS, C., GRIFO, J. & KREY, L. 2000. Oct-4 expression in inner cell mass and trophectoderm of human blastocysts. *Molecular human reproduction,* 6**,** 999-1004.

HARB, K., MAGRINELLI, E., NICOLAS, C. S., LUKIANETS, N., FRANGEUL, L., PIETRI, M., SUN, T., SANDOZ, G., GRAMMONT, F. & JABAUDON, D. 2016. Area-specific development of distinct projection neuron subclasses is regulated by postnatal epigenetic modifications. *Elife,* 5**,** e09531.

HARTING, M. T., SLOAN, L. E., JIMENEZ, F., BAUMGARTNER, J. & COX JR, C. S. 2009. Subacute neural stem cell therapy for traumatic brain injury. *Journal of Surgical Research,* 153**,** 188-194.

HAUS, D. L., LÓPEZ-VELÁZQUEZ, L., GOLD, E. M., CUNNINGHAM, K. M., PEREZ, H., ANDERSON, A. J. & CUMMINGS, B. J. 2016. Transplantation of human neural stem cells restores cognition in an immunodeficient rodent model of traumatic brain injury. *Exp Neurol,* 281**,** 1-16.

HAUS, D. L., NGUYEN, H. X., GOLD, E. M., KAMEI, N., PEREZ, H., MOORE, H. D., ANDERSON, A. J. & CUMMINGS, B. J. 2014. CD133-enriched Xeno-Free human embryonic-derived neural stem cells expand rapidly in culture and do not form teratomas in immunodeficient mice. *Stem cell research,* 13**,** 214-226.

HE, J., WANG, X.-M., SPECTOR, M. & CUI, F.-Z. 2012. Scaffolds for central nervous system tissue engineering. *Frontiers of Materials Science,* 6**,** 1-25.

HISAOKA, T., NAKAMURA, Y., SENBA, E. & MORIKAWA, Y. 2010. The forkhead transcription factors, Foxp1 and Foxp2, identify different subpopulations of projection neurons in the mouse cerebral cortex. *Neuroscience,* 166**,** 551-563.

HOANE, M. R., BECERRA, G. D., SHANK, J. E., TATKO, L., PAK, E. S., SMITH, M. & MURASHOV, A. K. 2004. Transplantation of neuronal and glial precursors dramatically improves sensorimotor function but not cognitive function in the traumatically injured brain. *Journal of neurotrauma,* 21**,** 163-174.

HONG, Y., DONG, X., CHANG, L., XIE, C., CHANG, M., AGUILAR, J. S., LIN, J., LIN, J. & LI, Q. Q. 2023. Microglia-containing cerebral organoids derived from induced pluripotent stem cells for the study of neurological diseases. *iScience,* 26**,** 106267.

HOPKINS, A. M., DESIMONE, E., CHWALEK, K. & KAPLAN, D. L. 2015. 3D in vitro modeling of the central nervous system. *Prog Neurobiol,* 125**,** 1-25.

HSU, T. T., HUANG, T. N. & HSUEH, Y. P. 2020. Anterior Commissure Regulates Neuronal Activity of Amygdalae and Influences Locomotor Activity, Social Interaction and Fear Memory in Mice. *Front Mol Neurosci,* 13**,** 47.

HU, B. Y., WEICK, J. P., YU, J., MA, L. X., ZHANG, X. Q., THOMSON, J. A. & ZHANG, S. C. 2010. Neural differentiation of human induced pluripotent stem cells follows developmental principles but with variable potency. *Proc Natl Acad Sci U S A,* 107**,** 4335-40.

HU, J., CHEN, L., HUANG, X., WU, K., DING, S., WANG, W., WANG, B., SMITH, C., REN, C., NI, H., ZHUGE, Q. & YANG, J. 2019. Calpain inhibitor MDL28170 improves the transplantation-mediated therapeutic effect of bone marrow-derived mesenchymal stem cells following traumatic brain injury. *Stem Cell Res Ther,* 10**,** 96.

HU, L., YANG, S., JIN, B. & WANG, C. 2022. Advanced Neuroimaging Role in Traumatic Brain Injury: A Narrative Review. *Front Neurosci,* 16**,** 872609.

HU, X., LEAK, R. K., SHI, Y., SUENAGA, J., GAO, Y., ZHENG, P. & CHEN, J. 2015. Microglial and macrophage polarization—new prospects for brain repair. *Nature Reviews Neurology,* 11**,** 56-64.

HUANG, G., YE, S., ZHOU, X., LIU, D. & YING, Q. L. 2015. Molecular basis of embryonic stem cell self-renewal: from signaling pathways to pluripotency network. *Cell Mol Life Sci,* 72**,** 1741-57.

HUANG, M. X., HUANG, C. W., HARRINGTON, D. L., NICHOLS, S., ROBB-SWAN, A., ANGELES-QUINTO, A., LE, L., RIMMELE, C., DRAKE, A., SONG, T., HUANG, J. W., CLIFFORD, R., JI, Z., CHENG, C. K., LERMAN, I., YURGIL, K. A., LEE, R. R. & BAKER, D. G. 2020. Marked Increases in Resting-State MEG Gamma-Band Activity in Combat-Related Mild Traumatic Brain Injury. *Cereb Cortex,* 30**,** 283-295.

HUANG, S., HUANG, F., ZHANG, H., YANG, Y., LU, J., CHEN, J., SHEN, L. & PEI, G. 2022. In vivo development and single-cell transcriptome profiling of human brain organoids. *Cell Prolif,* 55**,** e13201.

HUBERS, A., OREKHOV, Y. & ZIEMANN, U. 2008. Interhemispheric motor inhibition: its role in controlling electromyographic mirror activity. *Eur J Neurosci,* 28**,** 364-71.

HUGHES, C. S., POSTOVIT, L. M. & LAJOIE, G. A. 2010. Matrigel: a complex protein mixture required for optimal growth of cell culture. *Proteomics,* 10**,** 1886-90.

IMAI, R., TAMURA, R., YO, M., SATO, M., FUKUMURA, M., TAKAHARA, K., KASE, Y., OKANO, H. & TODA, M. 2023. Neuroprotective effects of genome-edited human iPS cell-derived neural stem/progenitor cells on traumatic brain injury. *Stem Cells,* 41**,** 603-616.

INMAN, G. J., NICOLÁS, F. J., CALLAHAN, J. F., HARLING, J. D., GASTER, L. M., REITH, A. D., LAPING, N. J. & HILL, C. S. 2002. SB-431542 is a potent and specific inhibitor of transforming growth factor-β superfamily type I activin receptor-like kinase (ALK) receptors ALK4, ALK5, and ALK7. *Molecular pharmacology,* 62**,** 65-74.

JAKOVCEVSKI, I., MILJKOVIC, D., SCHACHNER, M. & ANDJUS, P. R. 2013. Tenascins and inflammation in disorders of the nervous system. *Amino Acids,* 44**,** 1115-1127.

JGAMADZE, D., LIM, J. T., ZHANG, Z., HARARY, P. M., GERMI, J., MENSAH-BROWN, K., ADAM, C. D., MIRZAKHALILI, E., SINGH, S., GU, J. B., BLUE, R., DEDHIA, M., FU, M., JACOB, F., QIAN, X., GAGNON, K., SERGISON, M., FRUCHET, O., RAHAMAN, I., WANG, H., XU, F., XIAO, R., CONTRERAS, D., WOLF, J. A., SONG, H., MING, G. L. & CHEN, H. I. 2023.

Structural and functional integration of human forebrain organoids with the injured adult rat visual system. *Cell Stem Cell,* 30**,** 137-152 e7.

JHA, R. M., RAJASUNDARAM, D., SNEIDERMAN, C., SCHLEGEL, B. T., O'BRIEN, C., XIONG, Z., JANESKO-FELDMAN, K., TRIVEDI, R., VAGNI, V., ZUSMAN, B. E., CATAPANO, J. S., EBERLE, A., DESAI, S. M., JADHAV, A. P., MIHALJEVIC, S., MILLER, M., RAIKWAR, S., RANI, A., RULNEY, J., SHAHJOUIE, S., RAPHAEL, I., KUMAR, A., PHUAH, C. L., WINKLER, E. A., SIMON, D. W., KOCHANEK, P. M. & KOHANBASH, G. 2024. A single-cell atlas deconstructs heterogeneity across multiple models in murine traumatic brain injury and identifies novel cell-specific targets. *Neuron,* 112**,** 3069-3088 e4.

JI, X., ZHOU, S., WANG, N., WANG, J., WU, Y., DUAN, Y., NI, P., ZHANG, J. & YU, S. 2023. Cerebral-Organoid-Derived Exosomes Alleviate Oxidative Stress and Promote LMX1A-Dependent Dopaminergic Differentiation. *Int J Mol Sci,* 24.

JIANG, L., LI, R., TANG, H., ZHONG, J., SUN, H., TANG, W., WANG, H. & ZHU, J. 2019. MRI tracking of iPS cells-induced neural stem cells in traumatic brain injury rats. *Cell Transplantation,* 28**,** 747-755.

JIANG, L. L., LI, H. & LIU, L. 2021. Xenogeneic stem cell transplantation: Research progress and clinical prospects. *World J Clin Cases,* 9**,** 3826-3837.

JIN, Y., MIKHAILOVA, E., LEI, M., COWLEY, S., SUN, T., YANG, X., ZHANG, Y., LIU, K., CATARINO, D., SOARES, L. C., BANDIERA, S., SZELE, F. G., MOLNAR, Z., ZHOU, L. & BAYLEY, H. 2022. Functional Integration of 3D-Printed Cerebral Cortical Tissue into a Brain Lesion. *bioRxiv***,** 2022.10.28.513987.

JIN, Y., MIKHAILOVA, E., LEI, M., COWLEY, S. A., SUN, T., YANG, X., ZHANG, Y., LIU, K., CATARINO DA SILVA, D., CAMPOS SOARES, L., BANDIERA, S., SZELE, F. G., MOLNÁR, Z., ZHOU, L. & BAYLEY, H. 2023. Integration of 3D-printed cerebral cortical tissue into an ex vivo lesioned brain slice. *Nature Communications,* 14**,** 5986.

JO, J., XIAO, Y., SUN, A. X., CUKUROGLU, E., TRAN, H. D., GÖKE, J., TAN, Z. Y., SAW, T. Y., TAN, C. P., LOKMAN, H., LEE, Y., KIM, D., KO, H. S., KIM, S. O., PARK, J. H., CHO, N. J., HYDE, T. M., KLEINMAN, J. E., SHIN, J. H., WEINBERGER, D. R., TAN, E. K., JE, H. S. & NG, H. H. 2016. Midbrain-like Organoids from Human Pluripotent Stem Cells Contain Functional Dopaminergic and Neuromelanin-Producing Neurons. *Cell Stem Cell,* 19**,** 248-257.

JONES, E. G. & RAKIC, P. 2010. Radial columns in cortical architecture: it is the composition that counts. *Cereb Cortex,* 20**,** 2261-4.

JOUNG, D., TRUONG, V., NEITZKE, C. C., GUO, S. Z., WALSH, P. J., MONAT, J. R., MENG, F., PARK, S. H., DUTTON, J. R., PARR, A. M. & MCALPINE, M. C. 2018. 3D Printed Stem-Cell Derived Neural Progenitors Generate Spinal Cord Scaffolds. *Adv Funct Mater,* 28.

JUNPENG, M., HUANG, S. & QIN, S. 2011. Progesterone for acute traumatic brain injury. *Cochrane Database of Systematic Reviews*.

JURGA, A. M., PALECZNA, M., KADLUCZKA, J. & KUTER, K. Z. 2021. Beyond the GFAP-Astrocyte Protein Markers in the Brain. *Biomolecules,* 11.

KAAS, J. H. 2012. Evolution of columns, modules, and domains in the neocortex of primates. *Proceedings of the National Academy of Sciences,* 109**,** 10655-10660.

KADOSHIMA, T., SAKAGUCHI, H., NAKANO, T., SOEN, M., ANDO, S., EIRAKU, M. & SASAI, Y. 2013. Self-organization of axial polarity, inside-out layer pattern, and species-specific progenitor dynamics in human ES cell-derived neocortex. *Proc Natl Acad Sci U S A,* 110**,** 20284-9.

KADRI, A. & APRIANI, N. 2022. Electroencephalography findings in traumatic brain injury. *The Open Neurology Journal,* 16.
KANG, W. H. & MORRISON, B., 3RD 2015. Predicting changes in cortical electrophysiological function after in vitro traumatic brain injury. *Biomech Model Mechanobiol,* 14**,** 1033-44.
KARVE, I. P., TAYLOR, J. M. & CRACK, P. J. 2016. The contribution of astrocytes and microglia to traumatic brain injury. *Br J Pharmacol,* 173**,** 692-702.
KAUSHAL, V. & SCHLICHTER, L. C. 2008. Mechanisms of microglia-mediated neurotoxicity in a new model of the stroke penumbra. *J Neurosci,* 28**,** 2221-30.
KAVALALI, E. T., CHUNG, C., KHVOTCHEV, M., LEITZ, J., NOSYREVA, E., RAINGO, J. & RAMIREZ, D. M. 2011. Spontaneous neurotransmission: an independent pathway for neuronal signaling? *Physiology (Bethesda),* 26**,** 45-53.
KEPECS, A. & FISHELL, G. 2014. Interneuron cell types are fit to function. *Nature,* 505**,** 318-326.
KIM, D. S., ROSS, P. J., ZASLAVSKY, K. & ELLIS, J. 2014. Optimizing neuronal differentiation from induced pluripotent stem cells to model ASD. *Front Cell Neurosci,* 8**,** 109.
KIM, J. T., KIM, T. Y., YOUN, D. H., HAN, S. W., PARK, C. H., LEE, Y., JUNG, H., RHIM, J. K., PARK, J. J., AHN, J. H., KIM, H. C., CHO, S. M. & JEON, J. P. 2022. Human embryonic stem cell-derived cerebral organoids for treatment of mild traumatic brain injury in a mouse model. *Biochem Biophys Res Commun,* 635**,** 169-178.
KIRWAN, P., TURNER-BRIDGER, B., PETER, M., MOMOH, A., ARAMBEPOLA, D., ROBINSON, H. P. & LIVESEY, F. J. 2015. Development and function of human cerebral cortex neural networks from pluripotent stem cells in vitro. *Development,* 142**,** 3178-3187.
KITAHARA, T., SAKAGUCHI, H., MORIZANE, A., KIKUCHI, T., MIYAMOTO, S. & TAKAHASHI, J. 2020. Axonal Extensions along Corticospinal Tracts from Transplanted Human Cerebral Organoids. *Stem Cell Reports,* 15**,** 467-481.
KLEINMAN, H. K. & MARTIN, G. R. Matrigel: basement membrane matrix with biological activity. Seminars in cancer biology, 2005. Elsevier, 378-386.
KOFMAN, S., MOHAN, N., SUN, X., IBRIC, L., PIERMARINI, E. & QIANG, L. 2022. Human mini brains and spinal cords in a dish: Modeling strategies, current challenges, and prospective advances. *Journal of Tissue Engineering,* 13**,** 20417314221113391.
KOHWI, M. & DOE, C. Q. 2013. Temporal fate specification and neural progenitor competence during development. *Nature Reviews Neuroscience,* 14**,** 823-838.
KONDZIOLKA, D., GOBBEL, G. T., FELLOWS-MAYLE, W., CHANG, Y. F. & URAM, M. 2011. Injection parameters affect cell viability and implant volumes in automated cell delivery for the brain. *Cell Transplant,* 20**,** 1901-6.
KOSTOVIC, I. & GOLDMAN-RAKIC, P. S. 1983. Transient cholinesterase staining in the mediodorsal nucleus of the thalamus and its connections in the developing human and monkey brain. *Journal of Comparative Neurology,* 219**,** 431-447.
KOUTSOUDAKI, P. N., PAPASTEFANAKI, F., STAMATAKIS, A., KOUROUPI, G., XINGI, E., STYLIANOPOULOU, F. & MATSAS, R. 2016. Neural stem/progenitor cells differentiate into oligodendrocytes, reduce inflammation, and ameliorate learning deficits after transplantation in a mouse model of traumatic brain injury. *Glia,* 64**,** 763-779.
KRAGEL, J. E., VANHAERENTS, S., TEMPLER, J. W., SCHUELE, S., ROSENOW, J. M., NILAKANTAN, A. S. & BRIDGE, D. J. 2020. Hippocampal theta coordinates memory processing during visual exploration. *Elife,* 9.

KRIEGSTEIN, A. R. & NOCTOR, S. C. 2004. Patterns of neuronal migration in the embryonic cortex. *Trends Neurosci,* 27**,** 392-9.
KRUKOWSKI, K. 2021. Short review: The impact of sex on neuroimmune and cognitive outcomes after traumatic brain injury. *Brain Behav Immun Health,* 16**,** 100327.
KUIJLAARS, J., OYELAMI, T., DIELS, A., ROHRBACHER, J., VERSWEYVELD, S., MENEGHELLO, G., TUEFFERD, M., VERSTRAELEN, P., DETREZ, J. R., VERSCHUUREN, M., DE VOS, W. H., MEERT, T., PEETERS, P. J., CIK, M., NUYDENS, R., BRONE, B. & VERHEYEN, A. 2016. Sustained synchronized neuronal network activity in a human astrocyte co-culture system. *Sci Rep,* 6**,** 36529.
LANCASTER, M. A., CORSINI, N. S., WOLFINGER, S., GUSTAFSON, E. H., PHILLIPS, A. W., BURKARD, T. R., OTANI, T., LIVESEY, F. J. & KNOBLICH, J. A. 2017. Guided self-organization and cortical plate formation in human brain organoids. *Nat Biotechnol,* 35**,** 659-666.
LANCASTER, M. A. & KNOBLICH, J. A. 2014. Organogenesis in a dish: modeling development and disease using organoid technologies. *Science,* 345**,** 1247125.
LANCASTER, M. A., RENNER, M., MARTIN, C. A., WENZEL, D., BICKNELL, L. S., HURLES, M. E., HOMFRAY, T., PENNINGER, J. M., JACKSON, A. P. & KNOBLICH, J. A. 2013. Cerebral organoids model human brain development and microcephaly. *Nature,* 501**,** 373-379.
LANDER, A. D., STIPP, C. S. & IVINS, J. K. 1996. The glypican family of heparan sulfate proteoglycans: major cell-surface proteoglycans of the developing nervous system. *Perspect Dev Neurobiol,* 3**,** 347-58.
LATCHOUMANE, C. V., BETANCUR, M. I., SIMCHICK, G. A., SUN, M. K., FORGHANI, R., LENEAR, C. E., AHMED, A., MOHANKUMAR, R., BALAJI, N., MASON, H. D., ARCHER-HARTMANN, S. A., AZADI, P., HOLMES, P. V., ZHAO, Q., BELLAMKONDA, R. V. & KARUMBAIAH, L. 2021. Engineered glycomaterial implants orchestrate large-scale functional repair of brain tissue chronically after severe traumatic brain injury. *Sci Adv,* 7.
LEE, D. H., LEE, E. C., LEE, J. Y., LEE, M. R., SHIM, J. W. & OH, J. S. 2024. Neuronal Cell Differentiation of iPSCs for the Clinical Treatment of Neurological Diseases. *Biomedicines,* 12.
LEE, J.-Y., ACOSTA, S., TUAZON, J. P., XU, K., NGUYEN, H., LIPPERT, T., LISKA, M. G., SEMECHKIN, A., GARITAONANDIA, I. & GONZALEZ, R. 2019. Human parthenogenetic neural stem cell grafts promote multiple regenerative processes in a traumatic brain injury model. *Theranostics,* 9**,** 1029.
LEE, J. C., CALLAWAY, J. C. & FOEHRING, R. C. 2005. Effects of temperature on calcium transients and Ca2+-dependent afterhyperpolarizations in neocortical pyramidal neurons. *J Neurophysiol,* 93**,** 2012-20.
LEE, K. Y. & MOONEY, D. J. 2012. Alginate: properties and biomedical applications. *Prog Polym Sci,* 37**,** 106-126.
LEIBACHER, J. & HENSCHLER, R. 2016. Biodistribution, migration and homing of systemically applied mesenchymal stem/stromal cells. *Stem Cell Res Ther,* 7**,** 7.
LELE, A. V. 2022. Traumatic Brain Injury in Different Age Groups. *J Clin Med,* 11.
LEONE, D. P., SRINIVASAN, K., CHEN, B., ALCAMO, E. & MCCONNELL, S. K. 2008. The determination of projection neuron identity in the developing cerebral cortex. *Current opinion in neurobiology,* 18**,** 28-35.

LERTKIATMONGKOL, P., LIAO, D., MEI, H., HU, Y. & NEWMAN, P. J. 2016. Endothelial functions of platelet/endothelial cell adhesion molecule-1 (CD31). *Current opinion in hematology,* 23**,** 253-259.

LESNY, P., DE CROOS, J., PRADNY, M., VACIK, J., MICHALEK, J., WOERLY, S. & SYKOVA, E. 2002. Polymer hydrogels usable for nervous tissue repair. *J Chem Neuroanat,* 23**,** 243-7.

LETINIC, K., ZONCU, R. & RAKIC, P. 2002. Origin of GABAergic neurons in the human neocortex. *Nature,* 417**,** 645-9.

LI, J., ZHANG, D., GUO, S., ZHAO, C., WANG, L., MA, S., GUAN, F. & YAO, M. 2021. Dual-enzymatically cross-linked gelatin hydrogel promotes neural differentiation and neurotrophin secretion of bone marrow-derived mesenchymal stem cells for treatment of moderate traumatic brain injury. *Int J Biol Macromol,* 187**,** 200-213.

LI, J. Y., LAI, P. H. & CHEN, R. 2013. Transcallosal inhibition in patients with callosal infarction. *J Neurophysiol,* 109**,** 659-65.

LI, X., DUAN, L., KONG, M., WEN, X., GUAN, F. & MA, S. 2022. Applications and Mechanisms of Stimuli-Responsive Hydrogels in Traumatic Brain Injury. *Gels,* 8.

LI, X. H., HU, N., CHANG, Z. H., SHI, J. X., FAN, X., CHEN, M. M., BAO, S. Q., CHEN, C., ZUO, J. C., ZHANG, X. W., WANG, J. J. & MING, D. 2024. Brain organoid maturation and implantation integration based on electrical signals input. *J Adv Res*.

LIAO, G. P., HARTING, M. T., HETZ, R. A., WALKER, P. A., SHAH, S. K., CORKINS, C. J., HUGHES, T. G., JIMENEZ, F., KOSMACH, S. C., DAY, M. C., TSAO, K., LEE, D. A., WORTH, L. L., BAUMGARTNER, J. E. & COX, C. S., JR. 2015. Autologous bone marrow mononuclear cells reduce therapeutic intensity for severe traumatic brain injury in children. *Pediatr Crit Care Med,* 16**,** 245-55.

LIESI, P., KIRKWOOD, T. & VAHERI, A. 1986. Fibronectin is expressed by astrocytes cultured from embryonic and early postnatal rat brain. *Experimental Cell Research,* 163**,** 175-185.

LINARO, D., VERMAERCKE, B., IWATA, R., RAMASWAMY, A., LIBÉ-PHILIPPOT, B., BOUBAKAR, L., DAVIS, B. A., WIERDA, K., DAVIE, K. & POOVATHINGAL, S. 2019. Xenotransplanted human cortical neurons reveal species-specific development and functional integration into mouse visual circuits. *Neuron,* 104**,** 972-986. e6.

LINDVALL, O., REHNCRONA, S., BRUNDIN, P., GUSTAVII, B., ASTEDT, B., WIDNER, H., LINDHOLM, T., BJÖRKLUND, A., LEENDERS, K. L., ROTHWELL, J. C., FRACKOWIAK, R., MARSDEN, D., JOHNELS, B., STEG, G., FREEDMAN, R., HOFFER, B. J., SEIGER, A., BYGDEMAN, M., STRÖMBERG, I. & OLSON, L. 1989. Human fetal dopamine neurons grafted into the striatum in two patients with severe Parkinson's disease. A detailed account of methodology and a 6-month follow-up. *Arch Neurol,* 46**,** 615-31.

LISCHALK, J. W., EASTON, C. R. & MOODY, W. J. 2009. Bilaterally propagating waves of spontaneous activity arising from discrete pacemakers in the neonatal mouse cerebral cortex. *Dev Neurobiol,* 69**,** 407-14.

LIU, H., BOCKHORN, J., DALTON, R., CHANG, Y.-F., QIAN, D., ZITZOW, L. A., CLARKE, M. F. & GREENE, G. L. 2011. Removal of lactate dehydrogenase-elevating virus from human-in-mouse breast tumor xenografts by cell-sorting. *Journal of virological methods,* 173**,** 266-270.

LIU, S., SHI, L., HUANG, T., LUO, Y., CHEN, Y., LI, S. & WANG, Z. 2024a. Neural stem cells transplanted into rhesus monkey cortical traumatic brain injury can survive and differentiate into neurons. *International Journal of Molecular Sciences,* 25**,** 1642.

LIU, Y., ZHANG, J., JIANG, Z., QIN, M., XU, M., ZHANG, S. & MA, G. 2024b. Organization of corticocortical and thalamocortical top-down inputs in the primary visual cortex. *Nat Commun,* 15**,** 4495.

LO, F. S. & ERZURUMLU, R. S. 2002. L-type calcium channel-mediated plateau potentials in barrelette cells during structural plasticity. *J Neurophysiol,* 88**,** 794-801.

LOANE, D. J. & FADEN, A. I. 2010. Neuroprotection for traumatic brain injury: translational challenges and emerging therapeutic strategies. *Trends Pharmacol Sci,* 31**,** 596-604.

LOANE, D. J. & KUMAR, A. 2016. Microglia in the TBI brain: The good, the bad, and the dysregulated. *Exp Neurol,* 275 Pt 3**,** 316-327.

LODATO, S., SHETTY, A. S. & ARLOTTA, P. 2015. Cerebral cortex assembly: generating and reprogramming projection neuron diversity. *Trends in neurosciences,* 38**,** 117-125.

LÓPEZ-BENDITO, G. & MOLNÁR, Z. 2003. Thalamocortical development: how are we going to get there? *Nature Reviews Neuroscience,* 4**,** 276-289.

LOTHARIUS, J. & BRUNDIN, P. 2002. Pathogenesis of Parkinson's disease: dopamine, vesicles and alpha-synuclein. *Nat Rev Neurosci,* 3**,** 932-42.

LOVETT, M. L., NIELAND, T. J., DINGLE, Y. T. L. & KAPLAN, D. L. 2020. Innovations in 3D tissue models of human brain physiology and diseases. *Advanced functional materials,* 30**,** 1909146.

LOZANO, D., GONZALES-PORTILLO, G. S., ACOSTA, S., DE LA PENA, I., TAJIRI, N., KANEKO, Y. & BORLONGAN, C. V. 2015a. Neuroinflammatory responses to traumatic brain injury: etiology, clinical consequences, and therapeutic opportunities. *Neuropsychiatric disease and treatment,* 11**,** 97.

LOZANO, R., STEVENS, L., THOMPSON, B. C., GILMORE, K. J., GORKIN, R., 3RD, STEWART, E. M., IN HET PANHUIS, M., ROMERO-ORTEGA, M. & WALLACE, G. G. 2015b. 3D printing of layered brain-like structures using peptide modified gellan gum substrates. *Biomaterials,* 67**,** 264-73.

LU, D., MAHMOOD, A., QU, C., HONG, X., KAPLAN, D. & CHOPP, M. 2007. Collagen scaffolds populated with human marrow stromal cells reduce lesion volume and improve functional outcome after traumatic brain injury. *Neurosurgery,* 61**,** 596-602; discussion 602-3.

LU, Y. B., FRANZE, K., SEIFERT, G., STEINHÄUSER, C., KIRCHHOFF, F., WOLBURG, H., GUCK, J., JANMEY, P., WEI, E. Q., KÄS, J. & REICHENBACH, A. 2006. Viscoelastic properties of individual glial cells and neurons in the CNS. *Proceedings of the National Academy of Sciences of the United States of America,* 103**,** 17759-17764.

LUCKENBILL-EDDS, L. 1997. Laminin and the mechanism of neuronal outgrowth. *Brain Res Brain Res Rev,* 23**,** 1-27.

LUDWIG, P. E., THANKAM, F. G., PATIL, A. A., CHAMCZUK, A. J. & AGRAWAL, D. K. 2018. Brain injury and neural stem cells. *Neural Regen Res,* 13**,** 7-18.

LUHMANN, H. J., SINNING, A., YANG, J. W., REYES-PUERTA, V., STUTTGEN, M. C., KIRISCHUK, S. & KILB, W. 2016. Spontaneous Neuronal Activity in Developing Neocortical Networks: From Single Cells to Large-Scale Interactions. *Front Neural Circuits,* 10**,** 40.

LUSKIN, M. B. & SHATZ, C. J. 1985. Neurogenesis of the cat's primary visual cortex. *J Comp Neurol,* 242**,** 611-31.

MA, H., YU, B., KONG, L., ZHANG, Y. & SHI, Y. 2012. Neural stem cells over-expressing brain-derived neurotrophic factor (BDNF) stimulate synaptic protein expression and promote functional recovery following transplantation in rat model of traumatic brain injury. *Neurochemical research,* 37**,** 69-83.

MA, W., FITZGERALD, W., LIU, Q.-Y., O'SHAUGHNESSY, T., MARIC, D., LIN, H., ALKON, D. & BARKER, J. 2004. CNS stem and progenitor cell differentiation into functional neuronal circuits in three-dimensional collagen gels. *Experimental neurology,* 190**,** 276-288.

MAAS, A. I., HARRISON-FELIX, C. L., MENON, D., ADELSON, P. D., BALKIN, T., BULLOCK, R., ENGEL, D. C., GORDON, W., ORMAN, J. L., LEW, H. L., ROBERTSON, C., TEMKIN, N., VALADKA, A., VERFAELLIE, M., WAINWRIGHT, M., WRIGHT, D. W. & SCHWAB, K. 2010. Common data elements for traumatic brain injury: recommendations from the interagency working group on demographics and clinical assessment. *Arch Phys Med Rehabil,* 91**,** 1641-9.

MAAS, A. I., MENON, D. K., MANLEY, G. T., ABRAMS, M., ÅKERLUND, C., ANDELIC, N., ARIES, M., BASHFORD, T., BELL, M. J. & BODIEN, Y. G. 2022. Traumatic brain injury: progress and challenges in prevention, clinical care, and research. *The Lancet Neurology,* 21**,** 1004-1060.

MACLEAN, F. L., HORNE, M. K., WILLIAMS, R. J. & NISBET, D. R. 2018. Review: Biomaterial systems to resolve brain inflammation after traumatic injury. *APL Bioeng,* 2**,** 021502.

MAHENDIRAN, B., MUTHUSAMY, S., SAMPATH, S., JAISANKAR, S. N., POPAT, K. C., SELVAKUMAR, R. & KRISHNAKUMAR, G. S. 2021. Recent trends in natural polysaccharide based bioinks for multiscale 3D printing in tissue regeneration: A review. *Int J Biol Macromol,* 183**,** 564-588.

MAHMOOD, A., WU, H., QU, C., XIONG, Y. & CHOPP, M. 2013. Effects of treating traumatic brain injury with collagen scaffolds and human bone marrow stromal cells on sprouting of corticospinal tract axons into the denervated side of the spinal cord. *Journal of neurosurgery,* 118**,** 381-389.

MAKINEN, M. E., YLA-OUTINEN, L. & NARKILAHTI, S. 2018. GABA and Gap Junctions in the Development of Synchronized Activity in Human Pluripotent Stem Cell-Derived Neural Networks. *Front Cell Neurosci,* 12**,** 56.

MAKRI, G., LAVDAS, A. A., KATSIMPARDI, L., CHARNEAU, P., THOMAIDOU, D. & MATSAS, R. 2010. Transplantation of embryonic neural stem/precursor cells overexpressing BM88/Cend1 enhances the generation of neuronal cells in the injured mouse cortex. *Stem Cells,* 28**,** 127-39.

MALMERSJO, S., REBELLATO, P., SMEDLER, E., PLANERT, H., KANATANI, S., LISTE, I., NANOU, E., SUNNER, H., ABDELHADY, S., ZHANG, S., ANDANG, M., EL MANIRA, A., SILBERBERG, G., ARENAS, E. & UHLEN, P. 2013. Neural progenitors organize in small-world networks to promote cell proliferation. *Proc Natl Acad Sci U S A,* 110**,** E1524-32.

MANSOUR, A. A., GONÇALVES, J. T., BLOYD, C. W., LI, H., FERNANDES, S., QUANG, D., JOHNSTON, S., PARYLAK, S. L., JIN, X. & GAGE, F. H. 2018. An in vivo model of functional and vascularized human brain organoids. *Nature biotechnology,* 36**,** 432-441.

MARKOV, N. T., VEZOLI, J., CHAMEAU, P., FALCHIER, A., QUILODRAN, R., HUISSOUD, C., LAMY, C., MISERY, P., GIROUD, P., ULLMAN, S., BARONE, P., DEHAY, C., KNOBLAUCH,

K. & KENNEDY, H. 2014. Anatomy of hierarchy: feedforward and feedback pathways in macaque visual cortex. *J Comp Neurol,* 522**,** 225-59.
MARTINEZ-CURIEL, R., JANSSON, L., TSUPYKOV, O., AVALIANI, N., ARETIO-MEDINA, C., HIDALGO, I., MONNI, E., BENGZON, J., SKIBO, G., LINDVALL, O., KOKAIA, Z. & PALMA-TORTOSA, S. 2023. Oligodendrocytes in human induced pluripotent stem cell-derived cortical grafts remyelinate adult rat and human cortical neurons. *Stem Cell Reports,* 18**,** 1643-1656.
MARZOLA, P., MELZER, T., PAVESI, E., GIL-MOHAPEL, J. & BROCARDO, P. S. 2023. Exploring the Role of Neuroplasticity in Development, Aging, and Neurodegeneration. *Brain Sci,* 13.
MATSUSHITA, Y., SHIMA, K., NAWASHIRO, H. & WADA, K. 2000. Real-time monitoring of glutamate following fluid percussion brain injury with hypoxia in the rat. *J Neurotrauma,* 17**,** 143-53.
MAY, H. G., TSIKONOFILOS, K., DONAT, C. K., SASTRE, M., KOZLOV, A. S., SHARP, D. J. & BRUYNS-HAYLETT, M. 2023. Mild blast TBI raises gamma connectivity, EEG power, and reduces GABA interneuron density. *bioRxiv***,** 2023.12. 01.569541.
MCGINN, M. J. & POVLISHOCK, J. T. 2016. Pathophysiology of traumatic brain injury. *Neurosurgery Clinics,* 27**,** 397-407.
MCINTOSH, T., VINK, R., NOBLE, L., YAMAKAMI, I., FERNYAK, S., SOARES, H. & FADEN, A. 1989. Traumatic brain injury in the rat: characterization of a lateral fluid-percussion model. *Neuroscience,* 28**,** 233-244.
MCINTOSH, T. K., NOBLE, L., ANDREWS, B. & FADEN, A. I. 1987. Traumatic brain injury in the rat: characterization of a midline fluid-percussion model. *Cent Nerv Syst Trauma,* 4**,** 119-34.
MCKERRACHER, L., CHAMOUX, M. & ARREGUI, C. O. 1996. Role of laminin and integrin interactions in growth cone guidance. *Mol Neurobiol,* 12**,** 95-116.
MEDITHE, J. W. C. & NELAKUDITI, U. R. Study of normal and abnormal EEG. 2016 3rd International conference on advanced computing and communication systems (ICACCS), 2016. IEEE, 1-4.
MEI, Q.-J., WEN, J.-Q., XU, X.-X. & XIE, H.-Q. 2025. Generation of vascularized brain organoids: Technology, applications, and prospects. *Organoid Research,* 1**,** 8162.
MICHELSEN, K. A., ACOSTA-VERDUGO, S., BENOIT-MARAND, M., ESPUNY-CAMACHO, I., GASPARD, N., SAHA, B., GAILLARD, A. & VANDERHAEGHEN, P. 2015. Area-specific reestablishment of damaged circuits in the adult cerebral cortex by cortical neurons derived from mouse embryonic stem cells. *Neuron,* 85**,** 982-97.
MICHELUCCI, A., HEURTAUX, T., GRANDBARBE, L., MORGA, E. & HEUSCHLING, P. 2009. Characterization of the microglial phenotype under specific pro-inflammatory and anti-inflammatory conditions: Effects of oligomeric and fibrillar amyloid-beta. *J Neuroimmunol,* 210**,** 3-12.
MIURA, Y., LI, M. Y., BIREY, F., IKEDA, K., REVAH, O., THETE, M. V., PARK, J. Y., PUNO, A., LEE, S. H., PORTEUS, M. H. & PASCA, S. P. 2020. Generation of human striatal organoids and cortico-striatal assembloids from human pluripotent stem cells. *Nat Biotechnol,* 38**,** 1421-1430.
MIYOSHI, G. & FISHELL, G. 2011. GABAergic interneuron lineages selectively sort into specific cortical layers during early postnatal development. *Cerebral Cortex,* 21**,** 845-852.

MOLNÁR, Z., CLOWRY, G. J., ŠESTAN, N., ALZU'BI, A., BAKKEN, T., HEVNER, R. F., HÜPPI, P. S., KOSTOVIĆ, I., RAKIC, P. & ANTON, E. 2019. New insights into the development of the human cerebral cortex. *Journal of anatomy,* 235**,** 432-451.

MOLNÁR, Z., LUHMANN, H. J. & KANOLD, P. O. 2020. Transient cortical circuits match spontaneous and sensory-driven activity during development. *Science,* 370**,** eabb2153.

MOLNÁR, Z. & ROCKLAND, K. S. 2020. Cortical columns. *Neural circuit and cognitive development.* Elsevier.

MOLYNEAUX, B. J., ARLOTTA, P., MENEZES, J. R. & MACKLIS, J. D. 2007. Neuronal subtype specification in the cerebral cortex. *Nature reviews neuroscience,* 8**,** 427-437.

MOSHAYEDI, P., NG, G., KWOK, J. C., YEO, G. S., BRYANT, C. E., FAWCETT, J. W., FRANZE, K. & GUCK, J. 2014. The relationship between glial cell mechanosensitivity and foreign body reactions in the central nervous system. *Biomaterials,* 35**,** 3919-3925.

MOUMDJIAN, R. A., ANTEL, J. P. & YONG, V. W. 1991. Origin of contralateral reactive gliosis in surgically injured rat cerebral cortex. *Brain Res,* 547**,** 223-8.

MOUNTFORD, J. 2008. Human embryonic stem cells: origins, characteristics and potential for regenerative therapy. *Transfusion Medicine,* 18**,** 1-12.

MOUNTNEY, A., BLAZE, J., WANG, Z., UMALI, M., FLERLAGE, W. J., DOUGHERTY, J., GE, Y., SHEAR, D. & HAGHIGHI, F. 2021. Penetrating Ballistic Brain Injury Produces Acute Alterations in Sleep and Circadian-Related Genes in the Rodent Cortex: A Preliminary Study. *Front Neurol,* 12**,** 745330.

MRZLJAK, L., UYLINGS, H. B., KOSTOVIC, I. & VAN EDEN, C. G. 1988. Prenatal development of neurons in the human prefrontal cortex: I. A qualitative Golgi study. *Journal of comparative neurology,* 271**,** 355-386.

MUGURUMA, K., NISHIYAMA, A., KAWAKAMI, H., HASHIMOTO, K. & SASAI, Y. 2015. Self-organization of polarized cerebellar tissue in 3D culture of human pluripotent stem cells. *Cell Rep,* 10**,** 537-50.

MULDOON, S. F., BRIDGEFORD, E. W. & BASSETT, D. S. 2016. Small-World Propensity and Weighted Brain Networks. *Sci Rep,* 6**,** 22057.

MULLER, J., BALLINI, M., LIVI, P., CHEN, Y., RADIVOJEVIC, M., SHADMANI, A., VISWAM, V., JONES, I. L., FISCELLA, M., DIGGELMANN, R., STETTLER, A., FREY, U., BAKKUM, D. J. & HIERLEMANN, A. 2015. High-resolution CMOS MEA platform to study neurons at subcellular, cellular, and network levels. *Lab Chip,* 15**,** 2767-80.

MURATORE, C. R., SRIKANTH, P., CALLAHAN, D. G. & YOUNG-PEARSE, T. L. 2014. Comparison and optimization of hiPSC forebrain cortical differentiation protocols. *PLoS One,* 9**,** e105807.

MUZIO, L., DI BENEDETTO, B., STOYKOVA, A., BONCINELLI, E., GRUSS, P. & MALLAMACI, A. 2002. Conversion of cerebral cortex into basal ganglia in Emx2−/− Pax6Sey/Sey double-mutant mice. *Nature neuroscience,* 5**,** 737-745.

NARAYANAN, N. S. & LAUBACH, M. 2009. Methods for studying functional interactions among neuronal populations. *Methods Mol Biol,* 489**,** 135-65.

NCT06344026 2024. Phase 1/2a study of ANPD001 in Parkinson disease (ASPIRO).

NELSON, C. J. & BONNER, S. 2021. Neuronal Graphs: A Graph Theory Primer for Microscopic, Functional Networks of Neurons Recorded by Calcium Imaging. *Front Neural Circuits,* 15**,** 662882.

NESPOLI, E., HAKANI, M., HEIN, T. M., MAY, S. N., DANZER, K., WIRTH, T., BAUMANN, B. & DIMOU, L. 2024. Glial cells react to closed head injury in a distinct and spatiotemporally orchestrated manner. *Sci Rep,* 14**,** 2441.

NEWMAN, M. E. 2006. Modularity and community structure in networks. *Proc Natl Acad Sci U S A,* 103**,** 8577-82.

NGUYEN, Q. T., THANH, L. N., HOANG, V. T., PHAN, T. T. K., HEKE, M. & HOANG, D. M. 2023. Bone Marrow-Derived Mononuclear Cells in the Treatment of Neurological Diseases: Knowns and Unknowns. *Cell Mol Neurobiol,* 43**,** 3211-3250.

NI, Z., GUNRAJ, C., NELSON, A. J., YEH, I.-J., CASTILLO, G., HOQUE, T. & CHEN, R. 2009. Two phases of interhemispheric inhibition between motor related cortical areas and the primary motor cortex in human. *Cerebral Cortex,* 19**,** 1654-1665.

NICHOLSON, C. & SYKOVA, E. 1998. Extracellular space structure revealed by diffusion analysis. *Trends Neurosci,* 21**,** 207-15.

NIE, L., HE, J., WANG, J., WANG, R., HUANG, L., JIA, L., KIM, Y. T., BHAWAL, U. K., FAN, X. & ZILLE, M. 2024. Environmental enrichment for stroke and traumatic brain injury: mechanisms and translational implications. *Comprehensive Physiology,* 14**,** 5291-5323.

NIETO, M., MONUKI, E. S., TANG, H., IMITOLA, J., HAUBST, N., KHOURY, S. J., CUNNINGHAM, J., GOTZ, M. & WALSH, C. A. 2004. Expression of Cux-1 and Cux-2 in the subventricular zone and upper layers II–IV of the cerebral cortex. *Journal of Comparative Neurology,* 479**,** 168-180.

NIR, Y., STABA, R. J., ANDRILLON, T., VYAZOVSKIY, V. V., CIRELLI, C., FRIED, I. & TONONI, G. 2011. Regional slow waves and spindles in human sleep. *Neuron,* 70**,** 153-69.

NOCTOR, S. C., MARTÍNEZ-CERDEÑO, V., IVIC, L. & KRIEGSTEIN, A. R. 2004. Cortical neurons arise in symmetric and asymmetric division zones and migrate through specific phases. *Nature neuroscience,* 7**,** 136-144.

NORDEN, D. M. & GODBOUT, J. 2013. Microglia of the aged brain: primed to be activated and resistant to regulation. *Neuropathology and applied neurobiology,* 39**,** 19-34.

NOVIKOVA, L. N., MOSAHEBI, A., WIBERG, M., TERENGHI, G., KELLERTH, J. O. & NOVIKOV, L. N. 2006. Alginate hydrogel and matrigel as potential cell carriers for neurotransplantation. *Journal of Biomedical Materials Research Part A: An Official Journal of The Society for Biomaterials, The Japanese Society for Biomaterials, and The Australian Society for Biomaterials and the Korean Society for Biomaterials,* 77**,** 242-252.

NWOKOYE, P. N. & ABILEZ, O. J. 2024. Bioengineering methods for vascularizing organoids. *Cell Rep Methods,* 4**,** 100779.

O'LEARY, D. D., CHOU, S. J. & SAHARA, S. 2007. Area patterning of the mammalian cortex. *Neuron,* 56**,** 252-69.

OLANOW, C. W., GOETZ, C. G., KORDOWER, J. H., STOESSL, A. J., SOSSI, V., BRIN, M. F., SHANNON, K. M., NAUERT, G. M., PERL, D. P., GODBOLD, J. & FREEMAN, T. B. 2003. A double-blind controlled trial of bilateral fetal nigral transplantation in Parkinson's disease. *Ann Neurol,* 54**,** 403-14.

ONNELA, J. P., SARAMAKI, J., KERTESZ, J. & KASKI, K. 2005. Intensity and coherence of motifs in weighted complex networks. *Phys Rev E Stat Nonlin Soft Matter Phys,* 71**,** 065103.

OPITZ, T., DE LIMA, A. D. & VOIGT, T. 2002. Spontaneous development of synchronous oscillatory activity during maturation of cortical networks in vitro. *Journal of neurophysiology,* 88**,** 2196-2206.

ORMEL, P. R., VIEIRA DE SÁ, R., VAN BODEGRAVEN, E. J., KARST, H., HARSCHNITZ, O., SNEEBOER, M. A. M., JOHANSEN, L. E., VAN DIJK, R. E., SCHEEFHALS, N., BERDENIS VAN BERLEKOM, A., RIBES MARTÍNEZ, E., KLING, S., MACGILLAVRY, H. D., VAN DEN BERG, L. H., KAHN, R. S., HOL, E. M., DE WITTE, L. D. & PASTERKAMP, R. J. 2018. Microglia innately develop within cerebral organoids. *Nat Commun,* 9**,** 4167.

ORTINAU, S., SCHMICH, J., BLOCK, S., LIEDMANN, A., JONAS, L., WEISS, D. G., HELM, C. A., ROLFS, A. & FRECH, M. J. 2010. Effect of 3D-scaffold formation on differentiation and survival in human neural progenitor cells. *Biomed Eng Online,* 9**,** 70.

OTTOBONI, L., MERLINI, A. & MARTINO, G. 2017. Neural Stem Cell Plasticity: Advantages in Therapy for the Injured Central Nervous System. *Front Cell Dev Biol,* 5**,** 52.

PAAVILAINEN, T., PELKONEN, A., MAKINEN, M. E., PELTOLA, M., HUHTALA, H., FAYUK, D. & NARKILAHTI, S. 2018. Effect of prolonged differentiation on functional maturation of human pluripotent stem cell-derived neuronal cultures. *Stem Cell Res,* 27**,** 151-161.

PALMA-TORTOSA, S., TORNERO, D., GRØNNING HANSEN, M., MONNI, E., HAJY, M., KARTSIVADZE, S., AKTAY, S., TSUPYKOV, O., PARMAR, M. & DEISSEROTH, K. 2020. Activity in grafted human iPS cell–derived cortical neurons integrated in stroke-injured rat brain regulates motor behavior. *Proceedings of the National Academy of Sciences,* 117**,** 9094-9100.

PAOLICELLI, R. C., SIERRA, A., STEVENS, B., TREMBLAY, M. E., AGUZZI, A., AJAMI, B., AMIT, I., AUDINAT, E., BECHMANN, I., BENNETT, M., BENNETT, F., BESSIS, A., BIBER, K., BILBO, S., BLURTON-JONES, M., BODDEKE, E., BRITES, D., BRONE, B., BROWN, G. C., BUTOVSKY, O., CARSON, M. J., CASTELLANO, B., COLONNA, M., COWLEY, S. A., CUNNINGHAM, C., DAVALOS, D., DE JAGER, P. L., DE STROOPER, B., DENES, A., EGGEN, B. J. L., EYO, U., GALEA, E., GAREL, S., GINHOUX, F., GLASS, C. K., GOKCE, O., GOMEZ-NICOLA, D., GONZALEZ, B., GORDON, S., GRAEBER, M. B., GREENHALGH, A. D., GRESSENS, P., GRETER, M., GUTMANN, D. H., HAASS, C., HENEKA, M. T., HEPPNER, F. L., HONG, S., HUME, D. A., JUNG, S., KETTENMANN, H., KIPNIS, J., KOYAMA, R., LEMKE, G., LYNCH, M., MAJEWSKA, A., MALCANGIO, M., MALM, T., MANCUSO, R., MASUDA, T., MATTEOLI, M., MCCOLL, B. W., MIRON, V. E., MOLOFSKY, A. V., MONJE, M., MRACSKO, E., NADJAR, A., NEHER, J. J., NENISKYTE, U., NEUMANN, H., NODA, M., PENG, B., PERI, F., PERRY, V. H., POPOVICH, P. G., PRIDANS, C., PRILLER, J., PRINZ, M., RAGOZZINO, D., RANSOHOFF, R. M., SALTER, M. W., SCHAEFER, A., SCHAFER, D. P., SCHWARTZ, M., SIMONS, M., SMITH, C. J., STREIT, W. J., TAY, T. L., TSAI, L. H., VERKHRATSKY, A., VON BERNHARDI, R., WAKE, H., WITTAMER, V., WOLF, S. A., WU, L. J. & WYSS-CORAY, T. 2022. Microglia states and nomenclature: A field at its crossroads. *Neuron,* 110**,** 3458-3483.

PASCA, A. M., SLOAN, S. A., CLARKE, L. E., TIAN, Y., MAKINSON, C. D., HUBER, N., KIM, C. H., PARK, J. Y., O'ROURKE, N. A., NGUYEN, K. D., SMITH, S. J., HUGUENARD, J. R., GESCHWIND, D. H., BARRES, B. A. & PASCA, S. P. 2015. Functional cortical neurons and astrocytes from human pluripotent stem cells in 3D culture. *Nat Methods,* 12**,** 671-8.

PEARN, M. L., NIESMAN, I. R., EGAWA, J., SAWADA, A., ALMENAR-QUERALT, A., SHAH, S. B., DUCKWORTH, J. L. & HEAD, B. P. 2017. Pathophysiology associated with traumatic

brain injury: current treatments and potential novel therapeutics. *Cellular and molecular neurobiology,* 37**,** 571-585.
PEI, N., HAO, Z., WANG, S., PAN, B., FANG, A., KANG, J., LI, D., HE, J. & WANG, L. 2021. 3D Printing of Layered Gradient Pore Structure of Brain-like Tissue. *Int J Bioprint,* 7**,** 359.
PEINADO, A. 2001. Immature neocortical neurons exist as extensive syncitial networks linked by dendrodendritic electrical connections. *J Neurophysiol,* 85**,** 620-9.
PELLEGRINI, L., BONFIO, C., CHADWICK, J., BEGUM, F., SKEHEL, M. & LANCASTER, M. A. 2020. Human CNS barrier-forming organoids with cerebrospinal fluid production. *Science,* 369.
PERUZZARO, S. T., ANDREWS, M. M. M., AL-GHARAIBEH, A., PUPIEC, O., RESK, M., STORY, D., MAITI, P., ROSSIGNOL, J. & DUNBAR, G. L. 2019. Transplantation of mesenchymal stem cells genetically engineered to overexpress interleukin-10 promotes alternative inflammatory response in rat model of traumatic brain injury. *J Neuroinflammation,* 16**,** 2.
PERUZZOTTI-JAMETTI, L., BERNSTOCK, J. D., VICARIO, N., COSTA, A. S. H., KWOK, C. K., LEONARDI, T., BOOTY, L. M., BICCI, I., BALZAROTTI, B., VOLPE, G., MALLUCCI, G., MANFERRARI, G., DONEGA, M., IRACI, N., BRAGA, A., HALLENBECK, J. M., MURPHY, M. P., EDENHOFER, F., FREZZA, C. & PLUCHINO, S. 2018. Macrophage-Derived Extracellular Succinate Licenses Neural Stem Cells to Suppress Chronic Neuroinflammation. *Cell Stem Cell,* 22**,** 355-368 e13.
PETANJEK, Z., DUJMOVIC, A., KOSTOVIC, I. & ESCLAPEZ, M. 2008. Distinct origin of GABA-ergic neurons in forebrain of man, nonhuman primates and lower mammals. *Coll Antropol,* 32 Suppl 1**,** 9-17.
PETERSON, N. C. 2008. From bench to cageside: Risk assessment for rodent pathogen contamination of cells and biologics. *ILAR J,* 49**,** 310-5.
PETTA, D., D'AMORA, U., AMBROSIO, L., GRIJPMA, D., EGLIN, D. & D'ESTE, M. 2020. Hyaluronic acid as a bioink for extrusion-based 3D printing. *Biofabrication,* 12**,** 032001.
PFAFFL, M. W., TICHOPAD, A., PRGOMET, C. & NEUVIANS, T. P. 2004. Determination of stable housekeeping genes, differentially regulated target genes and sample integrity: BestKeeper--Excel-based tool using pair-wise correlations. *Biotechnol Lett,* 26**,** 509-15.
PHAM, M. T., POLLOCK, K. M., ROSE, M. D., CARY, W. A., STEWART, H. R., ZHOU, P., NOLTA, J. A. & WALDAU, B. 2018. Generation of human vascularized brain organoids. *Neuroreport,* 29**,** 588-593.
PHILIPS, M. F., MATTIASSON, G., WIELOCH, T., BJORKLUND, A., JOHANSSON, B. B., TOMASEVIC, G., MARTINEZ-SERRANO, A., LENZLINGER, P. M., SINSON, G., GRADY, M. S. & MCINTOSH, T. K. 2001. Neuroprotective and behavioral efficacy of nerve growth factor-transfected hippocampal progenitor cell transplants after experimental traumatic brain injury. *J Neurosurg,* 94**,** 765-74.
PISCHIUTTA, F., CARUSO, E., LUGO, A., CAVALEIRO, H., STOCCHETTI, N., CITERIO, G., SALGADO, A., GALLUS, S. & ZANIER, E. R. 2021. Systematic review and meta-analysis of preclinical studies testing mesenchymal stromal cells for traumatic brain injury. *NPJ Regen Med,* 6**,** 71.
PISCHIUTTA, F., D'AMICO, G., DANDER, E., BIONDI, A., BIAGI, E., CITERIO, G., DE SIMONI, M. G. & ZANIER, E. R. 2014. Immunosuppression does not affect human bone marrow

mesenchymal stromal cell efficacy after transplantation in traumatized mice brain. *Neuropharmacology,* 79**,** 119-26.
PLUCHINO, S. & MARTINO, G. 2008. Neural stem cell-mediated immunomodulation: repairing the haemorrhagic brain. *Brain,* 131**,** 604-5.
POPESCU, M., HUGHES, J. D., POPESCU, E. A., RIEDY, G. & DEGRABA, T. J. 2016. Reduced prefrontal MEG alpha-band power in mild traumatic brain injury with associated posttraumatic stress disorder symptoms. *Clin Neurophysiol,* 127**,** 3075-3085.
PRE, D., NESTOR, M. W., SPROUL, A. A., JACOB, S., KOPPENSTEINER, P., CHINCHALONGPORN, V., ZIMMER, M., YAMAMOTO, A., NOGGLE, S. A. & ARANCIO, O. 2014. A time course analysis of the electrophysiological properties of neurons differentiated from human induced pluripotent stem cells (iPSCs). *PLoS One,* 9**,** e103418.
PRESTON, M. & SHERMAN, L. S. 2011. Neural stem cell niches: roles for the hyaluronan-based extracellular matrix. *Front Biosci (Schol Ed),* 3**,** 1165-79.
RAKIC, P. 1971. Guidance of neurons migrating to the fetal monkey neocortex. *Brain Res,* 33**,** 471-6.
RAKIC, P. 2009. Evolution of the neocortex: a perspective from developmental biology. *Nature Reviews Neuroscience,* 10**,** 724-735.
REED, J., WALCZAK, W. J., PETZOLD, O. N. & GIMZEWSKI, J. K. 2009. In situ mechanical interferometry of matrigel films. *Langmuir,* 25**,** 36-9.
RENNER, M., LANCASTER, M. A., BIAN, S., CHOI, H., KU, T., PEER, A., CHUNG, K. & KNOBLICH, J. A. 2017. Self-organized developmental patterning and differentiation in cerebral organoids. *The EMBO journal,* 36**,** 1316-1329.
REVAH, O., GORE, F., KELLEY, K. W., ANDERSEN, J., SAKAI, N., CHEN, X., LI, M.-Y., BIREY, F., YANG, X. & SAW, N. L. 2022. Maturation and circuit integration of transplanted human cortical organoids. *Nature,* 610**,** 319-326.
RIESS, P., MOLCANYI, M., BENTZ, K., MAEGELE, M., SIMANSKI, C., CARLITSCHECK, C., SCHNEIDER, A., HESCHELER, J., BOUILLON, B. & SCHÄFER, U. 2007. Embryonic stem cell transplantation after experimental traumatic brain injury dramatically improves neurological outcome, but may cause tumors. *Journal of neurotrauma,* 24**,** 216-225.
RIESS, P., ZHANG, C., SAATMAN, K. E., LAURER, H. L., LONGHI, L. G., RAGHUPATHI, R., LENZLINGER, P. M., LIFSHITZ, J., BOOCKVAR, J. & NEUGEBAUER, E. 2002. Transplanted neural stem cells survive, differentiate, and improve neurological motor function after experimental traumatic brain injury. *Neurosurgery,* 51**,** 1043-1054.
RIVERA, C., VOIPIO, J. & KAILA, K. 2005. Two developmental switches in GABAergic signalling: the K+–Cl− cotransporter KCC2 and carbonic anhydrase CAVII. *The Journal of physiology,* 562**,** 27-36.
ROE, A. W. 2019. Columnar connectome: toward a mathematics of brain function. *Netw Neurosci,* 3**,** 779-791.
ROSENBERG, S. S. & SPITZER, N. C. 2011. Calcium signaling in neuronal development. *Cold Spring Harb Perspect Biol,* 3**,** a004259.
ROSENSTEIN, J. M. & KRUM, J. M. 2004. New roles for VEGF in nervous tissue—beyond blood vessels. *Experimental neurology,* 187**,** 246-253.
RUBINOV, M. & SPORNS, O. 2010. Complex network measures of brain connectivity: uses and interpretations. *Neuroimage,* 52**,** 1059-69.

RUOSLAHTI, E. 1996. Brain extracellular matrix. *Glycobiology,* 6**,** 489-492.
SAATMAN, K. E., CREED, J. & RAGHUPATHI, R. 2010. Calpain as a therapeutic target in traumatic brain injury. *Neurotherapeutics,* 7**,** 31-42.
SABERI, A., ALDENKAMP, A. P., KURNIAWAN, N. A. & BOUTEN, C. V. C. 2022. In-vitro engineered human cerebral tissues mimic pathological circuit disturbances in 3D. *Commun Biol,* 5**,** 254.
SABOORI, M., RIAZI, A., TAJI, M. & YADEGARFAR, G. 2024. Traumatic brain injury and stem cell treatments: A review of recent 10 years clinical trials. *Clin Neurol Neurosurg,* 239**,** 108219.
SAKAGUCHI, H., KADOSHIMA, T., SOEN, M., NARII, N., ISHIDA, Y., OHGUSHI, M., TAKAHASHI, J., EIRAKU, M. & SASAI, Y. 2015. Generation of functional hippocampal neurons from self-organizing human embryonic stem cell-derived dorsomedial telencephalic tissue. *Nat Commun,* 6**,** 8896.
SAKAGUCHI, H., OZAKI, Y., ASHIDA, T., MATSUBARA, T., OISHI, N., KIHARA, S. & TAKAHASHI, J. 2019. Self-Organized Synchronous Calcium Transients in a Cultured Human Neural Network Derived from Cerebral Organoids. *Stem Cell Reports,* 13**,** 458-473.
SALARIS, F., COLOSI, C., BRIGHI, C., SOLOPERTO, A., TURRIS, V., BENEDETTI, M. C., GHIRGA, S., ROSITO, M., DI ANGELANTONIO, S. & ROSA, A. 2019. 3D Bioprinted Human Cortical Neural Constructs Derived from Induced Pluripotent Stem Cells. *J Clin Med,* 8.
SANDOR, C., HONTI, F., HAERTY, W., SZEWCZYK-KROLIKOWSKI, K., TOMLINSON, P., EVETTS, S., MILLIN, S., KEANE, T., MCCARTHY, S. A., DURBIN, R., TALBOT, K., HU, M., WEBBER, C., PONTING, C. P. & WADE-MARTINS, R. 2017. Whole-exome sequencing of 228 patients with sporadic Parkinson's disease. *Sci Rep,* 7**,** 41188.
SANES, J. N. & DONOGHUE, J. P. 2000. Plasticity and primary motor cortex. *Annual review of neuroscience,* 23**,** 393-415.
SANVITALE, C. E., KERR, G., CHAIKUAD, A., RAMEL, M.-C., MOHEDAS, A. H., REICHERT, S., WANG, Y., TRIFFITT, J. T., CUNY, G. D. & YU, P. B. 2013. A new class of small molecule inhibitor of BMP signaling. *PloS one,* 8**,** e62721.
SAUVAGEOT, C. M. & STILES, C. D. 2002. Molecular mechanisms controlling cortical gliogenesis. *Current opinion in neurobiology,* 12**,** 244-249.
SAVAGE, J. T., RAMIREZ, J. J., RISHER, W. C., WANG, Y., IRALA, D. & EROGLU, C. 2024. SynBot is an open-source image analysis software for automated quantification of synapses. *Cell Rep Methods,* 4**,** 100861.
SAWAMOTO, N., DOI, D., NAKANISHI, E., SAWAMURA, M., KIKUCHI, T., YAMAKADO, H., TARUNO, Y., SHIMA, A., FUSHIMI, Y., OKADA, T., KIKUCHI, T., MORIZANE, A., HIRAMATSU, S., ANAZAWA, T., SHINDO, T., UENO, K., MORITA, S., ARAKAWA, Y., NAKAMOTO, Y., MIYAMOTO, S., TAKAHASHI, R. & TAKAHASHI, J. 2025. Phase I/II trial of iPS-cell-derived dopaminergic cells for Parkinson's disease. *Nature,* 641**,** 971-977.
SCHAEREN-WIERNERS, N., ANDRÉ, E., KAPFHAMMER, J. P. & BECKER-ANDRÉ, M. 1997. The ExDression pattern of the orphan nuclear receptor RORβ in the developing and adult rat nervous system suggests a role in the processing of sensory information and in circadian rhythm. *European Journal of Neuroscience,* 9**,** 2687-2701.
SCHANTZ, S. L., COSGRAVE, G. S., SCHIFINO, A. G., LEPAGE, T. H., DUBROF, S. T., SNEED, S. E., CHEEK, S. R., PARK, H. J., KINDER, H. A. & DUBERSTEIN, K. J. 2025a. Combined Human

Neural Stem Cell and Structured Treadmill Walking Therapy Enhances Recovery in a Pediatric Porcine Traumatic Brain Injury Model. *Journal of Neurotrauma*.

SCHANTZ, S. L., DUBERSTEIN, K. J., KAISER, E. E. & WEST, F. D. 2025b. Human Neural Stem Cell Therapy for Traumatic Brain Injury-A Systematic Review of Pre-Clinical Studies. *J Neurotrauma,* 42**,** 668-688.

SCHANTZ, S. L., SNEED, S. E., FAGAN, M. M., GOLAN, M. E., CHEEK, S. R., KINDER, H. A., DUBERSTEIN, K. J., KAISER, E. E. & WEST, F. D. 2024. Human-Induced pluripotent stem cell-derived neural stem cell therapy limits tissue damage and promotes tissue regeneration and functional recovery in a pediatric piglet traumatic-brain-injury model. *Biomedicines,* 12**,** 1663.

SCHLAEGER, T. M., DAHERON, L., BRICKLER, T. R., ENTWISLE, S., CHAN, K., CIANCI, A., DEVINE, A., ETTENGER, A., FITZGERALD, K., GODFREY, M., GUPTA, D., MCPHERSON, J., MALWADKAR, P., GUPTA, M., BELL, B., DOI, A., JUNG, N., LI, X., LYNES, M. S., BROOKES, E., CHERRY, A. B., DEMIRBAS, D., TSANKOV, A. M., ZON, L. I., RUBIN, L. L., FEINBERG, A. P., MEISSNER, A., COWAN, C. A. & DALEY, G. Q. 2015. A comparison of non-integrating reprogramming methods. *Nat Biotechnol,* 33**,** 58-63.

SCHMIDT, J., BROWN, K. E., FELDMAN, S. J., BABUL, S., ZWICKER, J. G. & BOYD, L. A. 2021. Evidence of altered interhemispheric communication after pediatric concussion. *Brain Inj,* 35**,** 1143-1161.

SCHWARTZ, J. P., NISHIYAMA, N., WILSON, D. & TANIWAKI, T. 1994. Receptor-mediated regulation of neuropeptide gene expression in astrocytes. *Glia,* 11**,** 185-190.

SCHWARTZ, P. H., BRICK, D. J., NETHERCOTT, H. E. & STOVER, A. E. 2011. Traditional human embryonic stem cell culture. *Methods Mol Biol,* 767**,** 107-23.

SEDMAK, G., JOVANOV-MILOSEVIC, N., PUSKARJOV, M., ULAMEC, M., KRUSLIN, B., KAILA, K. & JUDAS, M. 2016. Developmental Expression Patterns of KCC2 and Functionally Associated Molecules in the Human Brain. *Cereb Cortex,* 26**,** 4574-4589.

SEIDLITS, S. K., KHAING, Z. Z., PETERSEN, R. R., NICKELS, J. D., VANSCOY, J. E., SHEAR, J. B. & SCHMIDT, C. E. 2010. The effects of hyaluronic acid hydrogels with tunable mechanical properties on neural progenitor cell differentiation. *Biomaterials,* 31**,** 3930-40.

SEMPLE, B. D., BLOMGREN, K., GIMLIN, K., FERRIERO, D. M. & NOBLE-HAEUSSLEIN, L. J. 2013. Brain development in rodents and humans: Identifying benchmarks of maturation and vulnerability to injury across species. *Prog Neurobiol,* 106-107**,** 1-16.

SENSHARMA, P., MADHUMATHI, G., JAYANT, R. D. & JAISWAL, A. K. 2017. Biomaterials and cells for neural tissue engineering: Current choices. *Mater Sci Eng C Mater Biol Appl,* 77**,** 1302-1315.

SHANG, Z., LI, D., CHEN, J., WANG, R., WANG, M., ZHANG, B., WANG, X. & WANYAN, P. 2022. What is the optimal timing of transplantation of neural stem cells in spinal cord injury? A systematic review and network meta-analysis based on animal studies. *Frontiers in Immunology,* 13**,** 855309.

SHEAR, D. A., TATE, M. C., ARCHER, D. R., HOFFMAN, S. W., HULCE, V. D., LAPLACA, M. C. & STEIN, D. G. 2004. Neural progenitor cell transplants promote long-term functional recovery after traumatic brain injury. *Brain research,* 1026**,** 11-22.

SHEN, Q., GODERIE, S. K., JIN, L., KARANTH, N., SUN, Y., ABRAMOVA, N., VINCENT, P., PUMIGLIA, K. & TEMPLE, S. 2004. Endothelial cells stimulate self-renewal and expand neurogenesis of neural stem cells. *Science,* 304**,** 1338-40.

SHEN, Y. P. & KOKAIA, Z. 2025. Brain Organoid Transplantation: A Comprehensive Guide to the Latest Advances and Practical Applications-A Systematic Review. *Cells,* 14.

SHI, Y., KIRWAN, P. & LIVESEY, F. J. 2012a. Directed differentiation of human pluripotent stem cells to cerebral cortex neurons and neural networks. *Nature protocols,* 7**,** 1836-1846.

SHI, Y., KIRWAN, P., SMITH, J., ROBINSON, H. P. & LIVESEY, F. J. 2012b. Human cerebral cortex development from pluripotent stem cells to functional excitatory synapses. *Nature neuroscience,* 15**,** 477-486.

SHI, Y., SUN, L., WANG, M., LIU, J., ZHONG, S., LI, R., LI, P., GUO, L., FANG, A., CHEN, R., GE, W. P., WU, Q. & WANG, X. 2020. Vascularized human cortical organoids (vOrganoids) model cortical development in vivo. *PLoS Biol,* 18**,** e3000705.

SHIN, H. E., LEE, W. J., PARK, K. S., YU, Y., KIM, G., ROH, E. J., SONG, B. G., JUNG, J. H., CHO, K., HA, Y. H., YANG, Y. I. & HAN, I. 2024. Repeated intrathecal injections of peripheral nerve-derived stem cell spheroids improve outcomes in a rat model of traumatic brain injury. *Stem Cell Res Ther,* 15**,** 314.

SHULTZ, L. D., SCHWEITZER, P. A., CHRISTIANSON, S. W., GOTT, B., SCHWEITZER, I. B., TENNENT, B., MCKENNA, S., MOBRAATEN, L., RAJAN, T. V., GREINER, D. L. & ET AL. 1995. Multiple defects in innate and adaptive immunologic function in NOD/LtSz-scid mice. *J Immunol,* 154**,** 180-91.

SILVER, J. & MILLER, J. H. 2004. Regeneration beyond the glial scar. *Nature reviews neuroscience,* 5**,** 146-156.

SKARDELLY, M., GABER, K., BURDACK, S., SCHEIDT, F., HILBIG, H., BOLTZE, J., FÖRSCHLER, A., SCHWARZ, S., SCHWARZ, J. & MEIXENSBERGER, J. 2011. Long-term benefit of human fetal neuronal progenitor cell transplantation in a clinically adapted model after traumatic brain injury. *Journal of neurotrauma,* 28**,** 401-414.

SKARDELLY, M., GABER, K., BURDACK, S., SCHEIDT, F., SCHUHMANN, M. U., HILBIG, H., MEIXENSBERGER, J. & BOLTZE, J. 2014. Transient but not permanent benefit of neuronal progenitor cell therapy after traumatic brain injury: potential causes and translational consequences. *Frontiers in cellular neuroscience,* 8**,** 318.

SKARDELLY, M., GLIEN, A., GROBA, C., SCHLICHTING, N., KAMPRAD, M., MEIXENSBERGER, J. & MILOSEVIC, J. 2013. The influence of immunosuppressive drugs on neural stem/progenitor cell fate in vitro. *Exp Cell Res,* 319**,** 3170-81.

SOFRONIEW, M. V. & VINTERS, H. V. 2010. Astrocytes: biology and pathology. *Acta Neuropathol,* 119**,** 7-35.

SOMAA, F. A., WANG, T. Y., NICLIS, J. C., BRUGGEMAN, K. F., KAUHAUSEN, J. A., GUO, H., MCDOUGALL, S., WILLIAMS, R. J., NISBET, D. R., THOMPSON, L. H. & PARISH, C. L. 2017. Peptide-Based Scaffolds Support Human Cortical Progenitor Graft Integration to Reduce Atrophy and Promote Functional Repair in a Model of Stroke. *Cell Rep,* 20**,** 1964-1977.

SONG, C. G., ZHANG, Y. Z., WU, H. N., CAO, X. L., GUO, C. J., LI, Y. Q., ZHENG, M. H. & HAN, H. 2018. Stem cells: a promising candidate to treat neurological disorders. *Neural Regen Res,* 13**,** 1294-1304.

SOOD, D., CAIRNS, D. M., DABBI, J. M., RAMAKRISHNAN, C., DEISSEROTH, K., BLACK, L. D., 3RD, SANTANIELLO, S. & KAPLAN, D. L. 2019. Functional maturation of human neural stem cells in a 3D bioengineered brain model enriched with fetal brain-derived matrix. *Sci Rep,* 9**,** 17874.

SOOD, D., CHWALEK, K., STUNTZ, E., POULI, D., DU, C., TANG-SCHOMER, M., GEORGAKOUDI, I., BLACK III, L. D. & KAPLAN, D. L. 2016. Fetal brain extracellular matrix boosts neuronal network formation in 3D bioengineered model of cortical brain tissue. *ACS biomaterials science & engineering,* 2**,** 131-140.

SPORNS, O. 2013. Structure and function of complex brain networks. *Dialogues Clin Neurosci,* 15**,** 247-62.

SPRUSTON, N. 2008. Pyramidal neurons: dendritic structure and synaptic integration. *Nat Rev Neurosci,* 9**,** 206-21.

SPURLOCK, M. S., AHMED, A. I., RIVERA, K. N., YOKOBORI, S., LEE, S. W., SAM, P. N., SHEAR, D. A., HEFFERAN, M. P., HAZEL, T. G., JOHE, K. K., GAJAVELLI, S., TORTELLA, F. C. & BULLOCK, R. M. 2017. Amelioration of Penetrating Ballistic-Like Brain Injury Induced Cognitive Deficits after Neuronal Differentiation of Transplanted Human Neural Stem Cells. *J Neurotrauma,* 34**,** 1981-1995.

SRINIVASAN, K., LEONE, D. P., BATESON, R. K., DOBREVA, G., KOHWI, Y., KOHWI-SHIGEMATSU, T., GROSSCHEDL, R. & MCCONNELL, S. K. 2012. A network of genetic repression and derepression specifies projection fates in the developing neocortex. *Proc Natl Acad Sci U S A,* 109**,** 19071-8.

SULLIVAN, S., FAIRCHILD, P. J., MARSH, S. G. E., MULLER, C. R., TURNER, M. L., SONG, J. & TURNER, D. 2020. Haplobanking induced pluripotent stem cells for clinical use. *Stem Cell Res,* 49**,** 102035.

SUN, D., GUGLIOTTA, M., ROLFE, A., REID, W., MCQUISTON, A. R., HU, W. & YOUNG, H. 2011. Sustained survival and maturation of adult neural stem/progenitor cells after transplantation into the injured brain. *Journal of Neurotrauma,* 28**,** 961-972.

SUN, X.-Y., JU, X.-C., LI, Y., ZENG, P.-M., WU, J., ZHOU, Y.-Y., SHEN, L.-B., DONG, J., CHEN, Y.-J. & LUO, Z.-G. 2022. Generation of vascularized brain organoids to study neurovascular interactions. *elife,* 11**,** e76707.

SUTTKUS, A., ROHN, S., WEIGEL, S., GLÖCKNER, P., ARENDT, T. & MORAWSKI, M. 2014. Aggrecan, link protein and tenascin-R are essential components of the perineuronal net to protect neurons against iron-induced oxidative stress. *Cell Death and Disease,* 5.

TABAR, V., SARVA, H., LOZANO, A. M., FASANO, A., KALIA, S. K., YU, K. K. H., BRENNAN, C., MA, Y., PENG, S., EIDELBERG, D., TOMISHIMA, M., IRION, S., STEMPLE, W., ABID, N., LAMPRON, A., STUDER, L. & HENCHCLIFFE, C. 2025. Phase I trial of hES cell-derived dopaminergic neurons for Parkinson's disease. *Nature,* 641**,** 978-983.

TAJIRI, N., DUNCAN, K., ANTOINE, A., PABON, M., ACOSTA, S. A., DE LA PENA, I., HERNADEZ-ONTIVEROS, D. G., SHINOZUKA, K., ISHIKAWA, H. & KANEKO, Y. 2014. Stem cell-paved biobridge facilitates neural repair in traumatic brain injury. *Frontiers in systems neuroscience,* 8**,** 116.

TAJIRI, N., KANEKO, Y., SHINOZUKA, K., ISHIKAWA, H., YANKEE, E., MCGROGAN, M., CASE, C. & BORLONGAN, C. V. 2013. Stem cell recruitment of newly formed host cells via a successful seduction? Filling the gap between neurogenic niche and injured brain site. *PLoS One,* 8**,** e74857.

TAKAHASHI, A., CAMACHO, P., LECHLEITER, J. D. & HERMAN, B. 1999. Measurement of intracellular calcium. *Physiol Rev,* 79**,** 1089-125.

TAKAHASHI, K., TANABE, K., OHNUKI, M., NARITA, M., ICHISAKA, T., TOMODA, K. & YAMANAKA, S. 2007. Induction of pluripotent stem cells from adult human fibroblasts by defined factors. *cell,* 131**,** 861-872.

TAKAHASHI, K. & YAMANAKA, S. 2006. Induction of pluripotent stem cells from mouse embryonic and adult fibroblast cultures by defined factors. *cell,* 126**,** 663-676.

TAKAKI, J., FUJIMORI, K., MIURA, M., SUZUKI, T., SEKINO, Y. & SATO, K. 2012. L-glutamate released from activated microglia downregulates astrocytic L-glutamate transporter expression in neuroinflammation: the 'collusion' hypothesis for increased extracellular L-glutamate concentration in neuroinflammation. *J Neuroinflammation,* 9**,** 275.

TAN, X. & SHI, S. H. 2013. Neocortical neurogenesis and neuronal migration. *Wiley Interdiscip Rev Dev Biol,* 2**,** 443-59.

TANAKA, S., KAMACHI, Y., TANOUCHI, A., HAMADA, H., JING, N. & KONDOH, H. 2004. Interplay of SOX and POU factors in regulation of the Nestin gene in neural primordial cells. *Molecular and cellular biology,* 24**,** 8834-8846.

TANG, H., SHA, H., SUN, H., WU, X., XIE, L., WANG, P., XU, C., LARSEN, C., ZHANG, H. L. & GONG, Y. 2013. Tracking induced pluripotent stem cells–derived neural stem cells in the central nervous system of rats and monkeys. *Cellular Reprogramming (Formerly" Cloning and Stem Cells"),* 15**,** 435-442.

TANG-SCHOMER, M. D., WHITE, J. D., TIEN, L. W., SCHMITT, L. I., VALENTIN, T. M., GRAZIANO, D. J., HOPKINS, A. M., OMENETTO, F. G., HAYDON, P. G. & KAPLAN, D. L. 2014. Bioengineered functional brain-like cortical tissue. *Proc Natl Acad Sci U S A,* 111**,** 13811-6.

TAPIAS, V., MOSCHONAS, E. H., BONDI, C. O., VOZZELLA, V. J., COOPER, I. N., CHENG, J. P., LAJUD, N. & KLINE, A. E. 2022. Environmental enrichment improves traumatic brain injury-induced behavioral phenotype and associated neurodegenerative process. *Exp Neurol,* 357**,** 114204.

TATE, M. C., SHEAR, D. A., HOFFMAN, S. W., STEIN, D. G., ARCHER, D. R. & LAPLACA, M. C. 2002. Fibronectin promotes survival and migration of primary neural stem cells transplanted into the traumatically injured mouse brain. *Cell transplantation,* 11**,** 283-295.

TERRIGNO, M., BUSTI, I., ALIA, C., PIETRASANTA, M., ARISI, I., D'ONOFRIO, M., CALEO, M. & CREMISI, F. 2018. Neurons generated by mouse ESCs with hippocampal or cortical identity display distinct projection patterns when co-transplanted in the adult brain. *Stem cell reports,* 10**,** 1016-1029.

TIAN, C., WANG, X., WANG, X., WANG, L., WANG, X., WU, S. & WAN, Z. 2013. Autologous bone marrow mesenchymal stem cell therapy in the subacute stage of traumatic brain injury by lumbar puncture. *Exp Clin Transplant,* 11**,** 176-181.

TING, J. T., LEE, B. R., CHONG, P., SOLER-LLAVINA, G., COBBS, C., KOCH, C., ZENG, H. & LEIN, E. 2018. Preparation of Acute Brain Slices Using an Optimized N-Methyl-D-glucamine Protective Recovery Method. *J Vis Exp*.

TJIA, M., YU, X., JAMMU, L. S., LU, J. & ZUO, Y. 2017. Pyramidal Neurons in Different Cortical Layers Exhibit Distinct Dynamics and Plasticity of Apical Dendritic Spines. *Front Neural Circuits,* 11**,** 43.

TONNESEN, J., HRABETOVA, S. & SORIA, F. N. 2023. Local diffusion in the extracellular space of the brain. *Neurobiol Dis,* 177**,** 105981.

TSAI, M. H., WU, C. Y., WU, C. H. & CHEN, C. Y. 2024. The Current Update of Conventional and Innovative Treatment Strategies for Central Nervous System Injury. *Biomedicines,* 12.

TURNER, M., LESLIE, S., MARTIN, N. G., PESCHANSKI, M., RAO, M., TAYLOR, C. J., TROUNSON, A., TURNER, D., YAMANAKA, S. & WILMUT, I. 2013. Toward the development of a global induced pluripotent stem cell library. *Cell Stem Cell,* 13**,** 382-4.

UEMURA, M., REFAAT, M. M., SHINOYAMA, M., HAYASHI, H., HASHIMOTO, N. & TAKAHASHI, J. 2010. Matrigel supports survival and neuronal differentiation of grafted embryonic stem cell-derived neural precursor cells. *J Neurosci Res,* 88**,** 542-51.

ULAM, F., SHELTON, C., RICHARDS, L., DAVIS, L., HUNTER, B., FREGNI, F. & HIGGINS, K. 2015. Cumulative effects of transcranial direct current stimulation on EEG oscillations and attention/working memory during subacute neurorehabilitation of traumatic brain injury. *Clinical Neurophysiology,* 126**,** 486-496.

ULLOA SEVERINO, F. P., BAN, J., SONG, Q., TANG, M., BIANCONI, G., CHENG, G. & TORRE, V. 2016. The role of dimensionality in neuronal network dynamics. *Sci Rep,* 6**,** 29640.

USREY, W. M. & SHERMAN, S. M. 2019. Corticofugal circuits: Communication lines from the cortex to the rest of the brain. *J Comp Neurol,* 527**,** 640-650.

VAKORIN, V. A., DOESBURG, S. M., DA COSTA, L., JETLY, R., PANG, E. W. & TAYLOR, M. J. 2016. Detecting Mild Traumatic Brain Injury Using Resting State Magnetoencephalographic Connectivity. *PLoS Comput Biol,* 12**,** e1004914.

VANACORE, G., CHRISTENSEN, J. B. & BAYIN, N. S. 2024. Age-dependent regenerative mechanisms in the brain. *Biochem Soc Trans,* 52**,** 2243-2252.

VAUGHAN-JACKSON, A., STODOLAK, S., EBRAHIMI, K. H., JOHNSON, E., REARDON, P. K., DUPONT, M., ZHANG, S., MCCULLAGH, J. S. O. & JAMES, W. S. 2022. Density dependent regulation of inflammatory responses in macrophages. *Front Immunol,* 13**,** 895488.

VECCHIO, F., MIRAGLIA, F. & MARIA ROSSINI, P. 2017. Connectome: Graph theory application in functional brain network architecture. *Clin Neurophysiol Pract,* 2**,** 206-213.

VENTURA-ANTUNES, L., MOTA, B. & HERCULANO-HOUZEL, S. 2013. Different scaling of white matter volume, cortical connectivity, and gyrification across rodent and primate brains. *Front Neuroanat,* 7**,** 3.

VIRTANEN, M. A., UVAROV, P., MAVROVIC, M., PONCER, J. C. & KAILA, K. 2021. The Multifaceted Roles of KCC2 in Cortical Development. *Trends in Neurosciences,* 44**,** 378-392.

VITALIS, T., DAUPHINOT, L., GRESSENS, P., POTIER, M. C., MARIANI, J. & GASPAR, P. 2018. RORalpha Coordinates Thalamic and Cortical Maturation to Instruct Barrel Cortex Development. *Cereb Cortex,* 28**,** 3994-4007.

VOIGT, T., OPITZ, T. & DE LIMA, A. D. 2001. Synchronous oscillatory activity in immature cortical network is driven by GABAergic preplate neurons. *Journal of Neuroscience,* 21**,** 8895-8905.

VUE, T. Y., LEE, M., TAN, Y. E., WERKHOVEN, Z., WANG, L. & NAKAGAWA, Y. 2013. Thalamic control of neocortical area formation in mice. *J Neurosci,* 33**,** 8442-53.

VUKICEVIC, S., KLEINMAN, H. K., LUYTEN, F. P., ROBERTS, A. B., ROCHE, N. S. & REDDI, A. H. 1992. Identification of multiple active growth factors in basement membrane

Matrigel suggests caution in interpretation of cellular activity related to extracellular matrix components. *Exp Cell Res,* 202**,** 1-8.
WALLENQUIST, U., BRANNVALL, K., CLAUSEN, F., LEWEN, A., HILLERED, L. & FORSBERG-NILSSON, K. 2009. Grafted neural progenitors migrate and form neurons after experimental traumatic brain injury. *Restor Neurol Neurosci,* 27**,** 323-34.
WANG, D. & FAWCETT, J. 2012. The perineuronal net and the control of cns plasticity. *Cell and Tissue Research,* 349**,** 147-160.
WANG, H., YU, H., ZHOU, X., ZHANG, J., ZHOU, H., HAO, H., DING, L., LI, H., GU, Y., MA, J., QIU, J. & MA, D. 2022a. An Overview of Extracellular Matrix-Based Bioinks for 3D Bioprinting. *Front Bioeng Biotechnol,* 10**,** 905438.
WANG, J., CHAO, F., HAN, F., ZHANG, G., XI, Q., LI, J., JIANG, H., WANG, J., YU, G., TIAN, M. & ZHANG, H. 2013a. PET demonstrates functional recovery after transplantation of induced pluripotent stem cells in a rat model of cerebral ischemic injury. *J Nucl Med,* 54**,** 785-92.
WANG, J., CHU, R., NI, N. & NAN, G. 2020a. The effect of Matrigel as scaffold material for neural stem cell transplantation for treating spinal cord injury. *Sci Rep,* 10**,** 2576.
WANG, J., YIN, L. & CHEN, Z. 2013b. Neuroprotective role of fibronectin in neuron-glial extrasynaptic transmission. *Neural Regen Res,* 8**,** 376-82.
WANG, L., BAI, L., WANG, S., ZHOU, J., LIU, Y., ZHANG, C., YAO, S., HE, J., LIU, C. & LI, D. 2024. Biomimetic design and integrated biofabrication of an in-vitro three-dimensional multi-scale multilayer cortical model. *Materials Today Bio,* 28**,** 101176.
WANG, R., YANG, D.-X., LIU, Y.-L., DING, J., GUO, Y., DING, W.-H., TIAN, H.-L. & YUAN, F. 2022b. Cell cycle exit and neuronal differentiation 1-engineered embryonic neural stem cells enhance neuronal differentiation and neurobehavioral recovery after experimental traumatic brain injury. *Neural Regeneration Research,* 17**,** 130-136.
WANG, S., CHENG, H., DAI, G., WANG, X., HUA, R., LIU, X., WANG, P., CHEN, G., YUE, W. & AN, Y. 2013c. Umbilical cord mesenchymal stem cell transplantation significantly improves neurological function in patients with sequelae of traumatic brain injury. *Brain research,* 1532**,** 76-84.
WANG, X., AO, Q., TIAN, X., FAN, J., TONG, H., HOU, W. & BAI, S. 2017a. Gelatin-Based Hydrogels for Organ 3D Bioprinting. *Polymers (Basel),* 9.
WANG, Z., LUO, Y., CHEN, L. & LIANG, W. 2017b. Safety of neural stem cell transplantation in patients with severe traumatic brain injury. *Experimental and therapeutic medicine,* 13**,** 3613-3618.
WANG, Z., WANG, S. N., XU, T. Y., HONG, C., CHENG, M. H., ZHU, P. X., LIN, J. S., SU, D. F. & MIAO, C. Y. 2020b. Cerebral organoids transplantation improves neurological motor function in rat brain injury. *CNS Neurosci Ther,* 26**,** 682-697.
WARM, D., SCHROER, J. & SINNING, A. 2021. Gabaergic Interneurons in Early Brain Development: Conducting and Orchestrated by Cortical Network Activity. *Front Mol Neurosci,* 14**,** 807969.
WATANABE, K., NAKAMURA, M., OKANO, H. & TOYAMA, Y. 2007a. Establishment of three-dimensional culture of neural stem/progenitor cells in collagen Type-1 Gel. *Restor Neurol Neurosci,* 25**,** 109-17.
WATANABE, K., UENO, M., KAMIYA, D., NISHIYAMA, A., MATSUMURA, M., WATAYA, T., TAKAHASHI, J. B., NISHIKAWA, S., NISHIKAWA, S.-I. & MUGURUMA, K. 2007b. A ROCK

inhibitor permits survival of dissociated human embryonic stem cells. *Nature biotechnology,* 25**,** 681-686.
WATAYA, T., ANDO, S., MUGURUMA, K., IKEDA, H., WATANABE, K., EIRAKU, M., KAWADA, M., TAKAHASHI, J., HASHIMOTO, N. & SASAI, Y. 2008. Minimization of exogenous signals in ES cell culture induces rostral hypothalamic differentiation. *Proc Natl Acad Sci U S A,* 105**,** 11796-801.
WEI, Z. Z., LEE, J. H., ZHANG, Y., ZHU, Y. B., DEVEAU, T. C., GU, X., WINTER, M. M., LI, J., WEI, L. & YU, S. P. 2016. Intracranial Transplantation of Hypoxia-Preconditioned iPSC-Derived Neural Progenitor Cells Alleviates Neuropsychiatric Defects After Traumatic Brain Injury in Juvenile Rats. *Cell Transplant,* 25**,** 797-809.
WEILER, N., WOOD, L., YU, J., SOLLA, S. A. & SHEPHERD, G. M. 2008. Top-down laminar organization of the excitatory network in motor cortex. *Nat Neurosci,* 11**,** 360-6.
WENNERSTEN, A., MEIER, X., HOLMIN, S., WAHLBERG, L. & MATHIESEN, T. 2004. Proliferation, migration, and differentiation of human neural stem/progenitor cells after transplantation into a rat model of traumatic brain injury. *J Neurosurg,* 100**,** 88-96.
WENNING, G. K., ODIN, P., MORRISH, P., REHNCRONA, S., WIDNER, H., BRUNDIN, P., ROTHWELL, J. C., BROWN, R., GUSTAVII, B., HAGELL, P., JAHANSHAHI, M., SAWLE, G., BJORKLUND, A., BROOKS, D. J., MARSDEN, C. D., QUINN, N. P. & LINDVALL, O. 1997. Short- and long-term survival and function of unilateral intrastriatal dopaminergic grafts in Parkinson's disease. *Ann Neurol,* 42**,** 95-107.
WILLIAMS, A. J., HARTINGS, J. A., LU, X.-C. M., ROLLI, M. L., DAVE, J. R. & TORTELLA, F. C. 2005. Characterization of a new rat model of penetrating ballistic brain injury. *Journal of neurotrauma,* 22**,** 313-331.
WILSON, M. N., THUNEMANN, M., LIU, X., LU, Y., PUPPO, F., ADAMS, J. W., KIM, J. H., RAMEZANI, M., PIZZO, D. P., DJUROVIC, S., ANDREASSEN, O. A., MANSOUR, A. A., GAGE, F. H., MUOTRI, A. R., DEVOR, A. & KUZUM, D. 2022. Multimodal monitoring of human cortical organoids implanted in mice reveal functional connection with visual cortex. *Nat Commun,* 13**,** 7945.
WLODARCZYK, A. I., SYLANTYEV, S., HERD, M. B., KERSANTÉ, F., LAMBERT, J. J., RUSAKOV, D. A., LINTHORST, A. C., SEMYANOV, A., BELELLI, D. & PAVLOV, I. 2013. GABA-independent GABAA receptor openings maintain tonic currents. *Journal of Neuroscience,* 33**,** 3905-3914.
WOERLY, S., FORT, S., PIGNOT-PAINTRAND, I., COTTET, C., CARCENAC, C. & SAVASTA, M. 2008. Development of a sialic acid-containing hydrogel of poly[N-(2-hydroxypropyl) methacrylamide]: characterization and implantation study. *Biomacromolecules,* 9**,** 2329-37.
WU, H., XU, J., PANG, Z. P., GE, W., KIM, K. J., BLANCHI, B., CHEN, C., SUDHOF, T. C. & SUN, Y. E. 2007. Integrative genomic and functional analyses reveal neuronal subtype differentiation bias in human embryonic stem cell lines. *Proc Natl Acad Sci U S A,* 104**,** 13821-6.
WU, M. W., KOURDOUGLI, N. & PORTERA-CAILLIAU, C. 2024. Network state transitions during cortical development. *Nature Reviews Neuroscience***,** 1-18.
WU, Y. T., BENNETT, H. C., CHON, U., VANSELOW, D. J., ZHANG, Q., MUNOZ-CASTANEDA, R., CHENG, K. C., OSTEN, P., DREW, P. J. & KIM, Y. 2022. Quantitative relationship

between cerebrovascular network and neuronal cell types in mice. *Cell Rep,* 39**,** 110978.
XIANG, Y., TANAKA, Y., CAKIR, B., PATTERSON, B., KIM, K. Y., SUN, P., KANG, Y. J., ZHONG, M., LIU, X., PATRA, P., LEE, S. H., WEISSMAN, S. M. & PARK, I. H. 2019. hESC-Derived Thalamic Organoids Form Reciprocal Projections When Fused with Cortical Organoids. *Cell Stem Cell,* 24**,** 487-497.e7.
XIONG, L. L., HU, Y., ZHANG, P., ZHANG, Z., LI, L. H., GAO, G. D., ZHOU, X. F. & WANG, T. H. 2018. Neural Stem Cell Transplantation Promotes Functional Recovery from Traumatic Brain Injury via Brain Derived Neurotrophic Factor-Mediated Neuroplasticity. *Mol Neurobiol,* 55**,** 2696-2711.
XIONG, M., TAO, Y., GAO, Q., FENG, B., YAN, W., ZHOU, Y., KOTSONIS, T. A., YUAN, T., YOU, Z., WU, Z., XI, J., HABERMAN, A., GRAHAM, J., BLOCK, J., ZHOU, W., CHEN, Y. & ZHANG, S. C. 2021. Human Stem Cell-Derived Neurons Repair Circuits and Restore Neural Function. *Cell Stem Cell,* 28**,** 112-126 e6.
XIONG, Y., MAHMOOD, A. & CHOPP, M. 2013. Animal models of traumatic brain injury. *Nature Reviews Neuroscience,* 14**,** 128-142.
YAMAGUCHI, Y. 2000. Lecticans: Organizers of the brain extracellular matrix. *Cellular and Molecular Life Sciences,* 57**,** 276-289.
YAMANAKA, S. 2020. Pluripotent Stem Cell-Based Cell Therapy-Promise and Challenges. *Cell Stem Cell,* 27**,** 523-531.
YAN, F., LI, M., ZHANG, H. Q., LI, G. L., HUA, Y., SHEN, Y., JI, X. M., WU, C. J., AN, H. & REN, M. 2019. Collagen-chitosan scaffold impregnated with bone marrow mesenchymal stem cells for treatment of traumatic brain injury. *Neural Regen Res,* 14**,** 1780-1786.
YAN, Y., LI, X., GAO, Y., MATHIVANAN, S., KONG, L., TAO, Y., DONG, Y., LI, X., BHATTACHARYYA, A., ZHAO, X. & ZHANG, S. C. 2024. 3D Bioprinting of Human Neural Tissues with Functional Connectivity. *bioRxiv*.
YAN, Z. J., ZHANG, P., HU, Y. Q., ZHANG, H. T., HONG, S. Q., ZHOU, H. L., ZHANG, M. Y. & XU, R. X. 2013. Neural stem-like cells derived from human amnion tissue are effective in treating traumatic brain injury in rat. *Neurochem Res,* 38**,** 1022-33.
YANG, H., KIM, J., KIM, Y., JANG, S.-W., SESTAN, N. & SHIM, S. 2020. Cux2 expression regulated by Lhx2 in the upper layer neurons of the developing cortex. *Biochemical and Biophysical Research Communications,* 521**,** 874-879.
YANG, L., BENARDO, L. S., VALSAMIS, H. & LING, D. S. 2007. Acute injury to superficial cortex leads to a decrease in synaptic inhibition and increase in excitation in neocortical layer V pyramidal cells. *J Neurophysiol,* 97**,** 178-87.
YANG, X., LI, X., YUAN, Y., SUN, T., YANG, J., DENG, B., YU, H., GAO, A. & GUAN, J. 2022. 40 Hz Blue LED Relieves the Gamma Oscillations Changes Caused by Traumatic Brain Injury in Rat. *Front Neurol,* 13**,** 882991.
YENTUR, Z., KAGERMEIER, T., SARIEVA, K., JARBOUI, M. A., BECKER, K. & MAYER, S. 2025. Human dorsal forebrain organoids show differentiation-state-specific protein secretion. *iScience,* 28**,** 112935.
YU, S. P., TUNG, J. K., WEI, Z. Z., CHEN, D., BERGLUND, K., ZHONG, W., ZHANG, J. Y., GU, X., SONG, M., GROSS, R. E., LIN, S. Z. & WEI, L. 2019. Optochemogenetic Stimulation of Transplanted iPS-NPCs Enhances Neuronal Repair and Functional Recovery after Ischemic Stroke. *J Neurosci,* 39**,** 6571-6594.

YU, X. & ZECEVIC, N. 2011. Dorsal radial glial cells have the potential to generate cortical interneurons in human but not in mouse brain. *Journal of Neuroscience,* 31**,** 2413-2420.

YUAN, H., CORBI, N., BASILICO, C. & DAILEY, L. 1995. Developmental-specific activity of the FGF-4 enhancer requires the synergistic action of Sox2 and Oct-3. *Genes & development,* 9**,** 2635-2645.

YUSTE, R., PEINADO, A. & KATZ, L. C. 1992. Neuronal domains in developing neocortex. *Science,* 257**,** 665-9.

ZAMPONI, M., MOLLICA, P. A., KHODOUR, Y., BJERRING, J. S., BRUNO, R. D. & SACHS, P. C. 2023. Combined 3D bioprinting and tissue-specific ECM system reveals the influence of brain matrix on stem cell differentiation. *Frontiers in Cell and Developmental Biology,* 11.

ZECEVIC, N., CHEN, Y. & FILIPOVIC, R. 2005. Contributions of cortical subventricular zone to the development of the human cerebral cortex. *J Comp Neurol,* 491**,** 109-22.

ZHANG, C., SAATMAN, K. E., ROYO, N. C., SOLTESZ, K. M., MILLARD, M., SCHOUTEN, J. W., MOTTA, M., HOOVER, R. C., MCMILLAN, A., WATSON, D. J., LEE, V. M., TROJANOWSKI, J. Q. & MCINTOSH, T. K. 2005. Delayed transplantation of human neurons following brain injury in rats: a long-term graft survival and behavior study. *J Neurotrauma,* 22**,** 1456-74.

ZHANG, K., JIANG, Y., WANG, B., LI, T., SHANG, D. & ZHANG, X. 2022. Mesenchymal Stem Cell Therapy: A Potential Treatment Targeting Pathological Manifestations of Traumatic Brain Injury. *Oxid Med Cell Longev,* 2022**,** 4645021.

ZHANG, Y., PAK, C., HAN, Y., AHLENIUS, H., ZHANG, Z., CHANDA, S., MARRO, S., PATZKE, C., ACUNA, C. & COVY, J. 2013. Rapid single-step induction of functional neurons from human pluripotent stem cells. *Neuron,* 78**,** 785-798.

ZHANG, Z., JIAO, Y. Y. & SUN, Q. Q. 2011. Developmental maturation of excitation and inhibition balance in principal neurons across four layers of somatosensory cortex. *Neuroscience,* 174**,** 10-25.

ZHANG, Z.-X., GUAN, L.-X., ZHANG, K., ZHANG, Q. & DAI, L.-J. 2008. A combined procedure to deliver autologous mesenchymal stromal cells to patients with traumatic brain injury. *Cytotherapy,* 10**,** 134-139.

ZHAO, J. Y., ZHOU, Y., ZHOU, C. W., ZHAN, K. B., YANG, M., WEN, M. & ZHU, L. Q. 2025. Revisiting the critical roles of reactive microglia in traumatic brain injury. *Int J Surg,* 111**,** 3942-3978.

ZHAO, S., NICHOLS, J., SMITH, A. G. & LI, M. 2004. SoxB transcription factors specify neuroectodermal lineage choice in ES cells. *Molecular and Cellular Neuroscience,* 27**,** 332-342.

ZHENG, Y., WU, G., CHEN, L., ZHANG, Y., LUO, Y., ZHENG, Y., HU, F., FOROUZANFAR, T., LIN, H. & LIU, B. 2021. Neuro-regenerative imidazole-functionalized GelMA hydrogel loaded with hAMSC and SDF-1alpha promote stem cell differentiation and repair focal brain injury. *Bioact Mater,* 6**,** 627-637.

ZHOU, L., WOLFES, A. C., LI, Y., CHAN, D. C. W., KO, H., SZELE, F. G. & BAYLEY, H. 2020. Lipid-Bilayer-Supported 3D Printing of Human Cerebral Cortex Cells Reveals Developmental Interactions. *Adv Mater,* 32**,** e2002183.

ZHU, B., EOM, J. & HUNT, R. F. 2019. Transplanted interneurons improve memory precision after traumatic brain injury. *Nat Commun,* 10**,** 5156.

ZHU, Q., MISHRA, A., PARK, J. S., LIU, D., LE, D. T., GONZALEZ, S. Z., ANDERSON-CRANNAGE, M., PARK, J. M., PARK, G. H., TARBAY, L., DANESHVAR, K., BRANDENBURG, M., SIGNORETTI, C., ZINSKI, A., GARDNER, E. J., ZHENG, K. L., ABANI, C. P., HU, C., BEAUDREAULT, C. P., ZHANG, X. L., STANTON, P. K., CHO, J. H., VELISEK, L., VELISKOVA, J., JAVED, S., LEONARD, C. S., KIM, H. Y. & CHUNG, S. 2023. Human cortical interneurons optimized for grafting specifically integrate, abort seizures, and display prolonged efficacy without over-inhibition. *Neuron,* 111**,** 807-823 e7.

ZOU, J., WANG, Y.-X., DOU, F.-F., LÜ, H.-Z., MA, Z.-W., LU, P.-H. & XU, X.-M. 2010. Glutamine synthetase down-regulation reduces astrocyte protection against glutamate excitotoxicity to neurons. *Neurochemistry international,* 56**,** 577-584.

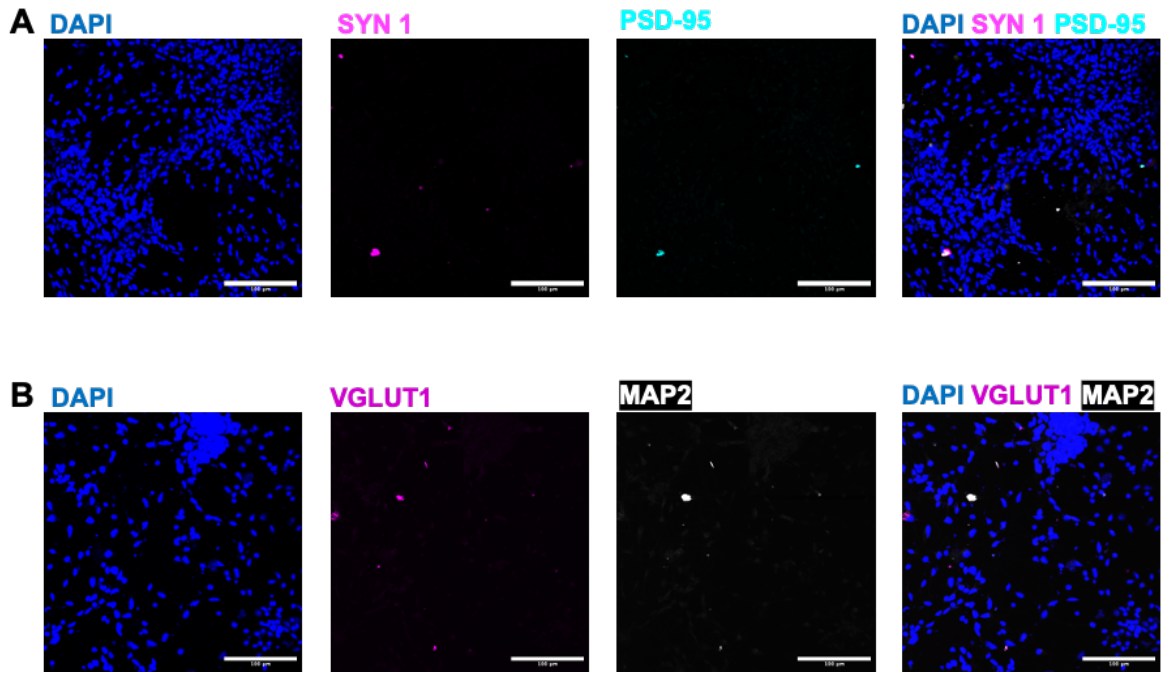

Figure 6.1 Negative controls of immunocytochemistry
(A) Representative confocal images of negative control staining of SYN1 and PSD-95.
(B) Representative confocal images of negative control staining of VGLUT1 and MAP2 channels show no specific immunoreactivity above background. Scale bar: 100 µm

Table 6.1 Cell culture consumables used for human iPSC culture and neuronal differentiation

Item	Final conc.	Stock conc.	Supplier	Catalogue no.
Advanced DMEM/F-12	–	–	Gibco® Life Technology	12634010
BrainPhys™ Imaging Optimized Medium	–	–	STEMCELL Technologies	5796
BrainPhys™ Neural Medium	–	–	STEMCELL Technologies	5792
Distilled water	–	–	Life Technologies	15230089
DPBS	–	–	Sigma-Aldrich Corporation	D8537
Geltrex™ LDEV-Free hESC-qualified Reduced Growth Factor	–	–	Gibco® Life Technology	A1413302
Laminin (LAM)	–	–	Sigma-Aldrich Corporation	L2020-1MG
mTeSR™ Plus Medium	–	–	STEMCELL Technologies	1027-076
Penicillin-Streptomycin	1%	100%	Gibco® Life Technology	15140122
Poly-ornithine (PO)	–	–	Sigma-Aldrich Corporation	P4957-50ML
StemPro Accutase	–	–	Life Technologies	A1110501
UltraPure 0.5 M EDTA	0.5 mM	0.5 M	Gibco® Life Technology	15575020
Y-27632 dihydrochloride (ROCK inhibitor)	10 µM	10 mM	STEMCELL Technologies	72304-5mg
Dimethyl Sulfoxide (DMSO)	10%	–	Sigma-Aldrich Corporation	D2650-100ML

Table 6.2 Consumables used for RNA extraction, cDNA synthesis, and qPCR

Item	Final conc.	Stock conc.	Supplier	Catalogue no.
LunaScript™ RT SuperMix Kit	–	–	New England Biolabs	E3010L
Monarch® Total RNA Miniprep Kit	–	–	New England Biolabs	T2010S
Luna® Universal qPCR Master Mix	–	–	New England Biolabs	M3003L
MicroAmp™ Fast Optical 96-Well Reaction Plate	–	–	Life Technologies	4346906

Table 6.3 Reagents used for calcium imaging experiments

Item	Final conc.	Stock conc.	Supplier	Catalogue no.
Fluo-4 AM	5 µM	1 mM (in DMSO)	Thermo Fisher Scientific	F14201
Fura-Red AM	12 µM	1 mM (in DMSO)	Thermo Fisher Scientific	F3021
Pluronic Acid F-127	0.125 %	20% (in DMSO)	Thermo Fisher Scientific	P3000MP
Picrotoxin	50 µM	10 mM in DMSO	Tocris	1128
GABA	100 µM	50 mM in water	Abcam	ab120359
Glutamate	30 µM	50 mM in Water	Abcam	ab120049
Tetrodotoxin citrate (TTX)	1 µM	1 mM Water	Tocris	1096
EGTA	4 mM	-	Sigma-Aldrich Corporation	E3889

Table 6.4 Consumables used for immunostaining, viability assays, and stereotaxic injection

Item	Final conc.	Stock conc.	Supplier	Catalogue no.
Ibidi µ-Slide 18 Well	–	–	Thistle Scientific	SKU 81816
Ibidi 4-well Ph+ plates	–	–	Thistle Scientific	80446
Ibidi Stage Top Incubator	–	–	Thistle Scientific	10720
Paraformaldehyde (PFA) 4%	4%	4%	Thermo Fisher Scientific	J61899.AK
Glycine 1 M Solution	–	–	Merck	67449-1ML-F
Triton X-100	–	X100	Thermo Fisher Scientific	85111
Normal Donkey Serum	–	–	Abcam	ab7475
DAPI Solution	1X	10,000X	Merck	MBD0015-1ML
Calcein-AM	1 µM	1 mg	Cambridge Bioscience	CAY14948
Propidium Iodide (PI)	100 µg/mL	10 mg	Sigma-Aldrich Corporation	P4170
Trypan Blue Solution, 0.4%	–	0.4%	Thermo Fisher Scientific	15250061

Vybrant™ DiI Cell-Labelling Solution	5 µM	–	Thermo Fisher Scientific	V22885
Hoechst 33258, pentahydrate (bis-benzimide)	1 µg/mL	–	Thermo Fisher Scientific	62249
Bovine Serum Albumin (BSA)	–	–	Sigma-Aldrich Corporation	A9418
FluorSave Reagent	–	–	Merck	4204990
Fast Green FCF	0.1X	–	Sigma-Aldrich Corporation	F7252
Mineral oil	–	–	Sigma-Aldrich Corporation	M8410
Compression Fitting, Removable Needle (RN) to 1/16" O.D. PEEK Tubing	–	–	Hamilton Company	55751-01
10 µL, Microliter Syringe, Removable Needle (RN)	–	–	Hamilton Company	80330
Clinell 2% Chlorhexidine in 70% Alcohol Surface Wipes	–	–	Zedmed	CA2C240
Stoelting Quintessential Stereotaxic Injector	–	–	Stoelting	53311
Solution for Injection for Dogs and Cats, Meloxicam	1 mg/kg	5mg/mL	Boehringer	–
4-Aminopyridine (4-AP)	200 µM	–	Abcam	Ab120122
Fresh razor blade	–	–	Scientific Laboratory Supplies Limited	BH10
Vetbond Tissue Adhesive	–	–	The Vetstore	1469

Table 6.5 List of primary antibodies

Target	Original species	Manufacturer (Cat. no.)	Dilution factor
SOX2	Goat	R&D Systems (AF2018)	1:200
PAX6	Rabbit	BioLegend (901302)	1:200
OCT4	Rabbit	Millipore (C30)	1:100
NANOG	Rabbit	Millipore (A30)	1:100
SOX10	Rabbit	Cell Signaling (D6D9)	1:100
Nestin	Rabbit	Abcam (ab5968)	1:2000
DCX	Rabbit	Abcam (ab15723)	1:200
TBR2	Rabbit	Abcam (ab23345)	1:200
CUX1	Goat	Santa Cruz (sc-514008)	1:1000
NeuN	Mouse	Millipore (MAB377)	1:400
MAP2 (clone 5F9)	Mouse	Millipore (05-346)	1:200
GABA	Rabbit	Sigma (A2052)	1:200
Ki-67	Rat	eBioscience (14-5698-82)	1:200
pHH3	Mouse	Abcam (ab180577)	1:200
CTIP2	Rat	Abcam (ab18465)	1:200
VGLUT1	Rat	Synaptic Systems (135303)	1:200
BRN2	Mouse	Abcam (ab243045)	1:200
SATB2	Rabbit	Abcam (ab92446)	1:200
hNCAM	Rabbit	Abcam (ab75813)	1:200
TUJ1	Mouse	Abcam (ab78078)	1:1000

TBR1	Rabbit	Abcam (ab10554)	1:200
Synapsin-1	Rabbit	Abcam (ab254349)	1:500
MAP2	Chicken	Abcam (ab5392)	1:1000
PSD-95	Mouse	Abcam (ab13552)	1:500
HuNu	Mouse	Merck (MAB1281)	1:200
PSD-95	Guinea Pig	Synaptic Systems (124014)	1:500
Human Synaptophysin	Mouse	Invitrogen (14-6525-80)	1:500
Cleaved Caspase-3	Rabbit	Cell Signalling (9661s)	1:200
S100β	Mouse	Sigma (S2532)	1:200
GFAP	Rat	Invitrogen (13-0300)	1:200
Iba1	Goat	Abcam (ab5076)	1:200
Human RORβ	Mouse	Perseus Proteomics (PP-N7927-00)	1:50

Table 6.6 List of Secondary Antibodies

Target species	Host species	Fluorophore	Manufacturer (Cat. no.)	Dilution
Rabbit	Donkey	Alexa Fluor 568	Invitrogen (A10042)	1:500
Rabbit	Donkey	Alexa Fluor 647	Invitrogen (A31573)	1:500
Goat	Donkey	Alexa Fluor 488	Invitrogen (A11055)	1:500
Mouse	Donkey	Alexa Fluor 647	Invitrogen (A31571)	1:500
Mouse	Donkey	Alexa Fluor 488	Invitrogen (A21202)	1:500
Rat	Chicken	Alexa Fluor 647	Invitrogen (A21472)	1:500
Guinea Pig	Goat	Alexa Fluor 568	Invitrogen (A11075)	1:500

Table 6.7 Consumables used for the droplet-based microfluidic technique

Item	Final conc.	Stock conc.	Supplier	Catalogue no.
Fluorinert™ FC-40	–	–	Sigma-Aldrich Corporation	F9755
Braun 5 mL Injekt syringe	–	–	Thermo Fisher Scientific	4606051V
Braun 1 mL Injekt-F fine dosage syringe	–	–	Thermo Fisher Scientific	9166017V
Corning® Matrigel® Growth Factor Reduced (GFR) Basement Membrane Matrix, LDEV-free, 10 mL	–	–	Corning	354230
Masterflex® microbore transfer tubing (size 11)	–	–	Emtechnik	MFLX06417-11
Masterflex® microbore transfer tubing (size 21)	–	–	Emtechnik	MFLX06417-21
Masterflex® microbore transfer tubing (size 31)	–	–	Emtechnik	MFLX06417-31
Sylgard® 184 Silicone Elastomer Kit	–	–	Dow	01673921
Vacuum desiccator	–	–	Thermo Fisher Scientific	11316984

Table 6.8 General laboratory consumables and plasticware

Item	Final conc.	Stock conc.	Supplier	Catalogue no.
Cryogenic vial, 1.8 mL	–	–	STARLAB	E3090-6222

Pipette tip, 10 µL	–	–	STARLAB	S1121-2710
Pipette tip, 20 µL	–	–	STARLAB	S1120-1710
Pipette tip, 200 µL	–	–	STARLAB	S1126-7810
Pipette tip, 1000 µL	–	–	STARLAB	S1120-8810
6-well tissue culture plate	–	–	Greiner Bio-One	657160
12-well tissue culture plate	–	–	Greiner Bio-One	665180
24-well tissue culture plate	–	–	Greiner Bio-One	662160
48-well tissue culture plate	–	–	Greiner Bio-One	677180
96-well tissue culture plate	–	–	Greiner Bio-One	655180
Stripette, 5 mL	–	–	Scientific Laboratory Supply	4487
Stripette, 10 mL	–	–	Scientific Laboratory Supply	4488
Stripette, 25 mL	–	–	Scientific Laboratory Supply	4489
Micropipettes	–	–	STARLAB	631-0448
MicroAmp™ Optical Adhesive Film	–	–	Thermo Fisher Scientific	4311971
96-Corning® Costar® Ultra-Low Attachment Multiple Well Plate	–	–	Merck	SL3474-24EA
24-Corning® Costar® Ultra-Low Attachment Multiple Well Plate	–	–	Merck	SL3473-24EA

Table 6.9 Frequently used solutions

Buffer / Solution	Components	Amount	Notes
PBS (10X, 1 M, pH 7.4)	Sodium chloride (NaCl)	80 g	Dissolve in dH_2O to 1000 mL
	Potassium chloride (KCl)	2 g	
	Potassium dihydrogen phosphate (KH_2PO_4)	2.4 g	
	Sodium phosphate dibasic (Na_2HPO_4, anhydrous)	14.4 g	
PB (0.1 M, pH 7.4)	Sodium phosphate monobasic (NaH_2PO_4, 0.2 M)	27.8 g in 1000 mL	Solution A
	Sodium phosphate dibasic (Na_2HPO_4, 0.2 M)	28.4 g in 1000 mL	Solution B
	Mix A + B (140 mL A + 360 mL B + dH_2O to 1000 mL)		
Cryoprotectant	Sucrose	300 g	Dissolve in PB 0.1 M to 1000 mL
	Ethylene glycol	300 mL	
ACSF (pH 7.4)	Sodium chloride (NaCl, 126 mM)	7.36 g	Bring to 1000 mL. 300 ± 10 mOsmol/L, Bubble with 95% O_2/5% CO_2.
	Potassium chloride (KCl, 4.9 mM)	0.365 g	
	Potassium dihydrogen phosphate (KH_2PO_4, 1.2 mM)	0.163 g	

	Magnesium sulphate ($MgSO_4$, 2.4 mM)	0.289 g	
	Calcium chloride ($CaCl_2$, 2.5 mM)	0.278 g	
	Sodium bicarbonate ($NaHCO_3$, 26 mM)	2.18 g	
	D-Glucose (10 mM)	1.80 g	
NMDG protective cutting solution (pH 7.4)	N-methyl-D-glucamine (NMDG), 93 mM	18.2 g	
	HCl, 93 mM (to pH 7.4)	—	
	Potassium chloride (KCl, 2.5 mM)	0.186 g	
	Sodium dihydrogen phosphate (NaH_2PO_4, 1.2 mM)	0.144 g	
	Sodium bicarbonate ($NaHCO_3$, 30 mM)	2.52 g	
	HEPES (20 mM)	4.77 g	
	D-Glucose (25 mM)	4.50 g	
	Sodium ascorbate (5 mM)	0.99 g	
	Thiourea (2 mM)	0.152 g	
	Sodium pyruvate (3 mM)	0.330 g	
	Magnesium sulphate ($MgSO_4$, 10 mM)	1.20 g	
	Calcium chloride ($CaCl_2$, 0.5 mM)	0.055 g	
Phenol red-free imaging medium (pH 7.4)	Sodium chloride (NaCl, 121 mM)	7.07124 g	Bring to 1000 mL, 300 ± 10 mOsmol/L, Bubble with 95% O_2/5% CO_2.
	Potassium chloride (KCl, 4.2 mM)	0.313152 g	
	Calcium chloride (CaCl2, 1.1 mM)	1.1 mL	
	Magnesium chloride (Mgcl2, 1mM)	1 mL	
	Sodium bicarbonate (NaHCO3, 22 mM)	1.84822 g	
	D-Glucose (2.5 mM)	0.4504 g	
	NaPyruvate (0.5 mM)	5 mL	
	Serine (0.002 mM)	0.0002102 g	
	Alanine (0.002 mM)	0.0001782 g	
	Glycine (0.002 mM)	0.00015 g	
Phenol red-free calcium-free imaging medium (pH 7.4)	Sodium chloride (NaCl, 121 mM)	7.07124 g	Bring to 1000 mL, 300 ± 10 mOsmol/L, Bubble with 95% O_2/5% CO_2.
	Potassium chloride (KCl, 4.2 mM)	0.313152 g	
	EGTA (4 mM)	1.52 g	

	Magnesium chloride (Mgcl2, 1mM)	1 mL	
	Sodium bicarbonate (NaHCO3, 22 mM)	1.84822 g	
	D-Glucose (2.5 mM)	0.4504 g	
	Na Pyruvate (0.5 mM)	5 mL	
	Serine (0.002 mM)	0.0002102 g	
	Alanine (0.002 mM)	0.0001782 g	
	Glycine (0.002 mM)	0.00015 g	